Hydrodynamics of Turbulent Bores Propagating Over a Canal

Nuri Eltaher Elsheikh

Thesis Submitted to the University of Ottawa in Partial Fulfillment of the Requirements for the Degree of Doctor of Philosophy in Civil Engineering

Department of Civil Engineering
Faculty of Engineering
University of Ottawa

Abstract

Recent tsunami events have inflicted devastating damage to coastal communities. Existing design standards provide a certain level of evaluation of tsunami effects such that critical infrastructure can be designed to resist tsunamis. Tsunami momentum flux, used to design structures is a function of water level height and velocity of tsunami bores. Understanding tsunamis and developing mitigation measures is essential. So far, some mitigation measures have been suggested, and to improve them, further investigations are required. The design of tsunami inundation effects mitigation canals is one of the suggested solutions which has received limited attention.

The first objective of this study was to investigate the effects of a rectangular canal on the hydrodynamics of turbulent bores before and after the canal by conducting a series of physical experiments. A dam-break wave was used to simulate the tsunami-like turbulent waves passing over a smooth and horizontal surface, in the presence and/or absence of a canal. Three canal water depths were used to model shallow, moderate, and deep conditions, and three canal widths were also selected to model narrow to wide conditions while the dam break waves were generated from three different impoundment depths in a reservoir located upstream of the canal. The dam-break wave propagation over a horizontal, dry, and smooth bed revealed four regimes describing the variations of bore height with time. The time to reach the maximum bore height and the quasi steady-state regime were correlated with each impoundment depth and an empirical formulation was proposed to estimate the onset of the quasi steady-state flow. The maximum bore heights measured before and after the mitigation canal location were approximately 40 % and 50 % respectively, higher compared with those recorded in the corresponding tests without the presence of a canal.

The second objective of this study was to experimentally investigate the effects of canal depth on the time history of bore height and its velocity. The experimental results were used for calibration and validation of a developed numerical model. The rapid release of an upstream impoundment water depth was employed to generate a bore analogous to a tsunami-induced inundation. The time histories of wave heights and velocity were measured upstream and downstream of the canal. The recorded time-series of the water surface levels and velocities were compared with the simulation results and good agreement was found between experimental and numerical water surface profiles using a Root Mean Square Error (RMSE) and the Relative Error. Three turbulence models:, namely the standard k-ε, the Realizable k-ε, and the RNG k-ε were tested, and it was found that all turbulence models perform well but the standard k-ε model provided satisfactory accuracy. The velocity contour plots for shallow, medium, and deep mitigation canals showed the formation and evolution of jets of different characteristics. The energy dissipation and air bubble entrainment of the tsunami bore, as it plunged into a canal, increased as the canal depth increased, and the jet flow of the maximum bore velocity decreased with increased canal depth. It was found that the eye of the vortex in the canal moved steadily in the downstream direction. Generally, the bore fully plunged almost nearly into the middle of the canal and started to divide into two small vortices.

The third objective of this study dealt with a sequence of numerical experiments conducted to investigate the impact of mitigation canals on the hydrodynamics of a tsunami-like turbulent bore moving across a flat bed. The effects of mitigation canal depth and its orientation on the reduction of maximum specific momentum and energy of turbulent bores crossing over it were investigated numerically. Variations in the ratio between the downstream and upstream maximum specific momentum and mean flow energy decreased as the canal depth increased, and the time history of the mean flow energy over a canal with a rectangular endwise profile revealed that the canal depth affects the jet stream of the maximum mean flow energy. As the canal depth increased, the period of time needed to dissipate the area of the jet stream with the maximum turbulent kinetic energy, vorticity, and energy dissipation rate decreased. Both the angled and perpendicular to flow direction canals caused the maximum specific momentum and energy of the turbulent bore to decrease downstream of the canal. The specific momentum and energy achieved their highest values for a canal orientation of 45º. The greatest reductions in maximum specific momentum for turbulent bores over canals with different depths and orientations were achieved for $\theta = 30°$.

Acknowledgement

I would first like to begin by expressing my utmost gratitude to my uOttawa supervisors, Professor Ioan Nistor, Professor Majid Mohammadian, and Associate Professor Amir Azimi, for all they have done. They gave me genuine direction, opportunities, and backing all through my Ph.D. studies, and their oversight, significant guidance, and comments have been tremendously appreciated. Together, they ignited my interest, assisted me in my development as a nascent scientist, and made my Ph.D. studies a highly rewarding experience. Without their backing and support, nothing would have been achieved.

I would also like to extend my thanks to expert laboratory technicians Mr. Mark Lapointe and Mr. Leo Denner, who provided great assistance and support, and who led the tests at uOttawa's Water Resources Engineering Laboratory. I would likewise like to thank several graduate students from France, who assisted me in various ways with this project.

It is difficult to adequately articulate the appreciation I feel for my parents. They have provided me with solace and support for as long as I can remember, particularly during my Ph.D. studies, despite us being far away from one another. It is to them that I credit my future accomplishments due to their endless help and love, and every part of this thesis is dedicated to them. Thank you as well to my deeply cherished brothers, sisters, and nieces for their reassurance, making seemingly impossible goals feel conceivable. Many thanks to my grandmother, uncles, and aunts for always being close at heart, commending my victories and lending me strength during the difficult periods.

Finally, I would like to recognize the University of Ottawa Ph.D. International Scholarship Program and the support of the NSERC Discovery grants held by Professors Nistor and Mohammadian which enabled my Ph.D. studies. I would also like to thank the Libyan Government for the scholarship they provided to me.

Table of Contents

List of Figures

List of Tables

List of Symbols

B	Flume width (m)
C_d	Drag coefficient (-)
C_o	Courant number (-)
C_α	The compression coefficient (-)
d	Canal depth (m)
d_o	Equivalent impoundment depth (m)
E	Specific energy (m)
E_L	Energy losses (m)
E_1	Specific energy upstream of the canal (m)
E_2	Specific energy downstream of the canal (m)
e/D	Pipe gap ratio (-)
f	Darcy-Weisbach friction factor (-)
Fr	Froude number (-)
Fr_1	Froude number upstream of the canal (-)
Fr_2	Froude number downstream of the canal (-)
g	Gravitational acceleration (m/s^2)
h	Water surface elevation (m)
h_1	Upstream water level (m)
h_2	Downstream water level (m)
h_d	Initial downstream water depth (m)
h_o	Maximum wave height without canal (m)
h_{max}	Maximum wave height with canal (m)
h_u	Initial upstream water depth (m)
hu^2	Momentum flux (m^3⁄s^2)
$(hu^2)_{max}$	Flux of the momentum / mass / width or maximum moment flux (m^3⁄s^2)
k	Turbulent kinetic energy (m^2⁄s^2)
K	Mean flow energy (m^2⁄s^2)
L	Reservoir length (m)
L/d_o	Reservoir aspect ratio (m)
$\bar{p}$	The mean fluid pressure component (N⁄m^2)
$\acute{p}$	The fluctuation fluid pressure component (N/m^2)
P	Fluid Pressure (Pa)
q	Flow discharge per unit width (m^2/s)
Re	Reynold number (-)
t	Time since gate opening (s)
t_o	Gate opening time (s)
t_*	Time since the surge front plunges into the canal (s)
t_q	Quasi steady-state time (s)

T_o	Non-dimensional removal time for the gate (-)
t/T	Non-dimensional time (-)
u	Turbulent surge velocity (m/s)
u_{max}	Maximum flow velocity or maximum depth-averaged velocity (m/s)
U	Wave front celerity (m/s)
U	Flow velocity (m/s)
$\boldsymbol{U}$	The velocity vector (m/s)
U_c	The compression velocity vector (m/s)
V	Bore front velocity (m/s)
w	Canal width (m)
We	Weber number (-)
w/d	Canal aspect ratio (-)
x	Distance in the flow direction (m)
x_s	Wave front location (m)
x/w	Ratio of horizontal distance of the vortex eye from the upstream wall of the canal with canal width (-)
y/d	Ratio of vertical distance of the vortex eye from the bottom of the canal with canal depth (-)
z	Vertical distance from the flume bed (m)
x, y, z	x-y-z components of position vector (m)
u, v, w	Components of velocity in the x-, y-, and z-directions, respectively (m/s)
$\bar{u}, \bar{v}, \bar{w}$	Components of mean velocity in the x-, y-, and z-directions, respectively (m/s)
u', v', w'	Turbulent fluctuation of velocity in the x-, y-, and z-directions, respectively (m/s)
g_x, g_y, g_z	x, y, z components of gravitational acceleration (m/s^2)
$\boldsymbol{\alpha}$	Constant (-)
α	Phase fraction (-)
k	Turbulent kinetic energy (m^2/s^2)
ε	Turbulent kinetic energy dissipation rate (m^2/s^3)
ν	Kinematic viscosity (m^2/s)
μ_t	Turbulent dynamic viscosity (N.s)/m^2)
μ	Dynamic viscosity ((N.s)/m^2)
θ	Canal orientation angle (°)
ρ	The density of the air-water mixture (kg/m^3)
ρ_a	The density of the air (kg/m^3)
ρ_w	The density of the water (kg/m^3)
τ	Stress tensor (pa)
σ	Standard deviation (m)
σ	Surface tension (N/m)
ω	Vorticity (Hz)
∇	Gradient
$\nabla.$	Divergence

List of Abbreviations

ADV	Acoustic Doppler Velocimeter
ASCE	American Society Civil Engineers
BR	Blockage ratio = structure width / flume width
CFD	Computational Fluid Dynamics
DES	Detached Eddy Simulation
DNS	Direct Numerical Simulation
DOF	Degree of Freedom
FEMA	Federal Emergency Management Agency
FVM	Finite Volume Method
LES	Large Eddy Simulation
NS	Navier-Stokes
NSE	Navier-Stokes Equation
MPS	Moving Particle Semi-implicit method
OpenFOAM	Open Field Operation And Manipulation
PED	Partial Differential Equation
PISO	Pressure Implicit with Splitting of Operators
PVC	Polyvinyl Chloride
RAS	Reynolds-Averaged Simulations
RANS	Reynolds-Averaged Navier-Stokes
RHS	Right Hand Side
RMSE	Root Mean Square Error
SGS	Sub-Grade Scale
SPH	Smoothed Particle Hydrodynamics
URANS	Unsteady Reynolds-Averaged Navier-Stokes
US	Ultrasonic Sensor
VOF	Volume of Fluid
WCSPH	Weakly Compressible Smoothed Particle Hydrodynamics
WG	Wave Gauge
3D	Three Dimensional

1 Introduction

1.1 Research needs and motivation of the study

Tsunamis, landslide-generated impulse waves, storm surges, and high floods do not occur very often, but are extremely damaging phenomena of coastal regions worldwide (Wüthrich et al. 2019). A tsunami is a naturally arising successive wave train which is generated when there is a rapid, large-scale disturbance of a volume of water which sets it in motion. Earthquakes near or below the ocean bed are the most common generating events, but a tsunami can also result from undersea slumps, volcanic activity, and impacts of extraterrestrial objects. The waves produced by these disruptions move extremely far away from the source (FEMAP646, 2012). Previously, the effects of hydrodynamic waves on structures and structural components were considered to be uncommon occurrences, and forces induced on infrastructure which are caused by these waves were generally ignored in the design procedures. Many reconnaissance missions conducted in the form of post-tsunami forensic engineering have shown that several buildings were destroyed or at least severely damaged during such events, even though they were previously assumed to be invulnerable to tsunamis (Nistor et al. 2005; Ghobara et al. 2006; Yeh et al. 2013). In addition, the comprehensive tsunami design literature review revealed that hydrodynamic forces occurring during tsunami inundation are not adequately taken into account when designing structures situated in tsunami-vulnerable areas (Nistor et al. 2009). In contrast to seismic forces, hydrodynamic forces were not investigated at the time of designing near-shore structures. The solid theoretical background of dam-break waves was employed to describe the behavior of hydrodynamic waves as their waves have similar behavior. Recently, several catastrophic events have occurred in the following regions: Indian Ocean (2004), Chile (2010), Japan (2011, Figure 1.1), and Indonesia (2018) with vast casualties and devastation.

Figure 1.1 Tsunami inundation advancing inland during the 2011 Tsunami in Japan Reprinted with permission from (Rajaie, et al. 2022) (2022, ASCE).

They revealed that benchmarks and measures had to be taken into consideration to decrease reconstruction costs and guarantee human safety in coastal regions (Wüthrich et al. 2017). A tsunami wave can reach the shore as either a crest-lead or trough-lead wave, with the usual period ranging from 10 to 45 min. In deep water, the wave velocity can approach speeds of up to 800 km/hr in the open sea regions and the wave is able to propagate across whole ocean basins with minimal loss of energy. Due to the very small steepness of tsunami waves in the deep sea, they can propagate beneath ocean ships without being observed or felt by anyone on board. In an example of the existence of a tsunami going unobserved, which struck Honshu, Japan, on June 15, 1896, fishermen in boats located nearly 32 km offshore did not notice the passing tsunami wave because its height at that location was less than 0.4 m. During previous tsunamis, eyewitnesses reported the water recession at coasts ahead of the arrival of the first tsunami wave (Al-Faesly, 2016). Thus, in shallow water near coastal areas, wave celerity can decrease to tens of km/hr. The height of a tsunami near the coast is related to the coastal bathymetry and can vary considerably in the longshore direction. Based on the features of the tsunami and the bathymetry, the leading edge of the wave can break even before arriving inland as a turbulent bore, as portrayed in Figure 1.2. For other examples, the tsunami is likely to propagate inland in the fashion of a fast-moving tide (a surge) when the situations are conducive (Douglas, 2016).

Figure 1.2. The surge generated from the first tsunami waves advancing nearly 1.5 km inland from the bay-front, by the 2011 Iwate Prefecture, Tohoku tsunami, Japan (Asadollahi, 2016).

Tsunamis are a threat to coastal areas and endanger the lives of inhabitants living there. Hence, horizontal evacuation to inland high enough locations is one mitigation strategy, but it requires a sufficient warning time to be accomplished efficiently. Thus, researchers concentrate on the urgent need to develop adequate warning systems for tsunamis, training designed to raise awareness and consciousness of an imminent tsunami threat and help evaluate the tsunami danger regions in time. Though, in several scenarios, tsunami warning systems were unable to properly report the near-source tsunami occasions. Besides, when the coastal areas struck are at low elevations, the horizontal evacuation would not significantly decrease the massive social, economic,

environmental harms. In this scenario, tsunami-resistant vertical evacuation structures can become the ultimate mitigation plan. Thus, researchers need to comprehend tsunami-exerting forces and specify the appropriate structure to resist the tsunami impact and associated loading forces (Sarjamee, 2016). The 2011 Tsunami inundation height alongside the Tohoku coastline was in the range of 5 to 35+ m. Under such loads, light-frame residential construction affected by inundation height of one story or more mostly break down. Such destruction occurred in approximately 100% of all regions affected by tsunami. In addition, 75%-95% of the low-rise structures were devastated in the inundated commercial and industrial areas, as the higher breakdown ratio happened as the tsunami height approached the upper range (Figure 1.3) (FEMAP646, 2012).

Figure 1.3. The near shore complete collapse of Minamisanriku (courtesy of I. Nistor, ASCE, 2012).

According to (FEMAP646, 2012), based on their origin, tsunamis are classified into three: far-source ($t > 2$ hrs), mid-source (30 min $< t <$ 2 hrs) and near-source ($t <$ 30 min). This is defined based on the time (Approximate Warning Time) required for the wave to approach a coastline from the position of the activating event. These above classifications provide a summary of the estimated warning times connected with the distance between a coastline and the position of the triggering event. As it can be seen, the latter is one in which very destructive tsunami waves can approach and strike the position with very little warning time of less than 30 minutes. Thus, the motivating strategy of mitigation may be deemed impractical. For instance, the 1993 tsunami that struck Okushiri, Hokkaido, Japan (Figure 1.4) arrived at the coastline within 5 minutes after the earthquake, and resulted in about 202 victims as many victims were struck by debris damming and were unable to flee toward safe locations, something which was a real surprise for the local community.

Figure 1.4. Devastation produced by the 1993 Okushiri Tsunami, Japan (FEMAP646, 2012).

In the United States, tsunami design criteria were not specifically developed until recently. As a consequence, substantial hazards resulted from the neglect of building engineering design in coastal area. Previously, the U.S. had mostly focused on evacuation planning rather than tsunami hazard maps that would be relevant to the design of resilient structures (Chock, 2015; Chock, 2016). However, Japan is not the only country around the Pacific at-risk area for tsunami strikes. The vulnerability of the five western states of North America have also been identified in a general regional assessment as an at-risk area for tsunami hazard. The American Society of Civil Engineers (ASCE) added a new chapter (Chapter 6) in the ASCE7-22, concentrating on Tsunami Loads and Effects, based on this risk as well as the extreme damage and destruction witnessed from the 2004 Indian Ocean and 2011 Tohoku Tsunami (Chock, 2016). Hence, the design requirements for tsunami loads and effects were introduced in these provisions (ASCE, 2022).

In addition to emergency preparedness for evacuation, the mitigation of tsunami hazard to allow recovery needs supporting structural flexibility of infrastructure, necessary facilities, and significant resources is required for a rapid response and social and economic recovery (Chock, 2015). Based on the ASCE 7-22 Standard, facilities are categorized in agreement with Risk Categories (four risk categories I, II, III, and IV) that cover the criticality or importance of the facility (ASCE, 2022). The ASCE 7-22 Standard indicated that the tsunami design requirements differ by tsunami risk category and height. The low-rise Risk Categories I and II are not subject to the ASCE tsunami provisions. Thus, the provisions are applied to Risk Category III and Risk Category IV buildings in the Tsunami Design Zone. When tsunami emergency preparedness and warning system strategies for evacuation enable communities with public awareness, low-rise Risk Category II structures are not expected to be occupied for the duration of a tsunami. Besides that, fleeing from the submerged region is impossible during the short time, and people are going to occupy higher structures to avoid the tsunami flooding (for instance, the scenario of Japan in 2011),

and tenants anticipate that such high-rise buildings will stay resilient and safe during the tsunami (Chock, 2015). The threshold height of the Risk Category II buildings equals approximately 20 m (65ft); thus, tsunami-resilient design is chosen to be implemented via Risk Category II. This recommended height became sufficient and in agreement with reasonable economic costs and reliable safety. Risk Category II buildings are often constructed in the tsunami-prone zones; however, such structures need not be designed for tsunami forces. Accordingly, operational response procedures and evacuation maps are still required for society (Chock, 2015).

Vertical Evacuation Refuge Structures represent a specific categorization of structures and buildings that is implemented within the tsunami impact zone. These vertical evacuations are considered as *alternative evacuation structures* where high land does not exist, or the available time following the warning of a tsunami is not sufficient to fully complete the evacuation before the arrival of the tsunami. Therefore, these structures and buildings must have the capacity to withstand the impact of the Maximum Considered Tsunami (2% possibility of being exceeded in 50 years, or a 2475-year mean repetition interval) (Chock, 2015; Chock, 2016). Despite the extreme and complete destruction and damage of the 2011 Tohoku Tsunami alongside Japan's northeast Honshu Island coastline, safe shelter for hundreds of survivors was provided by many tsunami evacuation buildings (Fraser et al., 2012).

In open sea, tsunami waves have very long wavelengths when compared to the water depth. For this reason, the shallow water-wave equations have been used to model tsunami waves (Al-Faesly, 2016). Occasionally, the first wave crest could be smaller than the second or third one, and by the time the first wave has already flooded the dry bed, a subsequent tsunami wave crest could proceed inland over a wet bed as a tsunami bore. Therefore, the design loads should be based on the possible hydrodynamic conditions, which are the tsunami surge traveling on dry ground and the tsunami bore spreading over a wet bed (Goseberg et al. 2016).

The tsunami that struck Japan in 2011 has offered a lot of precious practical lessons about the devastating effects and potential impact of such events. Owing to the underestimated potential of the tsunami, sea dikes and breakwaters alongside the Sendai coast were damaged, and as a result, scientists were given clues about tsunami waves in order to build highly robust structures capable of mitigating their effects. Understanding the interaction of waves with breakwaters in coastal areas is essential for hydraulic structure design (Dao et al., 2012; Dao et al., 2013). Many studies have been carried out to investigate the impact of natural and artificial structures, including pine tree forests, coastal headlands, cliffs, and dunes in mitigating tsunami inundations and energy to a substantial degree by reflecting the energy of a tsunami in the seaward direction based on the flow depth to ground elevation aspect ratio. Coastal vegetation has been broadly known as a natural way to diminish the momentum and energy of tsunami waves (Tanaka, 2009; Nandasena et al., 2012); moreover, it has been proven that the current common protective constructions, such as dikes, seawalls, and breakwaters, cannot be the only countermeasures against such catastrophic natural disasters in coastal areas (Rahman et al., 2017).

As a result of field investigations following the 2011 Tohoku Tsunami regarding the levee constructed alongside the Teizan Canal in Sendai City, and taking into account the different levels of damage to the forests in this region, Tokida and Tanimoto (2012) discovered a crucial lesson that the water pool created by the inundation stream, known as the "drug pool", is beneficial in decreasing the velocity of the tsunami inundation (Dao et al., 2012; Dao et al., 2013). In addition,

there were eyewitness testimonies indicting that the Teizan Canal reduced the height of the tsunami inundation (Miyagi Prefecture, 2013). Teizan Canal has a width of 25 to 45 m, a length of 49 km, and a depth of 0.3 to 2 m. This trend was also visible from field data collected after the 2011 Tohoku Tsunami (Watanabe et al., 2016). Similarly, in India, the Buckingham Canal substantially protected the lives of many fishermen in regions around Chennai and the coast of Andhra Pradesh during the 2004 Indian Ocean Tsunami (Ramalingeswara et al., 2005). However, studies on the function of a canal concerning tsunami mitigation have not been broadly conducted. Therefore, this study aims to comprehend the influences of a canal in decreasing tsunami momentum and energy (Dao et al., 2012; Dao et al., 2013) in order to study the mitigating influence of a canal through laboratory experiments to comprehend the characteristics of an inundating tsunami over a canal (Watanabe et al., 2016).

In this thesis, the first technical paper deals with a sequence of experiments conducted to examine the effects of the geometry of the canal on the hydrodynamics of turbulent surges upstream and downstream of a perpendicular rectangular mitigation canal. Current physical tests have concentrated on a slightly restricted range of canal aspect ratios and comparatively lower reservoir impoundment heads (i.e., $d_o \leq 0.25$ m). The suggested wide-ranging physical tests targeted at examining a wide variety of canal aspect ratios (i.e., $4 \leq w/d \leq 60$) are used to further inspect the influence of the geometry of the canal on the hydrodynamic properties of the turbulent surge downstream of the canal. The discrepancies of the water surface heights and velocities upstream and downstream of a rectangular mitigation canal are significant for the estimation of their performance and the aspect ratio optimization of the canal. Often, coastal infrastructure is built within close distance to natural streams. Thus, the prompt reaction of hydraulic surges passing over such streams, rivers, and artificial canals can assist coastal experts and engineers in designing and locating nearshore structures in tsunami prone areas.

A Computational Fluid Dynamics (CFD) three-dimensional transient model (OpenFOAM, 2019) was developed to replicate the propagation of the turbulent bore over a mitigation canal. The purpose of the second paper was to test the capabilities of the developed numerical model to simulate such transient and complex turbulent flow and to choose an appropriate turbulence model for more accurate simulation. The performance of the model was assessed by comparing the time-history of the bore elevation and associated velocity. The performance of the three turbulence models was also evaluated. Once the model was validated, the numerical model was further used to examine the influence of the canal depth on the characteristics of the wave and to understand the influence of a rectangular canal on the bore characteristics, by comparing the water surface depths and velocities upstream and downstream of the canal. The influence of the mitigation canal of the time-histories of the specific momentum, momentum flux, and energy dissipation were investigated in the third paper where the influence of canal inclination on energy dissipation of hydraulic bore was presented.

There are no recommendations available in the current design codes, either in the FEMA-P646 (2012) nor in the ASCE7-22, for determining the impact of mitigation canals on tsunami inundation. The main objective of the third paper is to examine the effect of canal orientation on the hydrodynamics of an inundation wave propagating over a rectangular mitigation canal completely filled with water. The results of the validated numerical model are used to extract dynamic parameters, such as the specific momentum flux, turbulent kinetic energy, mean flow, and vorticity. Temporal variations of the defined parameters were derived to comprehend the

momentum and energy transfer in a tsunami-like wave upstream and downstream of a rectangular mitigation canal, and the influences of canal alignment on surge impact as well as differences in specific momentum and energy are examined. The outcomes of this work may have a wide range of applications, including river and coastal flooding mitigation measures. Its results could hopefully be used to improve new design guidelines and parameters for infrastructure subjected to tsunami flows in the context of mitigation canals.

1.2 Thesis Objectives

The principal objective of this current work is to understand and investigate the hydrodynamics, momentum flux, and specific energy of tsunami bores flowing over a rectangular mitigation canal. It also endeavors to understand the substantial bore hydrodynamic changes at the upstream and downstream ends of a rectangular mitigation canal in order to suggest guidelines and rules for the location of potential mitigation canals to be located in coastal communities. This work aims to increase the degree of improvement of tsunami resistance of coastal communities in tsunami-prone coastal areas. Furthermore, it aims to estimate the time-histories of the water surface elevation, velocity, momentum, and energy dissipation using both experimental and numerical methods. The motivation of this study is the need to test additional methods to resist the impact of tsunami inundation. Thus, the outcomes of this experimental and numerical investigations attempt to pursue a reasonable understanding of tsunami characteristics to help researchers comprehend the parameters that can contribute to the assessment of tsunami effects. The main objectives of this work are as follows:

- Measure the effects of mitigation canal geometry on the hydrodynamics of turbulent bores at both the upstream and downstream of a rectangular mitigation canal by a series of physical experiments.
- Develop a three-dimensional transient Computational Fluid Dynamics (CFD) model in OpenFOAM to reproduce the results of the experimental program.
- Estimate the ability of the developed numerical model to simulate complex turbulent and transient flows and to select the most suitable turbulence model for accurate simulation.
- Employ a dam-break wave approach in the numerical model to simulate a tsunami wave propagating over a smooth and flat surface with and without the presence of a canal and evaluate it accuracy by comparing its results with the experimental data.
- Assess the numerical model capability to investigate the effect of canal depth on the bore transformation and to comprehend the mitigation effects of a rectangular canal by comparing water surface elevations and flow velocities before and after the canal.
- Estimate the influence of the mitigation canal on the momentum flux and specific energy before and after the canal.
- Estimate the effect of the canal orientation with respect to the incoming surge on energy dissipation and momentum.

1.3 Novelty

- The present study was the first comprehensive experimental study which investigated the effect of a rectangular mitigation canal completely filled with water on tsunami-like inundation.

- In this study, a sequence of physical experiments was conducted to examine the effects of geometry on the hydrodynamics of turbulent surges at locations upstream and downstream of a rectangular mitigation canal.
- Unlike few of the recent experimental studies (Watanabe et al., 2016; Rahman et al., 2017), this comprehensive experimental study tested a wide range of canal aspect ratios (i.e., $4 \leq w/d \leq 60$) to examine the influences of canal geometry on the hydrodynamic characteristics of a turbulent surge downstream of the canal.
- The majority of coastal infrastructure is built within a very short distance from natural streams and manmade canals, and the reaction of hydraulic surges propagating over such streams can help coastal engineers with appropriate designs for the placing of nearshore structures. To the authors' knowledge, no data on bore properties were recorded downstream of a canal (Dao et al., 2013; Watanabe et al., 2016) nor velocity measurements were collected far downstream of a canal (for instance, over a distance between five and ten times the canal width (Rahman et al., 2017).
- In this study, a novel three-dimensional numerical model was developed using the OpenFOAM software with three different turbulence models, and the numerical results were compared with laboratory experimental results.

1.4 Thesis Scope

The quantitative and qualitative comparison of analytical, experimental, and numerical results were carried out to estimate the performance of the experimental result and numerical solver and their capabilities. The main factors considered for the comparisons include (1) time-series of the water surface elevation, (2) time-series of the flow velocity, (3) time-histories of the momentum flux, and (4) time-series of specific energy. A comprehensive analysis of the generated data was executed to understand the essential physical mechanisms. As soon as the numerical model was validated through comparisons between the achieved numerical results and the available experimental records and analytical solutions, it was then applied to perform an analysis of changes in canal geometry domain and orientation. Since tsunamis arise as a sequence of waves, the ones following the first one may interact with the buildings that exist in a partially-flooded area. Accordingly, explaining the dry bed impacts on how surges interact with structures may have practical significance for tsunami design problems. Numerical results were carried out using a two-phase (water and air) three-dimensional numerical model within the OpenFOAM platform to better comprehend the hydraulic waves induced by a tsunami flowing over a flume bed with the existence of the canal and its influence on a square structure. Due to the physical constraints of the laboratory flume and environment:

- This study investigated the effects of the geometry of the mitigation canal on the hydrodynamics of turbulent bores upstream and downstream of it. However, as research work had been impacted by the situation of closure (Covid-19) of the laboratories at uOttawa, investigating the hydrodynamic loading on a vertical structure, was not investigated.
- The physical experiments were conducted at a small scale (1:25). This was the maximum scale that could be achieved in this research work due to the limitations of the available laboratory facilities.

- The physical experiments did not include investigating extended flumes with different canal orientations. These extended flumes were investigated and compared based on the numerical simulation results.

1.5 Contributions

1.5.1 Journal Papers

* **Bold article has not been published yet***

Elsheikh, N., Azimi, A. H., Nistor, I., and Mohammadian, A. (2020). Experimental Investigations of Hydraulic Surges Passing Over a Rectangular Canal. *Journal of Earthquake and Tsunami*, Vol. 14 No. 5, 2040004. 31p. 2040004. https://doi.org/10.1142/S1793431120400047

Elsheikh, N., Nistor, I., Azimi, A. H., and Mohammadian, A. (2022). Tsunami Induced Bore Propagating over a Canal-Part 1: Laboratory Experiments and Numerical Validation. *Fluids* 2022, 7, 213. https://doi.org/10.3390/fluids7070213.

Elsheikh, N., Azimi, A. H., Nistor, I., and Mohammadian, A. (2022). Tsunami-Induced Bores Propagating over a Canal- Part 2: Numerical Experiments Using the Standard *k-ε* Turbulence Model. *Fluids* 2022, 7, 214. https://doi.org/10.3390/fluids7070214.

Elsheikh, N., Azimi, A. H., Nistor, I., and Mohammadian, A. (2022). Experimental Studies on the Tsunami Like Bores Passing Over a Rectangular Mitigation Canal (under review).

1.5.2 Conference Papers

(The article has been officially accepted but not presented or published)

Elsheikh, N., Nistor, I., Mohammadian, A., and Azimi, A H. (2020). Numerical and Experimental Simulation of Tsunami-like Bores Passing over a Canal. *Canadian Society of Civil Engineering 48th Annual Conference, Saskatoon, Saskatchewan, Canada.*

1.6 Thesis Outline

This thesis has seven chapters Chapter 1 provides the research needs and motivation of this study, as well as the objectives, contribution and scopes, along with the novelty of the current work.

Chapter 2 presents a review of related scientific literature and focuses on past analytical, experimental, and numerical research which investigated tsunami bore characteristics and the related effects on a mitigation canal structure.

Chapter 3 presents the developed numerical model used to investigate surge-canal interaction.

Chapters 4, 5 and 6 are the main sections which present the results of this study. The key outcomes of this study are presented in the form of three technical papers already published.

Chapter 7 presents the main conclusions of this study and recommendations for future work.

Finally, the appendix presents data processing and considerations on the Froude number.

2 Literature Review

Investigating fluid dynamics phenomena has been conducted using numerical models and physical experimental models. The data derived from physical experiments are usually considered the most accurate for scientific investigation. Further, as physical experiments are obtained by the same laws as the original phenomenon being investigated, they often perform as an essential foundation for scientific investigation. It is easy to pay more attention and concentrate on the character of one variable and investigate its influences without even a small amount of interference from the other variables. This chapter focuses on previous contributions made possible via the application of laboratory experiments. In particular, where notable outcomes are documented, attention was paid to the study of the dam-break wave generation methods. Then, some previous analytical, experimental, and numerical investigations will also be revised, concentrating on the relationship between dam break waves, the bore surface elevation and velocity and their characteristics is presented and discussed.

2.1 Experimental Tsunami and Hydraulic Waves Modeling

It is important to understand the main parameters describing tsunamis behaviour as soon as they reach the shoreline: the offshore tsunami amplitude at the place where the depth of water becomes 100 m (Figure 2.1) (Chock, 2015), the run-up elevation, the inundation depth, and the inundation limit (maximum horizontal).

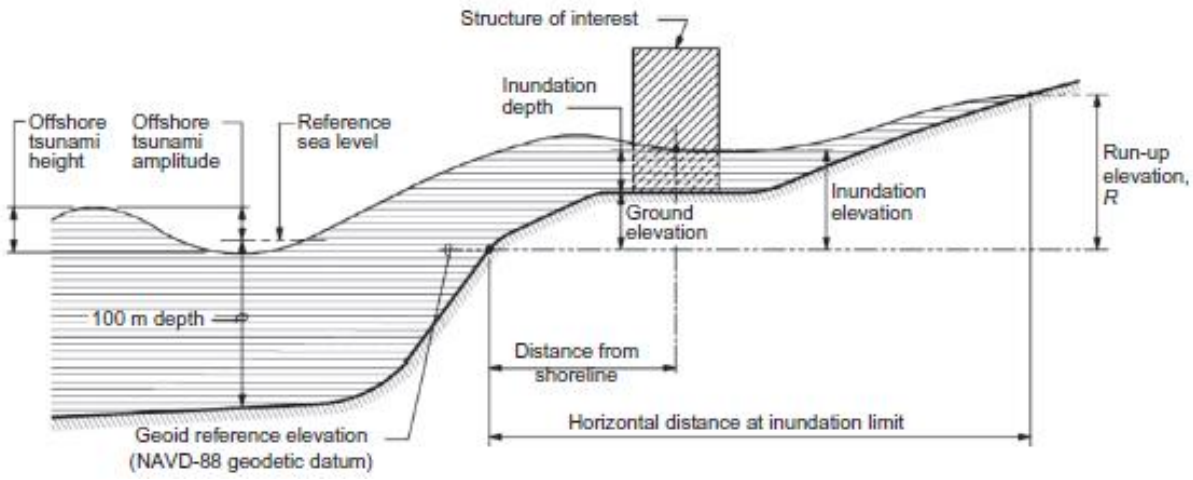

Figure 2.1. Explained terminology of ASCE tsunami (ASCE, 2016).

In addition, it is worth discussing the main differences in the inundation flowing over both dry and wet bed conditions. The dissimilarity in performance between dam-break waves spreading over wet and dry beds was proven by Ramsden (1993), Nistor et al. (2010) Nouri et al. (2010) and Al-Faesly, (2016) among others. (Figure 2.2) shows a case of a wave advancing upstream on France's Garonne River over dry and wet beds.

Figure 2.2. The difference in performance between a bore propagating over dry and wet beds, at the Garonne River, Podensac (France), October 2015 (Wüthrich, et al. 2017).

Using experimental facilities available to researchers during the past decades, several techniques have been improved for creating in laboratory settings surges and bores having characteristics similar to those of actual tsunami waves, including solitary waves, dam-break wave, and volume-driven wave generation (Arnason et al., 2009; Baldock et al., 2012; Wüthrich et al. 2018a; 2018b; von Häfen et al., 2019). The physical behavior of the waves prior to approaching the shore can influence the onshore hydrodynamics; the techniques reviewed for producing such waves are connected to the present work. Since the physical experiments that are implemented in this work used the dam-break generation technique for producing tsunami-like inundation, only the dam-break wave method is discussed in this review. Most of the previous experimental investigations on tsunami effects used solitary wave techniques to generate tsunami and impulse waves; for examples, piston-type wave generators were used to obtain such waves. However, Madsen et al. (2008) questioned why the solitary waves in laboratory conditions are used, and drew attention to their high dissipation of energy, in addition to their short-wave period and wavelength once compared with actual tsunami waves (Wüthrich, et al. 2017). The dam-break wave and solitary wave have been significantly employed to reproduce the coastal submergence by tsunamis in previous experimental modeling inspections. After Hammack's (1973) landmark work on the propagation and production of tsunamis, the solitary wave pattern used for tsunami simulation began to appear (Douglas, & Nistor, 2015). At present, the production of dam-break waves by the rapid release of a confined volume of water upstream of a vertical gate is deemed a more appropriate technique to duplicate the flood generated by tsunamis and impact waves (Chanson 2005, 2006). Several authors, including Lauber and Hager (1998), Arnason et al. (2009), and Nistor et al. (2009), among others, used this method. This development relies on the theory of Ritter (1892), and it indicates an ideal fluid condition, semi-finite reservoir, and a wave proceeding over the smooth and horizontal bed surface of the channel. The bore friction becomes non-negligible at the tip of the bore (Chanson 2005), and Whitham (1955) developed a modified dam-break theory (Wüthrich, et al. 2017).

2.2 Dam-Break Wave

The expression “dam-break wave” is typically used to define the two-dimensional flow produced by the rapid lifting of a vertical wall (gate) holding a volume of water at rest above the horizontal bed (Al-Faesly, 2016). Dam-break flow scenarios have remarkably been adapted, as a result of the extensive experimental and theoretical experience, related to problems in coastal and hydraulic engineering (Stolle et al. 2019). Baldock et al. (2012) displayed the dam-break solution used to imitate the propagation of a broken solitary wave bore of a flat, horizontal bed. In addition, owing to the relative ease of numerically inspecting the dam-break problem, these waves have been comprehensively employed in the confirmation of numerical models as a hydrodynamic forcing factor for impact and loading on structures (St-Germain et al., 2012). For the falling water column problem, no recommended boundary condition was needed (Stolle et al. 2019).

One extremely suitable method for generating a hydraulic bore experimentally is by the quick release of a confined amount of water from a reservoir upstream of the gate h_u into a downstream flume h_d. The impounded amount of water is usually released rapidly through a vertical lift gate or swing gate, following which a negative wave advances upstream in the reservoir while the dam-break wave advances downstream of the gate. Previous research showed agreement of the rapid discharge of the impounded amount of water upstream of the gate in the reservoir (St-Germain, 2012) with analytical solutions. Dressler (1954) compared his past mathematical formula (Dressler, 1952) and experimental data. His experimental data and the theoretical formula diverged, signifying that the Chezy resistance function, which is often used in steady flow formulas, is insufficient for highly turbulent flows (Al-Faesly, 2016). The analytical solutions were only found for some limited number of cases, because of the nonlinearity of the equations. Consequently, numerical methods became commonly applied with the advent of modern computers to solve the equations and identify the discontinuities of the result (Nouri, 2008). Chanson (2006) examined visual images of real tsunami hydraulic bores produced from the 2004 Indian Ocean Tsunami and confirmed that the flow properties of the examined bore and the hydraulic bore related to a dam-break wave were very similar.

2.3 Swing Gates and Vertical Lift Gates

The majority of past investigations used vertical lift gates built in relatively small flumes, which can decrease the cost of their construction. A current cost review indicated that the construction price of a vertical gate amplified exponentially with the width of the flume. Currently, the swing gate has been progressively used in wider flumes, since vertical release gates became considerably expensive beyond specific dimensions. One very essential reason for taking into consideration various types of gates is the necessity to study the influence of three-dimensional structures and obstacles subjected to dam-break bores proceeding downstream; accordingly, wider flumes are required (Stolle et al. 2019). The debris and hydraulic loads of a dam-break wave on vertical standing structures were examined by Nouri et al. (2010) and Al-Faesly et al. (2012). A hinged gate was used by Nandasena et al. (2011) to provide standard data for boulder dislocation over the sloping beach (Stolle et al. 2019). Several studies indicated a good match with the opening times

suggested by (Lauber and Hager, 1998). However, bearing in mind the dissimilarity in the gate lifting technique, the dam break wave hydrodynamics produced by both swing gates and vertical lift gates may deviate from each other. A long-duration gate opening would result in interactions between both the gate's wall and the vertically collapsing water column. Without a widespread examination of the effect of the lifting times of the swing gate and the subsequently-generated wave hydrodynamics, it is truly difficult to infer that the wave produced from swing-gates and the typical dam-break solutions can be quantitatively compared (Stolle et al. 2019). Lauber and Hager (1998) indicated that the gate lifting time for the vertical opening gate and swing gate, with significantly different opening mechanisms, is defined for the vertical opening gate as the time for the tip of the gate to surpass the confined depth, and the swing gate includes a vertical and horizontal element of movement from the tip of the gate.

2.4 Analytical Solutions

The influencing parameters such as spatial and temporal variation of cross-sectional area, friction characteristics, bottom slope, and speed of failure can make the solving of a real dam-break problem impossible. Therefore, an idealized dam-break case can be hypothesized, where a mass of water can be released by the sudden removal of a gate, as can be seen in (Figure 2.3) (Chanson 2005b).

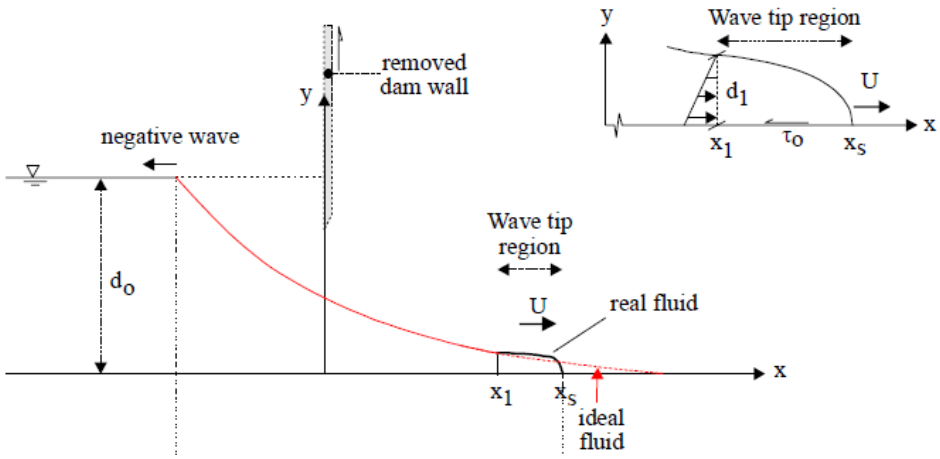

Figure 2.3. Idealized dam break diagram in a dry flat channel (Chanson, 2005b).

According to Chanson (2005b and 2006), the flow was divided into two separate regions: the wave tip region where the friction is the dominant term and the flow velocity does not differ quickly, and the following ideal-fluid region where the acceleration and inertial terms prevail. Chanson (2005b) considered the initial flow velocity upstream of the dam to be non-zero. Also, for the wave tip region and the ideal-fluid region, instantaneous free-surface profiles were provided.

The main current contributions to the analytical solution have been shown in the work as follows:

Ritter (1892) made the first efforts to answer the dam-break problem dated to 1892, when his significant contributions extracted an analytical solution for the problem of the dam-break wave of an inviscid fluid produced from the quick discharge of water from a semi-infinite reservoir propagating over a horizontal, frictionless and dry surface. He neglected the friction effect and

assumed a hydrostatic pressure field. In addition, the velocity varied linearly from the negative front to the positive front, and a parabolic shape of water surface profile flow that is concave upward was presented (Nouri, 2008). The measured longitudinal wave profile in the wave tip region with the theoretical solution of Ritter is obtained from the following equations.

$$\frac{h}{d_0} = \frac{1}{9} * \left(2 - \frac{x}{t * \sqrt{g * d_0}}\right)^2 \qquad (2.1)$$

$$-1 \leq \frac{x}{t * \sqrt{g * d_0}} \leq +2 \qquad (2.2)$$

Where, h is the water surface elevation (m), d_0 is the initial height of the impounded water (m), x is the distance in the direction of the flow (m), g is the gravitational acceleration (m/s^2), and t is the time since the release of the dam-break wave (sec).

Whitham (1955) also derived an analytical solution for a dam-break wave produced from the sudden removal of a gate impounding an amount of water at rest over a horizontal, dry channel with surface friction. The measured longitudinal wave profile in the wave tip region with the theoretical solution is obtained. Chanson (2009), recently**,** obtained an analytical expression that takes into consideration the flow resistance merely in the wave-tip region by counting the Darcy-Weisbach friction factor (f) and utilizing the diffusive wave equation. The measured longitudinal wave profile in the wave tip region with the theoretical solution of Chanson is obtained from the following equations (2.3).

$$\frac{h}{d_0} = \sqrt{\frac{f}{4}\left(\frac{U}{\sqrt{g d_0}}\right)^2 \left(\frac{x - x_s}{d_0}\right)} \qquad (2.3)$$

where U is the wave front celerity (m/s), and x_s the wave front location (m). Thus, the comparison of analytical solutions by Ritter (1892), Whitham (1955), and Chanson (2009) for a dam-break showed (Figure 2.4) that surges had some differences between curves in the wave tip region. The analytical solutions are only presented for some limited values within the wave tip region.

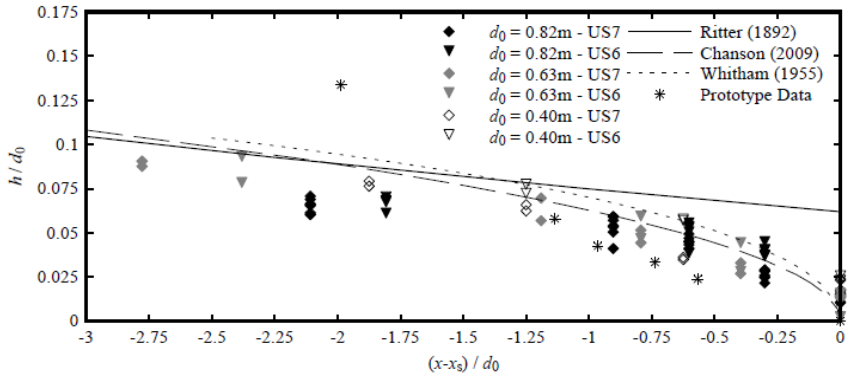

Figure 2.4. Comparison of the calculated longitudinal surge levels by the analytical answer of Ritter (1892), Whitham (1955), Chanson (2009), empirical and real results Chanson (2006) in the region of the surge tip (Wüthrich, et al. 2017).

2.5 Hydraulic Jump

A hydraulic jump is a phenomenon that occurs in open channel flows, such as in rivers and spillways when flow regime changes from supercritical to subcritical. When high-velocity water is discharged into a region of slower velocity, the water surface level rises abruptly. The swiftly moving water slows sharply and rises in height, transforming some of the initial kinetic energy flow into potential energy, with some energy lost irreversibly due to turbulence. This results in the quick flow slowing and stacking up on top of itself in the open channel flow, similar to how a shockwave originates.

A hydraulic jump might take several different forms depending on the approach Froude number, F_{r1} (Chow, 1959). Each of these forms has its own flow patterns and features, for instance the strength and production of eddies and rollers, which assist in determining the quantity of energy dissipated during the jump. The descriptions of the kinds of jump are dependent on certain Froude number ranges (Chow, 1959; Akan, 2006; Chaudhry, 2008); however, these ranges are not accurate, and overlap can happen adjacent to the endpoints. The flow is critical when the upstream Froude number is 1.0, but a jump cannot form; for a jump to occur, the flow must be supercritical ($F_{r1} > 1$**)** (Thompson & Kilgore, 2006).

2.5.1 Weak Jump (1 < F_{r1}< 2.5)

Only a very slight jump happens in the case when 1 < F_{r1}< 1.7, h_1, and h_2 are approximately equal. The water's surface in this circumstance displays small undulations, and hence jumps in this range are frequently referred to as undular jumps. The energy dissipation from these surface riffles is often very low. A series of little rollers appear to form on the water's surface near the location of the jump as F_{r1} reaches 1.7, but the water's surface downstream stays rather smooth (Chow, 1959; Akan, 2006; Chaudhry, 2008). In weak jumps, energy loss might reach up to 15% (Streeter & Wylie, 1979).

2.5.2 Hydraulic Jump and Energy Losses

In an open channel, the abrupt and quick transition from a supercritical to subcritical flow is known as a hydraulic jump (Figures 2.5 and 2.6).

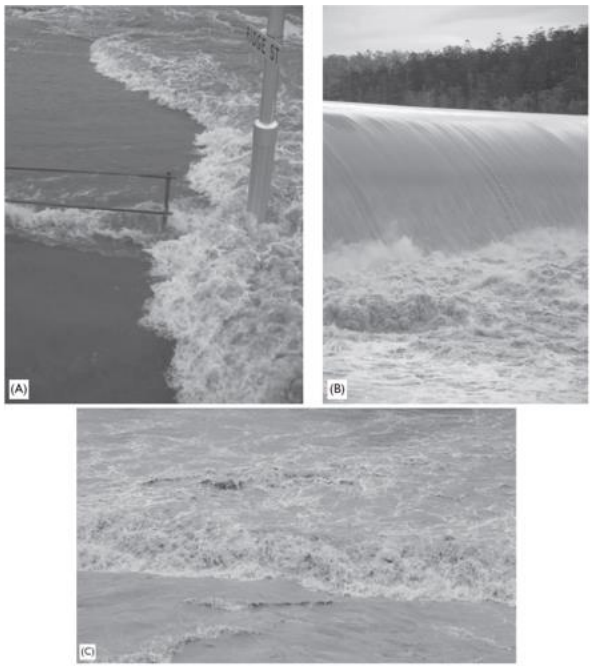

Figure 2.5. Applications of hydraulic jumps in civil engineering: (A) Hydraulic jump in a culvert intake during a flash flood, flow from left to right; (B) Hydraulic jump energy dissipator downstream of a stepped dam spillway during a major flood, looking upstream at the jump roller; (C) Smaller hydraulic jump along with the flood, flow from foreground left to background left, looking downstream (Chanson & Carvalho, 2015).

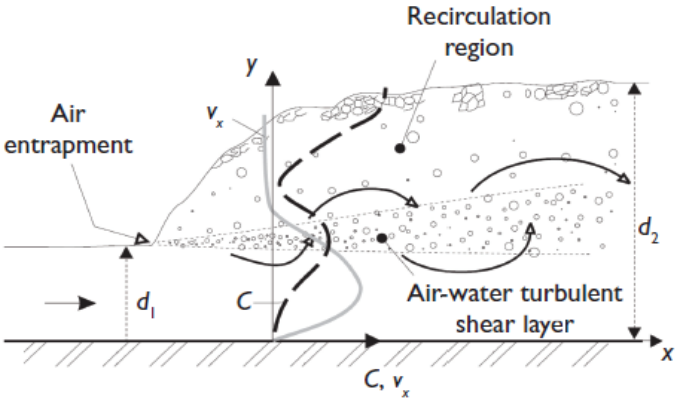

Figure 2.6. Hydraulic jump with a defined roller (Chanson & Carvalho, 2015).

The transition is a very turbulent flow characterized by significant dissipative processes and accompanied by the generation of large-scale turbulence, energy dissipation, surface waves and spray, and air entrainment (Figure 2.5) (Chanson & Carvalho, 2015). It is distinguished by the existence of large vortices, water splashes to the free surface conveying air, and significant dissipative energy. Hydraulic jumps are applied as energy dissipators in hydraulic construction to decrease flood and erosion damage to the greatest extent possible. They can be utilized for mixing in industries (Tcheukam-Toko et al., 2013). The hydraulic jump is frequently used as an energy dissipator beneath dam spillways or weirs, but gates, chutes, drops, and other structures can also be used (Hassanpour et al., 2017). Also, in streams and rivers, a hydraulic jump can be used as a flow aerator, as well as a mixer and energy dissipator in open hydraulic structures, urban water

treatment plants, and sewage systems (Wang & Chanson, 2015). Figure 2.5A shows a hydraulic jump in a culvert intake during a flash flood. Figure 2.5B displays a hydraulic jump downstream of a dam spillway during a major flood. Figure 2.5C illustrates a slighter hydraulic jump during inland inundation in South-East Queensland (Australia). The flow is extremely turbulent in each situation, and the white tone of the water reflects the substantial air bubble entrainment in the natural flow (Chanson & Carvalho, 2015).

The turbulent flow in a hydraulic jump is incredibly complex, and scientists and researchers are still struggling with it (Chanson, 2009a). The motion of the turbulent flow, with the construction of large-scale vortices, air bubble entrapment at the jump toe, and the extreme interactions between entrained air and coherent turbulent structures in the hydraulic jump roller, are some of the basic features of turbulent jumps, as shown in Figure 2.5 (Chanson & Carvalho, 2015).

Energy dissipation or head loss in channels, dam spillways, and other similar structures is one of the most essential engineering applications of the hydraulic jump so that additional kinetic energy does not damage these structures. The rate of energy dissipation or head loss across a hydraulic jump is a function of the hydraulic jump inflow Froude number and the height of the jump (Chanson, 2004). The energy loss in a hydraulic jump is equal to the variation between the specific energy upstream and downstream of the hydraulic jump, and it is defined as follows (Kim et al., 2015): $E_L = E_1 - E_2 = (h_1 + u_1^2/2g) - (h_2 + u_2^2/2g)$.

where E_L = Energy dissipation (m); E_1 = Specific energy upstream of the canal; and E_2 = Specific energy downstream of the canal.

2.5.3 Hydraulic Jump over Smooth and Rough Beds

The classical hydraulic jump is defined as a jump formed in a wide and flat rectangular channel with a smooth bed. Many researchers have investigated the classic jump (Hager, 1992; Wu and Rajaratnam,1995; Carollo et al. 2009). The flow in open channels is mostly driven by gravity, and as a result, the ratio of inertial forces to gravitational forces is likely to play a significant part in the open channel flow analysis. Once the first power law of velocity is used, as is conventional, the dimensionless number is defined, such as the Froude number. If h_1 is the depth of the supercritical flow, h_2 the subcritical flow depth, and F_{r1} the Froude number for the supercritical flow, the Belanger momentum equation can then be used to calculate the sequent depth ratio of a hydraulic jump (Chanson, 2009) as follows: $h_2/h_1 = {}^1/_2 (\sqrt{1 + 8F_{r1}^2} - 1)$; F_{r1} = Froude number for the incoming flow.

Many studies have revealed that if the bed over which the jump is made is rough, the tailwater depth h_2 necessary to produce the jump will be significantly less than the sequent depth h_2 required to form the jump (Hughes & Flack, 1984). Since the length of the jump is significantly decreased, this led to the idea of employing bed roughness to lower the length of the hydraulic jump, which would eventually lead to the length of the apron used to manage a hydraulic jump in relevant structures being reduced (Deshmukh et al., 2019).

The biggest concern with a hydraulic jump on a rough bed is cavitation over the upstream roughness element. Ead and Rajaratnam (2002) found that the effect of cavitation can be reduced by keeping the crest of the roughness element at the same level as the bed, such that no component of the roughness protrudes above the bed level. Gill (1980) discovered that neglecting the channel boundary flow resistance resulted in overestimation of the subsequent depth ratio. The properties of the air-water flow in a hydraulic jump have been widely investigated (Gualtieri & Chanson, 2007; Chanson & Gualtieri, 2008; Gualtieri & Chanson, 2010). According to previous research, the tailwater depth h_2 needed to generate a hydraulic jump on a rough bed could be significantly less than for a corresponding smooth bed (Ead & Rajaratnam, 2002). Hydraulic jumps on rough beds have been found to be substantially shorter than hydraulic jumps on smooth ones (Ead & Rajaratnam, 2002). Hughes and Flack (1984) examined hydraulic jump properties in a horizontal rectangular flume with smooth sidewalls on various artificially roughened beds, and their findings revealed that boundary roughness affects the length of a hydraulic jump and the sequent depth, with the observed reductions being related to both the degree of roughness and the inflow Froude number. Ead and Rajaratnam (2002) investigated hydraulic jumps on a corrugated bed and discovered significant axial velocity profile similitude at various hydraulic jump cross-sections. The impact level of tailwater on flow circumstances at a hydraulic jump was investigated by Mossa et al. (2003). Pagliara et al. (2008) carried out numerous laboratory studies to develop empirical relationships that might be used to forecast the key hydraulic jump features on a uniform rough and non-homogeneous granular bed material.

2.5.4 Hydraulic Jumps at Positive and Negative Steps

In recent years, drops have been the typical primary hydraulic structure seen in water distribution, irrigation, and wastewater collection systems, as well as stepped spillways. A drop can be applied to lower the level of a channel when the slope of the channel is less than the ground slope (Chamani & Beirami, 2002).

2.5.4.1 A positive Step

Consider a rectangular prismatic channel with an upward step. When comparing the stepped channel to the horizontal channel, the transition from supercritical to subcritical flow conditions is characterized by several types of hydraulic jumps, as seen in Figure 2.7.

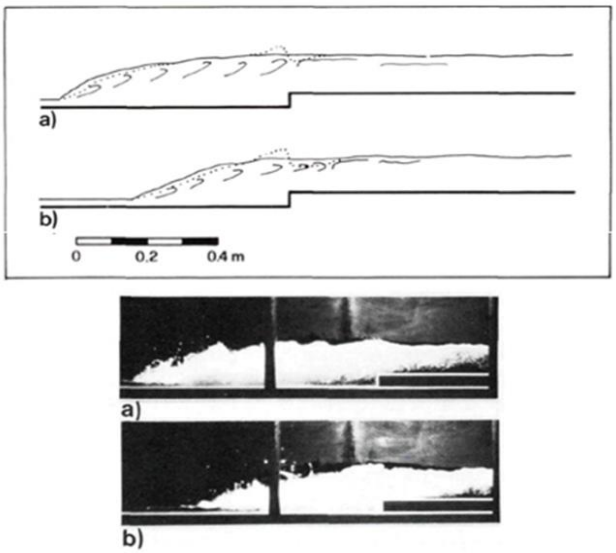

Figure 2.7. Flow kinds over a positive, sudden step: a) A-jump, b) B-jump. (——) surface profile, (----) bottom pressure profile along the axis of the channel (Hager & Bretz, 1986).

Hager and Bretz (1986) carried out experiments and discovered four positive step regimes. The A-jump is totally within the upstream zone of the step, and its length roller finishes right at the step. Raising the depth of the tailwater, h_2, pushes the hydraulic jump into the channel's horizontal upstream part, where the well-known flow pattern given by Chow (1959) and Rajaratnam (1967) applies. The A-jump becomes a B-jump when the tailwater flow depth is reduced, and its roller is situated in both the upstream and downstream zones of the step. The B-jump is described as a jump that divides into two independent sections at the bottom, i.e., a wave above the step and a downstream hydraulic jump. The flow region behind the step can be aerated or non-aerated, depending on the relative step height (step height/approaching flow depth). Substantial pressure lower than hydrostatic pressure can be detected at the horizontal step surface in the latter instance; the height of a non-aerated standing wave is thus significantly lower than that of an aerated flow (Hager, and Bretz, 1986).

While there have been numerous studies on negative step jumps, there have been few studies on positive step jumps. Mohammadi et al. (2021) proposed an improved Froude number for evaluating conjugate flow depth, while Husain et al. (1994), in another investigation, derived empirical equations to evaluate conjugate flow depth and jump length for any jump type at a positive step. Negm (1996) proposed an improved Froude number form for positive step jumps, in which channel slope and step height influences are individually incorporated. Although most proposed solutions for the hydraulic jump flow properties with a positive step have high levels of accuracy, none of them have a straightforward structure or a closed-form representation to work with the non-hydrostatic pressure distribution. Thus, Mohammadi et al. (2021) updated Hager and Sinniger's (1985) technique to offer a more accurate closed-form approximation for the conjugate flow depth. The current approximation is based on a quantity that can describe non-hydrostatic pressure at the step section, as well as a slight rise in the jump-free surface at the step brink.

2.5.4.2 A negative Step

The hydraulic jumps at a negative step were classified by Hager and Bretz (1986) into six different flow patterns. Consider the position of a rectangular, horizontal, and prismatic channel with a negative step, where many forms of hydraulic jump may occur in the proximity of the step if the arriving flow regime is supercritical and the downstream flow regime is subcritical (Figure 2.8).

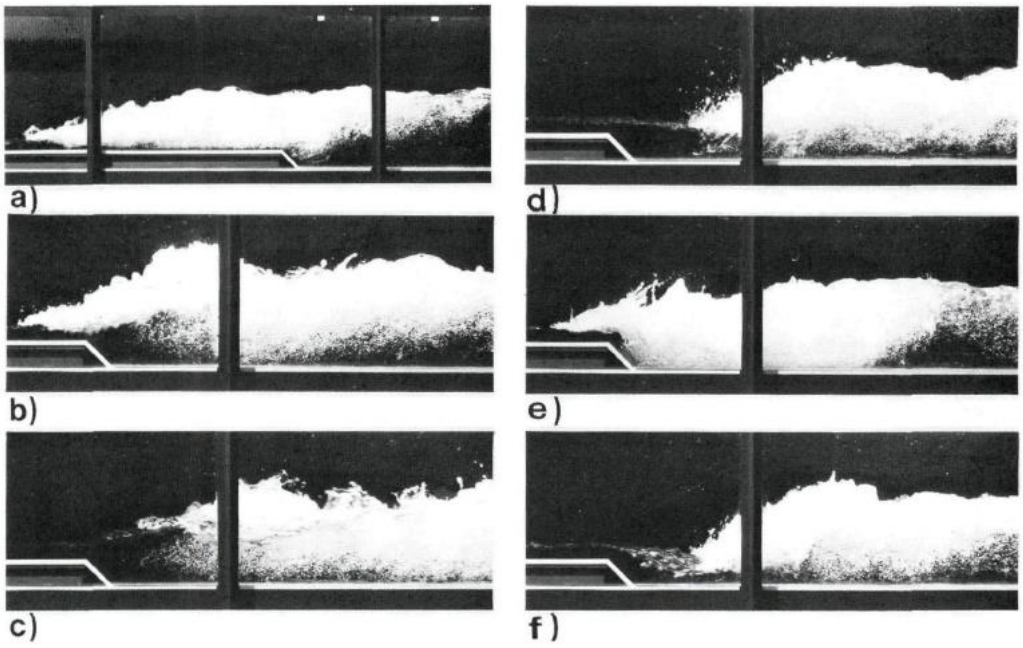

Figure 2.8. Several types of hydraulic jumps that are linked to negative steps: a) A-jump, b) wave, c) upward curved jet, d) downward curved jet, e) B-jump, f) minimum B-jump (Hager and Bretz, 1986).

An A-jump emerges when the hydraulic jump happens entirely on an inflowing channel reach; that is, the roller end is located almost at the step. On the downstream side of the step, reducing the tail-water creates a stagnant wave with a high level. As the tailwater depth is reduced further, an upward-curved jet configuration emerges, which then shifts into a downward-curved jet configuration. A high-velocity surface jet, a nearly horizontal upstream surface profile, and a distorted hydraulic jump at the lower extremities define each of these situations. The inflow conditions for this type of hydraulic jump are not the same as for the well-known A-jump, and strong oscillations spread far downstream. Once the tailwater is lowered further, the flow is abruptly changed into the so-called B-jump (Hager, 1985), which spreads over the whole step domain. Finally, “minimum B-jump” refers to a hydraulic jump that exists under the lowest tailwater depth. Its toe is the point at which the streamlines return to being parallel to the channel bottom. Classifications of jumps over a negative step described above were partly given by Moore and Morgan (1959); Sharp, (1974); Rajaratnam, and Ortiz, (1977).

The A-jump is defined by a hydrostatic pressure distribution on the step, as illustrated in Figure 2.9.

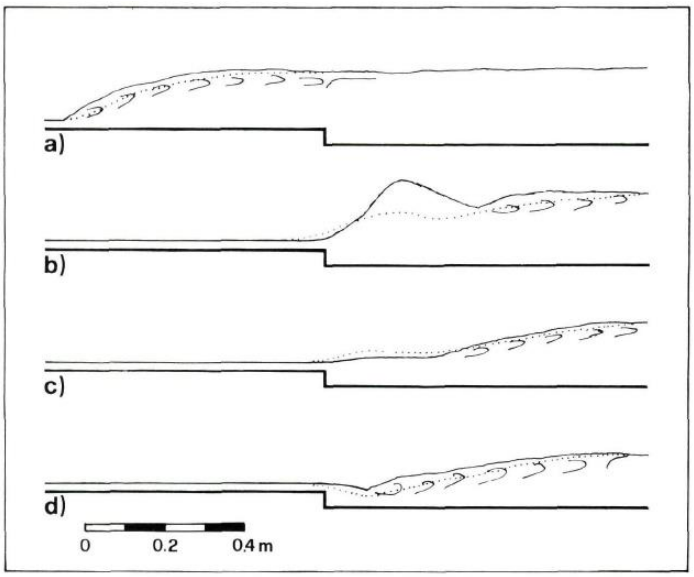

Figure 2.9. Typical flow kinds over a negative step: a) A-jump, b) wave formation, c) upward curved jet formation, d) minimum B-jump. (——) surface profile, (----) bottom pressure profile (Hager & Bretz, 1986).

The wave and upward-curved jet formations are caused by a step pressure distribution that is higher than the hydrostatic pressure distribution, whereas a downward-curved jet, B-jump, and minimum B-jump are caused by a step pressure distribution that is less than the hydrostatic pressure distribution (Hager, 1985).

2.6 Characteristics of the Hydraulic Bore

Tsunami bore fronts may be categorized into four different types: (1) on a flat dry bed, (2) on very shallow water, (3) in medium water depth, and (4) like undular bores, with no breaking (Nakamura, 1973). One of the main targets of this research is to calculate the hydrodynamic forces, water surface elevations, and velocities coupled with bores generated by a tsunami on nearshore structures. For this reason, this research will pay more attention to the first type indicated above. Based on Ritter (1892), Whittam (1956), Nakamura (1973), and Chanson (2009), both the tsunami bore of this type, and the bore produced from a perfect dam-break wave are identical. For this reason, the dam-break similarity was used in the current experimental investigations by confining an amount of water behind a quickly opening vertical lift gate. The gate quickly opened after the impounded amount of water reached the impoundment height defined for an experimental run (Al-Faesly, 2016).

2.6.1 Bore Characteristics in the Presence of a Trough

2.6.1.1 Influence of Trough on Flow Hydrodynamics

Many rivers with coarse-grained beds have longitudinal profiles defined by alternating topographic highs and lows connected with the establishment of macroscale bed forms such as bars, riffles, and pools (MacVicar & Rennie, 2012). Investigations at various field sites have discovered potentially significant hydrodynamic phenomena such as near-bed flow velocity reversal (Clifford & Richards, 1992), turbulent vortex generation (Thompson, 2006), and the lateral divergence and

convergence of flows (Sawyer et al., 2010), along with associated changes in shear stress (Wilkinson et al., 2004). To connect concepts derived from field measurements with a comprehension of the hydraulics of open channels, it is helpful to study experimental work on how a non-uniform channel boundary influences the distribution of flow and turbulence. In a uniform-depth open channel, it is commonly acknowledged that typical vertical velocity profiles and principal Reynolds stress evolve as a result of a balance between gravity's accelerating force and resistance from the channel bed and walls (MacVicar & Rennie, 2012).

Laboratory experiments are warranted to improve our understanding of how a gradual convective deceleration and acceleration of the flow, without flow separation, redistributes flow and turbulence in an open channel. The Reynolds stress and velocity profiles along the centerline of the channel match with prior non-uniform flow results for high velocity near the bed throughout acceleration and higher Reynolds stress throughout deceleration. Lateral flow convergence occurs when the depth increases, demonstrating that convergence occurs throughout the flow deceleration and does not necessitate a lateral flow constriction (MacVicar & Rennie, 2012). Turbulence distribution also displays various patterns in non-uniform channels owing to inequalities between the dissipation and production of turbulence away from the boundary in addition to vorticity advection (Van Balen et al., 2009). The Reynolds stress is an indicator of turbulent momentum exchange, appearing to rise over the bed in convectively decelerating flows compared to uniform flows owing to the formation of additional turbulence and reduction in convectively accelerating flow owing to turbulence suppression (Lee et al., 2010). The concept that pools have a major impact on the flow and turbulence distribution has been previously included in the leading hypotheses on pool creation and maintenance. Keller (1971), in his important work, assumed that the pool's bottom velocity increases more quickly than that of nearby riffles (with rising discharge) until the velocity at the pool's bottom surpasses that of the riffles. Since bed shear stress is a vital factor for predicting sediment entrainment, it was necessary to define the spatial variability of shear stress as a means of evaluating the influence of flow and turbulence redistribution on the channel boundary. Turbulence seems to be the major source of shear stress in the pool's upstream part. In this region, coherent turbulence events are dominated by moments of intense fast flow directed toward the bed and angled toward the channel's side walls (MacVicar & Rennie, 2012).

2.6.2 Influence of Upstream Model on Flow Hydrodynamics

2.6.2.1 Influence of Horizontal Surface Without Canal

Al-Faesly (2016) deployed eight capacitance water level devices longitudinally in the flume to calculate the flow depth-time series through the examinations of the dam break-induced bore characteristics. The distributions of these water level devices are shown in (Figure 2.10).

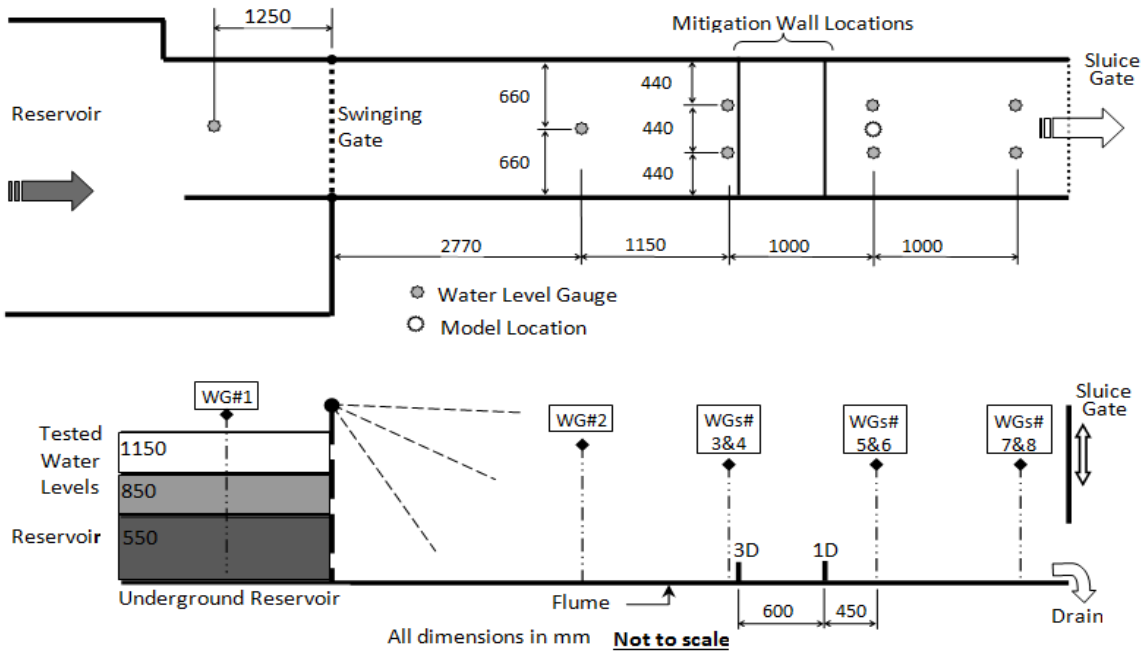

Figure 2.10. Diagram of the investigational setup with the position of mitigation walls and water level devices (Al-Faesly, 2016).

The first water level device (WG1) was mounted 1.25 m upstream from the swinging gate in the water reservoir along the flume centerline to record the confining water level-time-series. The second water level device (WG2) was also mounted along the flume centerline, 2.77 m downstream of the gate, whereas the other remaining six devices (WG3 - WG8) were mounted downstream from the swinging gate in pairs in three rows situated at 3.92, 4.92, and 5.92 m. Thus, these three paired devices were situated at an equal distance from the sides of the flume. Hence, the middle pair was mounted at 4.92 m from the swinging gate downstream at the position dedicated to the structural models. The distribution of water level devices was employed and no structural model was mounted in the flume to evaluate the bore front velocity and observe the bore profile. The two devices of the middle pair (WG5 and WG6) were removed, as the two models were prepared with devices attached to their front, back, and lateral to directly calculate the time-histories of the flow depth around the structural models. The bore depth time-series created from the 850 mm confiscating water level are simply shown in (Figure 2.11).

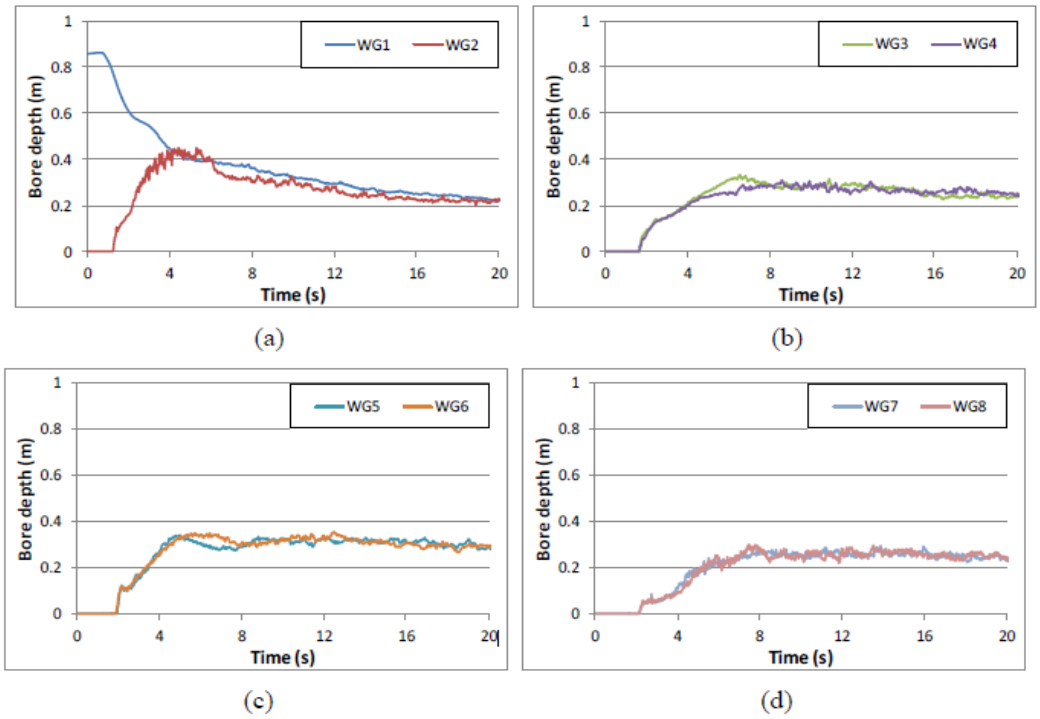

Figure 2.11. The bore depth time-series at different water level devices alongside the flume created from the 850 mm confined water level (Al-Faesly, 2016).

To ensure repeatability of the data recorded and examine the uniformity (consistency) of the bore profile, the test was repeated three times for each confined water depth. For each pair of water level devices on the same row, the relative variances in the records were compared using the least square method and were found to be less than 10%. At 2.07 m downstream from the gate, the largest variance was recorded where the cross-waves had a trivial influence. A sample of the data collected from repeating the examinations is shown in (Figure 2.12).

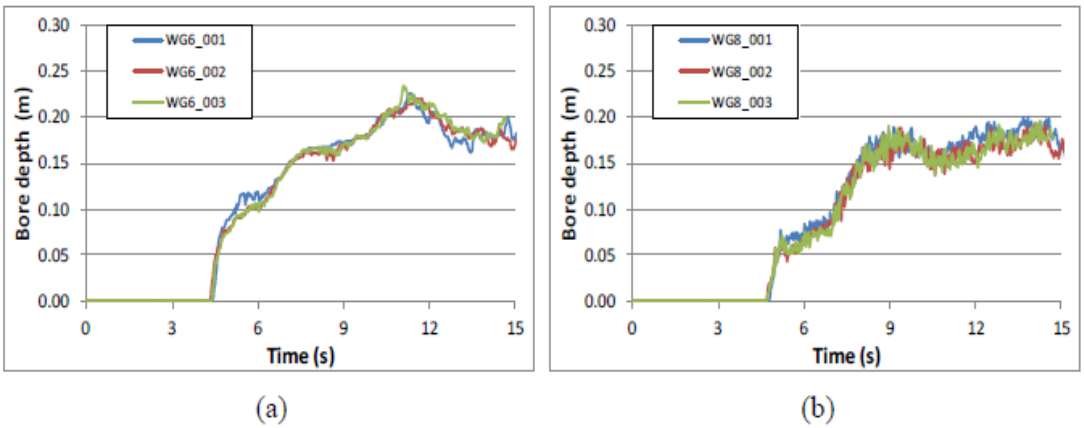

Figure 2.12. The bore depth time-series for three repeated examinations generated with the 550 mm impoundment reservoir head: a) at the model position; and b) 1 m behind the model position (Al-Faesly, 2016).

The experiments were produced from 550 mm confined water depth without the presence of the structural model. The (WG6) was at the model position, while the water level device (WG8) was 1 m behind the model position (Al-Faesly, 2016).

2.6.2.2 Influence of Rectangular Canal Presence

The catastrophic energy of tsunami induced waves could be dissipated as soon as the waves pass over an extenuation canal, completely empty and partially filled by water, according to a hypothesis investigated recently (Watanabe et al., 2016). The canal geometry influences on the hydrodynamic characteristics of surges, including velocity and run-up height, can provide energy dissipation measures before and after passing over a canal in relation to the geometry of the canal. Further, a detailed and comprehensive exploration of this matter should also provide the design considerations for the precise design of an optimized extenuation canal. A laboratory experiment conducted by Watanabe et al. (2016) investigated the attenuation effects of tsunami induced surges spread over a rectangular canal constructed perpendicular to the direction of the wave. Hydraulic surge propagation was studied using three specific water impoundment depths d_o = 0.55 m, 0.79 m, and 0.80 m over a dry bed condition. A single canal with a width (w = 0.30 m) and a depth (d = 0.05 m) was examined, which had a canal aspect ratio (w/d = 6). The mitigation canal was partially occupied with different water levels of 0.02 m and 0.04 m, respectively, and was tested for a dry canal with (d = 0). The experimental results showed that the overflow wave speed decreased in the presence of the canal, and the height of the wave downstream of the canal increased.

Watanabe et al. (2016) pointed out that the quantity of the water that went over the canal (overflow) of a flume with a canal partially filled by water is smaller than the quantity of a flume without a canal when the water depth inside the canal is 0.04 m (Figure 2.13).

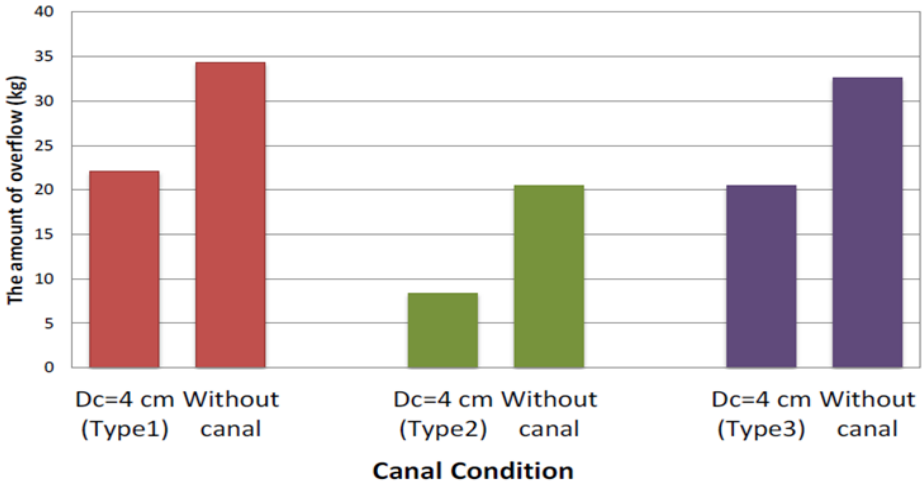

Figure 2.13. Difference in quantity of overflow without canal and with canal (Watanabe et al., 2016)

The damping rate of the quantity of overflow is 35.7%, 59.2%, and 32.1% in Type1, Type2, and Type3 (according to the duration of water level, wave height, extent of valve opening, and impoundment depth), respectively. Watanabe et al.'s (2016) results showed that the damping rate of the quantity of overflow in Type2 is the highest of the three types, and that the damping rate of the quantity of overflow becomes less important when the water level is low. Watanabe et al. (2016) revealed that the quantity of overflow rises as long as the water depth inside the canal increases. Thus, their results indicate that the quantity of overflow is controlled not only by the wave height but also by the wave form.

A series of laboratory experiments conducted by Rahman et al. (2017) studied the efficiency of a rectangular canal, constructed perpendicular to the direction of the surge wave to mitigate the influence of tsunami waves in a vulnerable coastal area. Their laboratory outcomes showed that the maximum mitigation for the wave velocity after the canal occurred when the surge was passing over the deepest and widest canal. The above-mentioned experimental investigation was controlled based on a constricted range of canal aspect ratios that ranged from (w/d = 4 to 10). The significant reflected surge heights were produced by two canal dimensions inspected, and they had the larger widths among other canals that were examined in their investigation. The experiments showed similar tsunami-reduction influences once the canal had the same width and different depths. Nevertheless, the observation showed a delay in tsunami arrival time, and velocity mitigation happened in all canal configurations. It was clearly perceived that the wave energy of a tsunami could be incompletely absorbed by the reflected wave produced by the canal. Rahman et al. (2017) conducted a series of laboratory experiments in an open channel 10 m long, 0.60 m wide, and 0.40 m deep at a point 3.0 m downstream of a mitigation canal, with an impoundment depth of 0.20 m, to examine the impact of a rectangular canal positioned perpendicular to a tsunami inundation, with the canal filled only to a certain level. There was a comparison of tsunami propagation with and without the canal, and the basic case with no canal. The geometry of the canal was altered to permit fluctuations in the tsunami flow. The canal cases considered in this investigation are listed in Table 2.1. In this series of experiments, Case A covers the widest and deepest canal, whereas Case D covers the narrowest and shallowest canal. As can be seen in Figure 2.14, in Cases A and B, the maximum inundation depths rose by 10% and 19%, respectively, whereas in Cases C and D, the maximum inundation depths rose by 13% and 18%, respectively. From the results, most canal conditions produced time histories of the inundation depth that were either greater than or similar to the basic case (Rahman et al., 2017).

Table 2.1. Canal geometric for different cases (Rahman et al. 2017)

Case	Canal condition	Maximum inundation depths increase (%)	Maximum velocity decrease (%)
A	Wide and deep	10	17
B	Wide and shallow	19	17
C	Narrow and deep	13	48
D	Narrow and shallow	18	29

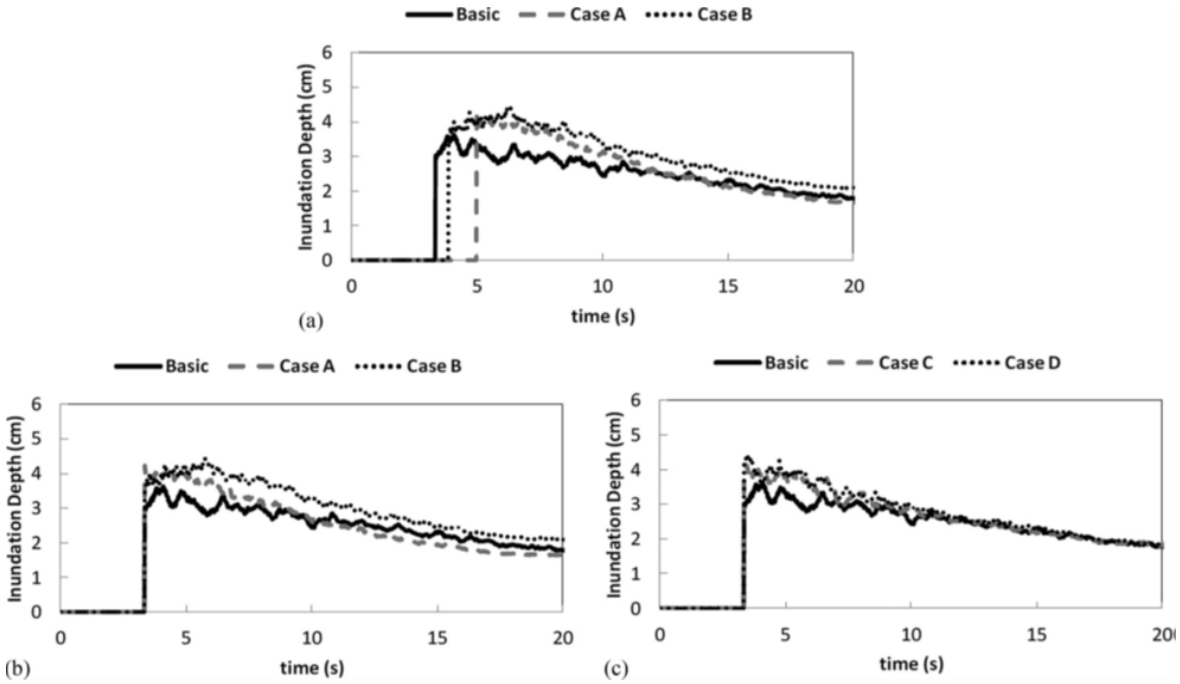

Figure 2.14. Time history of inundation-depth profile passing over a horizontal bed and a rectangular canal with different dimensions at 3.0 m downstream of the canal: (a) different arrival times; (b and c) same arrival as for without canal case (to allow the time histories of the inundation-depth profiles to be more simply compared, the arrival times for canal Cases A–D were set the same as for the case without a canal) (Rahman et al., 2017).

Figure 2.15 displays the time history of the velocity profile passing over a horizontal bed and a rectangular canal with different canal dimensions at a point 3.0 m downstream of the canal.

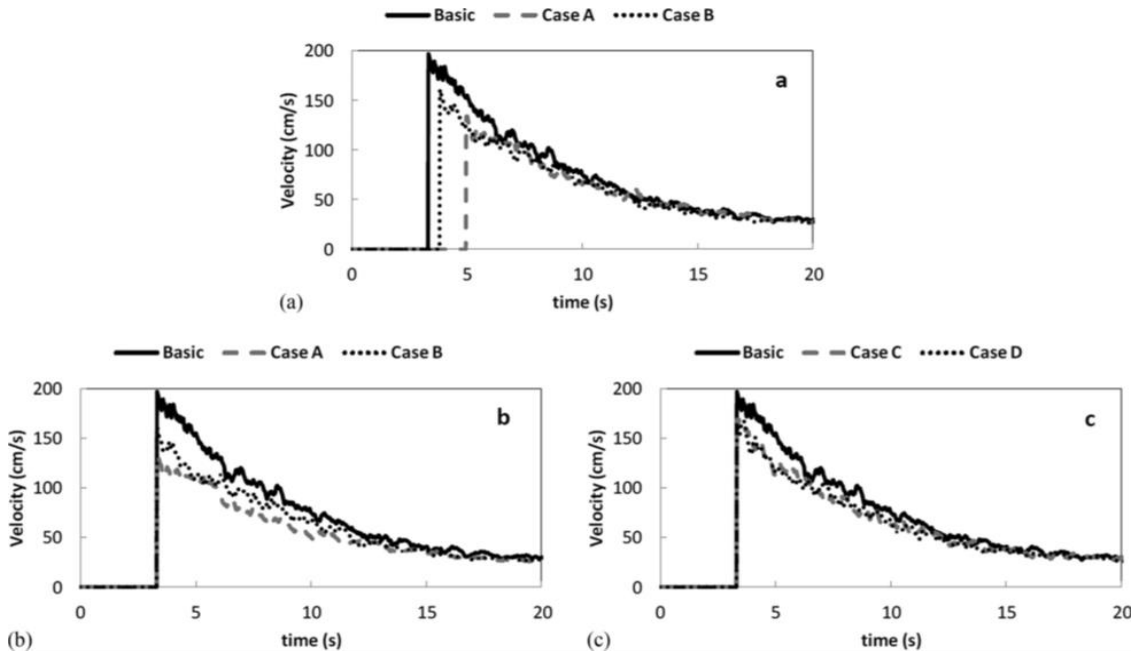

Figure 2.15. Time history of velocity profile passing over a horizontal bed and a rectangular canal with different dimensions at 3.0 m downstream of the canal: (a) different arrival times; (b and c) same arrival as for without canal case (to allow the time histories of the velocity profiles to be more simply compared, the arrival times for canal Cases A–D were set the same as for the case without a canal) (Rahman et al., 2017)

As listed in Table 2.1, in Cases A and B, the highest velocities decreased by nearly 48 and 29% respectively. Cases C and D likewise had lower time history velocity profiles than the case without a canal, and the maximum velocity decreased by about 17%. Dao et al. (2013) also noted that the time history of the velocity profile was reduced by a canal. They showed that when a tsunami surge enters a canal, it can exhibit turbulent behavior and that the canal can play an essential role in decreasing the tsunami's surge velocity (Rahman et al., 2017).

2.6.2.3 Influence of Horizontal Pipeline Presence

Ghodoosipour et al. (2019a) studied the flow characteristics at the position of the pipe to investigate the forces impacting the pipeline. (Figure 2.16) displays the characteristics of the surge of the dry bed such as normalized water level profile (WG3), normalized Froude number, flow velocity, and normalized momentum flux, respectively, at the position of the pipeline.

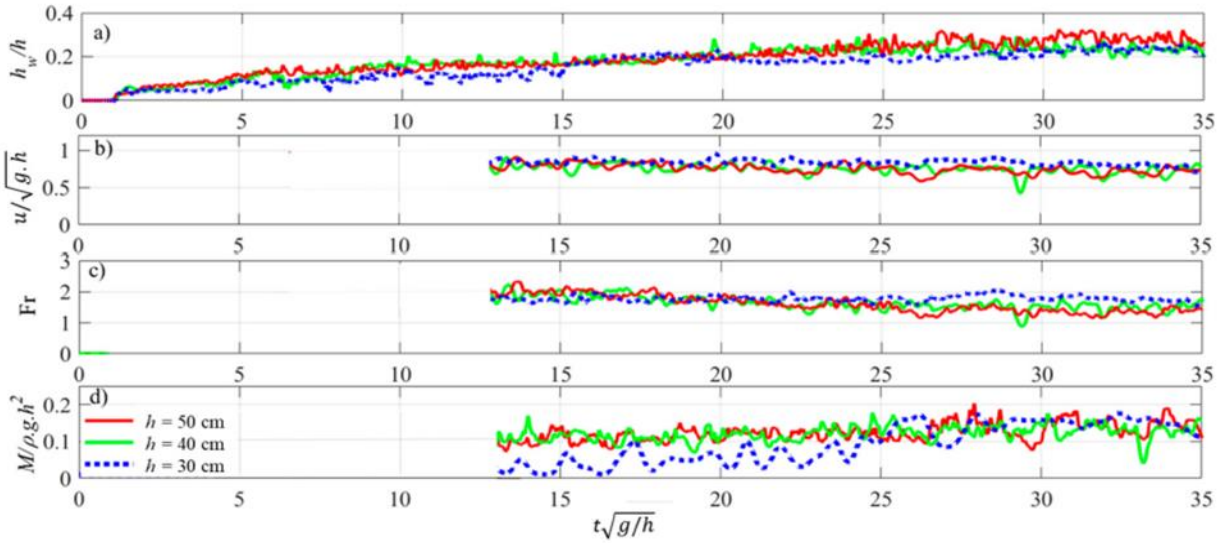

Figure 2.16. The characteristics of dry bed surges at x = 5.5 m for impoundment depths 0.30, 0.40 m, and 0.50 m (a) time-series of water surface profile (WG3), (b) time-series of the flow velocity, (c) time-series of Froude number, and (d) time-series of momentum flux (Ghodoosipour et al., 2019a).

The arrival time of the surge at WG3 was the standard time of the whole cases. In (Figure 2.16b-d), the velocity measurements through the ADV were delayed owing to the entrainment of the air near the arrival time of the wave that matches the zone without data in the first few seconds. For the reservoir impoundment depth of 0.30 m, the water surface elevation rises, and the velocity of the flow reduces gradually compared to the conditions with impoundment depths of 0.40 m and 0.50 m. Figure 2.16c displays the calculated Froude numbers, $F_r > 1$, during the time frame studied for three different impoundment heads. It stays nearly the same in the condition of the reservoir impoundment depth of 0.30 m while it regularly declines for impoundment depths 0.40 m and 0.50 m. Figure 2.16d explains that the dimensionless calculated momentum flux is lower for impoundment depth of 0.30 m at the start of the surge. This might be attributed to a remarkably slower flow speed, along with lower water level profiles in the condition of impoundment depth of 0.30 m. Ghodoosipour et al. (2019a) indicated that the lower momentum flux produces a lower drag force.

Ghodoosipour et al. (2019b) studied the time-histories of the computed water level profile and the three force components: drag, lift, and total force for the condition of dry surface for *e/D* = 0.30 (*e*/D is the pipe gap ratio, *e* is the distance between the lower edge of the pipe and the ground, m, and D is the pipe diameter, m) and confinement heights of 0.30, 0.40, and 0.50 m as shown in (Figure 2.17).

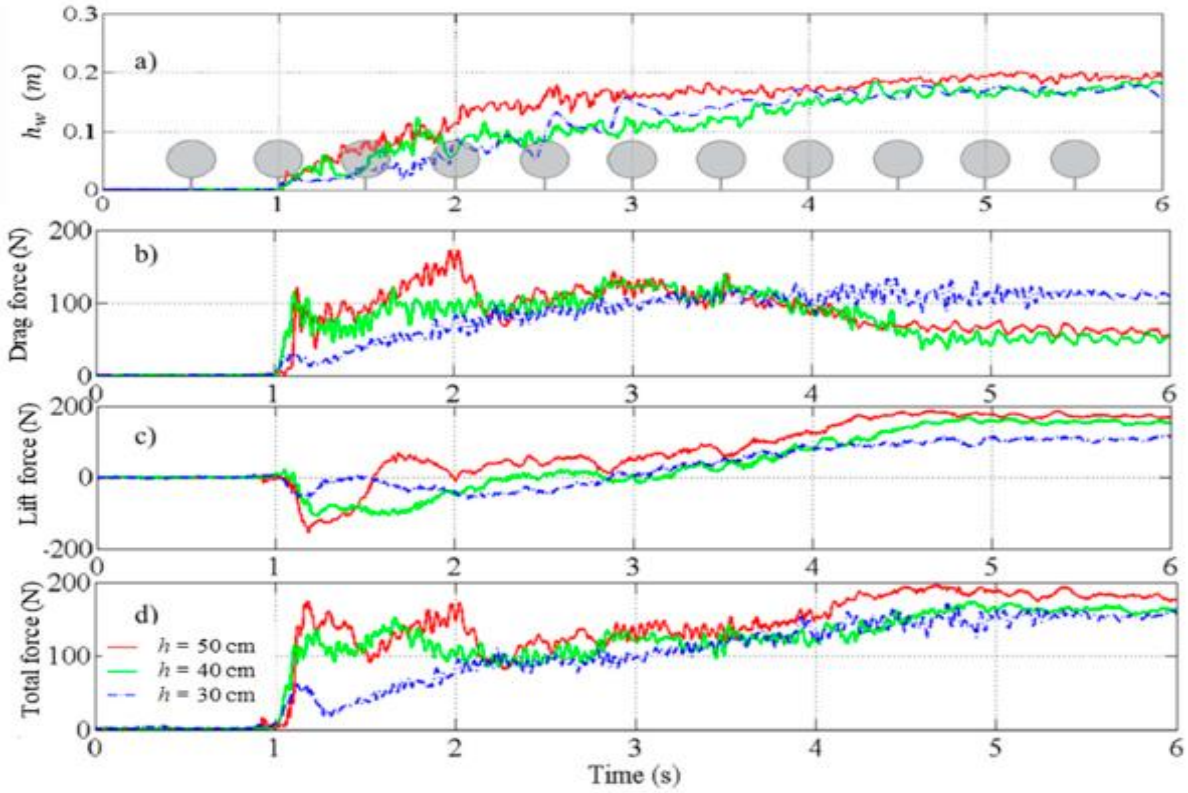

Figure 2.17. The time-history of the computed elevation profiles and the three force components: drag, lift and total force for the condition of dry bed for e/D = 0.30 and upstream heights 0.30, 0.40, and 0.50 m (a) water surface profile at WG3, (b) the time-series of drag force profiles (c) lift force profiles, and (d) total force profiles (Ghodoosipour et al., 2019b).

As anticipated, the reservoir impoundment depth 0.50 m produced the highest magnitudes of the three force components owing to the higher initial impoundment head that was converted into the highest flow depth of dam-break wave (Figure 2.17b).

Ghodoosipour et al. (2019a) concluded that the larger initial impoundment heads lead to larger surge heights and velocities; therefore, the exerted drag force increased. The impact force for the lower initial impoundment head of 0.30 m was significantly lower compared to the other two higher impoundment heads. Waves produced from higher impoundment depths displayed considerably steeper surge fronts that impinged upon the front side of the pipe and produced a quick water elevation increase and a higher impingement load at the point of surge impact. (Figure 2.18) displays the further rapid rise in the water surface, which causes a higher impingement load at larger impoundments of the reservoir.

Figure 2.18. The impact of the bore for three upstream heights on the pipe: (a) 0.50 m, (b) 0.40 m, and (c) 0.30 m (Ghodoosipour et al., 2019b)

After the initial impulse, high standing waves are produced before the pipe for higher impoundment heads of 0.50 and 0.40 m. After t = 4 s, they scattered and began to move upstream in the direction of the gate surface roller that caused the reduction of drag force. The returning surface rollers and standing waves were not perceived for the lowest impoundment depth at 0.30 m. As a result, the drag force slowly rose until the extreme amount was reached and then remained the same. For the three cases, the time-history of the lift force revealed a downward peak that increased with a rise in the impoundment depth from 0.30 to 0.50 m. In (Figure 2.17c), for impoundment depths of 0.30, 0.40, and 0.50 m, the negative peak of the lift force ranged from −25 N to −50 N and −150 N, respectively. It is owing to the larger quantity of water flowing above the upper face of the pipe and forcing it toward a downward direction as the wave grows greater. The lift force usually was greater for waves produced by the higher impoundment heads, mostly owing to the larger velocity of the dam-break wave flow produced with larger impoundment depths. The aggregate force value, which is a combination of the lift and the drag forces, was supreme for waves produced with an impoundment depth of 0.50 m (Figure 2.17d) (Ghodoosipour et al., 2019b).

2.6.3 Numerical Modeling of the Tsunami Bore and Structure Interaction

Dao et al. (2012) used a numerical NEWFLUME model to simulate tsunami propagation and run-up along the Sendai coast with and without the presence of a canal in order to evaluate the effect of the canal on tsunami reduction at an output point. The computational domain is shown in Figure 2.19.

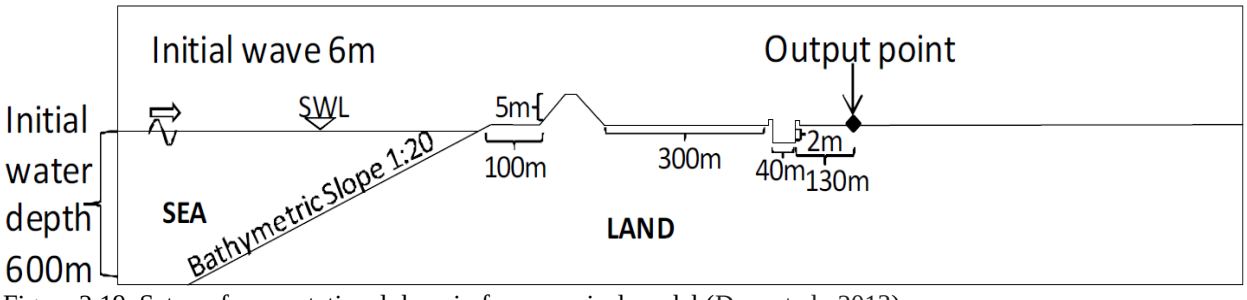

Figure 2.19. Setup of computational domain for numerical model (Dao, et al., 2013).

After roughly 14 minutes of tsunami travel from the open boundary, and at the output point after the rectangular canal, the inundation depth was 4.89 m, the depth-averaged velocity was 11.67 m/s, and the maximum discharge flux became 57.09 m²/s, while in the absence of a canal, the inundation depth was 4.82 m, the depth-averaged velocity was 13.43 m/s, and the maximum flux discharge became 64.74 m²/s. It should be noted that due to the presence of the canal, the inundation depth was increased by 0.07 m, whereas the depth-averaged velocity and flux discharge were reduced by 1.76 m/s and 7.65 m²/s respectively (see Table 2.2).

Table 2.2. Inundation depth, depth-averaged velocity, and flow discharge with and without canal

	Without canal	With canal	Differences
Inundation depth (m)	4.82	4.89	0.07
Depth-averaged velocity (m/s)	13.43	11.67	1.76
Discharge (m²/s)	64.74	57.09	7.65

As can be perceived in Figure 2.20, the depth-averaged velocity in the situation with the canal was rapidly reduced at the canal location in comparison with the situation without the canal.

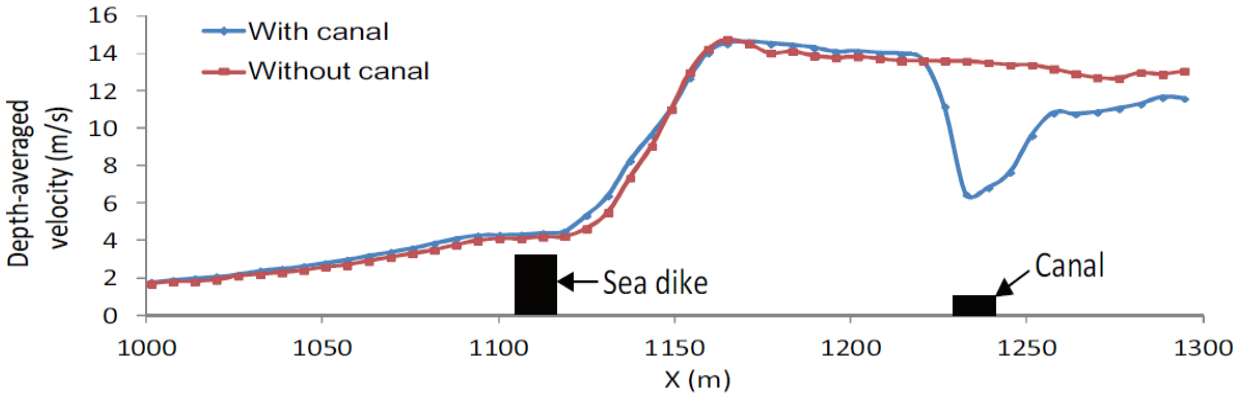

Figure 2.20. Comparison of depth-averaged velocity profile with and without canal (Dao, et al., 2012).

It can be perceived that as a result of the influence of the canal, the maximum depth-averaged velocity was reduced to 7.14 m/s. This case can be explained by the influence of the time necessary for a tsunami to fill up the canal with water before propagating further downstream. The depth-averaged velocity was also decreased as a result of the tsunami energy's dissipation into the canal, resulting in a delayed tsunami arrival time in the case of the canal. Dao et al. (2012) indicated that the tsunami had not yet arrived at the end of the domain in the scenario with the canal at the time of the snapshot, whereas the tsunami had already passed it in the case without a canal (see Figure 2.21). Furthermore, the tsunami depth-averaged velocities in the case with the canal were much lower than in the case without the canal.

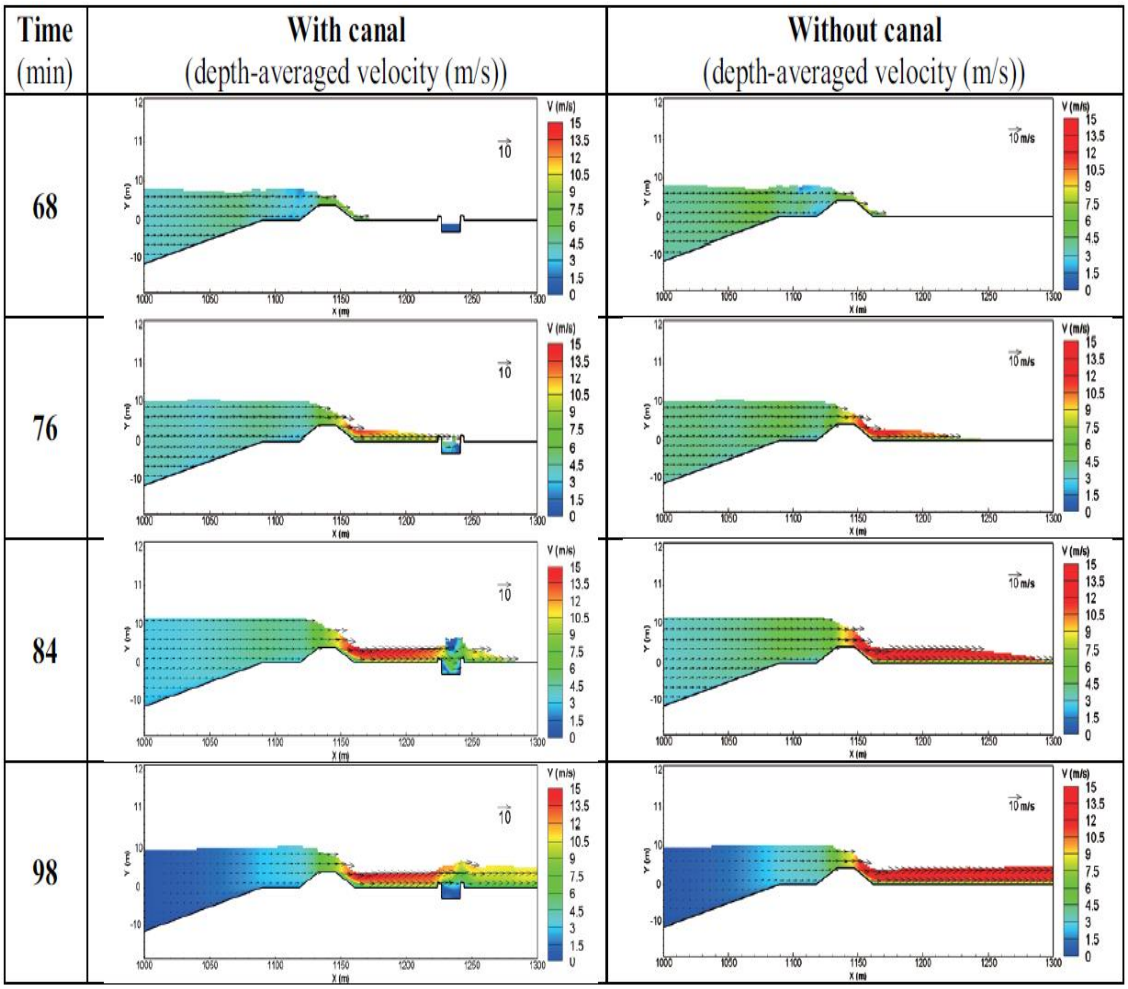

Figure 2.21. Qualitative comparison of specific depth-averaged velocity times with and without canal (Dao, et al., 2012).

Figure 2.22 displays the different outcomes for the maximum depth-averaged velocity (u_{max}) profiles for five cases.

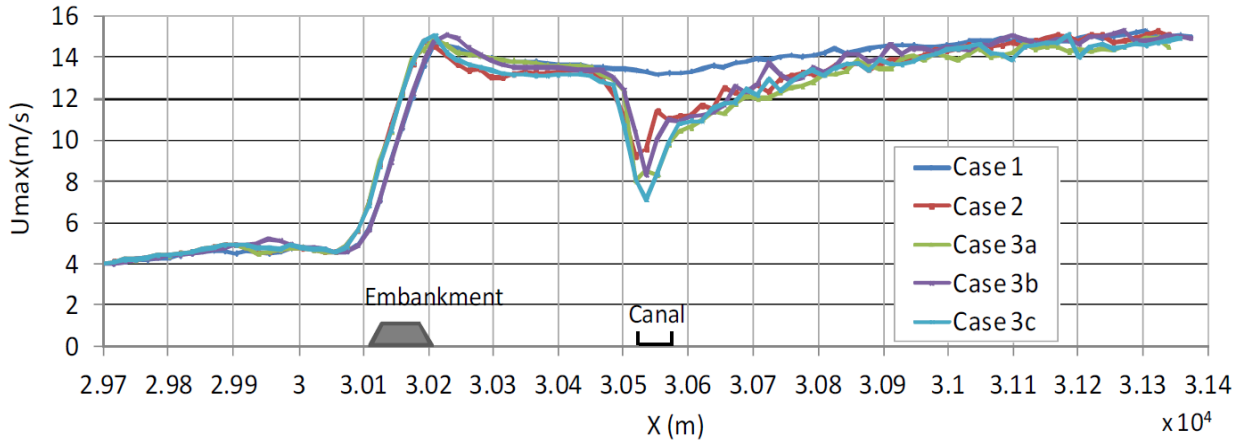

Figure 2.22. Effect of different canal scenarios in decreasing tsunami energy (Dao, et al., 2013).

As indicated in Table 2.3, Dao et al. (2013) ran simulations of five cases to perform a sensitivity analysis of a perpendicular canal in decreasing tsunami energy.

Table 2.3. Effect of different perpendicular canal scenarios at the output point (130 m from canal embankment) in decreasing tsunami energy (Dao, et al., 2013).

Cases	Canal condition	Width (m)	Depth (m)	u_{max} (m/s)	Differences (m/s)
Case 1	Without canal	none	none	13.91	-
Case 2	Existing canal	40	2	12.70	1.21
Case 3a	Extended width	60	2	12.00	1.91
Case 3b	Extended depth	40	3	12.69	1.22
Case 3c	Extended width and depth	60	3	12.16	1.75

The first case was with no canal, and the other four cases were with a canal 300 m downstream of a coastal embankment, and were intended to examine the influence of canal shape on tsunami wave mitigation. Dao et al. (2013) also studied an existing canal which had a depth of 2 m (d = 2 m) and a width of 40 m (w = 40 m). It can be perceived (Table 2.3) that in the case of the canal, the maximum depth-averaged velocity was significantly decreased, indicating that the tsunami energy was dissipated at the canal. Figure 2.22 shows that the tsunami depth-averaged velocity in the inland region ranged between 10 and 15 m/s, which is consistent with the flow velocity evaluated from video footage (Fritz et al., 2006; Bhattacharya et al., 2011). Usually, a tsunami hits a coastal area as a supercritical flow, with a typical tsunami velocity evaluated to be 10 – 18 m/s (Fritz et al., 2006; Bhattacharya et al., 2011).

Nouri et al. (2010) developed a numerical model of their experimental investigations by implementing a single-phase 3D Weakly Compressible Smoothed Particle Hydrodynamics (WCSPH) numerical model. To study the characteristics of the interaction of the bore and a square column at the impact point, a large-scale investigation was set up. They compared the numerical time series of hydrodynamic force being resisted by the model and the water profile with the experimental investigation. The tests were conducted in a 12.87 m long × 2.7 m-wide × 1.4 m deep release flume. They confirmed that the suitability of the comparatively new numerical techniques for imitating such nonlinear and forceful water impacts depends on the quantitative comparison of numerical with experimental outcomes and considerable analysis of numerical outcomes.

St-Germain et al. (2012), conducted the modeling of the effect of tsunami waves with models flowing over wet and dry bed surfaces using a 3D numerical model established by the Smoothed Particle Hydrodynamics (SPH) technique. The conclusion of force versus time on the wall located vertically and a structure (the width of a vertical wall matching the width of the flume test and a slender square column) owing to the bores' effect were compared quantitatively. In their study, firstly, the physical findings of the time series of net total base horizontal force acting on a slender square model were repeated effectively using the numerical model. Whereas during the experimental investigations substantial air entrainment was perceived, the air phase was not measured and taken into consideration in the numerical model as these characteristics were supposed to be predominantly responsible for the perceived disagreements in the measurable comparison of the numerical and experimental findings. That study indicated that the hydrodynamic loads generated from the propagation of tsunami-bores on structural models were

greatly reliant on whether the bed surface on which the waves were spreading was wet or dry. Thus, to eliminate the current weaknesses of model validation by contrasting the experimental and numerical outcomes, a new technique of validation was suggested by Altomare et al. (2014), where the method is validated against laboratory experimental outcomes of run-up waves and propagation above sandy beaches. Thus, that technique used a combination of two dissimilar numerical models, characterized by dissimilar computational capabilities and cost, that could give a clear picture of the occurrence of wave spread, interaction, and transformation with structures in the coastal area.

In Ramsden's (1993) work, the comparisons of physical experiments of bores propagating over wet beds (h_u = 0.28m) and dry beds (h_d= 0m) were made, and a decrease in velocity of this magnitude would not have been anticipated. Interestingly, even though a considerably smaller front celerity was displayed by the wet bed bore, the whole force acting on the square structure at the initial impact was described to be higher than the dry bed scenarios. Based on St-Germain et al. (2012), the additional resistance imposed layer of water covering the bottom caused the steeper and deeper surge front. This behavior seems to conflict with the result of Al-Faesly et al. (2012) who had found the impulsive force to be larger for dry bed conditions.

(Asadollahi, et al. 2019a) investigated the influences of square column orientation on the net stream-wise force regarding its original alignment (θ). (Figure 2.23) provides the qualitative quantities of water surface elevations during the impingement and transient stages for cases θ= 0° and θ=45° at specific times to understand the discrepancies of the resulting force.

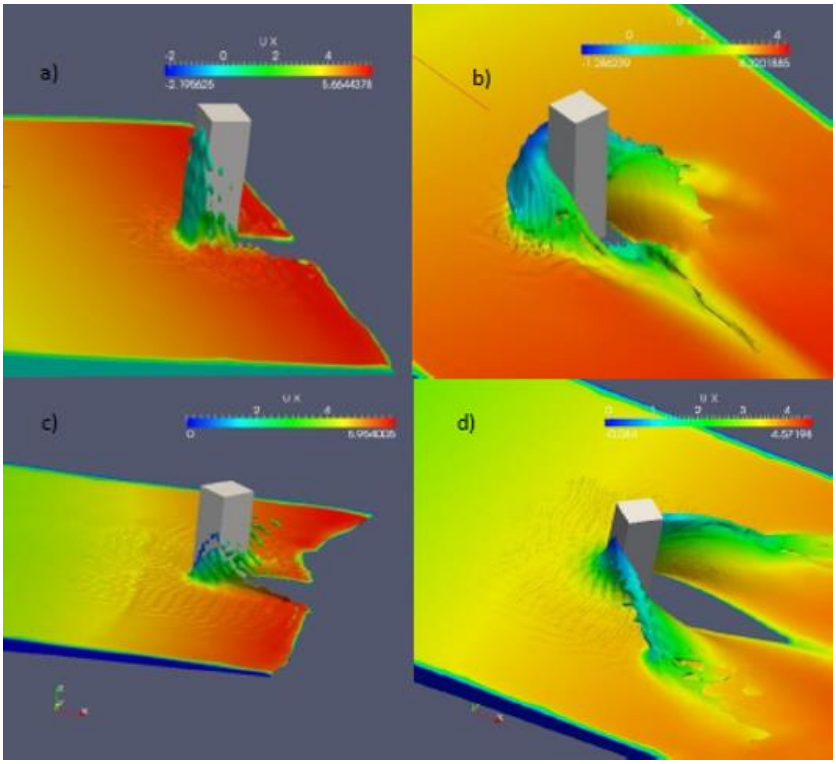

Figure 2.23. The qualitative comparison of specific times through first impingement and transitory stages of the oriented square column θ = 0° at a) 1.3s, b) 2.3s and θ = 45° at c) 1.3s d) 2.3s (Asadollahi, et al. 2019a).

For the case, θ= 0° at t = 1.3s (Figure 2.23a) displays the run-up surge on the upstream side of the structure. While for case θ= 45° at t = 1.3s, (Figure 2.23c) shows no run-up surge on the upstream side, as the flow is separated into two streams by the corner edge facing the arriving surge. In addition, the discrepancy between the cases θ= 0° and θ=45° may be discovered during the transient stage (Figure 2.23b and d). In the case θ= 0° at t = 2.3s, owing to the surge reflection from the upstream face of the column, the surface-roller produced this result in a higher water elevation behind the upstream side and higher hydrodynamic force compared to the case θ=45° at the same time. Shafiei et al. (2016) achieved analogous outcomes in their experimental work. They examined the influence of column orientation on the resulting net stream-wise force applied on the square model for different directions: θ= 0°, 30°, and 45°. The maximum hydrodynamic load and initial impingement load achieved by laboratory experiments were for θ=0° and 45°, respectively. Arnason (2005) found a greater hydrodynamic load for the condition of θ = 45° with a ratio lower than 1.414 relating to the condition θ=0° (Asadollahi, et al. 2019a).

(Asadollahi, et al. 2019b) conducted simulations of the time series of stream-wise force impacting the column and bore depth-averaged velocity for both smooth and rough beds, as shown in (Figure 2.24).

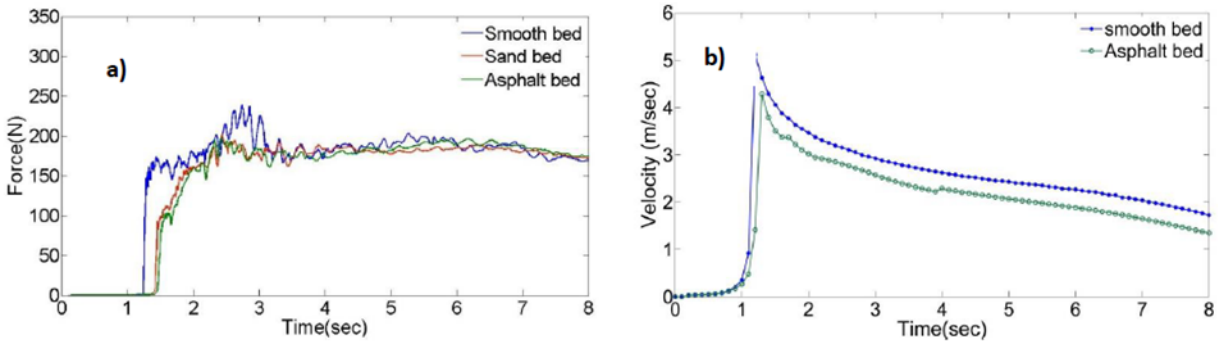

Figure 2.24. The time-series of smooth and rough bed conditions for impoundment depth 0.85 m for a) force acting on the model, and b) speed (Asadollahi, et al. 2019b).

(Figure 2.24a) shows that the impulsive force is significantly diminished at the initial effect for the rough surface case, and the force converged for rough and smooth beds after nearly 6.0 s. (Figure 2.24b) displays the reduction in both the velocity of the surge front and the following velocity of the bore owing to the dissipation of the energy caused by the friction of the bottom in the condition of the rough surface. The resulting force displays a marginal difference between sand and asphalt bed conditions. A higher velocity was achieved at the quasi-steady state in the smooth surface case due to higher velocities far from the bed (Asadollahi, et al. 2019b).

2.6.4 Comparison of Numerical and Experimental Results

Figure 2.25 shows the time histories for qualitative comparison of water surface profiles of the experimental data and the numerical simulation results for a surge passing over a canal.

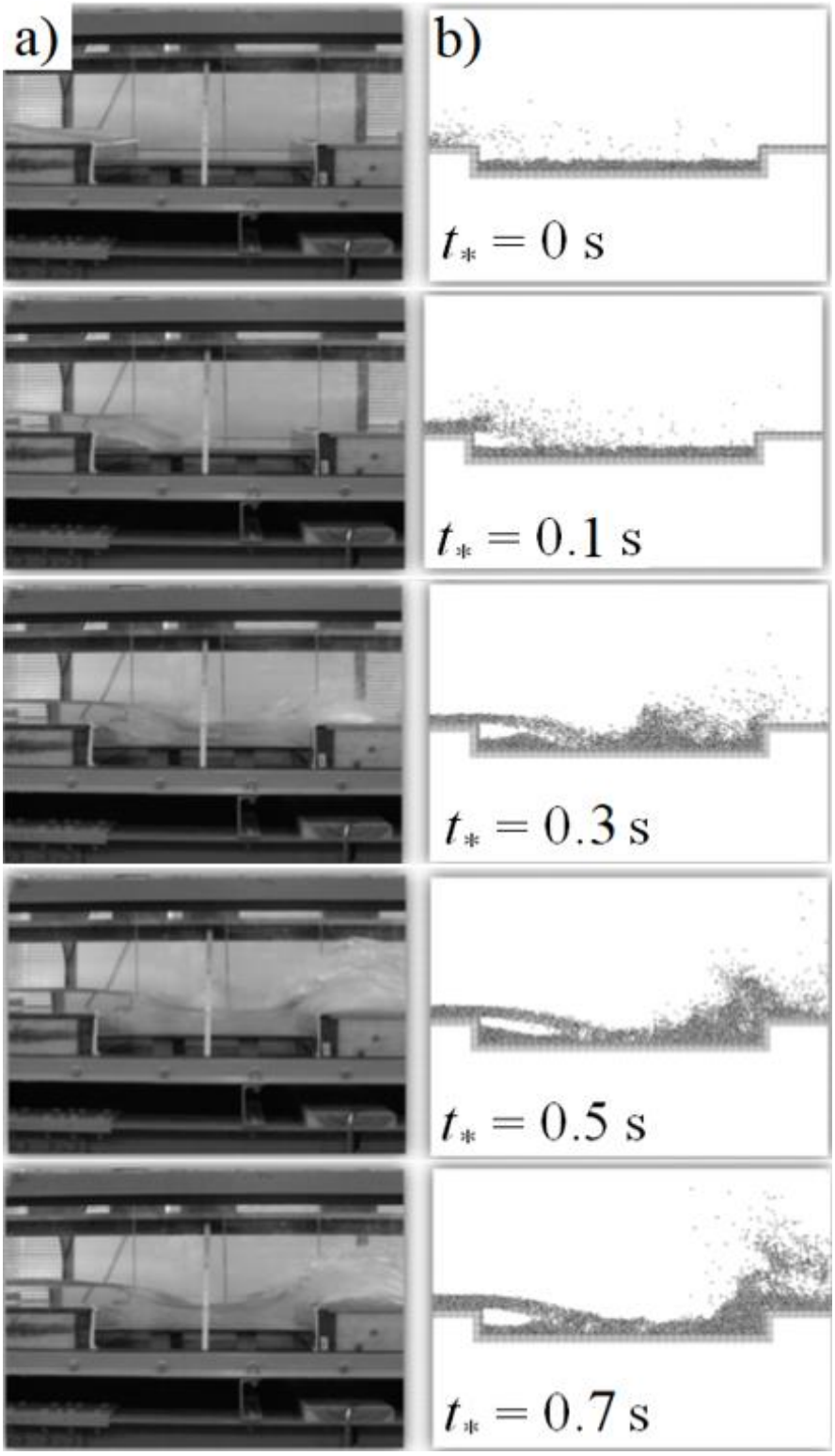

Figure 2.25. Qualitative comparison between experimental and numerical simulation time histories of water surface profiles for a surge passing over a canal: a) side-view images, b) simulated water surface profiles (Rahman et al. 2017).

Figure 2.25a shows a series of consecutive images of water surface profiles as the surge propagates over the canal. The tsunami surge front plunged downward into the canal in this experiment,

generating a minor splash and interacting with the stagnant water in the canal. The canal was then filled with water, whereas the reflected tsunami wave propagated back upstream. Dao et al. (2013) revealed that a tsunami's surge front may lose energy when it enters the stagnant water of a canal. Rahman et al. (2017) discovered that when a canal was present in a flume, the tsunami flowed at a lower velocity than when there was no canal. The energy of the tsunami's surge front was lost owing to the turbulence generated by the splashing in the canal and the resulting reflected wave. Figure 2.25b shows a series of consecutive images of simulated water surface profiles. Even though there were some differences between the surge front splashes in the experimental results and numerical simulations, a comparison of the water surface profiles from the images and the numerical simulations indicated a very good agreement.

Figure 2.26 displays the comparison of the inundation depth time histories for the experimental results and numerical simulations.

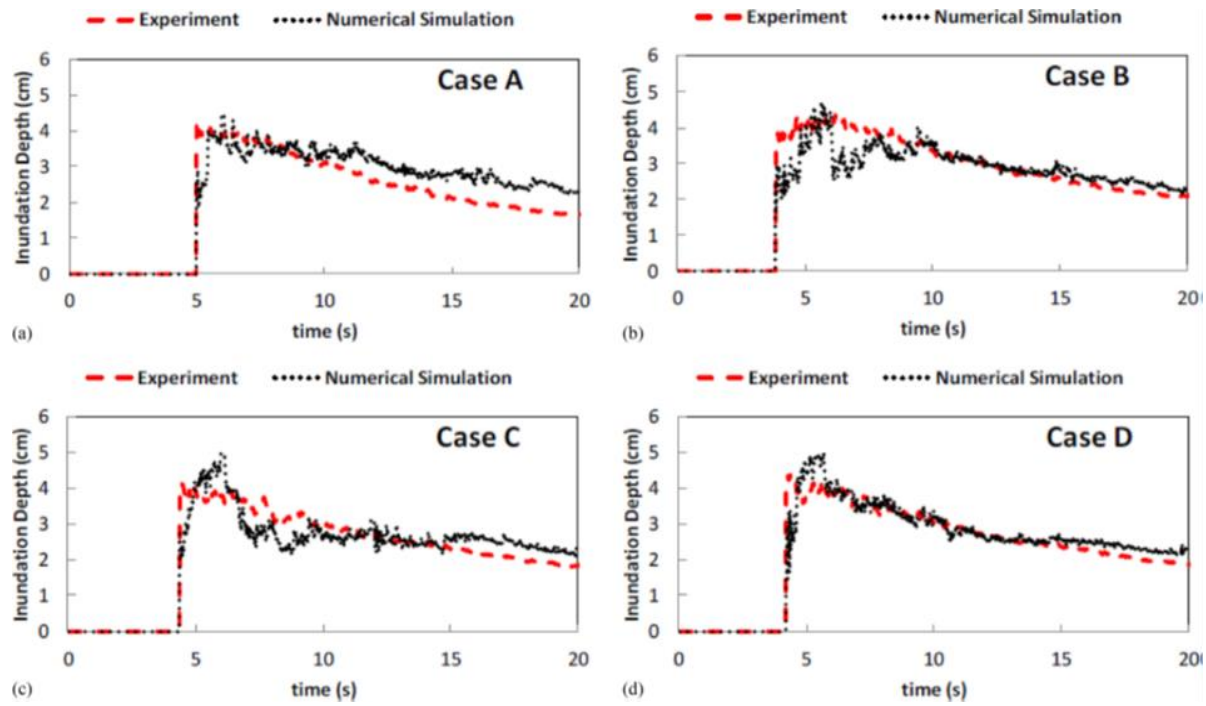

Figure 2.26. Quantitative comparisons of numerical results with laboratory measurements of water surface profiles at 3 m downstream of the canal: (a) Case A, (b) Case B, (c) Case C, (d) Case D (Rahman et al. 2017).

The experimental results were performed to validate the numerical simulation results using the improved Moving Particle Semi-implicit (MPS) method. Case A displayed remarkable agreement between the experimental and simulation results only at the beginning of the inundation-depth profile, but Cases B–D displayed overall remarkable agreement between the numerical simulation results and the experimental data overall (Rahman et al., 2017). Figure 2.27 shows the comparison of the velocity-time histories for the experimental and numerical simulations, which were found to be in good agreement.

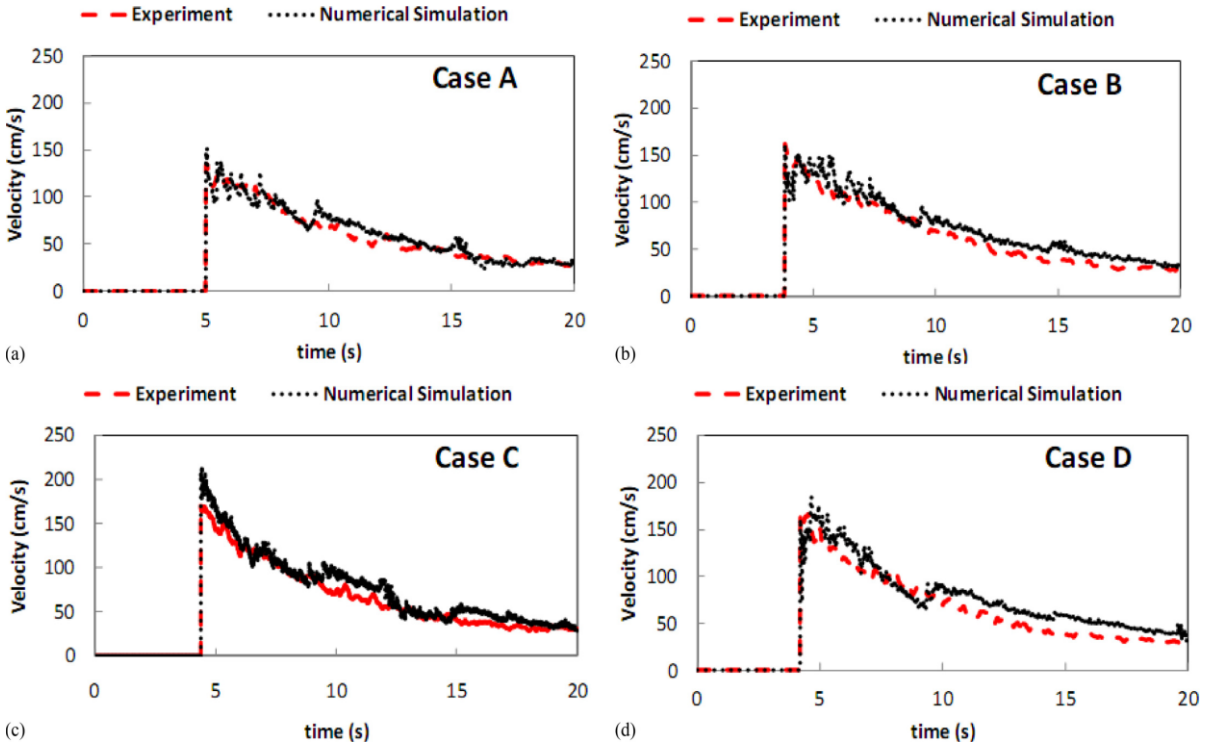

Figure 2.27. Quantitative comparisons of numerical results with laboratory measurements of velocity profiles at 3 m downstream of the canal: (a) Case A, (b) Case B, (c) Case C, (d) Case D (Rahman et al. 2017).

The experimental and simulated velocity-time history profiles displayed better agreement than the experimental and simulated inundation-depth profiles, though there were still some differences. Cases A and B displayed slightly lower velocity time history profiles than Cases C and D (Rahman et al., 2017).

Douglas & Nistor (2015) performed a sensitivity analysis by examining various mesh resolutions to quantify the influence on OpenFoam model results. Even though they examined many different cell sizes, they mentioned that any cell size larger than 2 cm did not effectively provide information in the model area, for example, the splash at initial impact. They experimentally observed and simulated water surface elevations at WG9 (run-up on the model upstream side) for the three different meshes of changing cell size: uniformly distributed 2 cm grids, uniformly distributed 1.5 cm grids and a mesh produced firstly with a uniform distribution of 2 cm cells which then was refined to 1 cm cells in the adjacent model area. Douglas & Nistor, (2015) demonstrated that the first peak in the time-series of water level displays the splash that happens after the impact of the quickly propagating wave. They also proved that the mesh resolution has a considerable effect at this period, up until a specific threshold (Figure 2.28). A substantial increase in the computed water surface elevation is perceived when refining the mesh from the 2 cm cells to the 1.5 cm cells, improving the agreement with the experimental data. Nevertheless, further refining the mesh from 2 cm cells to 1 cm cells in the adjacent model region does not seem to have any further effect on the splash height.

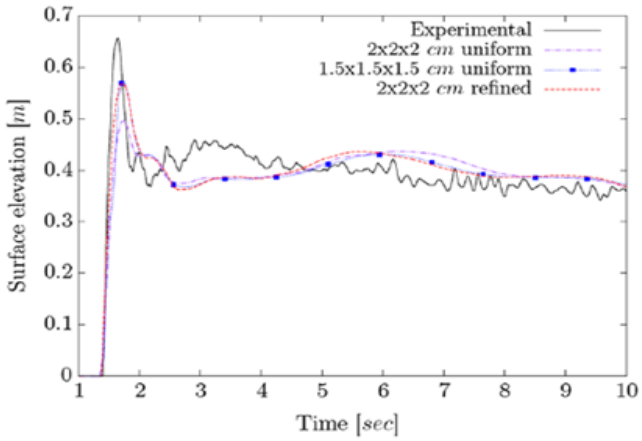

Figure 2.28. The sensitivity of a model to mesh resolution changes for replicated water surface run-up at the model for upstream water depth, h_u= 0.55 m (Douglas & Nistor, 2015).

As a procedure of validating the suggested numerical model, Sarjamee, et al. (2017a) conducted a comparison for the time-series of the water level profiles at several time points alongside a flume with a triangular barrier. The comparison achieved via the computational OpenFoam model with the findings of the physical data of Soarez-Frazao (2002) performed at Université Catholique de Louvain (UCL) in addition to the computational outcomes achieved by Biscarini et al. (2010) who employed an OpenFoam computational model as well. The standard $k-\varepsilon$ turbulence model was employed as the suggested model. As observed, at time t = 1.8 s after the gate opening, the triangular obstacle has been overtopped by the dam break wave, which arrived at approximately the midpoint of the downstream slope and splashed further on the end face of the wall of the trivial flume. (Figure 2.29) shows the comparative outcomes of the computational simulations and experimental investigations.

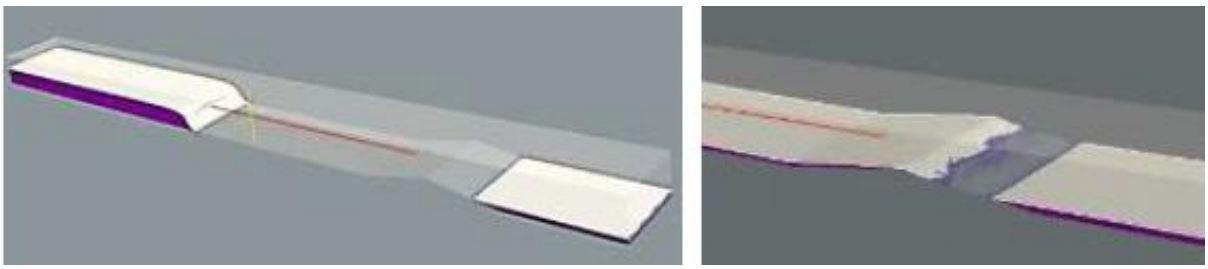

Figure 2.29. Optical view of the water surface level when time equals 1.8 s after the opening of the gate (Sarjamee, et al. 2017a).

Generally, the results of the numerical simulations (the standard $k-\varepsilon$ turbulence model) agree well with the numerical results of Biscarini et al. (2010) and with the experimental model results (Figure 2.30a). However, it can be noticed that the modeled data and the physical test results of the time-series of the water surface elevations above the downstream slope do not show good agreement; this may be attributed to the fact that the air bubbles trapped in the water pool shaped above the downstream slant were triggered by the splashing water. Thus, the trapped air was probably not simulated properly by the employed numerical model (Sarjamee, et al. 2017a). Furthermore, an analogous inclination can be preserved between the experimental and simulated data at t = 3 s (Figure 2.30b), and the numerically measured water surface elevation from the position X = 4.2 m to 4.4 m from gate lifting displays less precision compared to the water

elevation measured in the physical examinations. However, the maximum differences in the water elevation are preserved in the water pool executed above the downstream slope.

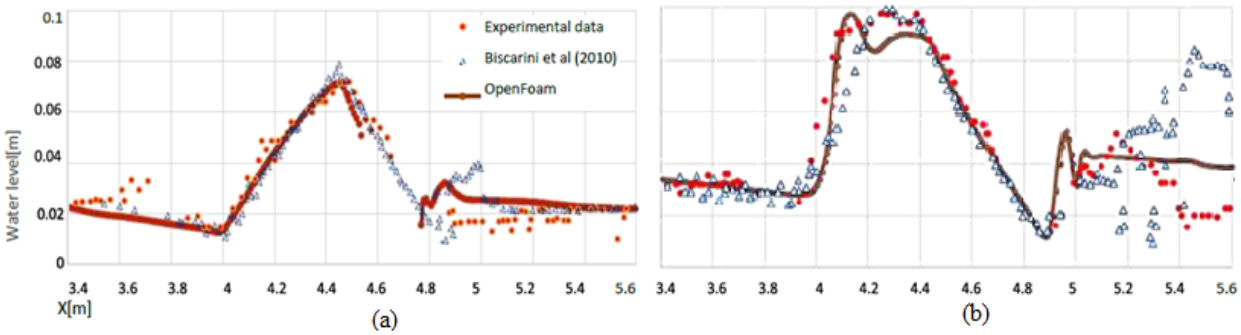

Figure 2.30. Comparison of the maximum flow elevation for OpenFOAM model, modeled results of Biscarini et al. (2010), and the laboratory results after the lifting of the gate at (a) 1.8 s, and (b) 3.0 s (Sarjamee, et al. 2017a).

A simulation with an upstream water depth h_u = 1.15 m was carried out without the presence of a structural column (Figure 2.31).

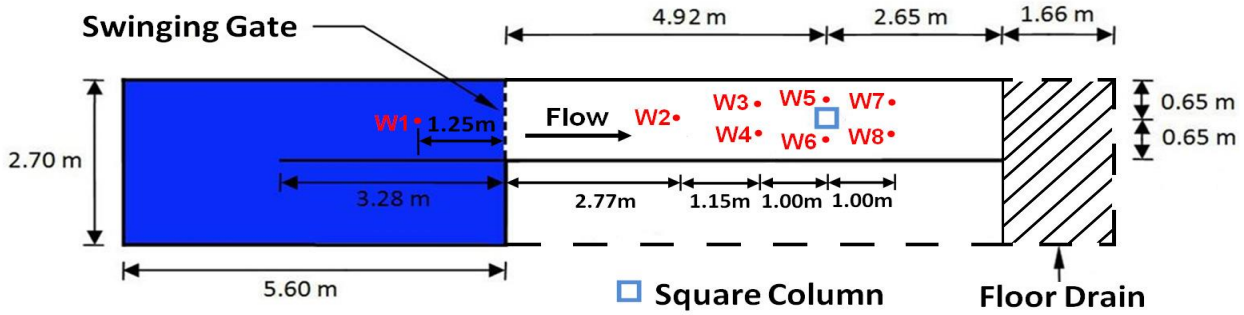

Figure 2.31. The locations of wave gauges throughout experiments with the absence of the column (Nistor et al. 2010).

For validation purposes, numerical elevations of the water surface were compared to the physical results at four different wave gauges WG1, WG2, WG3, and WG6 (Figure 2.32).

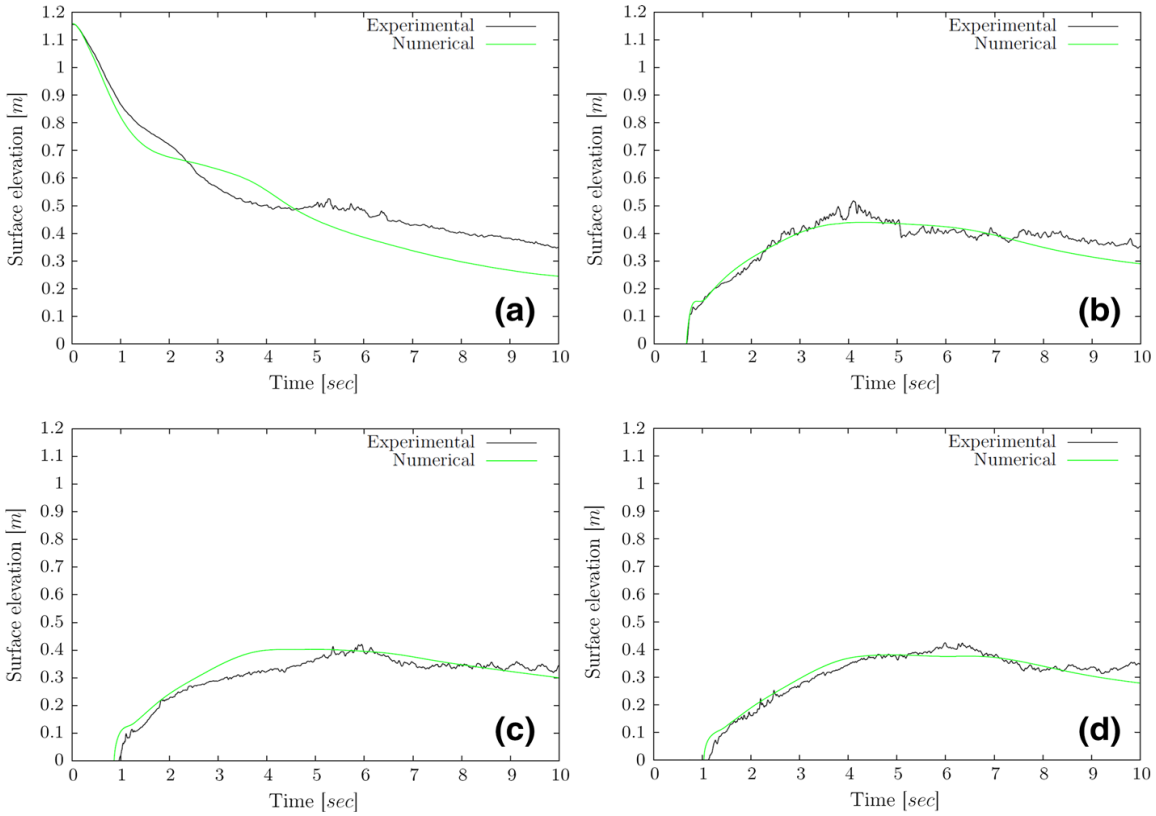

Figure 2.32. Comparison of simulated (OpenFOAM) and experimentally observed surface elevations at a) WG1, b) WG2, c) WG3, and d) WG6 without a column. The upstream water height h_u = 1.15 m (Douglas & Nistor, 2015).

Although the numerical water levels seem to be a very worthy match with the laboratory ones, particularly at WG2, WG3, and WG6, some differences start to be exhibited early on at WG1 when the water surface elevations begin to plateau at nearly t = 1.5 s. For a larger period, the numerical water surface level plateau shows that the upstream end of the numerical reservoir is arriving at the downstream end at a faster rate than that measured through the laboratory tests. For that reason, the simulated water surface elevation momentarily exceeds the laboratory result. According to the latter description, the numerical water surface elevation at WG1 would, at some point, have to decrease at a faster pace than the experimental level perceived owing to a higher ratio in reservoir depletion. Even though this could be the case, the disagreement may be because the computational domain did not take into account an extra amount of water remaining inside the pipe that provides the high-discharge flume. It should be noted that water elevations seem to be duplicated with a great degree of precision in the channel section, despite the discrepancies preserved in the reservoir (Douglas & Nistor, 2015).

Nistor et al. (2010) performed a simulation with an impoundment water depth of h_u = 0.85 m in the presence of a structural model. (Figure 2.33) indicates that a difference happens in the early times of the bore and structure interaction; this is due to the substantial water splash happening at the initial impact that is not accurately reproduced by the numerical model. However, later in the modeling, after nearly 3 s the agreement in the run-up is reasonably good.

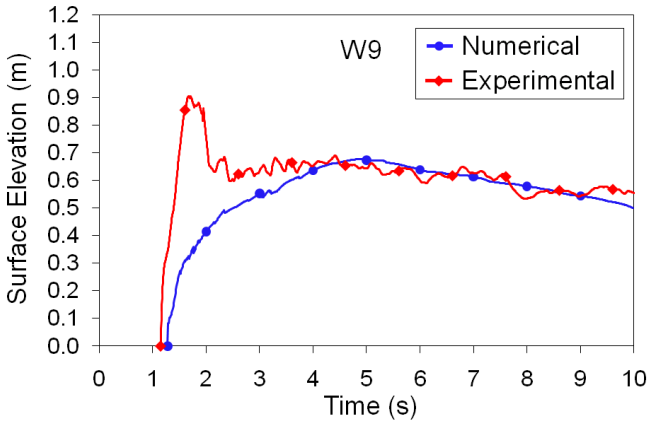

Figure 2.33. Comparison of the time-series of numerical (SPHysics) and laboratory flow level at the column front side W9 (run-up) for h_u = 0.85 m (Nistor et al. 2010).

(Figure 2.34) displays a qualitative comparison of the experimental and computed profiles of water elevations for upstream impoundment heads h_u = 0.85 m at various times.

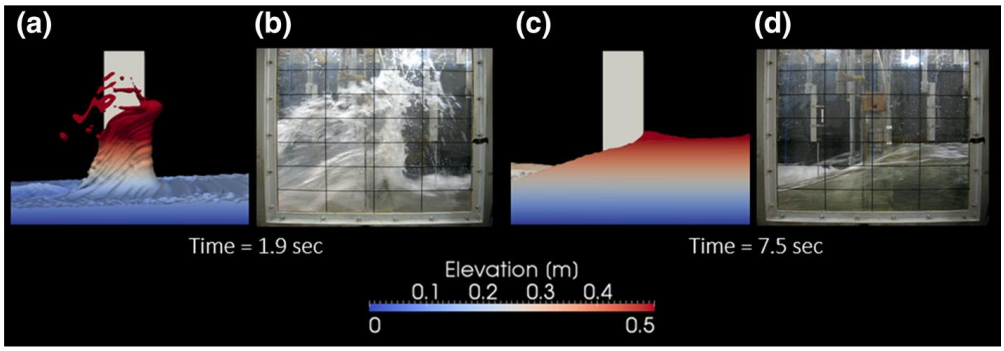

Figure 2.34. Comparison of modeled (a and c) and laboratory (b and d) flow levels for h_u = 0.85 m qualitatively (Douglas & Nistor, 2015).

In the first still-frame comparison, at t = 1.9 s, the first run-up tongue has peaked and then starts to fall immediately under the effect of gravity. Throughout this period, the hydrodynamic surface breakup is widespread and moving around the four sides of the column, and looks like spray reflecting off the column upstream side. Douglas & Nistor (2015) mentioned that the hydrodynamic surface breakup is moderately regenerated, whereas the simulated splash height seems to be reasonably in line with the physical experiments. The local mesh resolution is substantially affected by this phenomenon and would need significantly fewer cells to raise the excellence of the visual comparison. At a later phase throughout the simulation, at t = 7.5 s, water surface profiles are compared. The quick variation in water level before and after the column has produced a powerful acceleration in the flow around the model.

Douglas & Nistor, (2015) pointed out that time-series of the net stream-wise force acting on the structure could be executed by incorporating the computed pressures across the four model sides at each time step and compared to laboratory tests measured by the 6-DOF dynamometer. (Figure 2.35) shows a distinct peak of the experimental force happening at nearly t = 2 s, nearly 0.6 s after the initial interaction between the front of the bore and the upstream side of the column.

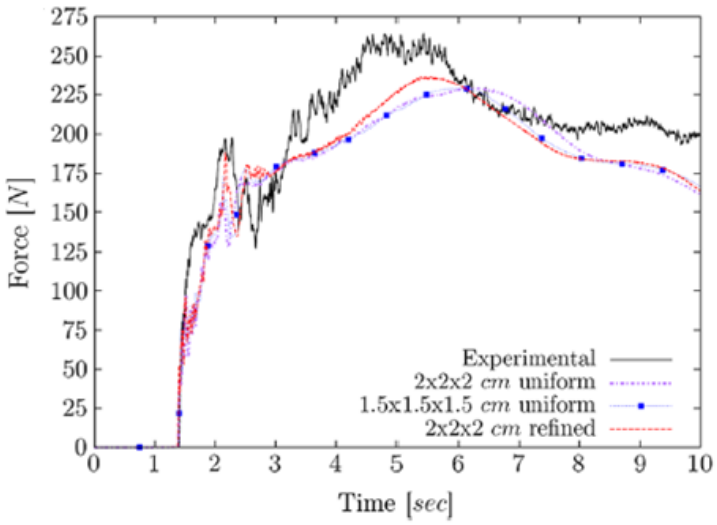

Figure 2.35. The sensitivity analysis of a model to mesh resolution changes: load on the model for upstream water height, h_u= 0.55 m (Douglas & Nistor, 2015).

The computational results show an analogous inclination. According to further investigation, Douglas & Nistor (2015) discovered that the peak occurs simultaneously with the initial run-up tongue breaking onto the arriving flow, a similar comment also mentioned in the tests of Ramsden (1993). The three various mesh resolutions displayed changing values of this initial peak. The force value seems to be regenerated precisely by the refined mesh with 1 cm cells in the near-model region, even though the experimental peak happens over a larger duration of time. After the initial peak, the numerical and experimental results start to diverge owing to different rates at which the force rises. It should be noted that slightly better agreement was produced as the peak hydrodynamic force is shifted in the value and occurrence time by using the refined mesh. Sarjamee et al. (2017a) made an effort to obtain appropriately precise results independent of the mesh resolution on the magnitude of the total base shear force exerted on a square column. They ran trial simulations starting from initially coarse mesh cells to obtain a suitable grid. They compared their numerical results with the physical data of Al-Faesly et al. (2012).

Sarjamee, et al. (2017b) executed a sensitivity analysis to create the proper cell for the suggested numerical model, to confirm that the model is mesh resolution-independent. They achieved the analysis by running many simulations with changed grid sizes of 3 cm, 2 cm, and, lastly, 1 cm. They indicated that the 1 cm grid cell size did not produce the best outcome, but the 2 cm grid cell size generated the best results. Thus, the 2 cm grid size was used to execute all the simulations. They tested different models like RANS ($k-\varepsilon, k-\omega$, and LRR) and LES to improve accuracy to produce an accurate model proficient in simulating certain situations. The results shown in (Figure 2.36) indicated that the different conditions were not precisely simulated by the RANS model.

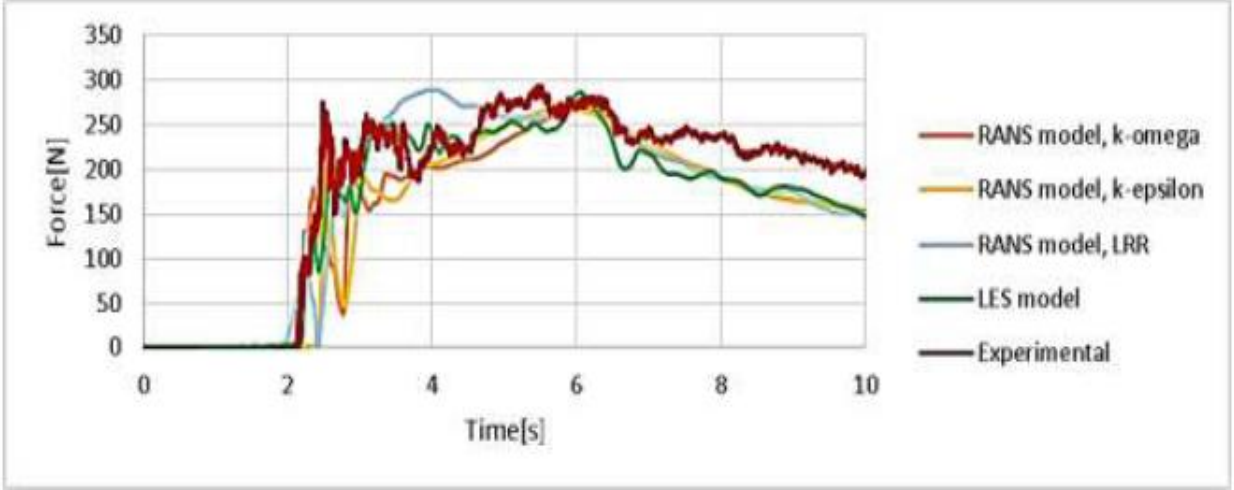

Figure 2.36. Testing influence of different turbulence models (Sarjamee, et al. 2017b).

However, the LES approach reproduced the experimental data more accurately. They argued that due to high Reynolds numbers, LES can be reasonably more effective since it does not deal with the whole length scale spectrum. It should be noted that it simulates merely the influence of smaller scale eddies and it models larger scale eddies of the flow.

2.7 Discussion and Research needs

The literature review provided in this chapter focuses on existing research performed about the effects of canal geometry on the hydrodynamics of tsunami-like turbulent bores upstream and downstream of a rectangular mitigation canal by a series of physical experiments as well as the variations of specific momentum and energy upstream and downstream of the canal. However, the previous studies concentrated on a narrow work to examine this subject properly. The previous sections explain some gaps in understanding and the necessity for further examinations that motivated the recent research as follows:

- Although several experimental and numerical research works focus on rectangular mitigation canals subjected to turbulent bore propagations, little attention has been paid to address the impact of high transient flows in extreme events such as tsunamis bores on mitigation canals. Their available data may not reflect the effect of the mitigation canal on bore hydrodynamics. Therefore, there is a need to continue the investigation of the influences of tsunami turbulent bores by relatively larger impoundment depths.

- Existing research contains a narrow range of canal aspect ratios for different canal geometries to investigate the effects of canal geometry on hydrodynamic characteristics. There is a gap in the literature for suggestions on the comprehensive experimental study testing a wide range of canal aspect ratios to investigate the effects of the canal geometry on the hydrodynamic characteristics of the turbulent bore before and after the canal.

- Existing studies exhibit either no data on bore properties recorded downstream of the canal or velocity data collected far downstream from the canal. The downstream bore velocity was collected at a distance between five and ten times the canal width. Therefore, their available data

may not reflect the impact of the mitigation canal on surge hydrodynamics. There is a gap in the literature for suggestions on investigating the effects of the mitigation canal on turbulent bore propagation by collecting wave heights and velocities in the vicinity upstream and downstream of the canal.

- Analogous to the physical experiment examinations, some researchers have studied hydrodynamics upstream and downstream mitigation canals impacted by the transient flow. Such a study has been performed by a numerical modeling technique such as MPS. There is a gap in the literature on the numerical investigation of the entrapped air when a bore plunges into a canal to decrease its effect on water surface profiles and inspect different turbulence models with RANS, LES, and DES.

3 The Numerical Model

3.1 OpenFOAM Explanation – the Online Open Source CFD Toolbox

The open-source software implemented in this study is OpenFOAM (Open Field Operation and Manipulation), which runs on the Linux operating system. The OpenFOAM code is a numerical simulation package that provides customized numerical models and solvers written in C++ language, which are applicable for different science and engineering problems. It is also applicable for solving continuum mechanics problems, for example, CFD (Computational Fluid Dynamic) analysis. The open-source feature of OpenFOAM, which is one of the most interesting functional features of this software, enables the users to modify and stretch its offered functionality and make it thoroughly effective, depending on their project requirements. For instance, the extensibility features permit operators to produce typical modeling components such as initial conditions, turbulence models, or boundary conditions, with no need to alter the present source code. Besides that, there are other useful tools, such as meshing, pre-processing, and post-processing tools. Furthermore, if the model necessitates extra functionality, the user can add it. Another attractive feature of the available libraries in OpenFOAM is that they are object-oriented, which provides the programmers with a new technique that removes the difficulty of conventional programming languages. Hence, the object-oriented programming techniques of C++ and its employment in OpenFOAM enable a tensor operations syntax that looks significantly like the PDEs being solved. This characteristic of OpenFOAM can provide users the freedom to customize the code or to develop wholly new solvers with relative ease. The OpenFOAM software is useful for modeling a wide variety of engineering problems via solving the form of partial differential equations (PDE) through employing the Finite Volume Method (FVM) that is inherently mass conservative (OpenFOAM 2014).

This software model applies the Finite Volume Method with a polyhedral grid, and it can be implemented for tremendously simultaneous computing as well (Jasak et al., 2007). It is worth mentioning that one of the OpenFOAM characteristics is equation representation, as it offers very close similarity to the equations being solved, and enables software model users to develop diverse custom solvers. The OpenFOAM solver applied for the current case is InterFoam. It is capable of manipulating the free-surface problem where two different fluids are divided from each other by a sharp boundary. The flow can be predicted by InterFoam as long as the discretization procedure that captures the interface is achieved using FVM. Generally, the appropriate equations are incompressible RANS. The turbulence is simulated using an incompressible RANS model. The modeling domain employed structured meshes in this current study (OpenFOAM 2014).

3.2 Governing Equations

The Navier-Stokes (NS) equations have the potential to predict the fluid motion by explaining how flow coefficients such as velocity, density, pressure, and temperature are derived from conservation laws and how they are related to each other. These equations are the principal partial differential equations and can control the motion of all types of flows irrespective of their type. Thus, the flow coefficients can be achieved directly (Direct Numerical Simulation, DNS) in a

temporal averaged form (Reynolds-Averaged Navier-Stokes, RANS) or by using the spatially-filtered form (LES) as explained in the following section.

3.2.1 The Continuity and Momentum Equations

The essence of mass conservation that is defined by the continuity equation and depends on the idea that the fluid mass needs to be preserved. Thus, the number of fluid particles moving in a fluid area must be equal to those moving out of the same area. Furthermore, the derivation of the continuity equation is particularly relied on considering the shape of the control volume of a cube and matching the net flow to zero to achieve the mass conservation law requirement.

3.2.1.1 Reynolds-Averaged Continuity Equation

The partial differential form of the continuity equation for a three-dimensional system is written as (Chamani, 2013, p. 209)

$$\frac{\partial \bar{u}}{\partial x}+\frac{\partial \bar{v}}{\partial y}+\frac{\partial \bar{w}}{\partial z}=0 \qquad (3.1)$$

$$u\,(t)=\bar{u}+\acute{u} \quad v\,(t)=\bar{v}+\acute{v} \quad w\,(t)=\bar{w}+\acute{w} \quad p\,(t)=\bar{p}+\acute{p} \qquad (3.2)$$

where $\bar{u}$, $\bar{v}$ and $\bar{w}$ are the mean velocity components, $u´$, $v´$, and $w´$ are the fluctuation velocity components, $\bar{p}$ and $\acute{p}$ are the mean and fluctuation fluid pressure components in the $x, y, and\ z$ directions, respectively.

The average flow velocity governs the Reynolds-Averaged continuity equation.

3.2.1.2 Reynolds-Averaged Momentum Equation

Likewise, the partial differential form of the momentum equation for a three-dimensional system can be written as (Chamani, 2013).

$$\bar{u}\frac{\partial \bar{u}}{\partial x}+\bar{v}\frac{\partial \bar{u}}{\partial y}+\bar{w}\frac{\partial \bar{u}}{\partial z}=-\frac{1}{\rho}\frac{\partial \bar{p}}{\partial x}+g_x+v\left(\frac{\partial^2 \bar{u}}{\partial x^2}+\frac{\partial^2 \bar{u}}{\partial y^2}+\frac{\partial^2 \bar{u}}{\partial z^2}\right)-\left(\overline{\frac{\partial \acute{u}^2}{\partial x}}+\overline{\frac{\partial \acute{u}\acute{v}}{\partial y}}+\overline{\frac{\partial \acute{u}\acute{w}}{\partial z}}\right) \qquad (3.3)$$

$$\bar{u}\frac{\partial \bar{v}}{\partial x}+\bar{v}\frac{\partial \bar{v}}{\partial y}+\bar{w}\frac{\partial \bar{v}}{\partial z}=-\frac{1}{\rho}\frac{\partial \bar{p}}{\partial y}+g_y+v\left(\frac{\partial^2 \bar{v}}{\partial x^2}+\frac{\partial^2 \bar{v}}{\partial y^2}+\frac{\partial^2 \bar{v}}{\partial z^2}\right)-\left(\overline{\frac{\partial \acute{v}^2}{\partial y}}+\overline{\frac{\partial \acute{u}\acute{v}}{\partial x}}+\overline{\frac{\partial \acute{v}\acute{w}}{\partial z}}\right) \qquad (3.4)$$

$$\bar{u}\frac{\partial \bar{w}}{\partial x}+\bar{v}\frac{\partial \bar{w}}{\partial y}+\bar{w}\frac{\partial \bar{w}}{\partial z}=-\frac{1}{\rho}\frac{\partial \bar{p}}{\partial z}+g_z+v\left(\frac{\partial^2 \bar{w}}{\partial x^2}+\frac{\partial^2 \bar{w}}{\partial y^2}+\frac{\partial^2 \bar{w}}{\partial z^2}\right)-\left(\overline{\frac{\partial \acute{w}^2}{\partial z}}+\overline{\frac{\partial \acute{w}\acute{v}}{\partial y}}+\overline{\frac{\partial \acute{u}\acute{w}}{\partial x}}\right) \qquad (3.5)$$

Where p is the fluid pressure, t is the time, ρ is the fluid density, and g is the gravitational acceleration.

3.2.2 Indicator Function

The phase fraction, an additional field variable, is incorporated into the system to define the spatial distribution of the two fluids at any given time step. The phase fraction α is a scalar function which

can be a magnitude bound between one and zero depending on the fraction of two phases: liquid and air. It can be assessed mathematically from the following indicator function:

$$\alpha = \begin{cases} 0, & in\ fluid\ a \\ 0 < \alpha < 1, & in\ the\ transitional\ region \\ 1, & in\ fluid\ b \end{cases} \qquad (3.6)$$

In a physical sense, the phase fraction specifies the percentage of a computational grid cell that is filled with a certain liquid at a given time step. It is also denoted as an indicator function because of its ability to denote the phase-state of a given region in space. Adhering to the classification equation (3.6), the phase fraction is equal to either zero or one for cells that are entirely air or entirely water, respectively. On the other hand, the intermediate zone indicates a very slight layer between the two pure phases that have combined and exist in a mixed condition; accordingly, a phase fraction magnitude between zero and one exists for cells containing the interface. The phase fraction parameter α is a conserved quantity and follows a transport equation of the form:

$$\frac{\partial \alpha}{\partial t} + \nabla . (\boldsymbol{U}\alpha) = 0 \qquad (3.7)$$

The volume of fluid (VOF) method is considered one of the proposed interface-capturing techniques capable of tracking the free surface. This technique can simply determine the flow happening in a two-phase domain, for instance, air and water, by taking into consideration that each phase is considered as a single fluid that experiences physical properties variation throughout the interface. The value of the phase fraction α firstly should be calculated due to the magnitude of ρ and μ based on that parameter. The VOF technique considers an advection process for the phase fraction the case of a system with two phases. The significant advection term's role is its capability to calculate the position of the free surface, and its key benefit is that it offers sharp boundaries for the free surface, which is sensitive to the grid cell size in most other techniques.

The weighted average uses the spatial distribution of the liquid phase fraction once it has been calculated to update the fluid properties in each cell according to

$$\rho = \rho_a\ (1 - \ \alpha) + \rho_w\ \alpha \qquad (3.8)$$

Where a and b indicate the values for the two different fluids.

If the perception of the phase fraction were put to practical use, it would perform similar to that of a step function with intermittent jumps from zero to one via the boundary between the two phases. But despite that, a crucial matter with simulating the convection of such a function is the need to sustain the sharp interface transport while considering the boundedness preservation and the phase fraction conservation (Berbeovic, 2010). Many approaches have been implemented to treat this problem. The technique of the VOF solvers, which exist in OpenFOAM, utilizes the approach developed by Weller (2008). In this approach, the numerical treatment of the phase fraction steep gradients is described by the offering of an artificial compression term (last term on the RHS of the bellow equation) into the transport equation, taking on the form of

$$\frac{\partial \alpha}{\partial t} + \nabla \cdot (\boldsymbol{U}\alpha) + \nabla \cdot (U_c\, \alpha(1 - \alpha)) = 0 \qquad (3.9)$$

Where U is the velocity vector, and U_c the compression velocity. The above stated synthetic compression term in the transport equation is active only for a narrow transitional region neighboring the theoretical interface position. It is calculated by multiplying $\alpha(1 - \alpha)$ by the divergence of the compression velocity**.** On the other hand, for locations in a direction away from and normal to the interface, the artificial compression term gradually disappears at both extreme limits of the phase fraction; the original indicator function should be used for evaluation, and it is reduced to equation (3.7). It should be understood that the synthetic compression term does not have any relation to the compressibility of the flow, but as an alternative denotes its inclination to shrink the smeared interface induced by numerical diffusion of the phase fraction. Other than being active only in the region of the interface, the flow of the phase fraction should be limited by the artificial convective term to a direction that is perpendicular to the interface (Berberović, 2010). Thus, in this condition, the artificial compressive force acts only as a vector in the reverse side of the interface and will not influence the natural flow of the phase fraction α, according to equation (3.7). Accordingly, to meet these criteria, OpenFOAM uses the following equation capable of evaluating the compression velocity U_c generally.

$$U_c = \min\left[C_\alpha\, |\boldsymbol{U}|, max\ (|\boldsymbol{U}|)\right] \frac{\nabla \alpha}{|\nabla \alpha|} \qquad (3.10)$$

Usually, the first term in equation (3.10) controlled the compression velocity. However, in order to maintain the stability of the solution, it is restricted from going beyond the maximum velocity happening in the system. The interface compression intensity is governed by the compressive coefficient C_α. If set to one, it yields a conservative compression, while any value beyond one matches the improved compression of the interface. Alternatively, a compressive coefficient value of zero, the artificial compressive term in equation (3.13) gradually vanishes, and suppression of the numerical diffusion of the interface is turned off (Open CFD Ltd., 2015a).

3.2.3 Turbulence Modeling

Usually, turbulent flow contains a coherent rotating structure called an eddy and can be classified into different velocity and length scales. Thus, the shear generated in the flow is caused by the largest, called energy-bearing or production-scale eddies, through the interaction with some other bodies. Once generated, there is a sequence of energy to smaller scales of motion until viscous stresses in the fluid completely stop the motion. However, the chaotic and random fluctuations in flow properties can increase due to stretching, warping, and combining of these coherent rotating structures with one another in extremely complex ways. The aggregate of these turbulence interactions tends to result in the augmented mixing of energy, dissipation, heat transfer, and drag (George, 2013).

In both practical and research engineering problems, the way turbulence is treated in numerical simulations has therefore been a significant subject. One alternative amongst others is a method called Direct Numerical Simulation (DNS) that utilizes the Navier-Stokes equations (NSE) to resolve all scales of turbulence explicitly. This method is impractical for a majority of problems,

as it carries the strictest meshing requirements and often demands a high level of computational effort. Another popular technique is called Large Eddy Simulation (LES), which is used to separate turbulent length scales into two groups, and a spatial filtering operation is implemented. Thus, the influences of the smaller eddies on the solution are applied by a Sub-Grid Scale (SGS) model. Conversely, bigger vortices are resolved, and their influences on the average flow are simulated immediately. The basic assumption of the LES models is that the large vortices (those larger than a grid cell) are the most important, carrying more energy and influencing flow behavior. As a result, this model ignores the existence of small vortices, an assumption that reduces model accuracy in situations where small-scale turbulence is critical, such as near-wall region flows and situations where several flows interact. Instead, in LES models, the energy dissipation by small scale eddies is simulated using approximate models.

Though LES techniques have been approaching universality, the so-called Reynolds-Averaged Simulations (RAS) or Reynolds-Averaged Navier-Stokes (RANS) technique remains the most broadly employed. Thus, in Reynolds-Averaged Simulations (RAS) approaches, the flow parameters in the (NS) equations are separated into average and turbulent oscillation components. These decomposed parameters are substituted into the (NS) equations and integrated throughout time. The main significant motivation for this was to improve a system of equations for which the solution can produce mean flow parameters. Thus, these mean flow variables would greatly reduce the required computational effort. However, an extra unknown stress term, called the Reynolds stress, is created during the procedure of the derivation. Consequently, the famous closure problem arises for which many solutions have been offered but are too numerous to explain. Here, we concentrate our explanation on a general overview of the RANS models distributed with OpenFOAM.

There is no single completely valid and specific turbulence model. In addition, the improvement in the computational approaches for partial differential equations, in addition to the flow properties and the advancement of computing tools, can deeply influence the development of the Computational Fluid Dynamics (CFD) field. Usually, there are four stages required for solving CFD problems, which are: generating a computational model of the problem, determining the geometry and generating the numerical grid, and solving and analyzing the attained data. Furthermore, it is important to completely discover the principle of the related physics for each case since the creation of a physical model is not essentially a perfect approach for turbulent flow. The developing turbulence models can be achieved by the time-dependent, nonlinear, 3D properties of the (NS) equations.

3.2.4 Classification of RANS Turbulence Models

It is not necessary to find a solution to all the details of the turbulent fluctuations for most engineering problems. Generally, data regarding the time-averaged flow properties (e.g., average, speeds, average stresses, average pressures, etc.) can satisfy CFD users. Therefore, the turbulent flow calculations were performed using Reynolds-averaged Navier–Stokes (RANS) equations based procedures**.** Owing to the method of time-averaging on the momentum equations, which dispenses with all details relating to the flow condition presented in the instantaneous fluctuations, a clarification of the turbulence influences on the average flow is still highly required. To calculate turbulent flows of the RANS equations, it is necessary to improve turbulence models to anticipate

the Reynolds stresses and the conditions of scalar transport, and close the average flow equations. However, a wide range of qualities such as being accurate, simple, and economical are essential for a turbulence model to be valuable in a general-purpose CFD code to run. It depends on the aggregate of added transport equations required to be calculated together with the RANS flow equations; thus, the most famous RANS turbulence models are categorized (Versteeg and Malalasekera, 2007).

3.2.4.1 Two-Equation Models

The two-equation turbulence models are mentioned among the most popular turbulence models, including $k-\varepsilon$, realizable $k-\varepsilon$, RNG $k-\varepsilon$, $k-\omega$, and $k-\omega\ SST$ turbulence models. They are generally employed for many different kinds of problems in engineering, and also have become industry standard models. The $k-\varepsilon$ model is largely employed for general and developed turbulence. The effect of transportation of turbulence characteristics through diffusion, convection, and the destruction and production of turbulence is permitted by the family of models. The explanation of turbulence is shown by two transport equations (PDEs), which are the turbulent kinetic energy (k), and the rate of dissipation of turbulent kinetic energy (ε), since it is a two-equation model. According to Versteeg and Malalasekera (2007), the turbulent viscosity is considered to be isotropic; consequently, the relation of average deformation rate and Reynolds stress is equal in every way.

3.2.4.2 The k $-\ \varepsilon$ Turbulence Model

The Navier-Stokes equations are capable of predicting the motion of a fluid. According to the technique that the user needs to deal with turbulent fluctuations in the flow, OpenFOAM provides various techniques. These equations are stated in Cartesian coordinates and tensor notation while disregarding body forces. Thus, the RANS conservation equations of mass and momentum of an incompressible fluid are shown as (Ferziger and Peric´ 2002, p. 293).

$$\frac{\partial(\rho\bar{u}_i)}{\partial x_i}=0 \qquad (2.11)$$

$$\frac{\partial(\rho\bar{u}_i)}{\partial t}+\frac{\partial}{\partial x_j}\left(\rho\,\bar{u}_i\,\bar{u}_j+\rho\,\overline{u_i'u_j'}\right)=-\frac{\partial\bar{p}}{\partial x_i}+\frac{\partial\bar{\tau}_{ij}}{\partial x_j} \qquad (3.12)$$

$$\bar{\tau}_{ij}=\mu\left(\frac{\partial\bar{u}_i}{\partial x_j}+\frac{\partial\bar{u}_j}{\partial x_i}\right) \qquad (3.13)$$

where $\bar{u}_i$ = mean velocity component, u_i' = fluctuating velocity component, ρ = fluid density, p= fluid pressure, μ = dynamic viscosity of the fluid and $\bar{\tau}_{ij}$ = the mean viscous stress tensor components.

It is impossible to answer the momentum and continuity equations analytically, except for a very few straightforward conditions. To close equations (3.11) and (3.12), in 1877, a novel idea of turbulent viscosity was developed by Boussinesq and the Reynolds stresses ($\rho\overline{u_i'u_j'}$) numerically defined by time-averaging the flow equations (Ferziger and Peric´ 2002, p. 294), which led to:

$$-\rho\,\overline{u_i'\,u_j'} = \mu_t\left(\frac{\partial \overline{u}_i}{\partial\, x_j} + \frac{\partial \overline{u}_j}{\partial\, x_i}\right) - \frac{2}{3}\,\rho\,\delta_{ij}\,k \qquad (3.14)$$

As can be noticed in the above equation (3.14), there is one more unknown parameter (μ_t) presented in the new equation, and an appropriate turbulence model must be utilized to assess it and close the solution system. Therefore, to obtain an accurate result, it is extremely significant to choose an appropriate turbulence model.

The two-equation turbulence models are among the most common turbulence models. Several two-equation models are presented for turbulent flow such as $k-\varepsilon$, realizable $k-\varepsilon$, RNG $k-\varepsilon$, $k-\omega$, and $k-\omega\ SST$ models. They are universally employed and converted as manufacturing criteria for significant engineering problems of many kinds. For example, these two-equation models were implemented for simulating ship flows (Xing et al., 2007), and also for some other conditions related to heat conduction in a porous medium (Fourie and Plessis 2003), aerodynamic flux (Menter, 1993), etc. The $k\ -\ \varepsilon$ model is briefly reviewed herein as it has been implemented in this experiment.

The two-equation turbulence models were revealed after the major achievement effort by Kolmogorov (1942), whereas the $k\ -\ \varepsilon$ model was presented many years later for turbulence. Thus, the turbulent kinetic energy, *k*, and its dissipation rate, *ε*, are computed from the following transport equations (3.15) and (3.16) (Ferziger and Peric´ 2002, p. 295, 296). They are solved concurrently along with the continuity, momentum, and phase fraction transport equations.

$$\frac{\partial(\rho k)}{\partial t} + \frac{\partial(\rho \overline{u}_j\, k)}{\partial x_j} = \frac{\partial}{\partial x_j}\left(\mu\ +\ \frac{\mu_t}{\sigma_k}\right)\frac{\partial k}{\partial x_j} + P_k - \rho\varepsilon \qquad (3.15)$$

$$\frac{\partial(\rho \varepsilon)}{\partial t} + \frac{\partial(\rho \overline{u}_j\, \varepsilon)}{\partial x_j} = C_{\varepsilon 1}\, P_k\, \frac{\varepsilon}{k} - \rho\, C_{\varepsilon 2}\, \frac{\varepsilon^2}{k} + \frac{\partial}{\partial x_j}\left(\frac{\mu_t}{\sigma_\varepsilon}\right)\frac{\partial \varepsilon}{\partial x_j} \qquad (3.16)$$

Furthermore, both the turbulent dynamic (eddy) viscosity (μ_t), which is given as a function of k and ε, and the production rate of turbulent kinetic energy by the mean flow (P_k) are calculated from equations (3.17) and (3.18)

$$\mu_t = \rho\, C_\mu\, \frac{k^2}{\epsilon} \qquad (3.17)$$

$$P_k = \mu_t\left(\frac{\partial \overline{u}_i}{\partial x_j} + \frac{\partial \overline{u}_j}{\partial x_i}\right)\frac{\partial \overline{u}_i}{\partial x_j} \qquad (3.18)$$

For the RAS turbulence models, the model coefficients have been given assumed magnitudes in their relevant source codes. However, these default values can be redefined differently in a sub-dictionary comprised in the case folder if the user wants to override them. The standard $k\ -\ \varepsilon$ turbulence model depends on equations (3.15) and (3.16), which are broadly utilized. Thus, the default coefficient values of the model allocated standard magnitudes of $C_{\epsilon 1}$= 1.44, $C_{\epsilon 2}$ =1.92, C_μ = 0.09, σ_k = 1.0, and σ_ϵ = 1.3 in the source code.

3.2.4.3 The *k*-*ε* Family

The *k*-*ε* family of turbulence models (standard *k*-*ε*, renormalization group *k*-*ε*, and realizable *k*-*ε* turbulence models, etc.) has become among the most extensively applied, although it does not perform well in the presence of high adverse pressure gradients (Wilcox, 1998). It comprises two-equation models, which means there are two additional transport equations to account for a flow's turbulent characteristics. This permits the two-equation model to account for historical effects such as turbulent energy diffusion and convection. For a vast variety of turbulent flows, a *k*-*ε* model provides robustness, economy, ease of implementation, low computational cost, and reasonable accuracy (Cable, 2009). Many authors have stressed these models' capability to produce reasonable expectations and acceptable results, as well as their low computational time, in addition to being simple enough to be numerically tractable (Lien et al., 2004). *k*-*ε* models have been demonstrated to be beneficial for free-shear-layer flows with relatively low-pressure gradients, as discussed in Bardina et al. (1997). Likewise, the models produce satisfactory results for wall-bounded and internal flows, but only when mean pressure gradients are low; accuracy has been demonstrated experimentally to be decreased for flows with substantial adverse pressure gradients. As a result, it is reasonable to conclude that a *k*-*ε* model is unsuitable for situations involving inlets and compressors (Cable, 2009). According to developments to the standard model that have been made to increase efficiency, OpenFOAM now has multiple variants including the renormalization group model and the realizable model. In the present study, three different types of *k*-*ε* model have been investigated. The standard, renormalization group, and realizable models all contain transport equations for *k* and *ε*, and the turbulent velocity and length scales were independently solved using the two transport equations. The three models differ mostly in the following ways: the method of estimating the turbulent viscosity, destruction, and production terms in the equation for *ε* (Cable, 2009). These three turbulence models are widely utilized in a variety of applications (Salim et al., 2011), including pollutant transport (Xie et al., 2006) and wind loading (Huang et al., 2011).

3.2.4.3.1 *k*-*ε* (Standard)

The standard *k*-*ε* model is the most widely used RANS closure model. This model was developed for fully turbulent flows and is based on two basic assumptions: the fluid and its Reynold stresses are isotropic, and the turbulence is exclusively linked to local flow speed. Thus, the accuracy of the model is reduced as a result of these assumptions. For example, the isotropic supposition may be incorrect near the sidewalls of the flume, where the closeness of the sidewall alters the fluid characteristics in some cases. This also eliminates the possibility of adequately representing anisotropic non-Newtonian fluids. The second assumption restricts the model in the case of strongly mixing fluids, as substantial turbulence from nearby eddies will affect local turbulence in those situations (Ghodoosipour, 2021).

3.2.4.3.2 *k*-*ε* (RNG)

The Renormalization Group (RNG) approach was used to obtain a newer version of the *k*-*ε* model derived from instantaneous Navier-Stokes equations (Yakhot & Orszag, 1986). In terms of turbulent dissipation rate (*ε*), the RNG *k*-*ε* model differs from the standard *k*-*ε* model in a few parameters and constants. These modifications in the (*ε*) equation permit for an additional precise explanation of how the effective Reynolds number (or eddy scale) impacts the effective turbulent

transport. This improves the model's performance for low-Reynolds-number flows and near-wall flows. The swirling effect is included in the RNG *k*-model, utilizing a swirl alteration element in the eddy viscosity equation. The RNG *k*-*ε* model has a lower turbulence viscosity in rapidly strained flows than the standard *k*-*ε* model, making it more accurate for modeling streamline curvature and rapidly strained flows. In general, the RNG *k*-*ε* model outperforms the standard *k*-*ε* model in predicting fluid rotation, low Reynolds flows flow separation, near-wall flows, and boundary layers under significant adverse pressure gradients. Furthermore, developments in the (*ε*) equation result in reduced turbulence levels, allowing the model to more accurately anticipate complicated characteristics such as significant streamline curvature and vortices (Ghodoosipour, 2021).

3.2.4.3.3 *k*-*ε* (Realizable)

The standard *k*-*ε* model has been updated to produce the realizable *k*-*ε* model. The goal of the model is to enhance the standard *k*-*ε* model in predicting various cases such as the spreading rate of axisymmetric and planar jets. The (*ε*) equation was altered such that the normal stresses are always positive, making the equation "realizable" at all times (Ghodoosipour, 2021).

3.3 Solution Procedure

The Newtonian laws of viscosity control the fluids considered in recent research, and they are treated as fully incompressible. The pressure and velocity become inseparably associated as a result of the following simplification. At a given position in the system, a change to one variable will have an immediate influence on the other at a different position in the system, not influenced by the distance of segregation. The velocity and pressure cannot be detached and must be iteratively solved together through the whole system until the solution has converged. One numerical method by Issa (1986) is called the Pressure Implicit with Splitting of Operators (PISO) algorithm for transient (unsteady) flows to sustain coupling of velocity and pressure throughout the solution procedure. A summary of this approach is presented here.

3.3.1 The PISO Algorithm

The PISO algorithm applies the following three-step process:
(1) In the momentum predictor step, from the prior time step, the pressure field was borrowed and employed in the momentum equation to determine an approximation of the velocity field. At this point, the divergence-free condition required for mass conservation in an incompressible flow will not be satisfied by the velocity field.
(2) In the pressure solution step, to assemble the matrix for the pressure equation, the expected velocities are employed, which are then calculated to attain an approximate pressure field.
(3) The explicit velocity correction step, the new pressure field, is employed for calculating the new conservative flow, and the velocity field is adjusted to be consistent with the new pressures.

The correction to velocity should be composed of two parts: the collective influence of the corrections executed on its adjacent cells in addition to the correction owing to the alterations in pressure presented in step (2). As the explicit correction disregards the first part, steps (2) and (3)

must be iterated until a pre-defined tolerance is accomplished. The turbulent kinetic energy and its dissipation rate, as well as the transport equation for the phase fraction, only needs to be solved once at the end of the sequence.

3.3.2 Courant Number and Computational Time Step

The most significant and challenging feature of any computational simulation is the calculation of a suitable time step. However, the adaptive time step control feature was implemented by optimizing the use of available computer resources. Furthermore, the calculation of the time step is automated and dynamically regulated following each time step by explicitly governing the Courant number. A smaller time step achieves extra-precise outcomes, which increases the modeling period. However, implementing time-stepping is a skill that permits changing the time step as the evaluation progresses, instead of setting a specific magnitude for the step size for the entire simulation. The Finite Volume library of OpenFOAM does have this kind of technique, and it is implemented in several standard solvers, including InterFoam. It is established based on having a particular maximum Courant number described below (Berberović, 2010):

$$C_O = \frac{|U|}{d}\Delta t \qquad (3.19)$$

Where vector d is the distance between the two computational grid cell interfaces and Δt time step. The number of computational grid cells that an amount of fluid propagates through in a single time step is known as a physical interpretation of the dimensionless courant number. Often, the courant number is directly dominant in the stability of the solution. The following expression may be utilized for calculating the Courant number value (Co_0) to calculate the time step.

$$\Delta t = min\left\{min\left[min\left(\frac{Co_{max}}{Co_0}\,\Delta t_0, \left(1 + \lambda_1\,\frac{Co_{max}}{Co_0}\right)\Delta t_0\right), \lambda_2\,\Delta t_0\right], \Delta t_{max}\right\} \qquad (3.20)$$

Where the adaptive time step control aspect Δt accepts a maximum allowable Courant number $\mathrm{Co}_{\max}$ from the user. To stop modeling fluctuations through governing the rise in the time step, two variables λ_1 = 0.1 and λ_2 = 1.2, are used in the previous equation.

4 Article 1

Experimental investigations of hydraulic surges passing over a rectangular canal

Nuri Elsheikh, Amir H. Azimi, Ioan Nistor, and Abdolmajid Mohammadian

Abstract

The purpose of this experimental study was to investigate the effects of a rectangular canal on the hydrodynamics of turbulent surges before and after the canal by implementing a series of physical experiments. A dam-break wave model was used to simulate the tsunami-like turbulent waves passing over a smooth and horizontal surface, in presence and absence of a canal. Three canal depths of d = 0.05 m, 0.10 m, 0.15 m were used to model shallow, moderate, and deep conditions and three canal widths of w = 0.60 m, 1.60 m, 3.0 m were selected to model narrow to wide canals. The front velocity of the dam-break induced surges were controlled by rapidly releasing upstream impounded set volumes of water with depths of d_o = 0.20 m, 0.30 m, 0.40 m. The dam-break wave propagation over a horizontal, dry, and smooth bed revealed four regimes describing the variations of surge height with time. The arrival time to reach the maximum surge height and the quasi steady-state regime were correlated with each impoundment depth and an empirical formulation was proposed to estimate the onset of the quasi steady-state flow. The maximum surge heights measured before and after the mitigation canal location were compared with those recorded in the corresponding tests without the presence of the canal. It was found that the peak surge height upstream of the canal could increase up to 40% comparing to the test without the presence of the canal in relatively small impoundment depth and in presence of a narrow canal due to momentum dissipation. The wave height downstream of the canal increased between 10% and 50% of the wave height without the presence of the canal and the minimum change in the wave height occurred for the canal width to depth ratio of 20. The time-history of surge velocity after the mitigation canal indicated a significant decay of between 40% and 60% in the presence of a canal due to the bed friction changes and momentum dissipation.

Keywords: Hydraulics of surge; tsunami wave; dam-break wave; tsunami mitigation; wave hydrodynamics; surge height; wave celerity.

4.1 Introduction

Large tsunami waves are infrequent but, when occurring, they generate catastrophic consequences which can tremendously impact the communities and damage infrastructures in coastal regions around the world. Recent tsunami events such as 2004 Indian Ocean Tsunami, the 2011 Tohoku Tsunami, and 2018 Indonesia Tsunami have shown that effective prevention and mitigation

measures need to be taken to protect infrastructure and reduce reconstruction costs of communities in coastal areas (Nistor et al., 2005; Al-Faesly et al., 2012; Wüthrich et al., 2019). Recent tsunami design guidelines (FEMAP646, 2012; ASCE7-16 2017; Macabuag et al., 2018) have shown that the hydrodynamic forces occurring during tsunami inundation are significantly higher than the equivalent hydrostatic force and the ratio of hydrodynamic to hydrostatic forces depends on many field and geometric parameters. As a result, several physical model studies and numerical simulations have been performed to understand such complicated hydrodynamic phenomena (Nistor et al., 2009; Nistor and Palermo 2015; Sarjamee et al., 2017a; Wüthrich et al. 2018a, 2018b, 2018c; Asadollahi et al., 2019a, and 2019b).

In open ocean, tsunami waves exhibit extremely large wavelengths and relatively small amplitudes and they travel over thousands of kilometers at significant speed with minimal energy dissipation. As tsunami waves enter shallow waters in coastal areas, their wavelength decreases, their height increases while their period remains constant. This spatial transformation of the tsunami-waves is attributed to the seabed friction and its upslope orientation. Hence, tsunami waves often reach the shoreline within a wide range of inundation potential and energy levels (St-Germain et al., 2012).

Over the past decades, solitary-waves, vertically released volume-driven waves, as well as dam-break waves have been generated in laboratories to model tsunami waves in which they have shown similar hydrodynamic characteristics in the field (Arnason et al., 2009; Baldock et al., 2012; Wüthrich et al. 2018a; 2018b; von Häfen et al., 2019). Amongst all wave generation techniques, dam-break waves have shown better similarity to the characteristics of broken tsunami waves propagating inland. This similarity was confirmed by comparison of the visual images of tsunami-induced inundation which propagated over dry coastal areas during the 2004 Indian Ocean Tsunami (Chanson, 2006). Madsen, et al. (2008) also criticized the use of solitary waves due to their high energy dissipation rates in comparison with those of broken soliton waves.

The analytical solution of a dam-break problem was first introduced by Ritter (1892) for an inviscid fluid, a semi-finite reservoir, and a smooth horizontal bed. Ritter assumed a hydrostatic pressure distribution over the dam-break wave depth and neglected bed friction. Ritter's analytical solution is accurate for limited cases due to nonlinearity of the governing equations, bed roughness, flow viscosity, and the highly turbulent flow of the frontal head of the wave. Chanson (2005) considered a non-zero initial flow velocity behind the dam and developed a theoretical formulation to capture the instantaneous free surface profiles for both the wave tip and the ideal-fluid regions. Later on, he developed an analytical expression to consider flow resistance merely in the wave-tip region using Darcy-Weisbach friction factor, f, to accommodate surface roughness and employed a diffusive wave equation (Chanson, 2009). The analytical solution of a dam-break wave propagating over a horizontal surface was found to be suitable for the wave propagation simulation of a broken solitary wave as well (Baldock et al., 2012).

Several experimental studies have employed the dam-break wave generation mechanism by suddenly releasing an impounded volume of water behind a vertical gate to reproduce the inundation created by tsunami waves (Lauber and Hager, 1998; Nistor et al., 2009; Stolle et al., 2019; Sarjamee et al., 2017b; Asadollahi et al., 2019a, 2019b; Ghodoosipour et al., 2019a, 2019b). Dam-break waves can be generated by either a swing gate (Al-Faesly et al., 2012; Stolle et al.,

2019) or a vertically lifted gate (Crespo et al., 2008; Duarte et al. 2011; Oertel and Bung, 2012; Aureli et al., 2015). Wüthrich, et al. (2018a) showed that their suggested vertical release technique produced the dry bed surges within a good agreement with the analytical solution (Ritter, 1892).

The dissimilarities between the dam-break induced surges propagating on *dry bed* condition and hydraulic bores propagating over a layer of still water depth, known as *wet bed* condition, have been previously investigated using laboratory experiments and numerical simulations (Nistor et al., 2009; Nouri et al., 2010; Al-Faesly, 2016). It was reported that, for the same initial generated wave height, the bore height over a wet bed increased and its front became steeper in comparison to that of a surge propagating over a dry bed (Wüthrich et al., 2018a). It was also reported that the front bore velocity propagating over a wet bed depends on the initial still water depth. In addition, the hydraulic bores of similar impoundment depth experienced shorter arrival times for smaller still water depths (Ghodoosipour et al., 2019a).

The hydrodynamic of tsunami induced waves over many natural and man-made structures such as pine tree forests (Tanaka et al., 2009), coastal dunes (Fadly and Murakami, 2012), artificial and natural structures such as coastal headlands, buildings (St-Germain et al., 2014), rivers and canals (Dao et al., 2013), have been studied to investigate the effects of mitigation structures on reducing the energy of the incoming tsunami waves. Field observations have shown that the hydrodynamic characteristics of tsunami waves significantly changed during the surge propagation over natural streams. A hypothesis investigated in recent research studies indicated that the catastrophic energy of tsunami-induced waves can be dissipated once they passed over a mitigation canal (Watanabe et al., 2016). The impacts of canal geometry on the hydrodynamic parameters of hydraulic bores such as run-up height and velocity can provide a measure of energy dissipation before and after the passing over a canal and its correlation with canal geometry. A detailed and comprehensive research in this field should also provide design considerations for a proper design of an optimized mitigation canal.

Watanabe et al. (2016) performed laboratory experiments to study the damping effects of tsunami-induced waves that propagate over a rectangular canal installed perpendicular to the wave's direction. Experimental studies were performed to test the hydraulic surge propagation with three different impounded water depths of d_o = 0.55 m, 0.79 m, and 0.80 m on a dry bed condition. Only one canal was tested with a width of w = 0.30 m, and a depth of d = 0.05 m which gives a canal aspect ratio of w/d = 6. The mitigation canal was tested for dry canal (d = 0) and partially filled with different water levels of 0.02 m, and 0.04 m. The physical experiments demonstrated that the overflow wave velocity decreased by the presence of the canal and the wave height downstream of the canal increased.

Rahman et al. (2017) conducted a series of laboratory experiments to examine the performance of a rectangular canal, installed perpendicular to the surge wave flow direction, to reduce the impact of tsunami waves in coastal area. The experimental results indicated that the highest reduction of the wave velocity downstream of the canal occurred once the surge passed over the widest and deepest canal. Their experimental study was limited to a narrow range of canal aspect ratios which ranged from w/d = 4 to 10. The large reflected wave heights were generated by two of the canal dimensions investigated and which had the higher canal widths amongst other canals that were

tested in their study. The experiments displayed analogous tsunami-reduction effects when the canals had different depths but the same width. However, a delay in the tsunami arrival was observed and velocity mitigation occurred for all canal configurations. It was observed that the tsunami wave energy can be partially absorbed by the reflected wave generated by the canal.

In this study, a series of physical experiments were performed to investigate the influences of canal geometry on the hydrodynamics of turbulent surges before and after a rectangular mitigation canal. Recent experimental studies focused on a narrow range of canal aspect ratios and relatively shallow impoundment depths (i.e., $d_o \leq 0.25$ m). The proposed comprehensive experimental study aimed at testing a wide range of canal aspect ratios (i.e., $4 \leq w/d \leq 60$) to investigate further the effects of the canal geometry on the hydrodynamic characteristics of the turbulent surge after the canal. The variations of the surge heights and velocities before and after the mitigation canal are extremely important for evaluation of the canal performance and for the optimization of the canal aspect ratio. Most of coastal infrastructures are constructed within a very short distance from natural streams and the immediate response of hydraulic surges propagating over such streams and manmade canals can assist coastal engineers for a proper design and positioning of nearshore structures.

To the authors' knowledge, either no data were recorded downstream of the canal (Dao et al., 2013; Watanabe et al., 2016) or velocity measurements were collected far away, downstream from the canal. For instance, in the study of Rahman et al. (2017) the downstream wave velocity was collected at a distance between five and ten times the canal width. Therefore, their available data may not clearly reflect the impact of mitigation canal on surge hydrodynamics. The present study aims to investigate the effects of mitigation canal on the turbulent surge propagation by collecting wave heights and velocities *in the vicinity* of the canal. Both depth and velocity data were recorded upstream and downstream of the canal at distance between 1/15 and 1/3 of the canal width to study the immediate impacts of the canal on both the upstream reflection wave and on the dissipated wave in downstream direction.

4.2 Experimental Setup

Laboratory experiments were carried out in a 15.56 m long, 0.38 m wide, and 0.60 m deep glass-walled tilting flume in the Water Resources Engineering Laboratory at the University of Ottawa, Canada (Figure 4.1).

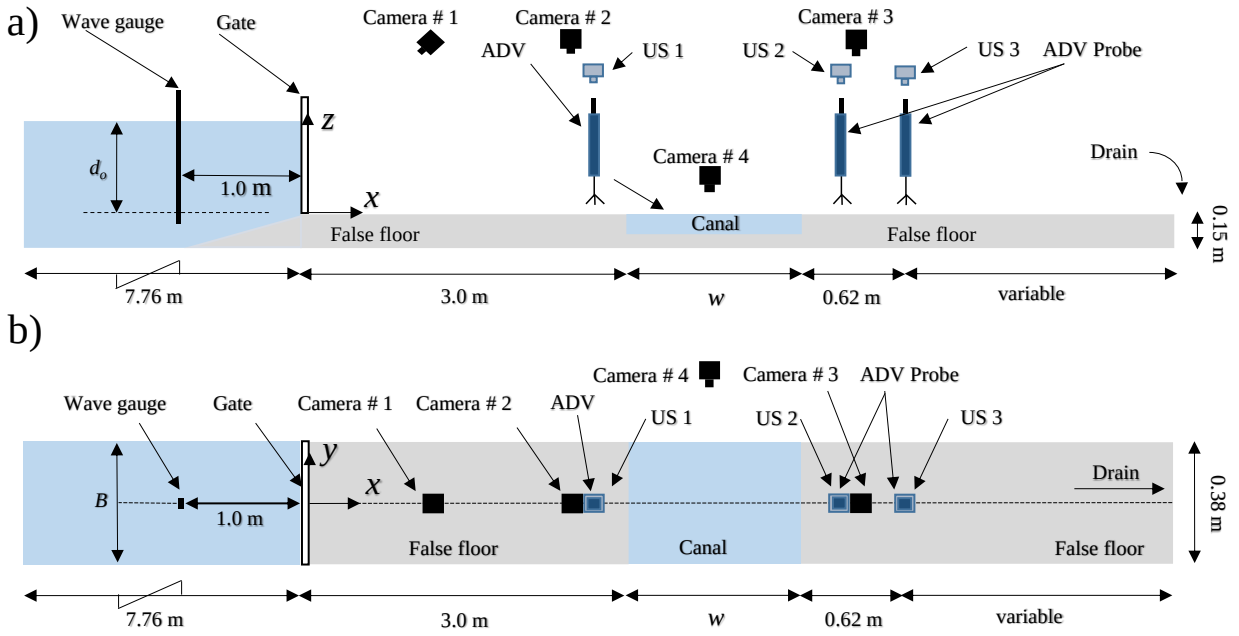

Figure 4.1. Schematic of experimental setup and coordinate system: a) side view; b) top view.

The impounded volume of water upstream of the gate consisted of three impoundment depths of d_o = 0.2 m, 0.3 m, and 0.4 m. The stored water volume was suddenly released by a rapidly opening lift gate installed upstream of the false bed to form turbulent hydraulic surges. The generated turbulent surges propagated over a smooth horizontal bed and interacted with a rectangular, so-called *mitigation* canal. The transformed turbulent surge then continued to propagate through the rest of the flume until it dropped through a vertical drain located at the end of the flume. A temporary PVC false floor was installed downstream of the vertical lift gate to accommodate for installing a mitigation canal with different canal widths, w, and depths, d. The false floor was fabricated in the form of several parallelepipeds with various lengths and heights which were glued to the flume bed to form various configurations discussed herein. Three canal widths of w = 0.60 m, 1.60 m and 3.0 m and three different canal depths of d = 0.05 m, 0.10 m, and 0.15 m were tested. The aspect ratios w/d of all nine mitigation canals were between 4 and 60 (see Table 4.1).

Table 4.1. Experimental parameters of the performed tests.

Test No.	Test name	Upstream water depth d_o (m)	Canal width w (m)	Canal depth d (m)	Canal aspect ratio w/d (-)	Surge front velocity u (m)	Maximum surge height h_{max} (m)	Froude number F_r (-)
1	C-0.4-12	0.40	0.60	0.05	12	2.604	0.199	1.9
2	C-0.4-6	0.40	0.60	0.10	6	2.479	0.204	1.8
3	C-0.4-4	0.40	0.60	0.15	4	2.332	0.205	1.6
4	C-0.4-32	0.40	1.60	0.05	32	2.607	0.202	1.9
5	C-0.4-16	0.40	1.60	0.10	16	2.524	0.290	1.5
6	C-0.4-32/3	0.40	1.60	0.15	32/3	2.466	0.345	1.3
7	C-0.4-60	0.40	3.00	0.05	60	3.060	0.200	2.2
8	C-0.4-30	0.40	3.00	0.10	30	2.515	0.240	1.6
9	C-0.4-20	0.40	3.00	0.15	20	2.459	0.250	1.6
10	F-0.4	0.40	0	0	0	2.851	0.207	2.0
11	C-0.3-12	0.30	0.60	0.05	12	2.289	0.162	1.8
12	C-0.3-6	0.30	0.60	0.10	6	2.260	0.185	1.7
13	C-0.3-4	0.30	0.60	0.15	4	1.964	0.192	1.4
14	C-0.3-32	0.30	1.60	0.05	32	2.463	0.170	1.9
15	C-0.3-16	0.30	1.60	0.10	16	2.386	0.230	1.6
16	C-0.3-32/3	0.30	1.60	0.15	32/3	2.322	0.267	1.4
17	C-0.3-60	0.30	3.00	0.05	60	2.193	0.158	1.8
18	C-0.3-30	0.30	3.00	0.10	30	2.152	0.182	1.6
19	C-0.3-20	0.30	3.00	0.15	20	2.116	0.205	1.5
20	F-0.3	0.30	0	0	0	2.483	0.160	2.0
21	C-0.2-12	0.20	0.60	0.05	12	1.89	0.135	1.6
22	C-0.2-6	0.20	0.60	0.10	6	1.844	0.166	1.4
23	C-0.2-4	0.20	0.60	0.15	4	1.603	0.175	1.2
24	C-0.2-32	0.20	1.60	0.05	32	1.880	0.135	1.6
25	C-0.2-16	0.20	1.60	0.10	16	1.835	0.163	1.5
26	C-0.2-32/3	0.20	1.60	0.15	32/3	1.739	0.176	1.3
27	C-0.2-60	0.20	3.00	0.05	60	1.780	0.129	1.6
28	C-0.2-30	0.20	3.00	0.10	30	1.758	0.139	1.5
29	C-0.2-20	0.20	3.00	0.15	20	1.670	0.144	1.4
30	F-0.2	0.20	0	0	0	1.98	0.113	1.9

Overall, 30 experiments were conducted covering the three (3) impoundment depths, nine (9) canal configurations; three (3) additional tests (i.e., Tests No. 10, 20, and 30) were performed to record the propagation of turbulent hydraulic surges without the presence of a canal to be used as benchmark tests.

Procedurally, the upstream reservoir was filled up with water and the inflow was constantly monitored to achieve the desired impoundment water depth. The impounded volumes of water for d_o = 0.2 m, 0.3 m, and 0.4 m were 0.81 m³, 1.21 m³, and 1.62 m³, respectively. The equivalent aspect ratio of the reservoir L/d_o were 53.21, 35.47, and 26.61. These were much larger than the minimum recommended reservoir aspect ratio of L/d_o = 11.05, as suggested by Lauber and Hager (1998). A steel frame was installed on the top of the flume to conveniently position four wireless video cameras (GoPro, Hero5, SanMateo, California, USA) used to record the surge front motion and the time history of the surge wave height over the canal. Three cameras were located horizontally at different positions between the gate and the upstream end of the canal to record the surge front motion. The fourth camera was located on the flume side and near the center of the canal (outside of the flume) to visualize the surge front and to capture surge wave profiles.

A lifting gate, manufactured from Plexiglas, was installed 7.76 m from the upstream end of the flume to impound water and great care was paid to minimizing water leakage around the gate. Figure 4.1 shows the experimental setup, the location of experimental instrumentation, and the adopted coordinate system in both side- and top-view. The opening time of a vertical lift gate is a key factor to generate a fully developed dam-break wave. According to Lauber and Hager (1998), a dam-break wave is fully developed if the non-dimensional gate opening time $T_o = t_o(g/d_o)^{1/2}$ becomes smaller than $2^{1/2}$ where t_o is the gate opening time and d_o is the impoundment depth. The required gate opening time is the time needed for the top water particles to fall downward and start to form a dynamic wave followed by its a horizontal translational motion. The horizontal motion due to static pressure is not delayed for $T_o < 2^{1/2}$. For this study, the actual gate opening time was recorded with a high-speed camera and the calculated non-dimensional gate opening times varied between $0.70 < T_o < 0.825$.

The gate used to release the impounded water was held at the bottom by the upstream end of the false floor. The gate was strengthened by Plexiglas square plates which were glued on the sidewalls of the flume in the vicinity of the top of the gate. Also, Plexiglas support plates were glued onto the sidewalls at the top of the gate to make sure that the gate moved in the vertical direction. A bubble level was used to ensure that the Plexiglas support plates were positioned vertically. A rectangular Plexiglas plate with a height of about 0.14 m was inserted in the bottom of the gate between the ramp and the upstream end of the false floor in order to facilitate and control the gate opening. The gate was manually opened by using a handle on the top of the gate. The gate was firstly situated in the locked position at the upstream end of the artificial bed, and the impoundment upstream of the gate was filled with water. Rubber strips were glued onto the lower and side edges of the gate in order to control and minimize water leakage when the gate was closed. The flume was positioned horizontally by using a bubble level.

The origin of the coordinates system was chosen in mid-channel width and at the gate position. The *x*-axis is along the direction of the surge propagation, *y*-axis is in the transverse direction, towards the flume wall, while *z*-axis is positive in vertical direction from the false bed. A 1V:6H ramp was installed at the upstream end of the false floor to form a transient depth reduction and thus avoid flow separation and local energy losses in the beginning of the false floor. The rectangular canal started at 3.0 m downstream of the gate (Figure 4.1) to ensure that the turbulent

hydraulic surge was fully developed prior to reaching the canal. A vertical drain was located at the downstream end of the flume to direct the wave into a large reservoir underneath of the flume.

Two different wave sensor types were used to measure the time-history of the water levels 1 m upstream of the gate and at three locations downstream of the gate. A capacitance-type wave gage (model WG-50, manufactured by RBR Ottawa, Canada) with a sampling frequency of 1200 Hz was used to measure the time history of the water level 1 m upstream of the gate; this gage was labeled as WG1. Three non-intrusive ultrasonic wave sensors (MASSA, M-5000/220, Massachusetts, USA) with the same sampling frequency of 1200 Hz were deployed downstream of the gate at various locations throughout the flume to measure the time-history of water surface level. An Acoustic Doppler Velocimeter probe (ADV) was used to measure instantaneous time-series flow velocity data (Nortek-AS, Vangkroken, Norway). The ADV probe measured the instantaneous flow velocity data at 0.01 m above the channel bed with a sampling frequency of 200 Hz. Both the water depth and velocity were measured at the flume centerline and 0.2 m upstream (US1), 0.2 m downstream, and 0.58 m downstream of the mitigation canal. All experimental runs were repeated three times to ensure the repeatability of the generated surges and to obtain averaged time-series data from sensors. Figure 4.2 shows the positioning of the water level sensors located in the flume.

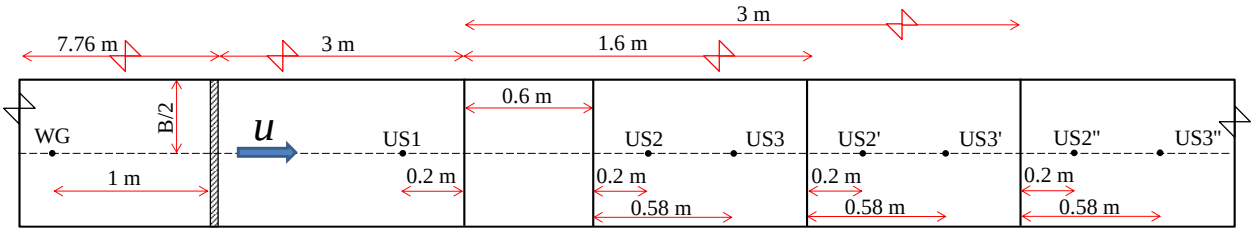

Figure 4.2. Positioning of a capacitance-type wave gauge and water level ultrasonic sensors upstream and downstream of canals with different widths.

The ultrasonic wave sensors located downstream of a 0.6 m wide canal were labeled as US2 and US3. For the 1.6 m and 3 m wide canals, the corresponding sensors located 0.2 m downstream of the canals were labelled as US2' and US2". Similarly, the sensors located at 0.58 m downstream of the 1.6 m and 3 m wide canals were labelled as US3' and US3", respectively. Similar labeling was used for the positioning of the ADV probe.

Good agreement was obtained between the time-series of surge heights measured by US1 (0.2 m upstream of the canal), US2 (0.2 m downstream of the canal), and US3 (0.58 m downstream of the canal) for the three repetitions of the benchmark tests (a flume without a canal, Tests No. 10, 20, and 30) and an average standard deviation, σ, of approximately 4.5% was achieved. Similar repeatability ranges were also reported in the recent studies dealing with dam-break waves generation with a rapidly opening gate (Ghodoosipour et al., 2019a), with a standard deviation of approximately 4% and 5% for dry and wet bed conditions, respectively.

The surge front velocity was measured using both visualization techniques (see Figure 4.3) and velocity measurements by the ADV probe.

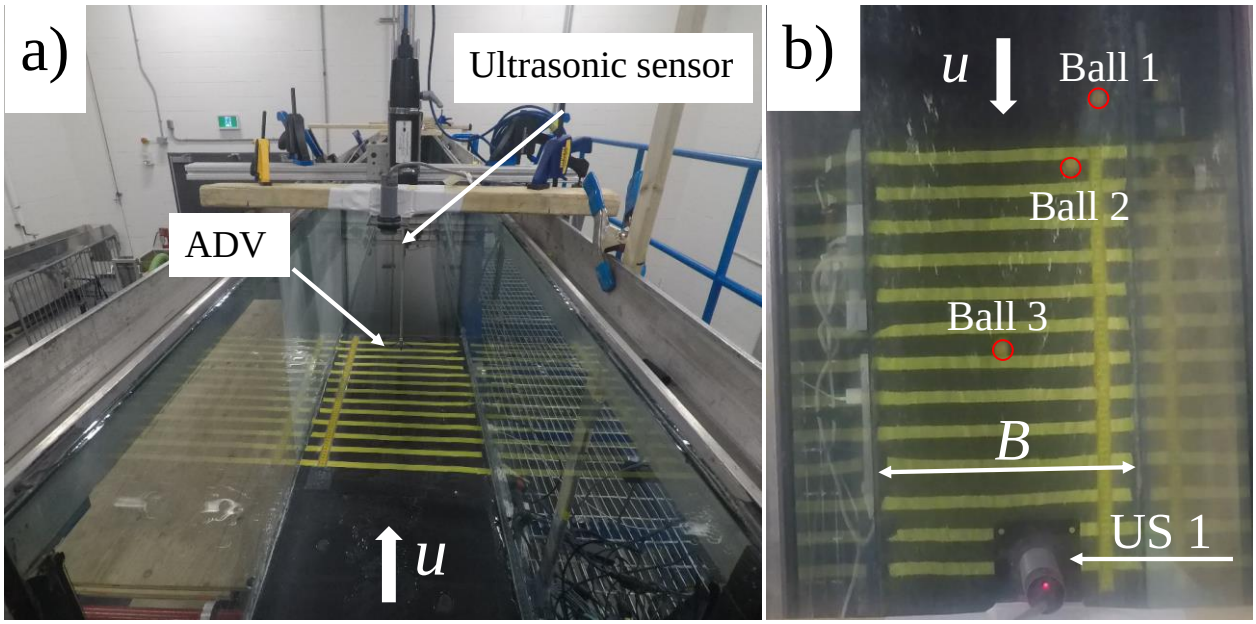

Figure 4.3. Images of experimental flume and probes: a) positioning ultrasonic sensor and ADV probe; b) top view recording of plastic balls for measuring surge front velocity.

As shown in Figure 4.3a, the false bed was painted with parallel lines drawn on the bed floor at 50 mm apart from the upstream edge of the canal and which extended by 0.6 m beyond the edge. This floor section was used to monitor the propagation of hydraulic surges (see Figure 4.3a). Plastic beads with a diameter of 15 mm were placed upstream of the gate and they were carried by water once the lift gate was opened. A GoPro camera was mounted above the flume to capture series of photographs with a shutter speed of 60 frames per second (see Figure 4.3b). The frontal velocity of the surge front along the flume was calculated by using the top view videos of the plastic beads moving over a 0.60 m long marked area. The surge frontal velocity was calculated by measuring the travel distance of the balls between two adjacent parallel lines in two consecutive images.

The time-series of water depths in tests with relatively small impoundment depths (d_o = 0.2 m) showed that the water depth became smaller than 0.07 m after 15 seconds in these tests. Knowing that the ADV probe measures water velocity 0.05 m below the probe tip, it was necessary to minimize the gap between the ADV probe head and the flume bed to avoid any wake effect and air bubble entrainment in the vicinity of the probe. To determine the minimum depth to properly measure the surge average velocity, the ADV probe was installed at several vertical distances from the bed. Figure 4.4 shows the time series of surge velocity at 2.8 m downstream of the gate and for different vertical distances from the bed of z = 0.005 m, 0.01 m, 0.015 m, 0.02 m.

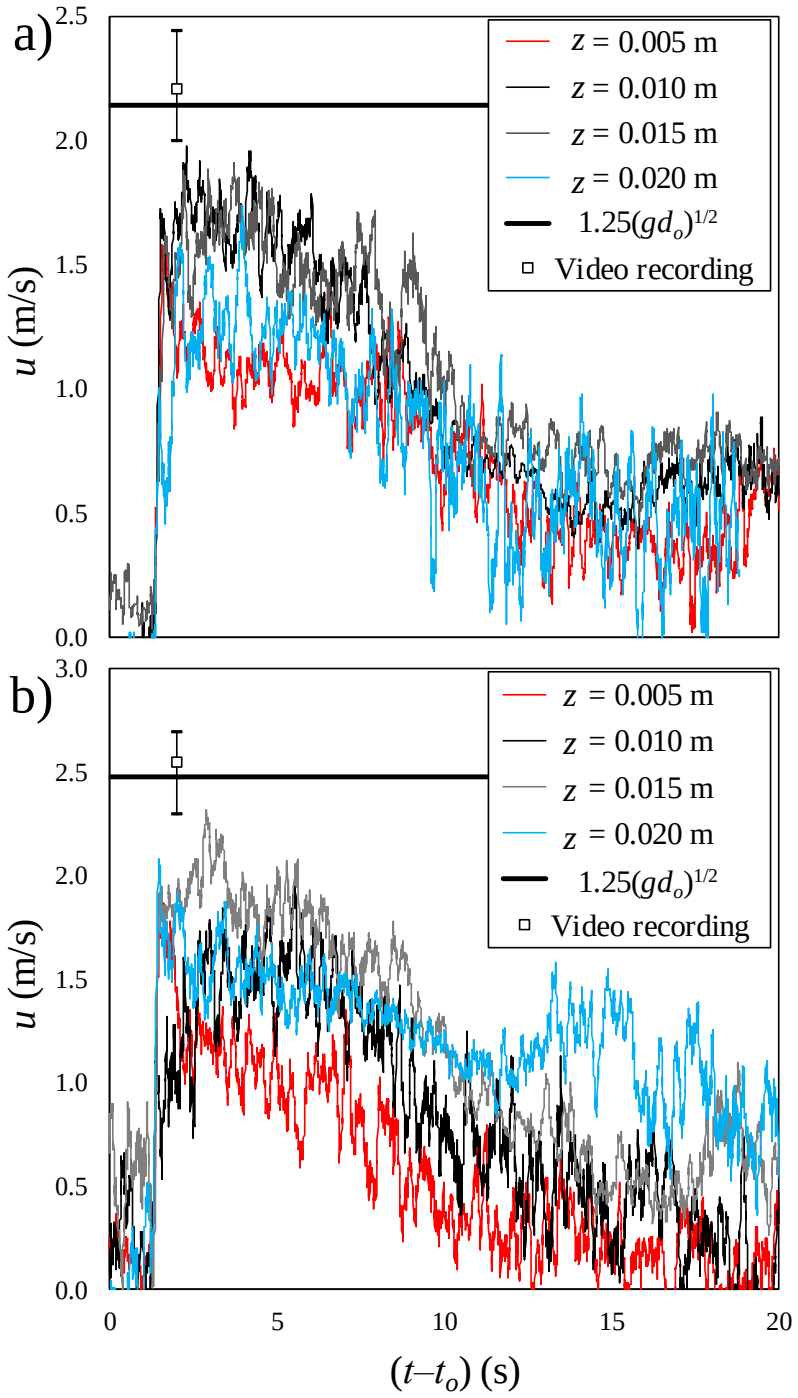

Figure 4.4. Effect of ADV measuring depth (z) on the instantaneous velocity of turbulent surge in a smooth and horizontal channel. Data were measured 2.8 m downstream of the gate (0.2 m upstream of the canal); a) d_o=0.3 m; b) d_o=0.4 m.

As shown in Figure 4.4, velocity data were slightly variant for 0.01 m ≤ z ≤ 0.02 m and they noticeably decreased for z = 0.005 m. A vertical distance of z = 0.01 m was then selected for the ADV velocity measurements which provided 0.06 m distance from the ADV probe tip and the channel bottom. The surge front velocity was obtained from the video analysis of the plastic balls

motion recordings and the results were compared with those from the ADV velocity measurements and with the wave celerity equation $u = \boldsymbol{\alpha}(gd_o)^{1/2}$ with the approximate value of $\boldsymbol{\alpha} = 1.25$ as recommended by (Wüthrich et al., 2018a). Recently, Ghodoosipour et al. (2019a) showed that $\boldsymbol{\alpha}$ depends on the bed roughness and the hydraulic radius of the flume, and proposed $\boldsymbol{\alpha} = 1.2$ for dry bed surge.

The Froude numbers in Table 4.1. were calculated using $F_r = u/(hg)^{1/2}$ (where u is the surge front velocity, h is the maximum surge height upstream of the canal, and g is the gravitational acceleration). The flow conditions were supercritical ($1.2 \leq F_r \leq 2.2$) upstream of the canal in this research. The model measurements were converted to prototype quantities using Froude-scale modeling. The geometrical similarity was assessed on the assumption that the highest surge height would correspond to the flow depth during a real tsunami. This assumption was dependent on field measurements of the inundation depth of previous tsunamis. Thus, a geometrical similarity scale of 1:25 was used in this research as a result of this assumption.

Fritz et al. (2012) estimated flow velocities of up to 11 m/s and inundation depths of up to 9 m using video processing of images filmed during the 2011 Tohoku Tsunami. Previous field and numerical modeling results from the 1993 Hokkaido-Nansei-Oki Tsunami indicated flow velocities of 3-15 m/s and water depths of 5-15 m. The surge front velocity and maximum surge height measured in this research, as shown in Table 4.1, are within the range of the above-mentioned results. Bricker et al. (2015) and Ghodoosipour (2021) indicated that once employing Froude scaling for tsunami modeling, the viscosity effects and surface tension must be considered. The Weber and Reynolds numbers are shown in Table 4.2. The Weber numbers were calculated using $We = \rho hu^2/\sigma$, where ρ is the water density (kg/m^3), h is the water depth (m), u is the flow velocity (m/s), and σ is the surface tension (N/m). All of the tested cases had a We that was greater than the critical We ($We_{crit} \leq 120$) (Peakall & Warburton, 1998; Ghodoosipour, 2021), and as a result, the influence of changing surface tension as it relates to the real-world scale could be overlooked in this research. The flow was considered to be fully turbulent ($2.23 \times 10^5 \leq Re \leq 8.49 \times 10^5$) in this research (Chow, 1959; Ghodoosipour, 2021). A tsunami flow, however, is commonly related with Reynolds numbers greater than 10^6, and thus the bottom boundary layer in the performed experiments may not have been adequately represented (Sumer & Fredsøe, 2006). The flow Reynolds numbers in the experiments were calculated using $Re = \rho hu/\mu = hu/\nu$, where ν is the kinematic viscosity (m^2/s) and μ is the dynamic viscosity kg/(m.s). The normalized maximum surge heights h_{max}/h_o for different distances from the canal are shown in Table 4.3.

Table 4.2. Maximum surge height passing over a rectangular canal h_{max} and horizontal surface h_o at different distances from the canal

Test No.	Test name	Upstream depth d_o (m)	Canal width w (m)	Canal depth d (m)	Reynold number R_e (-)	Weber number W_e (-)	Maximum surge height h_{max}		
							US1[1] (m)	US2 [2] (m)	US3[3] (m)
1	C-0.4-12	0.40	0.60	0.05	5.17×10^5	18545	0.199	0.293	0.220
2	C-0.4-6	0.40	0.60	0.10	5.05×10^5	17255	0.204	0.211	0.217
3	C-0.4-4	0.40	0.60	0.15	4.77×10^5	15336	0.205	0.226	0.201
4	C-0.4-32	0.40	1.60	0.05	5.25×10^5	18840	0.202	0.257	0.211
5	C-0.4-16	0.40	1.60	0.10	7.30×10^5	25369	0.290	0.259	0.199
6	C-0.4-32/3	0.40	1.60	0.15	8.49×10^5	28852	0.345	0.271	0.198
7	C-0.4-60	0.40	3.00	0.05	6.10×10^5	25698	0.200	0.251	0.206
8	C-0.4-30	0.40	3.00	0.10	6.02×10^5	20870	0.240	0.238	0.180
9	C-0.4-20	0.40	3.00	0.15	6.12×10^5	20731	0.250	0.248	0.176
10	F-0.4	0.40	0	0	5.88×10^5	23112	0.207	0.180	0.176
11	C-0.3-12	0.30	0.60	0.05	3.69×10^5	11652	0.162	0.187	0.157
12	C-0.3-6	0.30	0.60	0.10	4.16×10^5	12965	0.185	0.206	0.161
13	C-0.3-4	0.30	0.60	0.15	3.75×10^5	10152	0.192	0.215	0.159
14	C-0.3-32	0.30	1.60	0.05	4.18×10^5	14183	0.170	0.187	0.153
15	C-0.3-16	0.30	1.60	0.10	5.47×10^5	17994	0.230	0.187	0.151
16	C-0.3-32/3	0.30	1.60	0.15	6.19×10^5	19797	0.267	0.191	0.155
17	C-0.3-60	0.30	3.00	0.05	3.45×10^5	10438	0.158	0.187	0.147
18	C-0.3-30	0.30	3.00	0.10	3.91×10^5	11590	0.182	0.170	0.132
19	C-0.3-20	0.30	3.00	0.15	4.32×10^5	12608	0.205	0.177	0.128
20	F-0.3	0.30	0	0	3.96×10^5	13550	0.16	0.140	0.134
21	C-0.2-12	0.20	0.60	0.05	2.55×10^5	6644	0.135	0.113	0.102
22	C-0.2-6	0.20	0.60	0.10	3.06×10^5	7763	0.166	0.138	0.104
23	C-0.2-4	0.20	0.60	0.15	2.79×10^5	6159	0.175	0.146	0.113
24	C-0.2-32	0.20	1.60	0.05	2.54×10^5	6569	0.135	0.117	0.104
25	C-0.2-16	0.20	1.60	0.10	2.98×10^5	7530	0.163	0.117	0.103
26	C-0.2-32/3	0.20	1.60	0.15	3.05×10^5	7303	0.176	0.113	0.105
27	C-0.2-60	0.20	3.00	0.05	2.28×10^5	5593	0.129	0.111	0.100
28	C-0.2-30	0.20	3.00	0.10	2.43×10^5	5897	0.139	0.106	0.092
29	C-0.2-20	0.20	3.00	0.15	2.39×10^5	5505	0.144	0.100	0.085
30	F-0.2	0.20	0	0	2.23×10^5	6085	0.113	0.097	0.094

[1] 0.20 m upstream of the canal

[2] 0.20 m downstream of the canal

[3] 0.58 m downstream of the canal

Table 4.3. Normalized maximum surge height h_{max}/h_o at different distances from the canal.

Test No.	Test name	Upstream water depth d_o (m)	Canal width w (m)	Canal Depth d (m)	Canal aspect ratio w/d (-)	Normalized maximum surge height (h_{max} / h_o)		
						US1[1] (-)	US2[2] (-)	US3[3] (-)
1	C-0.4-12	0.40	0.60	0.05	12	0.962	1.550	1.170
2	C-0.4-6	0.40	0.60	0.10	6	0.987	1.115	1.154
3	C-0.4-4	0.40	0.60	0.15	4	0.992	1.193	1.069
4	C-0.4-32	0.40	1.60	0.05	32	0.975	1.404	1.214
5	C-0.4-16	0.40	1.60	0.10	16	1.401	1.414	1.147
6	C-0.4-32/3	0.40	1.60	0.15	32/3	1.669	1.481	1.141
7	C-0.4-60	0.40	3.00	0.05	60	0.965	1.486	1.239
8	C-0.4-30	0.40	3.00	0.10	30	1.160	1.412	1.086
9	C-0.4-20	0.40	3.00	0.15	20	1.206	1.467	1.060
10	F-0.4	0.40	0	0	0	-	-	-
11	C-0.3-12	0.30	0.60	0.05	12	1.012	1.291	1.086
12	C-0.3-6	0.30	0.60	0.10	6	1.155	1.421	1.114
13	C-0.3-4	0.30	0.60	0.15	4	1.198	1.482	1.101
14	C-0.3-32	0.30	1.60	0.05	32	1.064	1.328	1.146
15	C-0.3-16	0.30	1.60	0.10	16	1.438	1.328	1.128
16	C-0.3-32/3	0.30	1.60	0.15	32/3	1.671	1.358	1.159
17	C-0.3-60	0.30	3.00	0.05	60	0.988	1.389	1.183
18	C-0.3-30	0.30	3.00	0.10	30	1.139	1.250	1.060
19	C-0.3-20	0.30	3.00	0.15	20	1.281	1.317	1.031
20	F-0.3	0.30	0	0	0	-	-	-
21	C-0.2-12	0.20	0.60	0.05	12	1.198	1.097	1.048
22	C-0.2-6	0.20	0.60	0.10	6	1.471	1.343	1.064
23	C-0.2-4	0.20	0.60	0.15	4	1.544	1.418	1.162
24	C-0.2-32	0.20	1.60	0.05	32	1.197	1.226	1.079
25	C-0.2-16	0.20	1.60	0.10	16	1.441	1.221	1.063
26	C-0.2-32/3	0.20	1.60	0.15	32/3	1.556	1.179	1.085
27	C-0.2-60	0.20	3.00	0.05	60	1.137	1.205	1.147
28	C-0.2-30	0.20	3.00	0.10	30	1.229	1.143	1.059
29	C-0.2-20	0.20	3.00	0.15	20	1.272	1.078	0.980
30	F-0.2	0.20	0	0	0	-	-	-

[1] 0.20 m upstream of the canal

[2] 0.20 m downstream of the canal

[3] 0.58 m downstream of the canal

4.3 Results

4.3.1 Turbulent Surge Propagation over the Horizontal Bed

Figure 4.5 shows the time-history of the water lever for the turbulent surge propagation over a smooth bed surface for three different impoundment depths of d_o = 0.20 m, 0.30 m, and 0.40 m and at seven different locations along the flume.

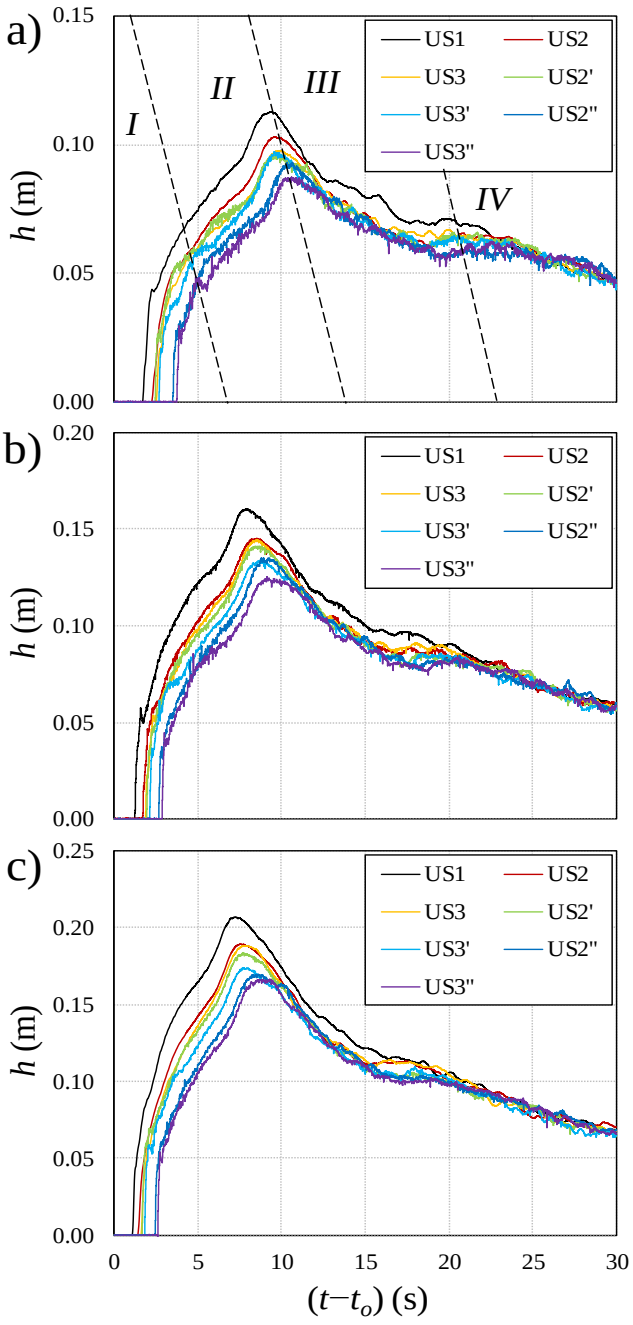

Figure 4.5. Time-history of turbulent surge propagation over a smooth and horizontal bed surface for different impoundment depths: a) d_o = 0.2 m, b) d_o = 0.3 m, c) d_o = 0.4 m.

The turbulent surge height gradually increased from zero, reached a peak, and then decreased with time. Eventually, at $t–t_o \approx 20$ s the surge flow became similar to a quasi steady-state and the surge height further linearly decreased with time. The maximum surge heights at 0.2 m upstream of the canal (US1) and for impoundment water depths of d_o = 0.2 m, 0.3 m, and 0.4 m were 0.113 m, 0.160 m, and 0.207 m, respectively. One can notice that the peak of the surge height is correlated with the depth of the impounded water. The time-history of the water level for the turbulent surge propagation was divided into four regimes (see Figure 4.5a). Regime I is characterized by a sudden increase in the surge height - the water level rose from zero to approximately 50% of the peak wave height. Regime II in the time-series was characterized by a relatively steep surge height until it reaches its maximum value. Then, the surge height decreased in Regime III and reached approximately 50% of its maximum height, h_{max}. The quasi steady-state condition (Regime IV) occurred when the surge height became independent of the sensor location and then linearly decreased with time. As shown in Figure 4.5, the quasi steady-state time to peak, t_q, decreased with an increase in the impoundment depth, d_o.

The variation of the maximum surge height, h_{max}, (Tests No. 10, 20, and 30) with the distance from the gate, x, for turbulent surges generated by different impoundment depths are shown in Figure 4.6.

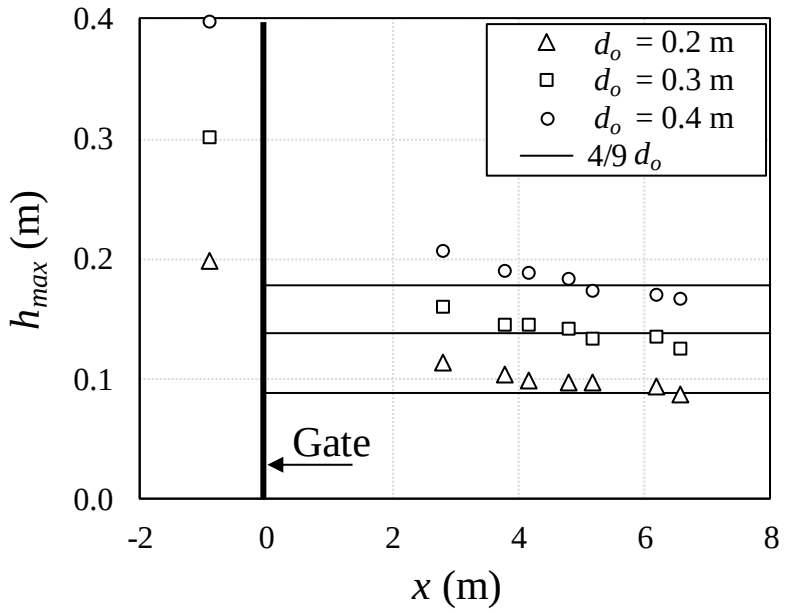

Figure 4.6. Variations of the maximum surge height (h_{max}) over a smooth and horizontal surface (Tests No. 10, 20, and 30) with downstream distance from the gate x.

The theoretical constant flow depth of $4/9d_o$ that occurs in the quasi steady-state flow condition were also included in Figure 4.6. A comparison of the measured peak surge height with the distance from the gate indicated that the peak surge heights decreased with the distance from the gate and reached to the theoretical constant flow depth with a value of $4/9d_o$.

Figure 4.7 shows the variations of the normalized maximum surge velocity with the canal aspect ratio for three different impoundment depths.

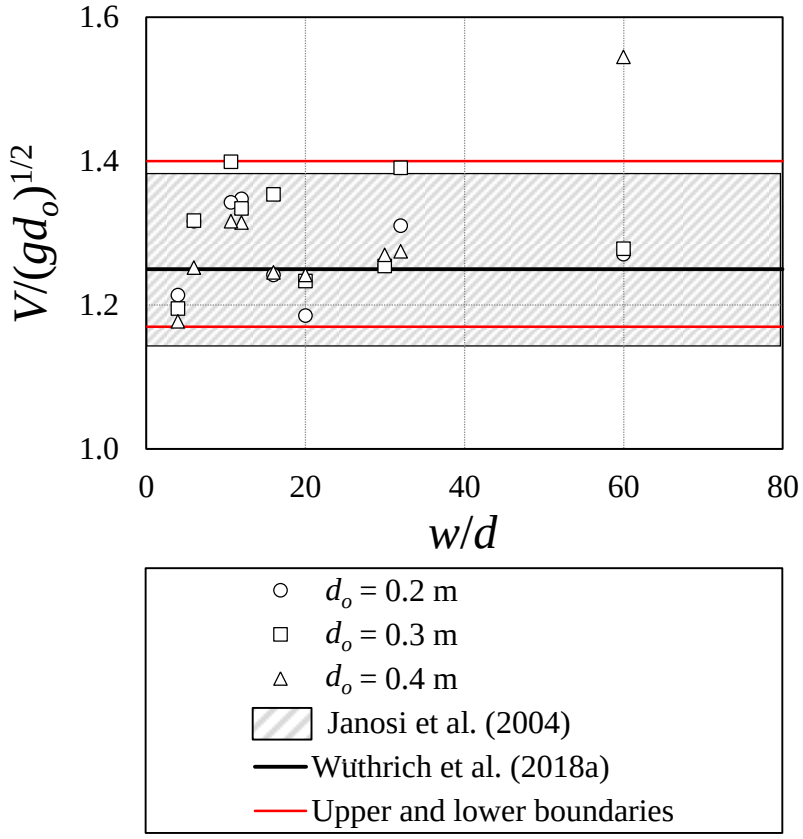

Figure 4.7. The normalized surge front velocity $V/(gd_o)^{1/2}$ of experiments with canals obtained by video recording at the downstream of the gate.

As shown in Figure 4.7, the surge front velocity fluctuated between 1.17 $(gd_o)^{1/2}$ and 1.4 $(gd_o)^{1/2}$ for the entire range of canal aspect ratios being tested in this study. This is consistent with results reported by Janosi et al. (2004) and Wüthrich et al. (2018a).

Figure 4.8 shows the time-history of the surge velocity over a horizontal surface for an impoundment depth of d_o = 0.40 m and at seven different locations along the flume.

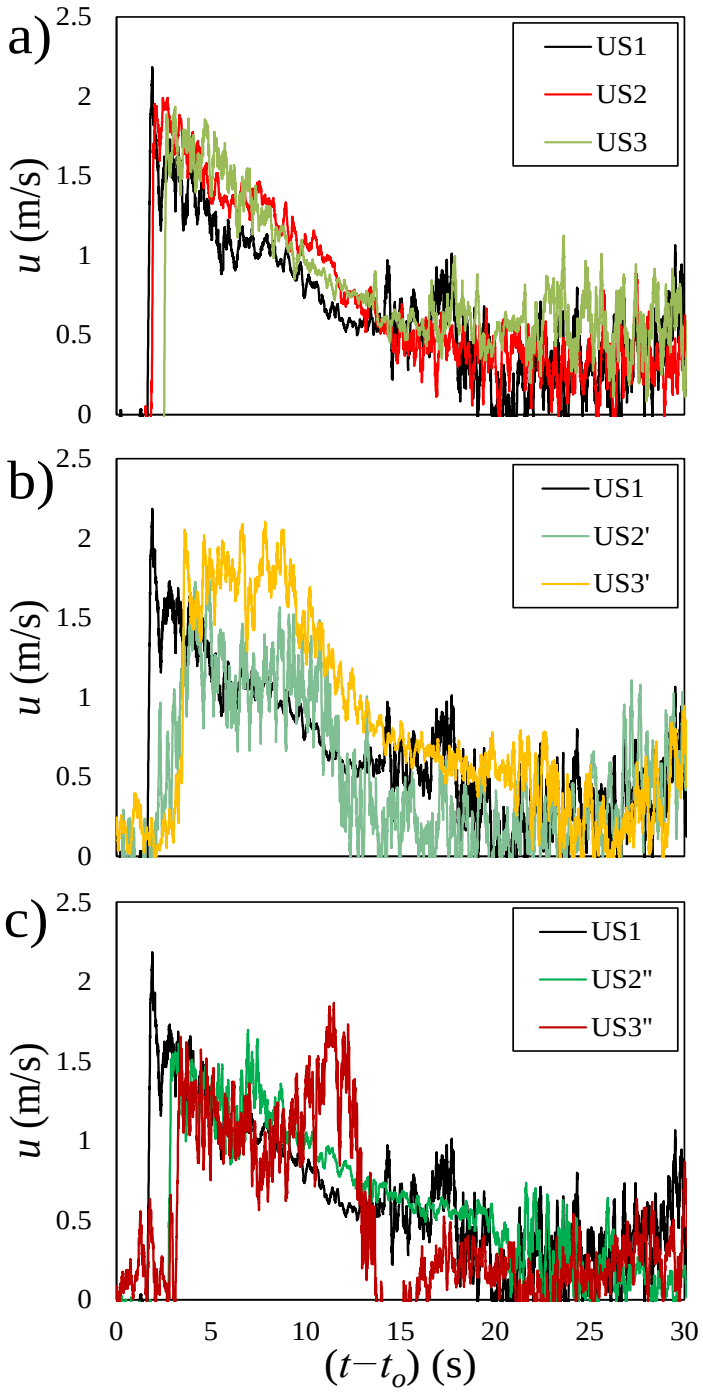

Figure 4.8. Variations of turbulent surge velocity over a smooth and horizontal surface with time for an impoundment depth of d_o = 0.4 m: a) x = 2.8 m, 3.8 m, 4.18 m; b) x = 2.8 m, 4.8 m, 5.18 m; c) x = 2.8 m, 6.2 m, 6.58 m. t is the recording time and t_o is the time when the gate is opened. The turbulent surge velocities were obtained in the absence of a canal at the same locations as in the cases with the presence of a canal. The data were collected through different experimental tests. Imagine there are three different canal widths, of 0.60 m, 1.6 m, and 3.0 m. US1 was located 0.20 m upstream of the three different-width canals, and US2 and US3 were located at 0.20 m and 0.58 m respectively downstream of 0.60 m-wide canal. Similarly, US2′ and US3′ were located at 0.20 m and 0.58 m, respectively downstream of 1.60 m-wide canal. Thus, US2″ and US3″ were located at 0.20 m and 0.58 m, respectively downstream of 3.0 m-wide canal.

The time-histories of the surge velocity over horizontal surface are used as a benchmark (i.e., Tests No. 10, 20, and 30) to study the effect of canal and canal aspect ratio on variations of surge velocity. Ultrasonic sensors US2 and US3 in Figure 4.8a show their positions downstream of the canal with a canal width of w = 0.6 m (see also Figure 4.2). Similarly, Figures 4.8b and 4.8c are used as benchmark to study the effect of canal width on surge velocity for canal widths of 1.6 m and 3 m, respectively. As shown in Figure 4.8, once the surge reached its peak velocity, it then gradually decreased and reached the quasi steady-state at approximately 20 seconds after the gate opening. The maximum surge velocity at US1 was approximately 2.2 m/s and slightly decreased at x =3.8 m and 4.18 m (Figure 4.8a).

The peak surge velocities decreased with increasing the distance from the gate and they were sustained over approximately 6 to 10 seconds (see Figure 4.8b, 4.8c). As shown in Figure 4.8b, the time-history of the surge velocity significantly changed with a steep velocity drop at x = 4.8 m and 5.18 m compared to the surge velocity measured at the US1 sensor location. Figure 4.8c shows the time-history of surge velocity at x = 6.2 m which indicates a significant velocity change with a steep slope, while the maximum surge velocity at x = 6.58 m slightly decreased with limited velocity fluctuations. However, the turbulent surge velocity reached quasi steady-state condition at time t = 20 seconds from the origin at all locations for the case of turbulent surge velocity over a smooth and horizontal surface for an impoundment depth of d_o = 0.4 m. As shown in Figure 4.8, the maximum surge velocity at x = 2.8 m was larger than the surge velocities measured downstream of the canal, and it significantly decreased with time until it reached a quasi steady-state condition.

The second peak of the surge velocity over the smooth horizontal bed without the presence of a canal at the location x = 6.58 m could have occurred due to noise from the ADV probe during the recording of the experimental tests, generated from elements of the surrounding environment such as pressure, temperature, etc. This also could be due to vibrations resulting from the ADV probe while recording data, which causes undesirable noises. Thus, noise in the signal affects the results. Even though the data were collected in different experimental tests, this may not be the reason for the odd results. The time series of the surge velocity passing over the smooth horizontal surface becomes quite noisy after about 15 s at all the different locations. It is understood that the oscillations at the end of the time series of the surge velocity are not due to wave reflections in the flume or the downstream wall effect, as these oscillations are not found in the time series of the surge height over the smooth horizontal bed. Overall, the accuracy of the results for the time series of surge velocity can be extremely dependent on the accuracy of the ADV probe.

4.3.2 Effect of Canal Geometry on the Turbulent Surge Height

Figure 4.9 shows the side view images of the surface profiles of turbulent surge front and their transformation with time for an impoundment depth of d_o = 0.4 m. The time at which the surge front entered the canal was set as t_* = 0 and the images were shown from t_* = 0 to t_* = 1.5 (t_* is the time since the surge front plunges into the canal).

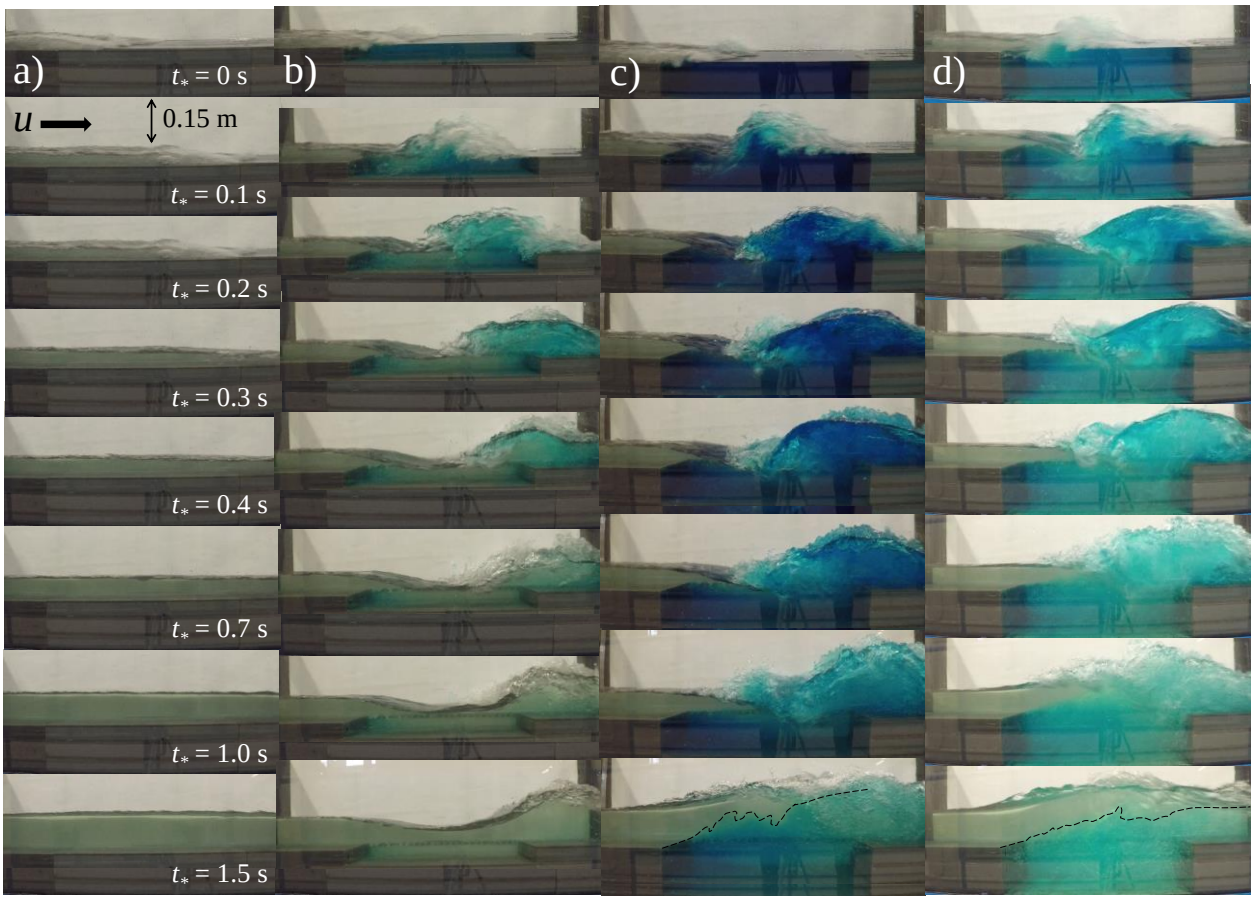

Figure 4.9. Time history of water surface profile passing over a horizontal bed and a rectangular canal of width w = 0.6 m and different depths for d_o = 0.40 m: a) d = 0 m (no canal); b) d = 0.05 m; c) d = 0.1 m; d) d = 0.15 m. (----) is the boundaries of the mixing shear layers of the water surface on the glass wall.

Figure 4.9 shows the propagation of the turbulent surge over both horizontal surface (Figure 4.9a) and in the presence of a 0.6 m wide canal with three different depths of h = 0.05 m, 0.1 m, and 0.15 m. A blue dye was mixed in the stagnant water placed in the canal for better visualization of the incoming surge and canal water mixing. The thin dashed curves at the bottom images of Figures 4.9c and 4.9d show the boundaries of the mixing shear layers. The propagation of turbulent surge over a horizontal surface showed a gradual water level increase, as it is expected to be in line with the 1D dam-break propagation theory introduced by Ritter (1892), and it reached to the quasi uniform condition at t_* = 1.5 s.

In the presence of a canal, the surge front plunged into the canal and formed a series of ripples in the middle and upstream end of the canal as the surge front slides over the canal surface. Following a short period of time (i.e., $\Delta t_* \approx 0.1$ s), the surge front plunged into the canal and formed a surface hydraulic jump within the canal width. This time indicated the onset of the initial interaction where the surge height rose as a result of a significant development of the pressure force by the surface hydraulic jump in the downstream edge of the canal. At time t_* = 0.3 s, the surge front carried more momentum to the canal and it developed a stronger surface jump reaching the downstream edge of the canal. A strong shear layer developed due to the presence of a quasi-steady flow in the

upstream of the canal and, as a result, a strong surface jump was formed in the downstream end of the canal nearly 0.5 s after the surge front had plunged into the canal. This was observation of the water surface elevation and water mixing in the canal. At this stage, the water level continued to increase with time and reached its maximum level between 5 s and 10 s from the opening time of the gate (see Figure 4.5). An analysis of the time-history images of water surface profiles over the 0.6 m wide canal (for all three depths) indicated that the water surface growth induced by a canal was no longer observed after 1.5 s (i.e., t/T = 7.5) from the plunging of the surge front.

The Froude numbers were calculated using $F_r = u/(g \times h)^{1/2}$ (where h is the flow depth, u is the flow velocity, and g is the gravitational acceleration) for the three impoundment depths of d_o = 0.20 m, 0.30 m, and 0.40 m for the tests with the presence of the canal with a width of w = 0.60 m and the three canal depths of d = 0.05 m, 0.10 m, and 0.15 m (see Figure 4.10).

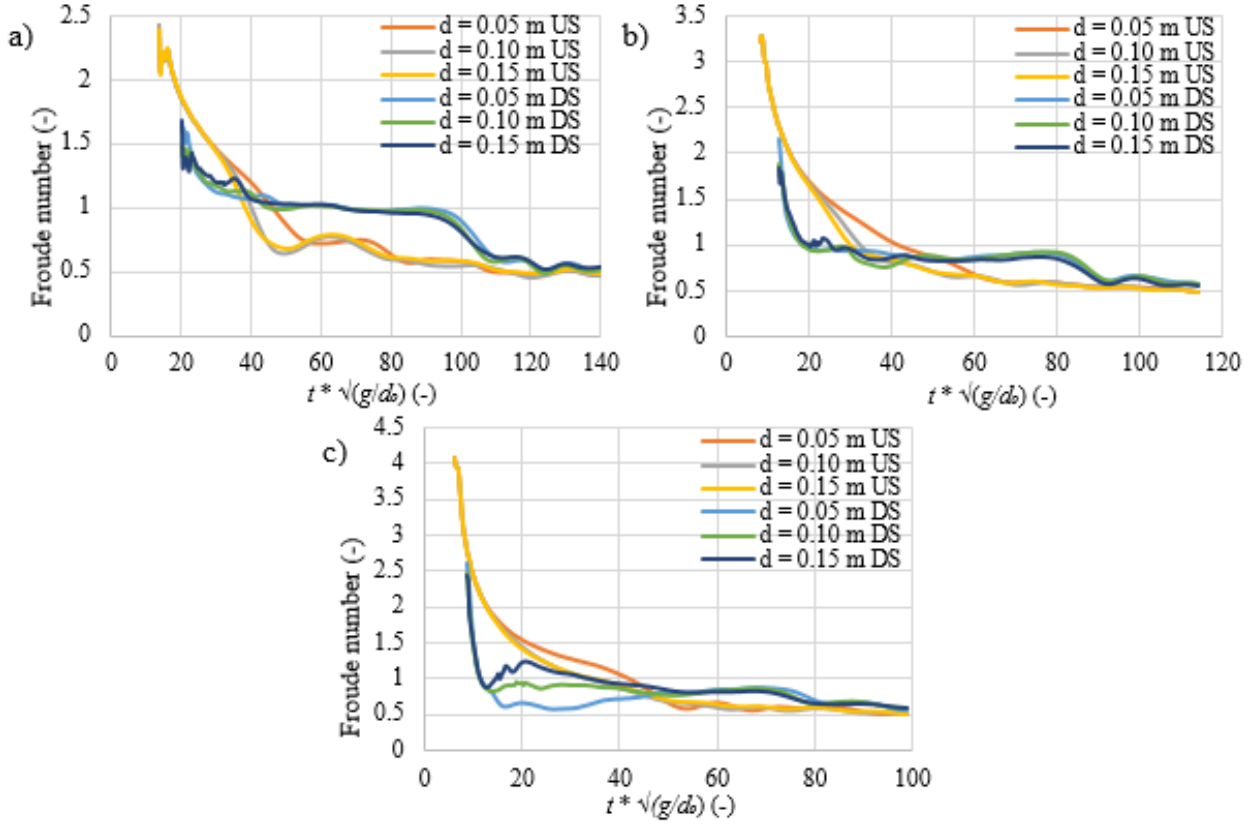

Figure 4.10. Time history of Froude number variations of 0.20 m upstream and downstream of the canal with width w = 0.60 m and three canal depths d = 0.05 m, 0.10 m, and 0.15 m for three impoundment depths: (a) 0.20 m, (b) 0.30 m, and (c) 0.40 m.

The recorded water surface elevations and velocities at 0.20 m upstream and downstream of the canal were used to calculate the Froude numbers. Figure 4.10a shows that the Froude numbers for the flow upstream of the canal resulting from the 0.20 m impoundment depth for the three canal depths decreased from nearly 2.4 to 1 for 32 non-dimensional times after the arrival of the surge.

The Froude numbers first decreased sharply and then more gradually before reaching a quasi-steady-state flow condition. For the three canal depths, the Froude numbers downstream of the canal declined from nearly 1.7 to 1 after 28 non-dimensional times from the surge arrival. The Froude number remained almost constant and equal to 1 for nearly 18 non-dimensional times, then first decreased gradually and the more suddenly to a quasi-steady-state flow condition.

The calculated Froude numbers for the flow resulting from the 0.30 m impoundment depth and the three canal depths at 0.20 upstream and downstream of the canals are shown in Figure 4.10b. The Froude number upstream of the canal decreased from nearly 3.3 to 1 after 34 non-dimensional times from the arrival of the surge for the three canal depths. Downstream of the canal, the Froude numbers decreased from nearly 2.2 to 1 after 12 non-dimensional times. For the 0.40 m impoundment depth (see Figure 4.10c), the Froude number before the canal decreased from approximately 4.1 to 1 after 36 non-dimensional times for the three depths. For the three depths, the Froude number after the canal decreased from approximately 2.6 to 1 after 4 dimensionless times from the arrival of the surge, then went below 1 for 3 non-dimensional times before returning to be approximately equal to 1 before going below 1 again. It should be noted that the surge for the three impoundment depths of d_o = 0.20 m, 0.30 m, and 0.40 m upstream of the canal was supercritical, $F_r > 1$, for almost 32, 34, and 36 non-dimensional times, respectively throughout the studied dimensionless time frame. The surge downstream of the canal was supercritical for almost 28, 12, and 4 non-dimensional times, respectively.

Figure 4.11 illustrates the variations of the maximum surge height, h_{max}, passing over a rectangular canal normalized by the maximum surge height without a canal, h_o, for tests with impoundment depths of d_o = 0.2 m, 0.3 m, and 0.4 m.

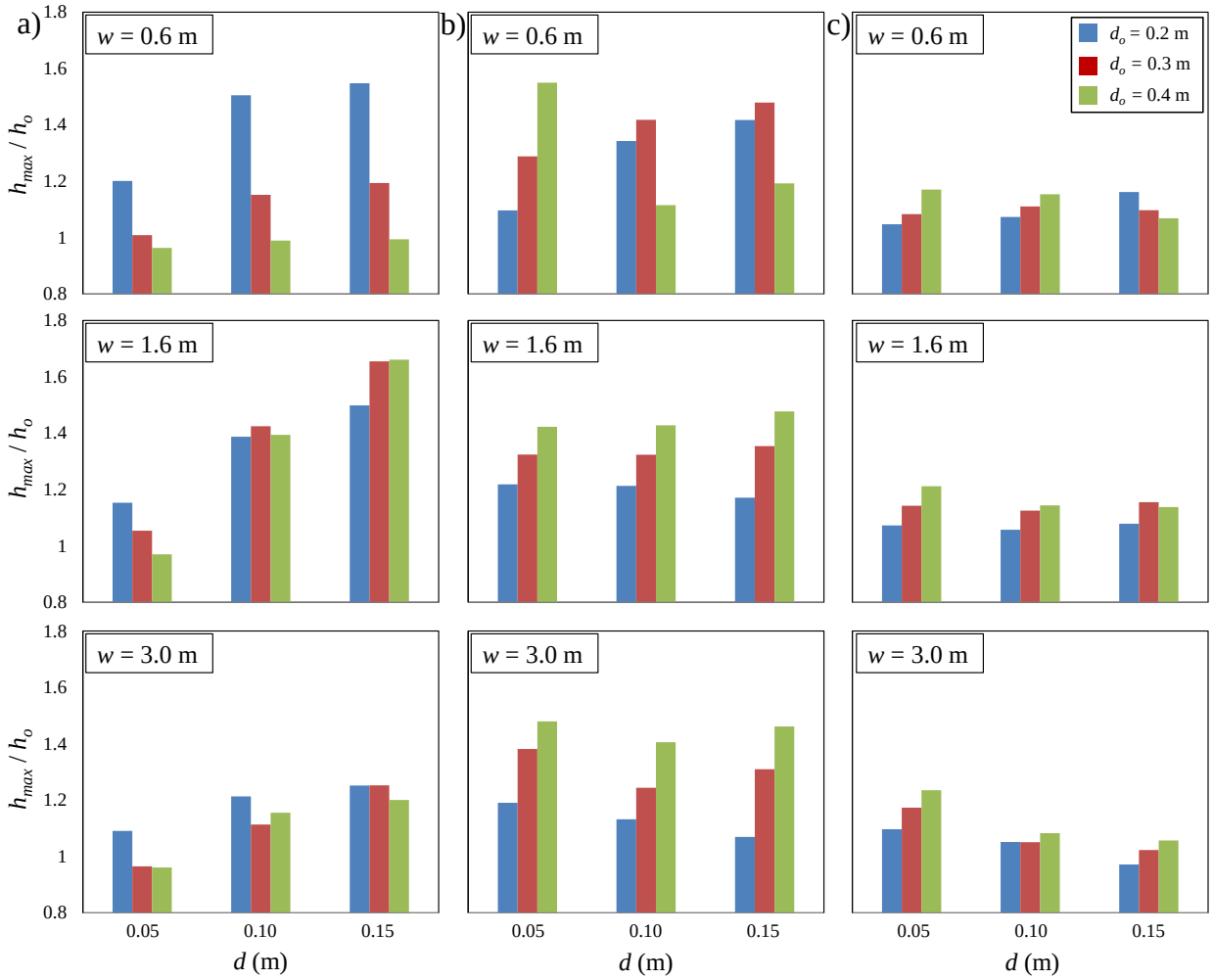

Figure 4.11. Variations of the maximum surge height passing over a rectangular canal h_{max} normalized with the maximum bore height without canal h_o for different impoundment depths and canal aspect ratios: a) 0.2 m upstream of the canal; b) 0.2 m downstream of the canal; c) 0.58 m downstream of the canal.

The wave heights were measured at different locations in the flume. Figure 4.11a shows the effect of canal geometry on variations of the normalized peak surge height at 0.2 m upstream of the canal (US1). The same values for the locations of 0.2 m and 0.58 m downstream of the canal are plotted in Figures 4.11b and 4.11c, respectively. The subplots in each figure indicated the effects of the canal width: the top subplot shows the variations of normalized surge height for w = 0.6 m, the middle subplot shows data for w = 1.6 m, and the bottom subplot shows the same results for w = 3 m. The column bars in each subplot show the effects of the canal depth, d, and impoundment depth, d_o.

Figure 4.11a shows the effect of mitigation canal and canal geometry on variations of the normalized maximum surge height in the upstream side of the canal. As shown in the upper subplot of Figure 4.11a, the peak surge height significantly increased by approximately 40% for $h \geq 0.1$ m and for the relatively small impoundment depth of $d_o = 0.2$ m. The effect of canal on variations of the normalized surge height became negligible for $d_o = 0.4$ m. The middle subplot in Figure 4.11a shows the effect of the canal depth on variations of the normalized surge height for $w = 1.6$ m in which the normalized surge height in the upstream of the canal increased with an increase in the canal depth. No significant changes were observed for $h = 0.05$ m, whereas for deeper canals, the peak surge height increased by 40% and 60% for $h = 0.1$ m and 0.15 m, respectively.

Figure 4.11b shows the effect of mitigation canal on variations of the normalized surge height at 0.2 m downstream of the canal. Overall, the surge height downstream of the canal increased between 10% and 50% of the surge height without a canal. In general, the normalized surge height increased with an increase in the impoundment depth, irrespective of the canal dimensions with the average values of 20%, 30%, and 40% for initial impoundment depths of $d_o = 0.2$ m, 0.3 m, and 0.4 m, respectively. In general, surges generated by higher impoundment depths exhibit higher momentum and thus are less affected by the presence of the canal while lower impoundment generated surges have less momentum and are thus more affected by the presence of the canal. In addition, in almost all cases, the surge height decreased as the canal width increased. This is assumed to occur due to an increase in the momentum dissipation over the longer canal width. Figure 4.11c shows that the effect of the mitigation canal on the normalized surge height which reduced as the turbulent surge propagated further downstream the flume. For the smaller impoundment depth of $d_o = 0.2$ m, the canal increased the surge height by an average +6.8% and ±2.8% variations due to formation of surface hydraulic jump within the canal width.

In order to study the effect of the canal's depth and width on variation of the maximum turbulent surge height, the aspect ratio of the mitigation canal, w/d, was plotted against with the normalized peak surge height, h_{max}/h_o, for the both locations upstream and downstream of the canal. Figure 4.12 shows the variation of the normalized maximum surge height, h_{max}/h_o, with, w/d, and for different impoundment depths.

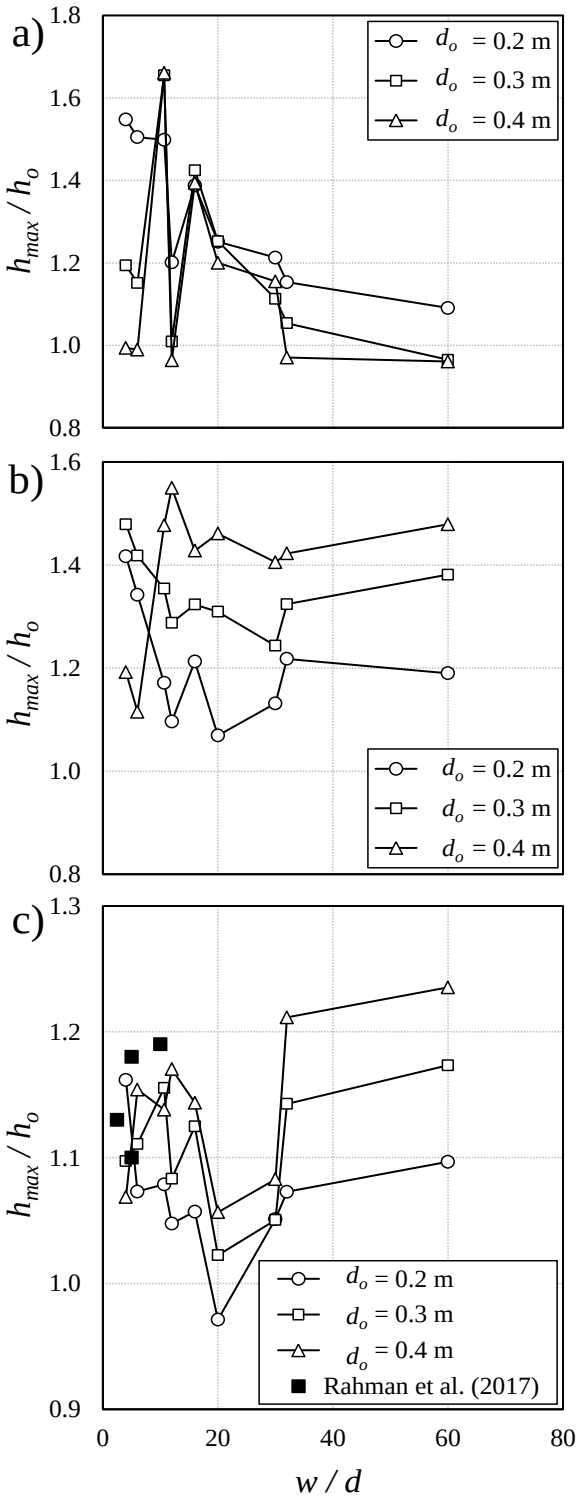

Figure 4.12. Variations of the normalized maximum surge height h/h_o with the canal aspect ratio w/d for different distances from the gate: a) 0.2 m upstream of the canal; b) 0.2 m downstream of the canal; c) 0.58 m downstream of the canal.

As shown in Figure 4.12a, the variation of normalized maximum surge height at the 0.2 m location upstream of the canal has a similar trend except for the aspect ratios less than 10.7. The maximum surge height was as high as 60% of the corresponding surge height without the presence of the canal and decreased as the canal aspect ratio increased. For the maximum aspect ratio of $w/d = 60$, the peak surge height increased by 10% over the peak surge height measured in the absence of the canal; no such change was observed for impoundment depths of d_o = 0.3 m and 0.4 m. The normalized maximum surge height increased considerably by nearly 50% for $w/d \leq 6$ and the small impoundment depth of d_o = 0.2 m, whereas for the impoundment depth of d_o = 0.3 m, the normalized peak surge height increased by nearly 20% for the same canal aspect ratio $w/d \leq 6$. For d_o = 0.4 m, the effect of canal aspect ratio on variations of the normalized peak surge height became very small for $w/d \leq 6$, and the normalized maximum surge height reached the lowest value for $w/d = 12$.

One can observe that the variation in normalized maximum surge height is correlated with the impoundment water depth. For the lower impoundment depth of d_o = 0.2 m, the normalized maximum surge heights had quite significant values for the entire canal aspect ratio $w/d \geq 4$, and the significant maximum surge height was as high as 54% of the corresponding surge height without the presence of the canal for $w/d = 4$. The normalized maximum surge heights generated by impoundment depth d_o = 0.3 m showed significant values for the entire canal aspect ratio $w/d \geq 4$, except for the shallow canals with canal aspect ratios of w/d = 12, 32, and 60. For the higher impoundment depth of d_o = 0.4 m, the normalized maximum surge heights displayed somewhat significant values; however, the normalized maximum surge heights became negligible for the narrow and shallow canals with aspect ratios of w/d = 4, 6, 12, 32, and 60.

Figure 4.12b shows the variation of the normalized peak surge height with the canal aspect ratio at the location of 0.2 m downstream of the canal. Obviously, the impoundment depth plays an important role in the variation of the peak surge height passing over the canal and for $w/d \geq 20$. It was also found that the normalized peak surge height is invariant with the canal aspect ratio. The normalized peak surge heights measured for d_o = 0.2 m, 0.3 m, and 0.4 m were 20%, 40%, and 50%, respectively, higher than the corresponding peak surge heights without the presence of a canal. For the impoundment depth of d_o = 0.2 m, the normalized peak surge heights showed significant values for the entire aspect ratio, but not for the smallest and largest canals with canal aspect ratios of w/d = 12 and 20, as the maximum surge heights were as low as 10% and 8% respectively of the corresponding surge heights without the presence of the canal. The normalized peak surge heights for d_o = 0.3 m displayed high values of more than 25% greater than the corresponding peak surge heights without a canal for the entire canal aspect ratio $w/d \geq 4$. The normalized peak surge heights generated by the higher impoundment depth of d_o = 0.4 m displayed extremely high values for all the canal aspect ratios, except for the narrow canals with the deeper depths of w/d = 4 and 6. Thus, the higher impoundment depth d_o = 0.4 is more affected by the higher canal aspect ratio $w/d > 6$.

Figure 4.12c shows the correlations of the normalized surge height with canal aspect ratio at 0.58 m from the canal downstream edge. The experimental results of Rahman et al. (2017) for relatively small canal aspect ratios (i.e., $w/d < 10$) are also included in Figure 4.12c. As it can be seen, the

normalized peak surge heights became independent of the impoundment depth for $w/d \leq 20$ and they decreased from 1.15 ± 0.05 and reached to a minimum value of $h_{max}/h_o = 1.02 \pm 0.035$ for $w/d = 20$. The normalized surge heights increased for the case when $w/d > 20$ and seemed to exhibit a more pronounced dependence on the initial impoundment depth. The normalized peak surge height passing over a wide mitigation canal (i.e., $w/d = 60$) and for $d_o = 0.2$ m, 0.3 m, and 0.4 m were 10%, 18%, and 24% higher than the corresponding peak surge heights in the absence of the canal. For the smaller impoundment depth $d_o = 0.2$ m, the normalized maximum surge height passing over a narrow canal with the small canal aspect ratio of $w/d = 4$ increased by nearly 16%, whereas the normalized maximum surge height passing over a canal with the higher aspect ratio of $w/d = 20$ increased only a little and attained negligible values. The normalized peak surge heights measured for $d_o = 0.3$ m show reasonable values higher than the corresponding peak surge heights without a canal, but for a narrow canal with shallow depth and a wide canal with deep depths with the canal aspect ratios of $w/d = 12$, 20, and 30, the maximum surge heights were as low as 9%, 3%, and 6% respectively. The normalized peak surge heights produced by the impoundment depth $d_o = 0.4$ m displayed values that were higher by approximately 21% and 24% for wide canals with shallow depth with the aspect ratios $w/d \geq 32$ and 60 respectively. The normalized peak surge heights also displayed reasonable values except for the narrow and deep canal and the wide canal with medium and deep depths with the canal aspect ratios $w/d = 4$, 20, and 30, as the maximum surge height was as low as approximately 7% higher than the corresponding peak surge heights without a canal.

Figure 4.13 shows the time-history of surge height generated by an impoundment depth of $d_o = 0.40$ m, a canal depth of $d = 0.05$ m, measured at three different locations with respect to the canal: 0.2 m upstream of the canal (US1) and 0.2 m and 0.58 downstream of the canal.

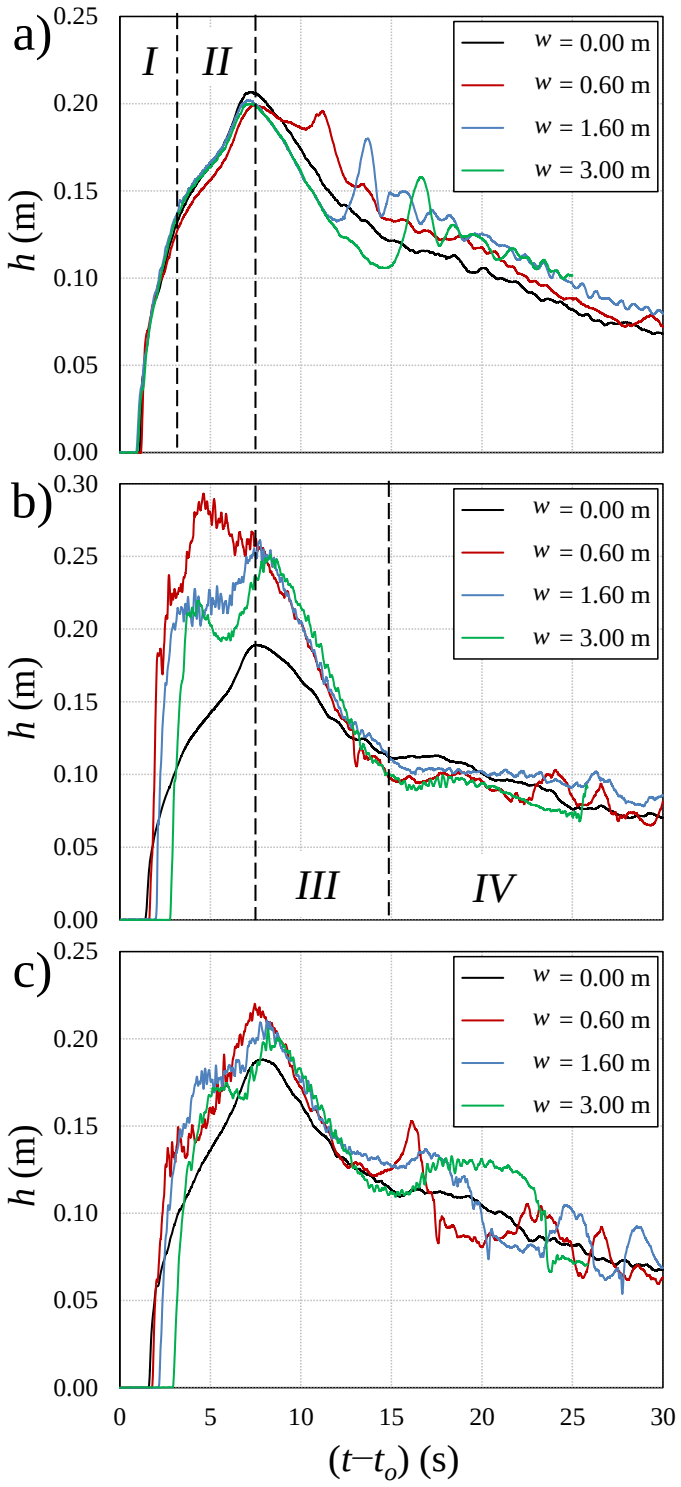

Figure 4.13. Time-history of water level for a surge with an impoundment depth of d_o = 0.4 m and canal depth of h = 0.05 m and different distances from the canal: a) 0.2 m upstream of the canal (US1); b) 0.2 m downstream of the canal; c) 0.58 m downstream of the canal.

The time-history profiles provide several observations with respect to the effect of canal width on variation of the maximum surge height, the quasi steady flow, and the surge height fluctuations in the upstream and downstream of the canal.

Figure 4.13 shows the four regimes in the time-history of surge height (previously described in Figure 4.5) for the case of the surge propagation over a horizontal and smooth bed surface. During Regime I, the surge height increased rapidly and reached approximately 70% of its peak which occurred between seconds 6 and 9. Regime II is categorized by a gradual increase of the surge height with lower amplitude water level fluctuations. The surge wave height in this regime increased up until the surge attained its maximum value. The surge height then rapidly decreased in Regime III and a series of oscillatory waves with a high degree of dampening was observed 0.2 m upstream of the canal entrance (US1). These oscillatory waves were generated due to the surge and canal interactions and formation of a surface hydraulic jump, as shown in Figure 4.8. The surge height gradually decreased after the peak, independent of the canal geometry and the location of measurement. This segment exhibited a high degree of water surface fluctuations at locations 0.20 m and 0.58 m downstream of the canal.

Figure 4.13b shows the time-histories of surge heights for different canal widths at a location 0.2 m downstream of the canal. At this location, the maximum surge heights passing over the canal with different widths were higher than the corresponding surge height over a smooth and horizontal surface (in the absence of the canal). However, all waves passing over the canal with different widths reached their quasi steady-state condition at the same time and depth of $t-t_o$ = 15 s and h = 0.1±0.01 m.

The differences between the maximum surge heights with and without canals were substantial at a location 0.2 m downstream of the canal and reached a value of approximately $1.355h_o$ for w = 0.60 m. The effect of the mitigation canal on the surge height diminished once the latter entered Regime IV. A time delay was observed on propagation of turbulent surge over a wide rectangular canal (w = 3 m) at locations 0.2 m and 0.58 m downstream of the canal – this indicates a deceleration of the turbulent surges as they interacted with the stagnant water in the canal. The surge heights demonstrated similar transient trend for surge propagation over horizontal surface for different canal widths for the location 0.58 m downstream of the canal (see Figure 4.13c). A slightly higher peak of the surge height was observed, with an average of 11% and with ±2% fluctuations, for the surge propagation over a canal in comparison with the same test without a canal.

Due to excessive turbulent formation within the canal and the surface hydraulic jump development observed at the downstream edge of the canal, the quasi steady-state (began at $t - t_o$ = 15 s) exhibited significant water surface fluctuations which led to increased energy losses at the far downstream of the canal. Although the arrival times of the turbulent surges over wider canals were longer due to surge plunging and mixing with water in the canal, the maximum surge heights occurred approximately at the same time at location 0.58 m downstream of the canal.

The oscillatory waves generated by the hydraulic surges on the waters' surface could be influenced by the presence of the canal, mainly on the downstream edge. The generated turbulent surges

propagated over a smooth horizontal bed downstream of the vertical lift gate and interacted with a mitigation canal, and the large portion of the turbulent surge continued to propagate through the rest of the flume until it dropped through a vertical drain located at the end. However, since the other portions of the hydraulic surges were reflected back from the downstream edge of the canal and collided with the propagating surge, the water's surface level initiated oscillatory waves. The water levels in the physical experiments showed that water reflection due to the existence of the canal scenario generated the oscillatory waves. Furthermore, when the propagating surge interacts with the returned wave near the location of the peak water surface, the oscillation of the water surface profile might be substantial.

A 1V:6H PVC ramp was fixed at the upstream end of the temporary artificial bed to produce a gradual slope in order to prevent local energy losses and flow separation ahead of the mitigation canal. The upstream end of the mitigation canal was situated 3.0 m downstream of the gate to guarantee the establishment of a fully developed hydraulic surge prior to approaching the canal. Also, a wave-absorbing system made with blue geotextile was fixed in the vicinity of the upstream end flume inside the reservoir to prevent wave reflection. There was no interaction of a supercritical flow with the flume walls, as the Froude number downstream of the canal was less than one for almost the whole time frame. Therefore, no shock waves were observed or detected in either the physical experiments or numerical computations.

These oscillatory waves were generated as a result of surge and canal interactions and the formation of a surface hydraulic jump. Figure 4.8 shows the velocity surge propagation over a horizontal smooth bed without a canal.

Figure 4.14 shows the effects of the canal width on the time-series of the surge height generated by an impoundment depth of d_o = 0.40 m and a canal depth of h = 0.10 m at three different sensor locations of 0.2 m upstream of the canal (US1), 0.2 m and 0.58 m downstream of the canal.

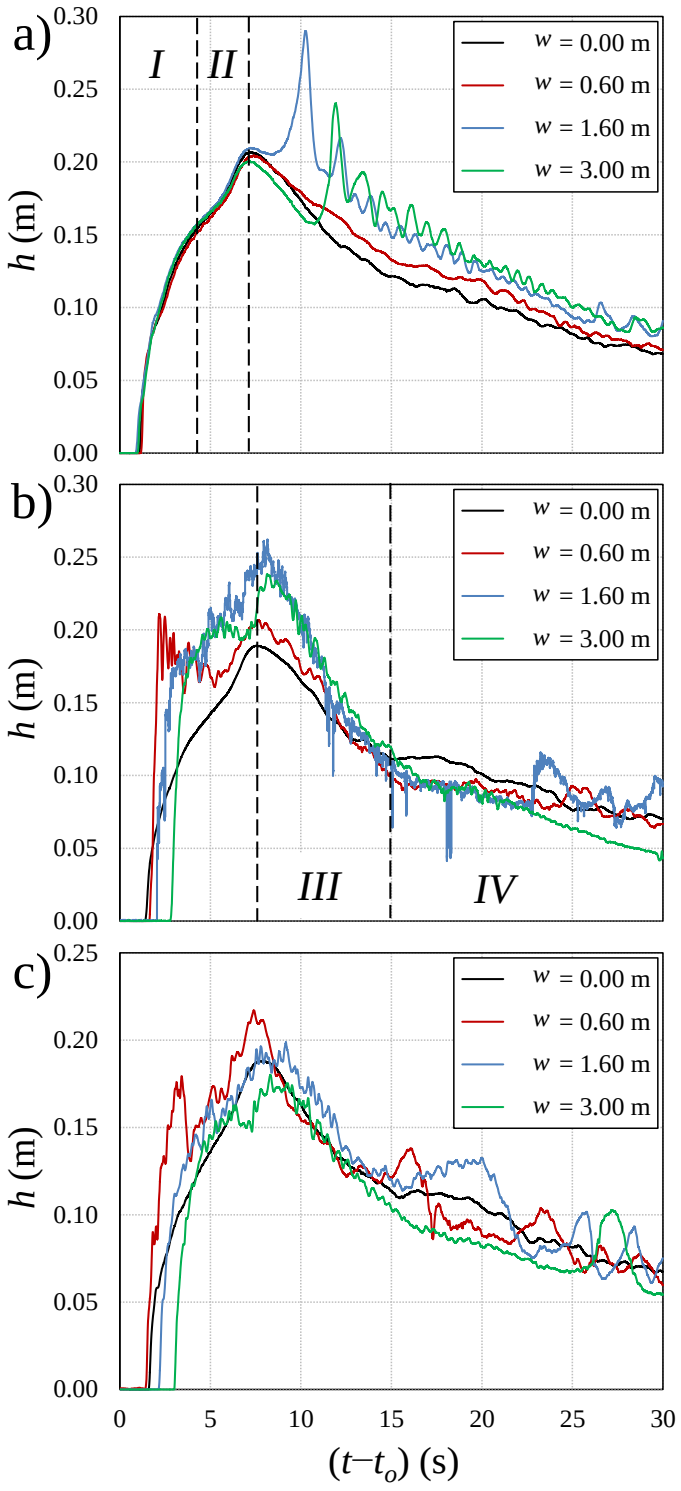

Figure 4.14. Time-history of water level for a surge with an impoundment depth of d_o = 0.4 m and canal depth of h = 0.10 m and different distances from the canal: a) 0.2 m upstream of the canal (US1); b) 0.2 m downstream of the canal; c) 0.58 m downstream of the canal.

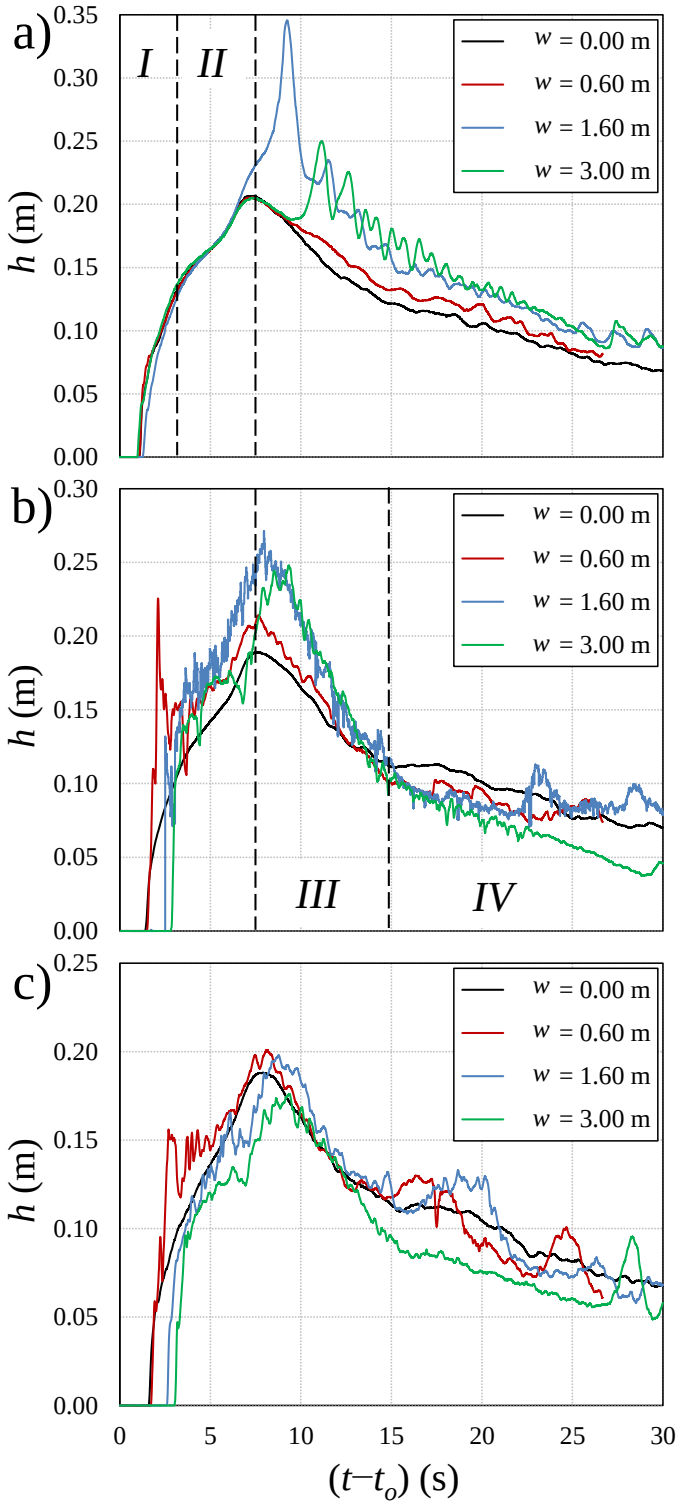

Figure 4.15. Time-history of water level for a surge with an impoundment depth of d_o = 0.4 m and canal depth of h = 0.15 m and different distances from the canal: a) 0.2 m upstream of the canal (US1); b) 0.2 m downstream of the canal; c) 0.58 m downstream of the canal.

A comparison of the surge heights at location 0.2 m upstream of the canals (see Figures 4.13a, 4.14a, and 4.15a) indicates that the amplitude of the oscillatory waves increased for the wider canals (i.e., w = 1.6 m, 3 m) whereas in the case of the narrow canal (w = 0.6 m), the weak oscillatory waves diminished as the canal depth increased. For example, the peak oscillatory wave for w = 1.6 m and h = 0.05 m increased by 56% and 91% for h = 0.1 m and 0.15 m, respectively. The peak oscillatory wave heights were observed to be closer to the maximum surge height as the canal depth increased. For a constant canal depth of w = 1.6 m, the peak oscillatory wave occurred 6.6 seconds following the peak surge height for h = 0.05 m, whereas the time delay for h = 0.1 m and 0.15 m were 3.1 s and 1.95 s, respectively.

As Figures 4.14b and 4.15b show, the canal depth attenuated the peak surge height at the location 0.2 m downstream of the canal. Additionally, the peak surge height became independent of the canal width for the width $w \geq 1.6$ m. It worth noting that, the canal geometry didn't change the boundary between the drawdown regime (Regime III) and the quasi steady-state regime (Regime IV) at the location 0.2 m downstream of the canal with a surge height of approximately 25% of the impoundment depth (see Figures 4.13b, 4.14b, and 4.15b). The difference between the maximum surge heights for the tests with and without canal was less significant at location 0.58 downstream of the canals. Figures 4.14c and 4.15c show that the maximum surge heights for w = 3 m and at 0.58 m downstream of the canal became smaller than the peak surge heights for the tests without the canal by −3% and −10.5% for h = 0.1 m and 0.15 m, respectively.

4.3.3 Effect of Canal Geometry on the Turbulent Surge Velocity

The presence of the mitigation canal resulted in a significant change in the surge height characteristics as it passed over the canal: these changes were noticeable in the exit time from the canal as well on the peak surge height variation over time immediately after the exit from the canal. However, the time-history of water level indicated that the canal did not significantly change the surge height at a location 0.58 m downstream of the canal. This section deals with the effects of the canal geometry on the changes in the turbulent surge velocity at both upstream and downstream of the canal.

Figures 4.16- 4.18 show the effects of canal geometry on the time-history of surge velocity generated by an impoundment depth of 0.4 m. The time-history plots were generated for three locations of 0.2 m upstream of the canal, 0.2 m and 0.58 m downstream of the canal. Figure 4.16 shows the time-history of the surge velocity for the shallow canal with a canal depth of h = 0.05 m (i.e, $h = 0.125d_o$).

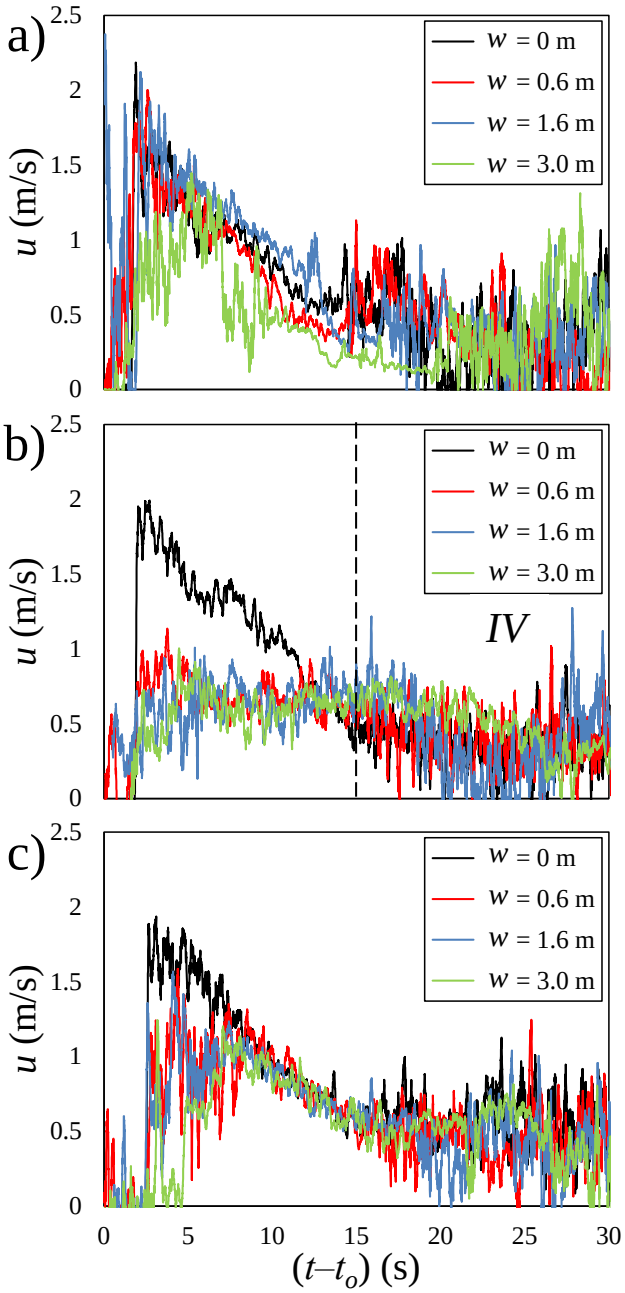

Figure 4.16. Time-history of water velocity for a surge with an impoundment depth of d_o = 0.4 m and canal depth of h = 0.05 m and different distances from the canal: a) 0.2 m upstream of the canal (US1); b) 0.2 m downstream of the canal; c) 0.58 m downstream of the canal. t is the recording time and t_o is the time when the gate is opened.

As shown in Figure 4.16a, the time-history of surge velocity remained unchanged at the 0.2 m location, immediately upstream of the canal with only a slight velocity decrease for a very wide canal (w = 3 m).

Figure 4.16b shows the time-history of the surge velocity at the 0.2 m location downstream of the canal where a significant velocity drop was observed right after the exit from the canal. The high degree of velocity fluctuations at the 0.2 m location downstream of the canal may be due to the

formation of strong swirling motions and air entrainment downstream from the surface hydraulic jump as shown in Figure 4.9b. The maximum surge velocity at this location was approximately 60% less than the peak velocity recorded without the canal. The time-histories of surge velocity at the exit from the canal showed that the velocity reduction was independent of the tested canal width. It should be noted that the ADV velocity measurements were taken at $z = 0.01$ m from the bed and only the stream wise velocities are shown in this section. At the 0.58 m location downstream of the canal, the stream wise velocity component was observed to have slightly increased. Figure 4.16c shows the variations of the stream wise surge velocity with time at the 0.58 m location downstream of the canal. The peak surge velocity decreased by 32% in presence of the canal and it was independent of the canal width.

The noise could be caused by the ADV probe, generated during the recording of the experimental tests as a result of the effect of surrounding environment parameters such as pressure and temperature. It also could be due to vibrations caused by the operation of the ADV probe while capturing data, which generates unwanted noise. As a result, noise in the signal influences the outcomes. Even though the data were obtained in several physical tests, this was not the cause of the strange results. The time histories of the surge velocity while traveling over a mitigation canal and a smooth horizontal surface before and after the canal become rather noisy after about 15 s, but this noise is not caused by flume wave reflections. Overall, the accuracy of the time histories of the surge velocity results is highly dependent on the precision of the ADV probe. Thus, this noise could be due to inaccurate recordings by the ADV.

Figure 4.17b shows the variations of surge velocity with time for a canal with a medium canal depth of $h = 0.25d_o$ in which the surge velocity decreased by approximately 50% of the test without canal whereas for the test with a deeper canal (i.e., $h = 0.375d_o$), the surge velocity decreased by approximately 40% (see Figure 4.18b) in comparison with the tests without a canal.

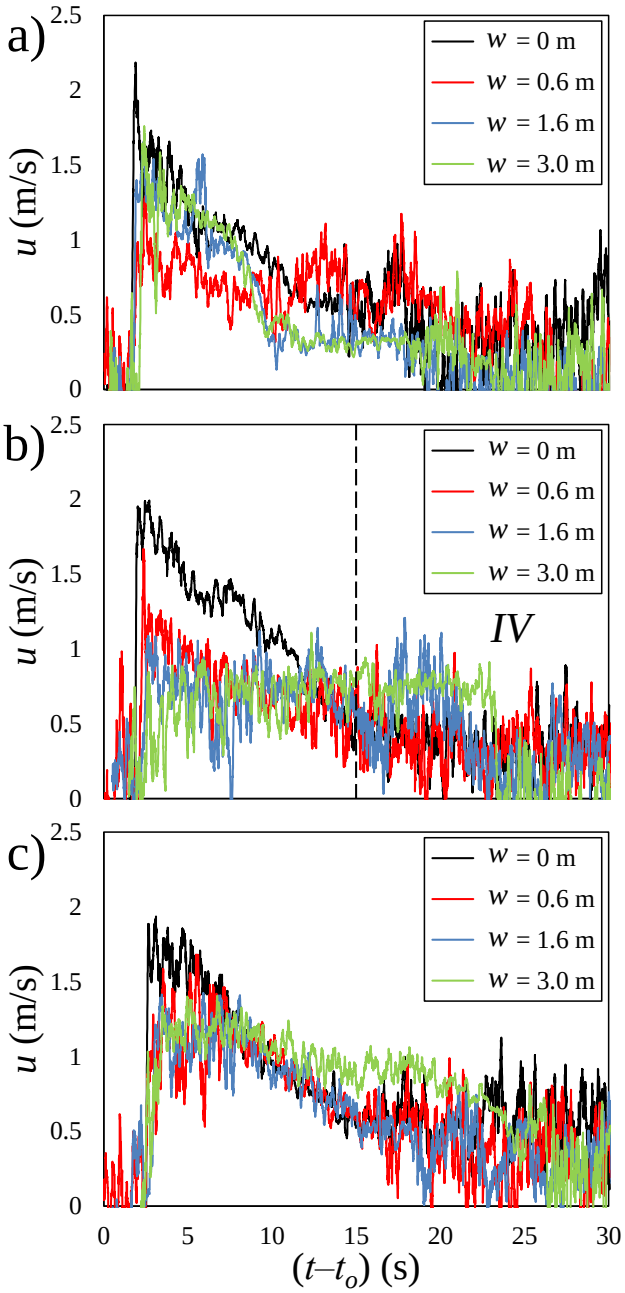

Figure 4.17. Time-history of water velocity for a surge with an impoundment depth of d_o = 0.4 m and canal depth of h = 0.10 m and different distances from the canal: a) 0.2 m upstream of the canal (US1); b) 0.2 m downstream of the canal; c) 0.58 m downstream of the canal. t is the recording time and t_o is the time when the gate is opened.

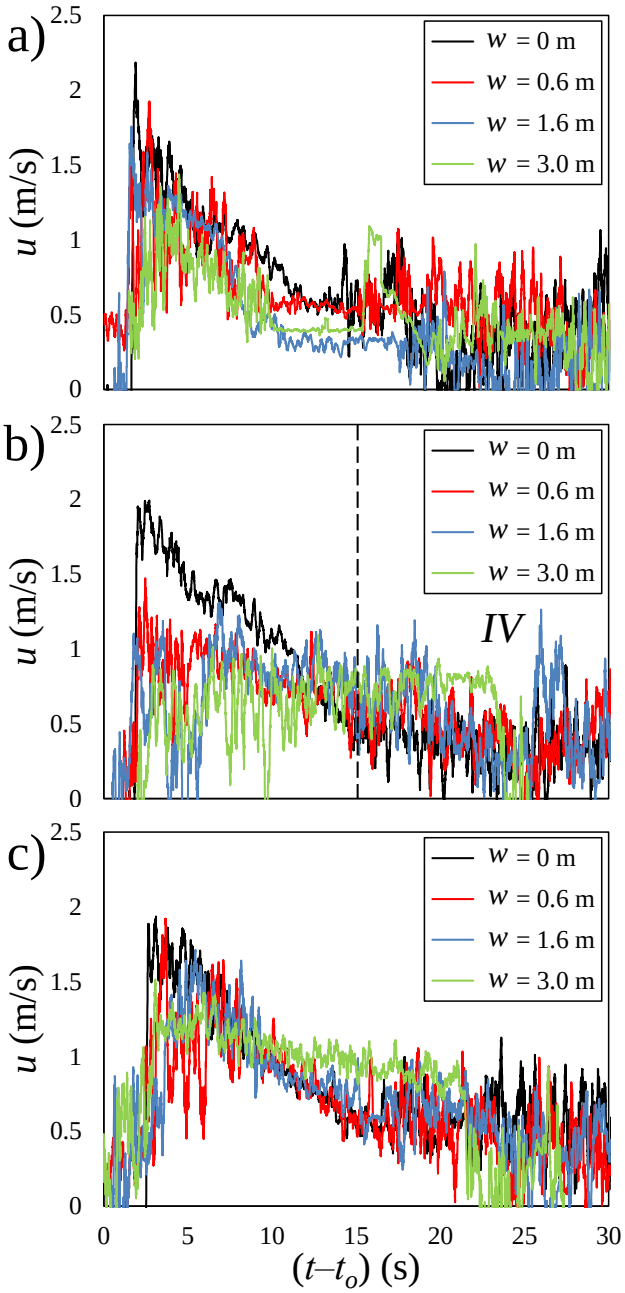

Figure 4.18. Time-history of water velocity for a surge with an impoundment depth of d_o = 0.4 m and canal depth of h = 0.15 m and different distances from the canal: a) 0.2 m upstream of the canal (US1); b) 0.2 m downstream of the canal; c) 0.58 m downstream of the canal. t is the recording time and t_o is the time when the gate is opened.

Similar to the turbulent surge propagation over a shallow canal (h = 0.05 m), the time-histories of the turbulent surge propagation over the medium depth and the deep canals are shown as quasi steady velocity profiles at the 0.2 m location downstream of the canal (see Figures 4.17b and 4.18b). It was found that the surge velocity variations with time decreased with increasing the canal width. Therefore, the wide and deep canals transformed the triangular time-history of velocity data over a smooth and horizontal surface into a rectangular-shaped one, indicative of a

quasi-uniform flow downstream of the canal (see Figures 4.17b and 4.18b). Such a flattening of the velocity profile generated due to the bore of a canal is useful by avoiding peak flow velocities which can lead to significant hydrodynamic loading onto structures. As such, one could use such canals to protect coastal or nearshore infrastructure against tsunami inundation hazards. At the 0.58 m location downstream of the canal edge, the time-history of surge velocity exhibited a maximum surge velocity drop of approximately 25% of the tests comparing to the without a canal (see Figures 4.17c and 4.18c).

4.4 Discussion

An experimental study was performed to examine the mitigation effects of canals with rectangular cross-section when extreme flows, in the form of dam-break induced surge waves, pass over them. The time-series of the surge heights and velocities were measured at upstream and downstream locations with respect to the canal to investigate the effects of the canal geometry on surge hydrodynamics for three impoundment depths. To assess the mitigation effects of the canal, time-histories of the surge heights and velocities passing over it were compared with the corresponding tests conducted without the canal. The surge propagation over a dry and smooth bed measured at seven locations along flow direction revealed four regimes describing the variation of surge height with time. In Regime I, the surge height suddenly increased from zero and reached approximately 50% of the peak wave height within 3 to 5 seconds from the gate opening. In Regime II, the surge height increased with a milder slope than the regime I and the surge height reached its peak, h_{max}. The time to the peak velocity was found to be scalable with the impoundment depth and the non-dimensional time at US1 and US3" were approximately equal to t/T = 47 and 11, respectively. Regime III in the time-history of the surge height started at the peak and lasted until 50% of the peak surge height at a specific time of t_q. The quasi steady state condition occurred in Regime IV, during which the surge height linearly decreased to the theoretical normal depth. A power law formula was proposed to correlate the onset of the quasi steady state time t_q with impoundment depth.

The maximum surge heights before and after the canal, h_{max}, were extracted from the time-history data and they normalized with the maximum surge heights without a canal, h_o. It was found that the peak surge height upstream of the narrow canal (w = 0.6 m) increased as high as $1.4h_o$ for a relatively small impoundment depth ratio of $d_o/d \leq 4$ and the effect of canal on variations of the normalized surge height became negligible for $4 < d_o/d \leq 8$. The effect of canal dimensions on the peak surge height upstream of the shallow canal was negligible; however, in the case of the deeper canals, the peak surge height increased by 40% and 60% for h = 0.1 m and 0.15 m, respectively. The surge height in the downstream of the canal increased between 10% and 50% of the surge height without a canal. It was found that the normalized surge height increased with an increase in the impoundment depth with average values of 20%, 30%, and 40% for d_o = 0.2 m, 0.3 m, and 0.4 m, respectively, irrespective of the canal dimensions.

The effects of canal aspect ratio on the maximum wave height in the downstream of the canal indicated that the normalized peak surge heights became independent of the impoundment depth for $w/d \leq 20$. The normalized peak surge height decreased from 1.15 ± 0.05 for $w/d = 4$ and reached

to a minimum value of $h_{max}/h_o = 1.02 \pm 0.035$ for $w/d = 20$. For $w/d > 20$, the normalized peak surge height correlated with the impoundment depth with values of 1.10, 1.18, and 1.24 for d_o = 0.2 m, 0.3 m, and 0.4 m when passing over a wide mitigation canal (i.e., $w/d = 60$).

The time-histories of surge velocity when passing over a mitigation canal were measured both upstream and downstream of the canal. The maximum surge velocity slightly decreased in the upstream of the canal in comparison with the corresponding test without a canal. The surge wave deceleration was due to the formation of a surface hydraulic jump at the downstream edge of the canal. It was found that the peak velocity reduction after the surge passed the canal was independent of the canal width. In shallow canals (i.e., $h/d_o = 1/8$), the maximum surge velocity at 0.2 m downstream of the canal decreased by approximately 60% of the peak velocity comparing to that recorded in the case without the canal and this is inferred that is due to significant momentum dissipation. For the medium and deep canals (i.e., $h/d_o = 1/4$ and 3/8), surge velocities were decreased by 50% and 40% of the peak velocity measured without a canal.

4.5 Conclusions

A series of laboratory investigations was performed to examine the effect of a mitigation canal on the time history of the water surface level and velocity of turbulent hydraulic waves upstream and downstream of the canal. A dam-break wave technique was employed in the physical experiments investigations to simulate a broken tsunami wave propagating on a horizontal and smooth surface with and without the presence of the canal. The authors drew the following conclusions:

- The normalized maximum bore height and the impoundment depths became independent for $w/d \leq 20$. For $w/d > 20$, the normalized maximum bore height correlated with the impoundment depths with magnitudes of 1.24, 1.18, and 1.10 for d_o = 0.4 m, 0.3 m, and 0.2 m as propagating on a wide extenuation canal ($w/d = 60$).

- The bore front velocity fluctuated between 1.17 $(gd_o)^{1/2}$ and 1.4 $(gd_o)^{1/2}$ for the entire range of canal aspect ratios.

- The capability of the canal to suppress the momentum of the bore increased as the canal depth increased.

- The mitigation canals more likely perform as measures that decrease hydrodynamic loading on critical infrastructure situated in tsunami-near regions.

5 Article 2

Tsunami-Induced Bore Propagating over a Canal-Part 1: Laboratory Experiments and Numerical Validation

Nuri Elsheikh, Ioan Nistor, Amir H. Azimi, and Abdolmajid Mohammadian

Abstract

This companion paper investigates the hydrodynamics of turbulent bores that propagate on a horizontal plane and have a striking resemblance to dam break waves and tsunami-like hydraulic bores. The focus of this paper is on the propagation of a turbulent bore over a mitigation canal using both laboratory experiments and numerical simulations. In the first part of this paper, the effects of canal depth on the time histories of wave height and velocity were experimentally investigated, and the experimental results were used for the validation of the numerical model. The rapid release of water from an impoundment reservoir at depths of d_o = 0.30 m and 0.40 m generated bores analogous to tsunami-induced inundations. The time histories of the wave heights and velocities were measured at 0.2 m upstream and at 0.2 m and 0.58 m downstream of the canal to study the energy dissipation effect of the mitigation canal. The recorded time series of the water surface levels and velocities were compared with simulation outputs, and good agreement was found between the experimental and numerical water surface profiles, with a Root Mean Square Error (RMSE) of less than 6.7% and a relative error of less than 8.4%. Three turbulence models, including the standard *k*-*ε*, Realizable *k*-*ε*, and RNG *k*-*ε*, were tested, and it was found that all these models performed well, with the standard *k*-*ε* model providing the highest accuracy. The velocity contour plots of the mitigation canal with different depths showed jet streams of different sizes in the shallow, medium-depth, and deep canals. The energy dissipation and air bubble entrainment of the bore as it plunged downward into the canal increased as the canal depth increased, and the jet stream of the maximum bore velocity decreased as the canal depth increased. It was found that the eye of the vortex created by the bore in the canal moved in the downstream direction and plunged downward in the middle of the canal, where it then began to separate into two smaller vortices.

Keywords: tsunami wave; dam-break wave; tsunami mitigation; wave hydrodynamics; OpenFOAM; surge height; bore velocity.

5.1 Introduction

Tsunami-induced bores are infrequent but are extremely destructive and can cause significant infrastructure damage in coastal regions. The most common source of tsunami waves are earthquakes, ones either near or beneath the ocean, and the resulting tsunami bores can become

massive far from their points of origin (FEMA-P646, 2012). Despite the availability of new design guidelines for coastal structures, post-tsunami field investigations of past events have revealed that many nearshore structures were completely destroyed or significantly damaged during these events (Nistor et al., 2005; Nistor and Palermo, 2015; Ghobarah et al., 2006). The recent tsunami events in the Indian Ocean in 2004, in Japan in 2011, and in Indonesia in 2018 showed the destructive energy of tsunami-induced loads. As a result, more safety measures and design guidance should be considered in order to minimize human casualties and ensure safe critical infrastructure in coastal areas (Wüthrich et al., 2017). Field observations of tsunami waves have indicated that return wave periods range from 10 min to 45 min (Douglas, 2016). In deep water and far from the shore, tsunami waves can reach velocities of the order of hundreds of kilometers/hour and can propagate toward the shoreline without a substantial loss in their kinetic energy. Once a tsunami wave approaches the coastal region, its velocity decreases, its height increases, while their wave period remains constant. Depending on the tsunami wave characteristics and the nearshore bathymetry, the wave's leading edge can break to form a turbulent bore or a bore even right before the wave reaches the shoreline (Ghodoosipour et al., 2019a, b).

An analysis of video images of the tsunami waves which propagated overland in several coastal regions of the Indian Ocean in 2004 showed a strong similarity between dam-break waves propagating on a horizontal plane and tsunami-like hydraulic bores (Chanson, 2006). As a result, researchers started employing dam-break waves to model tsunami inundation in laboratory studies (Nistor et al., 2009; Nistor and Palermo, 2015; Sarjamee et al., 2017a; Wüthrich et al., 2018a, b, c; Asadollahi et al., 2019a, b; Madsen et al., 2008; Leal et al., 2009; Khankandi et al., 2012; Shafiei et al., 2016a, b; Liu et al., 2017). Various water-release mechanisms have been used to generate dam-break bores. A volume of water stored in a reservoir could be released by a rapidly opening swing gate (Al-Faesly et al., 2012; Stolle et al., 2019), by the sudden removal of a vertical gate (Crespo et al., 2008; Duarte et al., 2011; Oertel and Bung, 2012; Aureli et al., 2015), or by releasing an elevated volume of water through vertical pipes (Arnason et al., 2009; Baldock et al., 2012; Wüthrich et al. 2018a, b; VonHäfen et al., 2019). In order to model tsunami wave inundations, several experiments generated dam-break waves by rapidly releasing water impounded from behind a vertical gate (Lauber and Hager, 1998; Nistor et al., 2009; Stolle et al., 2019; Sarjamee et al., 2017b; Asadollahi et al., 2019a, b; Ghodoosipour et al., 2019a, b). The differences between hydraulic bores flowing over dry beds and those flowing over stagnant water, known as a wet bed, have been examined using laboratory experiments and numerical simulations (Nistor et al., 2009; Nouri et al., 2010; Al-Faesly, 2016). For the same initial impoundment depth, a bore propagating over a wet bed is higher, and its wave front is steeper in comparison to that of a bore with an equivalent initial wave height propagating over a dry bed (Wüthrich et al., 2018a). Additionally, the velocity of a bore front propagating over a wet bed is affected by the still water depth. Hydraulic bores from impoundments of the same depth have higher velocities when propagating over the shallower still water depths (Ghodoosipour et al., 2019a).

The influences of tsunami mitigation structures on tsunami wave energy dissipation have been investigated in the past by studying the characteristics of wave hydrodynamics before and after different natural and manmade obstacles such as pine forests (Tanaka et al., 2009), coastal dunes (Fadly and Murakami, 2012), rivers and canals (Dao et al., 2013; Elsheikh et al., 2020), and natural

and artificial buildings (St-Germain et al., 2014). During bore propagation over natural streams or manmade canals, the upstream water level increases while the bore velocity decreases due to energy dissipation within the canal. Figure 5.1. shows an aerial image of the 2011 Japan Tsunami propagating over a canal running parallel to the coastline.

Figure 5.1. Image of tsunami propagating over a canal during the 2011 Japan Tsunami event Reprinted with permission from (Rajaie, et al. 2022) (2022, ASCE).

Laboratory experiments have shown that the hydrodynamic features of tsunami waves are considerably changed during their propagation over natural streams. Watanabe et al. (2016) showed how the destructive energy of tsunami waves was dissipated over a mitigation canal by conducting tests at three impoundment water depths of d_o = 0.55 m, 0.79 m, and 0.80 m. Only one canal geometry was tested, with a width of w = 0.30 m and a depth of d = 0.05 m, which gives a canal aspect ratio of w/d = 6. The overflow wave velocity was shown to have been reduced by the canal, while the wave height downstream of the canal increased. Rahman et al. (2017) indicated that the maximum reduction in wave velocity downstream of a canal occurred for the deepest and widest canals. A narrow range of canal aspect ratios of w/d = 4 to 10 was used. The physical experiments showed a similar wave velocity reduction when the canals had different depths but the same width. However, delays in the tsunami propagation were observed, and velocity mitigation occurred for all canal configurations. It was observed that the tsunami wave energy can be partially absorbed by the reflected wave generated by the canal. Recently, a series of laboratory experiments was conducted to examine the effects of canal geometry on the hydrodynamics of turbulent bores passing over a rectangular mitigation canal installed perpendicular to the flow direction (Elsheikh, et al. 2020). The surface water level and wave velocity were measured both upstream and downstream of the canal, and the effect of canal geometry was tested for a wide range of canal aspect ratios (i.e., $4 \leq w/d \leq 60$) in order to study the variations in wave heights and velocities for canal optimization.

Tsunami-like bores have been numerically simulated to provide more insight into the wave hydrodynamics and energy transfers during wave propagation and impact with coastal structures. Nistor et al. (2009) performed numerical simulations of tsunami-like bores with an upstream water depth of d_o = 0.85 m with the use of a structural model. A discrepancy was found in the early stages of the bore–structure interaction due to the significant splashing of water at the initial impact, which was not accurately reproduced by the numerical model. However, relatively good agreement was achieved between the numerical results and measurements after approximately 3 s of the bore initiation. St-Germain et al. (2012) investigated the effect of still water depth on the hydrodynamics of tsunami waves and wave structure interactions using a 3D Smoothed Particle Hydrodynamics (SPH) model. The time series of the net total base horizontal force acting on a slender square column were modelled, and it was found that the hydrodynamic loads due to hydraulic bore propagation were greatly correlated with still water depth. Douglas and Nistor (2015) performed a comparison of experimental and computational time series of water surface profiles for a dam-break wave with an upstream water depth of d_o = 0.85 m; they found that the initial run-up tongue reached its peak elevation at t = 1.9 s, and that it collapsed under the effect of gravity. In Sarjamee et al. (2017a), the time variations of bores' water surface profiles passing over a triangular obstacle were simulated using the OpenFoam software package, and the numerical results were compared with measurements. The results of the numerical simulation using the standard k-ε turbulence model agreed well with the experimental results, but the time series of the water surface downstream of the triangular obstacle was not in good agreement with the measurements.

The main objective of the present companion paper is to evaluate the performance of a three-dimensional transient Computational Fluid Dynamics (CFD) model (OpenFOAM, 2019) in simulating the propagation of a turbulent bore over a mitigation canal. The paper aims to evaluate the capability of the proposed numerical model to simulate such complex turbulent and transient flows and to select the most suitable turbulence model for accurate simulations. Model evaluation was achieved by comparing the time histories of water surface elevations and bore velocities, and the performance of three turbulence models was tested. After model validation, the numerical outputs were further analyzed to investigate the effect of canal depth on the wave characteristics and to understand the mitigation effects of a rectangular canal by comparing water surface elevations and velocities before and after the canal. The effects of the mitigation canal on variations in specific momentum and energy dissipation are studied in the second part of this companion paper. As shown in Figure 5.1., the tsunami wave propagated over a manmade canal with different angles of incidence against the tsunami wave. The effects of canal inclination on the energy dissipation of hydraulic bores are also presented in the second part of this companion paper.

5.2 Experimental Set-Up

Laboratory experiments were conducted in the Water Resources Laboratory at the University of Ottawa, Canada. A glass-walled tilting flume that was 15.56 m long, 0.38 m wide, and 0.60 m deep was used to perform the laboratory experiments. The schematic of the experimental setup and the coordinate system is shown in Figure 5.2. A false floor was made of several parallelepipeds (PVC, Canus Plastics Inc., Ottawa, ON, Canada) of different sizes to form a rectangular canal with

varying depths and widths. Two impoundment depths of d_o = 0.3 m and 0.4 m were set by installing a vertical gate (Plexiglas, Canus Plastics Inc., Ottawa, ON, Canada) located at 7.76 m downstream of the flume reservoir (see Figure 5.3a). The vertical gate was firmly fixed at the upstream end of the false floor such that water leakage would be minimized. The released impounded water generated a turbulent bore which propagated over the smooth horizontal bed. The generated bore interacted with the rectangular mitigation canal, which then continued to propagate to the end of the flume and then, through a drain, into the downstream reservoir. The canal width was constant (w = 0.60 m), and three depths of d = 0.05 m, 0.10 m, and 0.15 m were examined (see Table 5.1.).

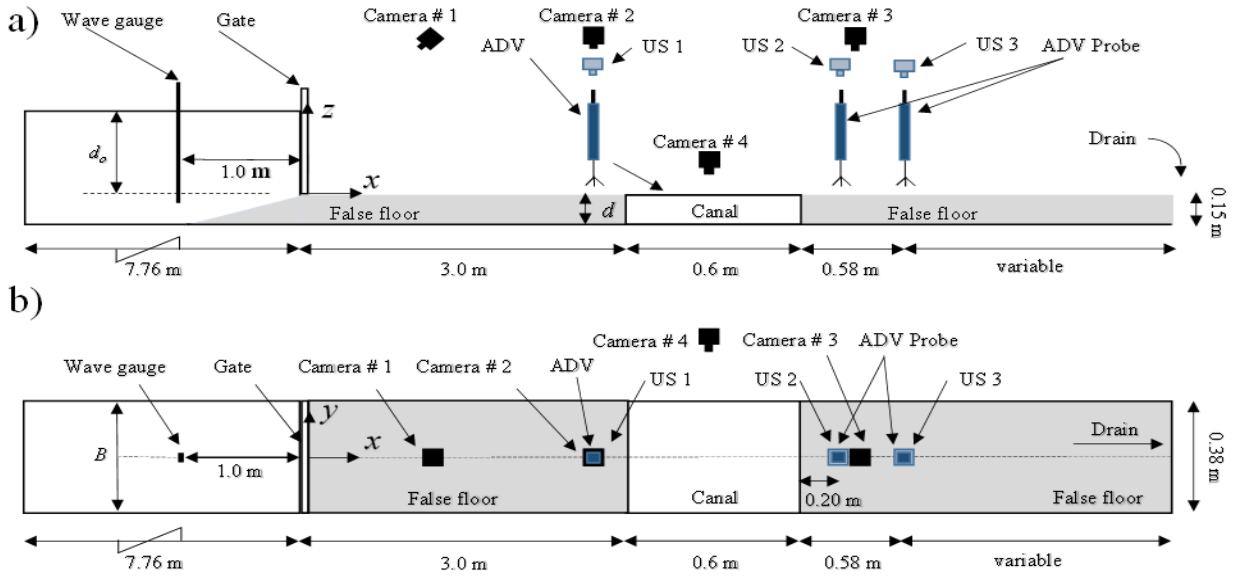

Figure 5.2. Schematic of experimental setup and coordinate system: (a) side view; (b) top view (not at scale).

Four wireless video cameras (GoPro, Hero5, SanMateo, CA, USA) were used to monitor the propagation of the bore front and the bore wave passing over the canal. The first camera was positioned on the side of the flume at the lengthwise half-way point of the canal in order to visualize the bore front and capture the bore profiles. The other three video cameras were positioned on top of the flume at different locations between the gate and the upstream end of the canal in order to monitor the motion of the bore front. A 1V:6H ramp (PVC, Canus Plastics Inc., Ottawa, ON, Canada) was installed at the upstream end of the false floor to reduce flow separation and local energy losses before the mitigation canal. The mitigation canal was located at 3.0 m downstream of the gate to ensure the formation of a fully developed hydraulic bore. The false floor was marked on the bed with parallel tape lines with a 0.05 m distance between each other (see Figure 5.3). The marked bed was used to measure the bore front velocity using a high-speed image-tracking technique (particle tracking velocity-based). Plastic beads with a diameter of 0.015 m were placed on the flume bed downstream of the gate. They moved as the lift gate was opened, and a GoPro camera with a shutter speed of 60 frames per second was positioned above the marked section to capture the propagation of the beads over a marked 0.60 m long section. The bore frontal velocity was measured by computing the travel distance of the beads between two adjacent parallel lines in two consecutive images.

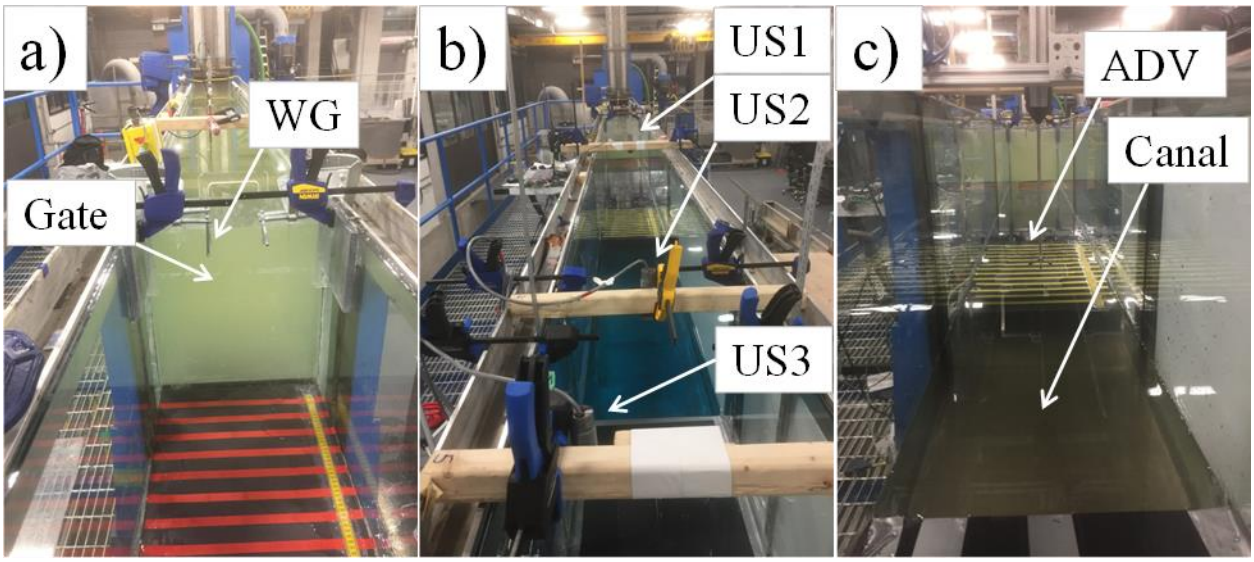

Figure 5.3. Laboratory experimental setup: a) upstream view of the flume and the vertical gate; b) positions of the ultrasonic depth sensors (US) in the flume; c) upstream view of the canal and the ADV probe.

Table 5.1. Parameters of the performed tests.

Test No.	Test name	d_o (m)	w (m)	d (m)	w/d
1	F-0.3	0.30	0	0	0
2	F-0.4	0.40	0	0	0
3	C-0.3-4	0.30	0.60	0.15	4
4	C-0.3-6	0.30	0.60	0.10	6
5	C-0.3-12	0.30	0.60	0.05	12
6	C-0.4-4	0.40	0.60	0.15	4

The volumes of water in the reservoir for the impoundment depths of d_o = 0.4 m and 0.3 m were 1.62 m^3 and 1.21 m^3, respectively. The equivalent aspect ratios of reservoir L/d_o for d_o = 0.4 m and 0.3 m were 26.61 and 35.47, respectively, both of which were considerably larger than the minimum reservoir aspect ratio (i.e., L/d_o = 11.05) suggested by Lauber and Hager (1998). To generate a fully developed dam-break wave, the lifting speed of the vertical gate was measured by a high-speed camera and compared with the maximum opening time. Lauber and Hager (1998) indicated that a dam-break wave would develop fully if the non-dimensional gate-opening time $T_o = t_o(g/d_o)^{1/2}$ was less than $2^{1/2}$, where t_o is the gate-opening time. Theoretically, the time required to open the gate is the time it takes for the topmost water particles to fall in order to produce a dynamic wave followed by a horizontal translational motion. In this study, the time to open the gate was monitored with a high-speed camera, and the measured non-dimensional gate-opening times were in the range of $0.70 < T_o < 0.825$.

Two wave gauge sensors were used to measure the time histories of the water surface levels. A capacitance-type wave gauge (model WG-50, manufactured by RBR Ottawa, Canada) was used

to measure the time history of the water level in the reservoir, with a sampling frequency of 1200 Hz. This capacitance-type wave gauge sensor was mounted 1 m upstream of the gate and was labeled as WG (see Figure 5.3a). Three ultrasonic wave gauge sensors (MASSA, M-5000/220, Hingham, MA, USA) were deployed upstream and downstream of the canal to measure the time series of the water surface, with a sampling frequency of 1200 Hz (see Figure 5.3b). An acoustic Doppler velocimeter (ADV) probe (Nortek-AS, Vangkroken, Rud, Norway) was used to measure the time histories of the velocity, with a sampling frequency of 200 Hz. The ADV probe measured the instantaneous velocity at z = 0.01 m above the surface of the false bed. The ultrasonic wave sensors were labelled as US, and the velocity sensors were labelled as ADV. Both the water surface levels and velocities were measured at the centerline of the flume and at 0.2 m upstream (US1/ADV1) and at 0.2 m (US2/ADV2) and 0.58 m (US3/ADV3) downstream of the canal (see Figure 5.3b). All the experimental runs were repeated three times to ensure the repeatability of the tests and to obtain averaged time-series data from the sensors.

5.3 Numerical Simulation

A two-phase (i.e., water and air), three-dimensional numerical model (OpenFOAM) v5.0 was used for the numerical simulations. Three types of turbulence models were analyzed in order to identify the most accurate numerical results. The open-source feature of OpenFOAM enables users to modify and expand the functionality of the solver package according to the requirements of their specific project. The Finite Volume Method (FVM) was used to model the hydraulic bore propagation over a smooth horizontal bed, and the InterFoam solver was used to solve the continuity, momentum (i.e., Navier-Stokes), and turbulence equations. The time-averaged form of the Navier–Stokes equations, known as the Reynolds-Averaged Navier–Stokes (RANS), was used in this study, and the turbulence closure equation was the well-known k-ε model with different modifications. The performances of the classic k-ε, Realizable k-ε, and Renormalization Group (RNG) k-ε turbulence models were examined to be able to select the most accurate numerical results.

The continuity equation in a cubic control volume was solved at each time step, and mass conservation was achieved by setting the net flow in the cubic control volume as (Sarjamee, 2016):

$$\frac{\partial \bar{u}}{\partial x} + \frac{\partial \bar{v}}{\partial y} + \frac{\partial \bar{w}}{\partial z} = 0 \qquad (5.1)$$

where $\bar{u}$, $\bar{v}$, and $\bar{w}$ are the components of the mean velocity in the x, y, and z directions, respectively. The instantaneous velocities were decomposed to the mean flow and velocity fluctuations as (Sarjamee, 2016):

$$u(t) = \bar{u} + u' \qquad v(t) = \bar{v} + v' \qquad w(t) = \bar{w} + w' \qquad (5.2)$$

where u', v', and w' are the velocity fluctuations in the x, y, and z directions, respectively. The momentum equation for a three-dimensional domain, known as a Navier-Stokes equation, can be expressed as follows (Versteeg and Malalasekera, 2007; Sarjamee, 2016):

$$\bar{u}\frac{\partial \bar{u}}{\partial x}+\bar{v}\frac{\partial \bar{u}}{\partial y}+\bar{w}\frac{\partial \bar{u}}{\partial z}=-\frac{1}{\rho}\frac{\partial \bar{p}}{\partial x}+g_x+\nu\left(\frac{\partial^2 \bar{u}}{\partial x^2}+\frac{\partial^2 \bar{u}}{\partial y^2}+\frac{\partial^2 \bar{u}}{\partial z^2}\right)-\left(\frac{\overline{\partial u'^2}}{\partial x}+\frac{\overline{\partial u'v'}}{\partial y}+\frac{\overline{\partial u'w'}}{\partial z}\right) \quad (5.3)$$

$$\bar{u}\frac{\partial \bar{v}}{\partial x}+\bar{v}\frac{\partial \bar{v}}{\partial y}+\bar{w}\frac{\partial \bar{v}}{\partial z}=-\frac{1}{\rho}\frac{\partial \bar{p}}{\partial y}+g_y+\nu\left(\frac{\partial^2 \bar{v}}{\partial x^2}+\frac{\partial^2 \bar{v}}{\partial y^2}+\frac{\partial^2 \bar{v}}{\partial z^2}\right)-\left(\frac{\overline{\partial v'^2}}{\partial y}+\frac{\overline{\partial u'v'}}{\partial x}+\frac{\overline{\partial v'w'}}{\partial z}\right) \quad (5.4)$$

$$\bar{u}\frac{\partial \bar{w}}{\partial x}+\bar{v}\frac{\partial \bar{w}}{\partial y}+\bar{w}\frac{\partial \bar{w}}{\partial z}=-\frac{1}{\rho}\frac{\partial \bar{p}}{\partial z}+g_z+\nu\left(\frac{\partial^2 \bar{w}}{\partial x^2}+\frac{\partial^2 \bar{w}}{\partial y^2}+\frac{\partial^2 \bar{w}}{\partial z^2}\right)-\left(\frac{\overline{\partial w'^2}}{\partial z}+\frac{\overline{\partial w'v'}}{\partial y}+\frac{\overline{\partial u'w'}}{\partial x}\right) \quad (5.5)$$

where t is the time, p is the fluid pressure, g is the gravitational acceleration, and ρ is the fluid density. A phase fraction equation is required to model the spatial distribution of two different fluids (i.e., air and water) at any particular time step. The phase fraction α is a scalar quantity, which is one for water and zero for air. The value of the phase fraction determines the transitional region. The phase fraction α parameter is a conserved quantity and can be described by the transport equation as follows (Heyns, et al. 2013):

$$\frac{\partial \alpha}{\partial t}+\nabla.(U\alpha)=0 \quad (5.6)$$

where $\nabla.$ is the divergence, and U is the velocity vector. The density of the air–water mixture in the water surface cells can be calculated as (Heyns, et al. 2013):

$$\rho = \rho_a(1-\alpha)+\rho_w\alpha \quad (5.7)$$

The Navier–Stokes equations can predict the motion of a fluid. Regarding the technique that the user needs to deal with turbulent fluctuations in the flow, OpenFOAM provides various techniques. These equations are stated in Cartesian coordinates and tensor notation while disregarding body forces. Thus, the RANS conservation equations of the mass and momentum of an incompressible fluid are shown in (Ferziger and Peric´ 2002). It is impossible to answer the momentum and continuity equations analytically, except for a very few straightforward conditions. To close the equations, a novel idea of turbulent viscosity was developed by Boussinesq, and the Reynolds stresses can be numerically defined by time-averaging the flow equations (Ferziger and Peric´ 2002).

All the parameters inside the flume domain (except for the canal and the reservoir), such as water depth, phase fraction, pressure, velocity, and force, had an initial value of zero. The phase fractions for the canal and the reservoir were equal to 1, indicating that those domains were filled with water.

Parallel processing is a computing technique in which discrete elements of a complex task are divided up and run simultaneously on multiple cores, thereby decreasing the time for processing. Each task is divided and assigned to a different core, and is typically performed with the assistance of parallel processing software tools implemented in OpenFOAM, which will also work to collect and read the data after each core has completed its particular task. In our numerical simulations, a Dell computer (1TB HD, 16GB RAM, Processor i7-6700 CPU @3.40GHz, System type 64bit, Video card 4G, Quad Cores) was used to accomplish this process. The multiple cores in a computer that is running in parallel is referred to as parallel processing. The *decomposePar* utility is used to decompose the mesh and fields. The fundamental idea is to split up the domain with minimal effort

but in a way that ensures a cost-effective solution. The fields and geometry are split up based on settings defined in the *decomposeParDict* dictionary, which must be found in the *system* directory of the case of interest. If the operator requires one, an example *decomposeParDict* dictionary is obtainable from the *interFoam / damBreak* tutorial (OpenFOAM, 2021). The numerical simulation can be run in one core but it runs more easily in four cores (1 simulation each in 4 cores). The mesh is decomposed using a certain dictionary in the *system* which is called *decomposeParDict*. The *simple* method is used to run four cores in parallel simulations, dividing them twice in the *x*-direction and twice in the *y*-direction with an equal number of cells in each core and a low number of faces between the cores.

Mesh independence is usually achieved by repeating a simulation with increasing mesh qualities until the results converge to a constant solution which will remain nearly the same even with increased mesh resolution. If the solution changes as the mesh is refined, a mesh-independent solution has not been reached, and the mesh should continue to be refined and the procedure repeated until a solution that is independent of the mesh is achieved. Mesh-independent results must be achieved in order to estimate how reliant the results are on the mesh that was produced. The mesh was at first refined over the complete computational domain of the flume and then locally around a specific location of interest, such as the location of ultrasonic sensors. Local mesh independence around a specific location of interest is more commonly performed than mesh independence over the complete computational domain owing to the prohibitive cost connected with complete mesh independence. In our numerical simulation, the cell size was gradually reduced from the upstream end towards the downstream end of the flume at the location of the ultrasonic sensors.

The higher mesh resolution was carefully chosen downstream of the gate, particularly around the canal, as more accurate results are needed at the locations of the ADVs and USs. As a result, the resolution is more refined downstream of the gate in order to perceive the surge turbulence effects more accurately. A study of the numerical results with various mesh resolutions revealed that a domain with a cell size of 10 mm x 10 mm x 10 mm accurately duplicated the experimental results. The overall numerical results are based on the standard k-ε model, as it provided the most accurate results during the simulation of the original canals. The time step is established at the start of the temporal simulation, but describing the time step is a difficult issue that requires a trade-off between obtaining precise findings and a long computational time by using shorter and longer time steps, respectively. The time step in OpenFOAM software is dynamic in order to ensure that the highest Courant number does not exceed 1.0, and it was always on the order of thousandths of a second for all of our simulations (0.006 s). The smaller the Courant number, the better; if it remains below 1.0, the mesh and time step are considered stable to allow the simulation converges.

Since the gate-opening was reasonably quick in the formerly explained laboratory experiments, the sudden dam-break criteria as stated by Lauber and Hager (1998) were considered to be perfect. This computational domain accurately replicated the measurements of the physical experiments. There was no downstream wall to permit the fluid particles to depart the computational domain after they arrived at the end of the flume, and the influence of the floor drain in the laboratory experiment setup was properly replicated. The threshold for the gate opening was instantaneous in

OpenFOAM software as soon as the numerical simulation started, and proper readings were observed from the terminal software. Thus, the water was assumed to be released instantly in the numerical simulations for simplicity, and no gates were modeled. The gate was opened once the simulation started, as there was no special configuration such as moving mesh to describe the gate opening.

Figure 5.4a shows the computational domain for the water surface profile upstream of the gate and inside the canal. The simulated flume dimensions and water level at the beginning of the test at $t = 0$ are also shown in this figure. The length of the upstream reservoir is exactly half of the overall flume length. The desired upstream impoundment depth and the amount of water in the canal were established by setting a different initial phase fraction than for the rest of the flume. Figures 5.4b and 5.4c show the mesh resolution in the upstream reservoir and in the canal. The mesh size for all directions was set to 10 mm, and the number of mesh layers was controlled by the impoundment and canal depths. Figures 5.4d and 5.4e display the three-dimensional water surface profiles of the turbulent bore front and its interaction with the canal at $t_* = 0.25$ s and 0.50 s after the bore front plunged into the canal; $t_* = 0$ is when the bore reaches the upstream edge of the canal. At $t_* = 0.25$ s, a deep plunge and water surface rolling were observed as a result of a heavy shear layer formation. A surface jump started to occur at $t_* = 0.50$ s, and then, over time, the water depth in the canal increased.

All boundary conditions were set as “wall boundary with no-slip”, except for the wall located downstream of the flume, on which an “outlet with a zero gradient” was imposed. This latter outlet boundary condition permitted water to exit from the computational domain. A systematic mesh independence analysis was performed, similar to those in the studies by Azimi et al. (2011, 2012). A comparison of the numerical outcomes using different mesh resolutions indicated that a domain with a cell size of 10 mm × 10 mm × 10 mm replicated the experimental results with a reasonable accuracy, with a root mean square error (RMSE) of less than 6.7% and a relative error of less than 8.4%.

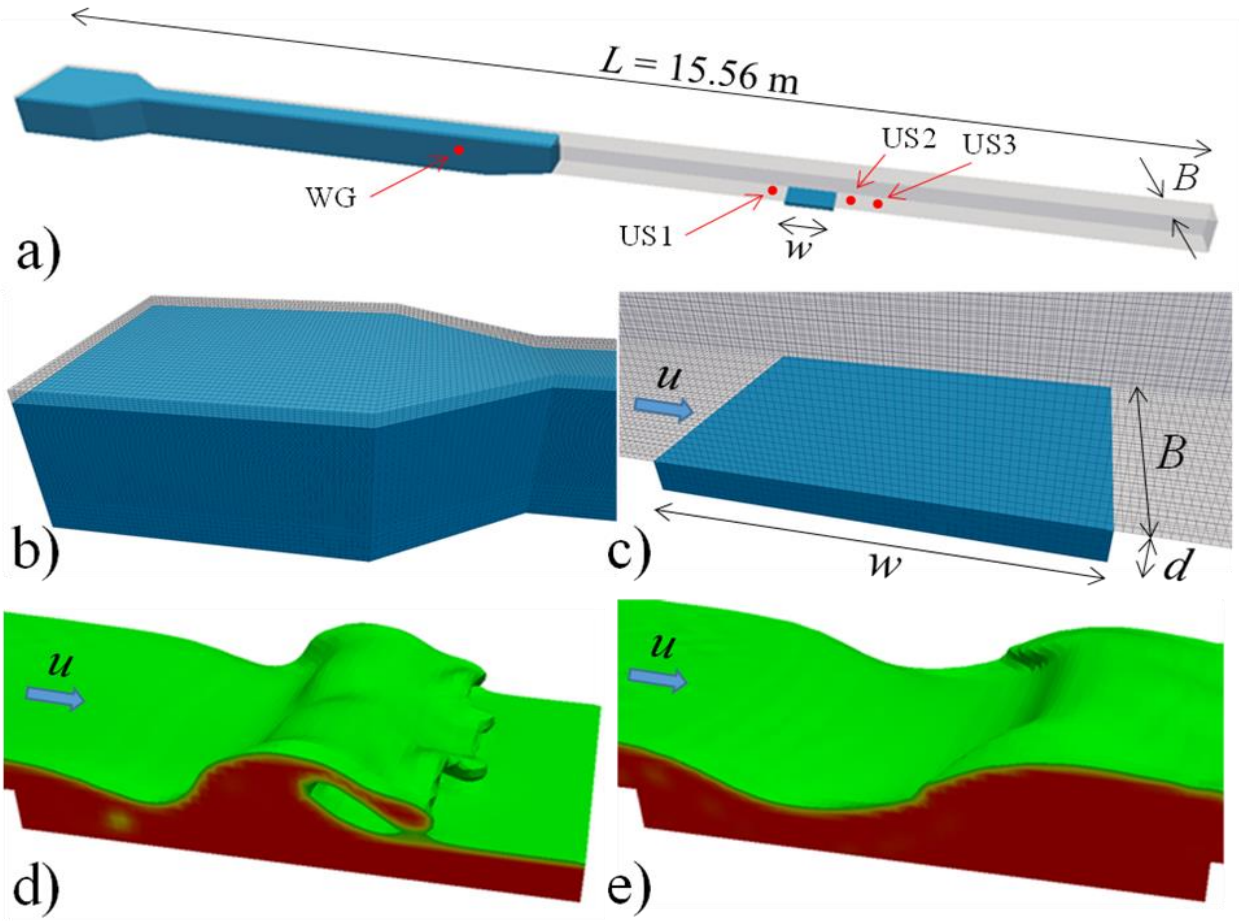

Figure 5.4. Computational domain and three-dimensional water surface profile: a) computational domain of the full channel; b) mesh resolution of the reservoir in the initial condition; c) mesh resolution in the canal; d) three-dimensional water surface profile at t_*= 0.25 s; e) three-dimensional water surface profile at t_*= 0.5 s. t_* is the time when the bore front reaches the canal.

5.4 Results

5.4.1 Model Validation

The time histories of the water surface levels and velocities at four locations: 1.0 m upstream of the gate, 0.2 m upstream of the canal, and 0.2 m and 0.58 m downstream of the canal, were extracted from the numerical models, and the results were compared with the measurements. Model validations were performed in both the absence and presence of a rectangular canal and for an impoundment depth of d_o = 0.4 m. The canal dimensions for model validation were w = 0.6 m and d = 0.15 m. Figure 5.5. shows the comparison of the simulated time histories of water surface profiles with the experimental results. The subplots in the left column show the time histories of the water depth in the absence of a canal, while the subplots in the right column show the same variables in the presence of a rectangular canal. Sensitivity analyses have been conducted in previous studies to select a proper turbulence model (Sarjamee et al., 2017a, 2017b; Asadollahi et al., 2019a, 2019b), and in order to improve simulation accuracy, three k-ε-based turbulence models (i.e., classic k-ε, Realizable k-ε, and RNG k-ε) were implemented.

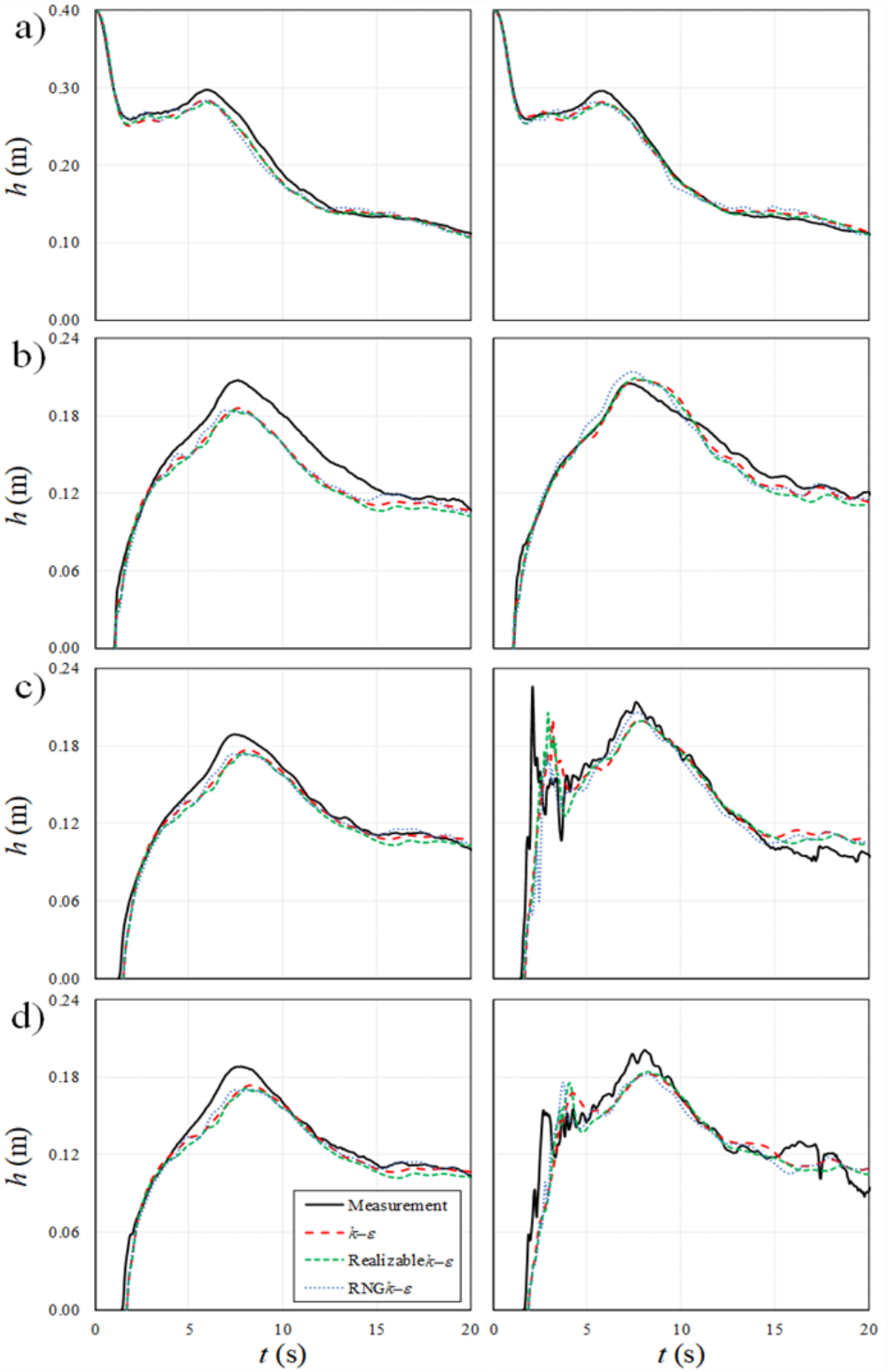

Figure 5.5. Effect of different turbulence models on the prediction of the time history of the water surface profiles, and comparisons of numerical results with laboratory measurements for d_o = 0.4 m. Left column shows the time history of the water surface profiles over the horizontal bed section, while the right column shows the time history of the water surface profiles over a rectangular canal (w = 0.6 m, d = 0.15 m): a) WG; b) US1; c) US2; d) US3.

Figure 5.5a shows the performance of the numerical model at 1.0 m upstream of the gate; the numerical results were compared with the measurements from the capacitance-type wave gauge (WG). As it can be seen, the turbulent bore height peaked and then gradually decreased over time. For the water surface profiles of the bore propagating over the horizontal surface, the maximum simulated water level was approximately 4% less than the measured peak water depth. The experimental and numerical results for the maximum bore heights measured at 1.0 m upstream of the gate and without a canal were 0.30 m and 0.28 m, respectively. The peak water levels occurred at approximately the same time (i.e., t = 5.9 s) for both laboratory experiments and numerical simulations. For the water surface profiles when propagating over the canal, the peak water elevation was about 5% smaller than the measured peak water depth. The experimental and numerical results for the maximum bore heights at 1.0 m upstream of the gate and in presence of a canal were 0.30 m and 0.28 m, respectively. For the water surface profiles over the horizontal bed, a small discrepancy was found between the experimental and numerical results for 5 s $\leq t <$ 13 s. For 13 s $\leq t <$ 17 s, the bore became almost similar to a quasi-steady flow. The bore height linearly decreased with time for the water surface profiles over a horizontal surface and over the rectangular canal for $t \geq$ 17 s. The results revealed that all three turbulence models were able to simulate the experiments at the position of the WG.

The time series of water surface profiles at 0.2 m upstream of the canal (US1) are shown in Figure 5.5b. As it can be seen, in the absence of a canal, the maximum simulated water surface profile was approximately 10% lower than that measured. The water surface profile rose steadily from zero, reached its peak, and then declined over time. The maximum measured and simulated water levels at this location were 0.21 m and 0.19 m, respectively. In the presence of the canal, the measured and simulated peak water depths were the same, with a value of 0.21 m. The times to reach the peak water depth in the absence and presence of a canal were 7.7 s and 7.8 s, respectively. For $t \geq$ 15 s, the water surface profiles in the absence and presence of a rectangular canal became similar to a quasi-steady state profile. At this location, the three turbulence models provided approximately the same water surface profiles.

Figure 5.5c displays the temporal variations in the water surface levels at 0.2 m downstream of the canal (US2). The maximum simulated water depths for both cases with and without a canal were 6% smaller than those measured. The maximum experimental and numerical water depths in the absence of a canal were 0.19 m and 0.18 m, respectively. However, in the presence of a canal, the water depths were 0.21 m and 0.20 m, respectively. In addition, the times to reach the peak water depth without and with the canal were t = 8.0 s and 7.8 s, respectively. The slight difference in the simulations of peak water depth after the canal may be attributed to air entrainment and bubble formation in the canal. The entrained bubbles were formed by the bore plunging into the canal. The time histories of the bore height at 0.58 m downstream of the gate (US3) are shown in Figure 5.5d. It was observed that the simulated water surfaces in the absence of a canal were 7% smaller than those measured, but the times to reach the peak were similar, with a value of t = 8.2 s. In the presence of the canal, the simulated peak water depth was 9% smaller than that measured. The performance of the standard k-ε model in reproducing this element was slightly better than that of the other turbulence models (see Table 5.2.).

Table 5.2. Percentage error values of the compared numerical results versus laboratory measurements of the maximum water surface levels and velocities.

Parameter	Location	In the absence of the canal (%)	In the presence of the canal (%)
WSL	WG	4	5
	US1	10	1
	US2	6	6
	US3	7	9
Velocity	ADV1	9.5	20
	ADV2	11	1
	ADV3	11.5	17

The time series of the water velocities of the bore generated by an impoundment depth of d_o = 0.4 m were extracted from the numerical model results for both the absence and presence of the rectangular canal (w = 0.6 m, d = 0.15 m). The simulated bore velocity profiles were compared with measurements at three different positions: ADV1, ADV2, and ADV3 (see Figure 5.6). Comparison of the numerical outcomes with the measurements indicated that the simulated time histories of the water velocities were overestimated compared to the measurements. As shown in Figure 5.6, the bore front in the horizontal bed tests reached the canal earlier than the front identified by the measurements, whereas in the presence of a canal, the simulated bore front velocities were similar to those from the measurements.

Figure 5.6a shows the time histories of the bore velocities in the absence and in the presence of a canal at 0.20 m upstream of the canal (ADV1). For the bore velocity profiles over a horizontal bed without a canal, the maximum measured peak bore velocity was approximately 9.5% lower than the simulated peak bore velocity. The measured and simulated peak bore velocities in the horizontal bed tests were 2.19 m/s and 2.42 m/s, respectively. For the bore velocity profiles over a canal, the maximum measured bore velocity was approximately 20% less than that from the simulation results. The measured and simulated bore velocities in the presence of a canal were 1.93 m/s and 2.41 m/s, respectively. Figure 5.6b shows the temporal variations of the bore velocity profiles at 0.20 m downstream of the canal (ADV2). In the absence of a canal, the peak measured bore velocity was 11% smaller than the simulated ones; however, the maximum measured and simulated bore velocities were approximately the same over the canal surface. In the absence of a canal, the experimental and numerical bore velocities at 0.20 m downstream of the canal (ADV2) were 1.99 m/s and 2.24 m/s, respectively. In the presence of a canal, the experimental and numerical bore velocities were 1.47 m/s and 1.49 m/s, respectively.

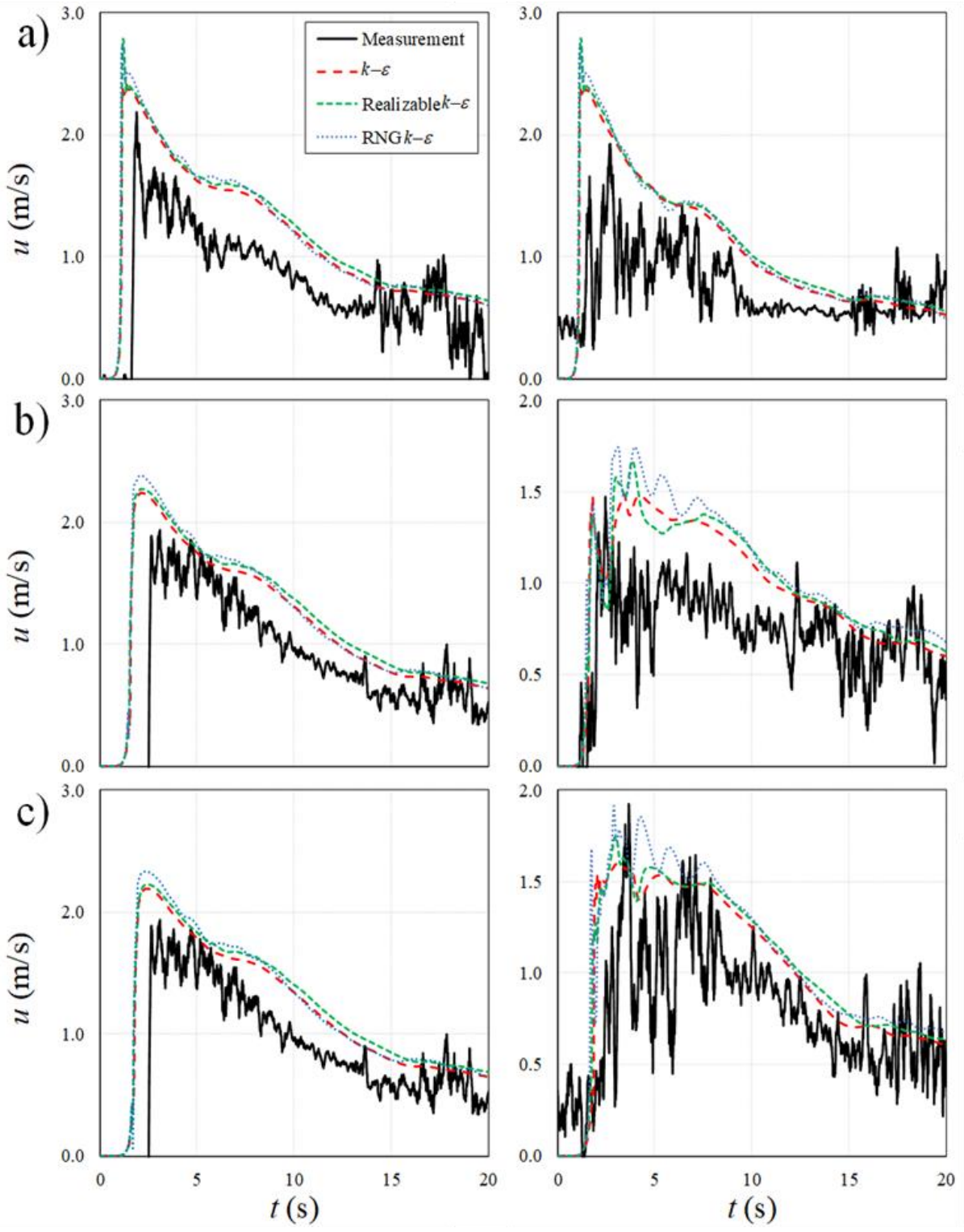

Figure 5.6. Effect of different turbulence models on the prediction of bore velocity profiles, and comparisons of the numerical results with laboratory measurements for d_o = 0.4 m. Left column shows the bore velocity profiles over a horizontal surface, and right column shows the bore velocity profiles over a rectangular canal (w = 0.6 m, d = 0.15 m): a) ADV1; b) ADV2; c) ADV3.

The time series of the bore velocities at 0.58 m downstream of the canal (ADV3) are shown in Figure 5.6c. It was observed that the maximum measured bore velocity in the absence of a canal was lower than the simulated velocity by 11.5%, with values of 2.19 m/s and 1.94 m/s, respectively. In contrast, in the presence of a canal, the maximum measured bore velocity was higher than the simulated peak velocity by 17%, with values of 1.92 m/s and 1.60 m/s, respectively. However, the inaccuracy in predicting the commencement of the bore and the maximum bore velocity still appeared in the horizontal bed tests, as shown in Figures 5.6b and 5.6c (see Table 5.2).

The underestimation of the velocity measurements obtained with the ADV probe is due to the fact that ADV data tend to be affected by the high turbulence. The high turbulence can occasionally generate cavitation around the tip of the AVD, which induces unwanted noise in the signal, thus influencing the results. The effect of the high turbulence on the ADV recording can be observed indirectly since the time histories of the experimentally measured and the calculated bore velocities are almost the same after about 15 s, when flow turbulence reduces significantly. Overall, the accuracy of the time histories of the measured bore velocity results is highly dependent on the precision of the ADV probe.

The water surface elevation profiles from the numerical and laboratory measurements results were compared to the analytical solutions from Ritter (1892) for a frictionless bed and Chanson (2006) for a bed with friction. Figure 5.7. shows the dimensionless water surface elevation profiles over a horizontal surface without the presence of a canal at US1, US2, and US3 as a function of time. The effect of bed friction was prominent in the early stages of the flow. According to Chanson (2006), flow resistance caused a drop in flow velocity as well as a rise in wave steepness and water surface elevation over the surge front. In this study, a quick increase in the water surface elevation ($H = h/d_o$) at the wave tip region can be perceived in Figure 5.7. This quick increase shows a sharper wave front produced by bed friction and increased flow resistance caused by the thin water layer (Chanson, 2006). After the passage of the surge front (wave tip region), the water surface elevation profiles from the numerical and laboratory measurements closely followed the water depth profiles calculated by Chanson (2006). In contrast, a small discrepancy was found between the water surface elevation profiles from the experimental and numerical results for the entire non-dimensional time ($T = t\times\sqrt{(g/d_o)}$ in comparison with the corresponding ones calculated by Ritter (1892).

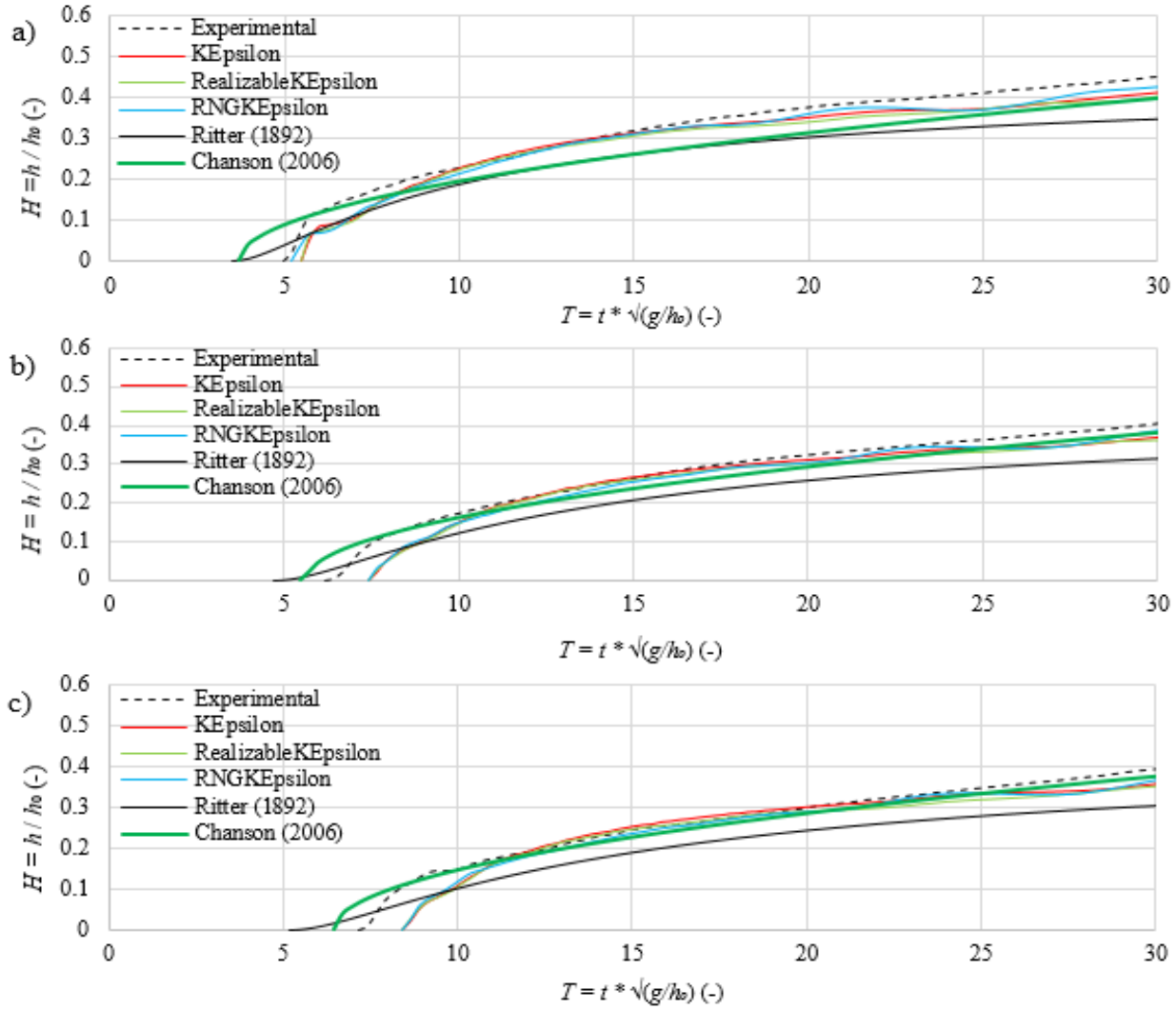

Figure 5.7. Normalized water surface elevation profiles for the three ultrasonic wave gauges: (a) US1 0.20 m upstream, (b) US2 0.20 m, and (c) US3 0.58 m downstream of the canal. Experimental and three numerical profiles are compared to the analytical solutions by Ritter (1892) and Chanson (2006).

The influence of bed roughness on the time histories of the water surface elevation profiles was investigated using sensitivity analysis. The original roughness height and roughness constant were set to 0.002 m and 0.7, respectively. In the rougher model, the height of the roughness was increased to 0.003 m, and the outcomes of the model with increased roughness were compared to the outcomes of a model with 0.002 m original roughness height. The outcomes reflect that increasing the bed roughness from 0.002 m to 0.003 m caused almost no change to the water surface elevation profiles and maximum magnitudes, which were nearly identical to those for the original roughness, showing that the roughness does not significantly affect the water surface elevation magnitude. The flow velocity over the 0.003 m bed was slightly smaller compared to the 0.002 m rough bed. Thus, increasing the bed roughness height does not seem to affect the flow velocity and water surface elevation profile magnitudes because of the flow in a fully turbulent regime.

5.4.2 Water Surface Variations with Time

Figure 5.8a shows a series of consecutive images of water surface profiles as the bore propagates over a canal with a depth of d = 0.05 m.

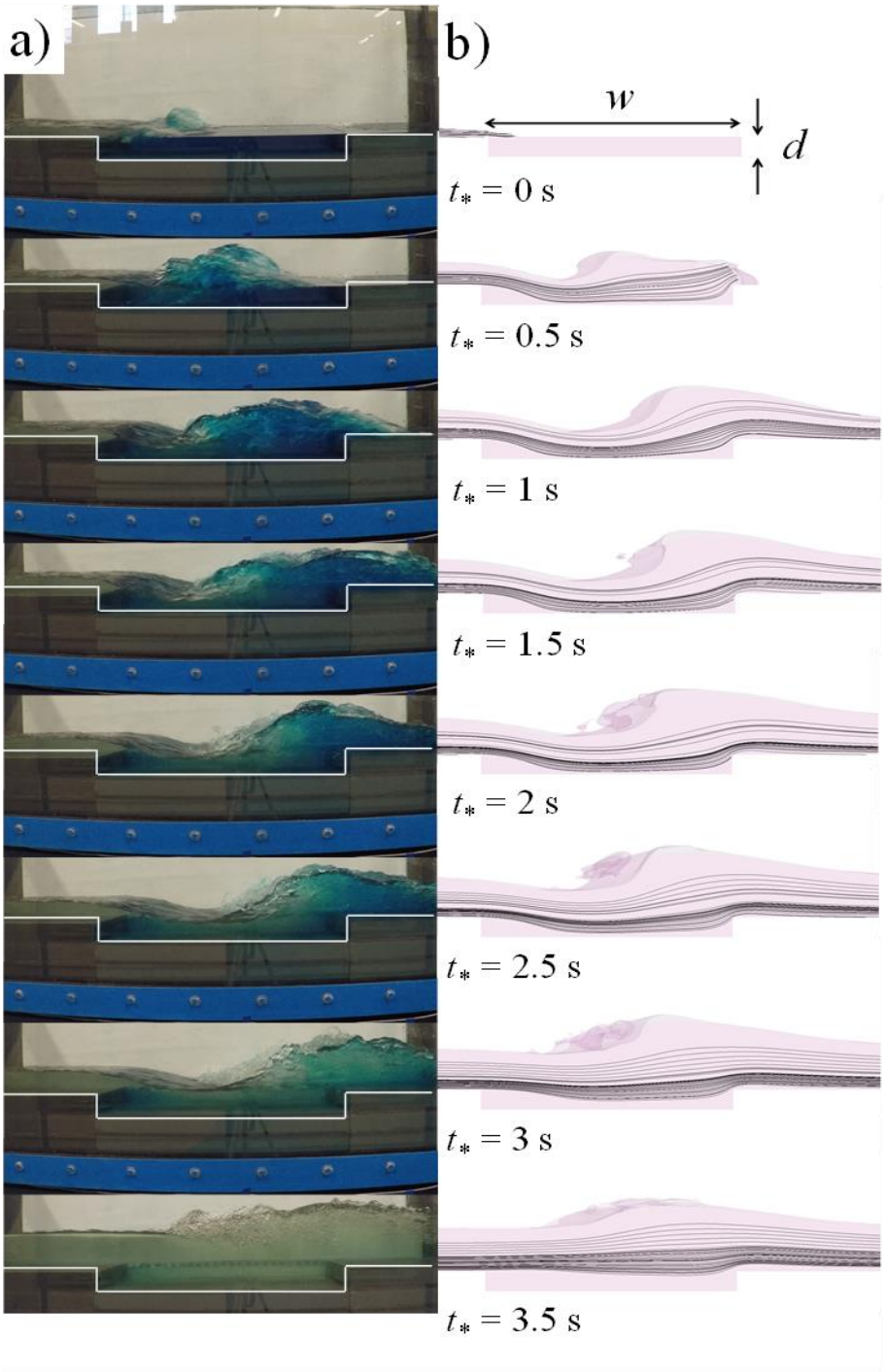

Figure 5.8. Time history of water surface profiles of a bore from an impoundment with a depth of d_o = 0.3 m, passing over a canal with a width of w = 0.6 m and a depth of d = 0.05 m: a) side-view images; b) simulated water surface profile and streamlines.

Blue dye was added to the stationary water in the canal for a better visualization of the bore arrival and mixing. Once the bore front reached the upstream edge of the canal, a sequence of ripples formed on the surface of the bore as it travelled over the canal. At $t_* = 0.50$ s, the bore front plunged into the canal and initiated a surface hydraulic jump. The bore height was amplified due to a substantial increase, and a surface hydraulic jump formed in the middle of the canal. After a short period of time, at $t_* = 1.0$ s, the bore height increased again and reached the downstream edge of the canal. At $t_* = 1.5$ s, the bore front expended some of its momentum into the stagnant water in the canal, displacing the water in the canal and causing it to peak. A strong shear layer formed due to the existence of a quasi-steady flow in the upstream of the canal, and as a result, a strong surface jump formed at the downstream end of the canal, at $2 \text{ s} \leq t_* \leq 2.5$ s. At this stage, the water surface level increased with time and reached its maximum value at $3 \text{ s} \leq t_* \leq 3.5$ s. For $t_* > 3.5$ s, a rapid change in the water surface profile occurred, flattening the water surface profile.

This bore–canal interaction suppressed the energy of the bore. As such, one could use such canals to protect coastal or near-shore infrastructure against tsunami inundation hazards. The simulated three-dimensional water surface profiles and streamlines observed when the bore passed over the canal were extracted from validated numerical models. Figure 5.8b shows consecutive images of the simulated water surface profiles, starting from $t_* = 0$ s and with a time interval of 0.5 s. A comparison of the experimental water surface profiles obtained from video images and those from the numerical simulations indicated very good agreement. At $t_* = 0$ s, the simulated water surface profile and streamlines reached the upstream edge of the canal. At $t_* = 0.5$ s, the measured bore front reached the downstream edge of the canal, whereas the simulated streamlines reached the canal bottom at a distance of approximately 0.17 m from the upstream edge of the canal. At $t_* = 1.0$ s, the bore propagated further downstream of the canal, but no change was observed in the spreading of the simulated bore front. The measured and simulated bores showed a similar trend in water surface level for $1.5 \text{ s} \leq t_* \leq 2.0$ s. The simulated turbulent bores continuously affected the volume of water observed in the sector of the canal for $0.5 \text{ s} \leq t_* \leq 3.5$ s.

Analogous to simulations of a hydraulic bore passing over a shallow canal with a depth of $d = 0.05$ m, the time histories of the water surface profiles and flow streamlines passing over medium-depth and deep canals with depths of $d = 0.10$ m and $d = 0.15$ m, respectively, are shown in Figures 5.9 and 5.10. As can be seen in Figure 5.9, the simulated turbulent bore passing over a medium-depth canal with a depth of $d = 0.10$ m reached the canal end at $t_* = 0.5$ s, while the toe of the surface jump was located at approximately 0.28 m from the upstream edge of the canal. At the bottom of the canal, the simulated streamlines slowly rose at time at $t_* = 1.0$ s. The time histories of the water surface profiles and streamlines passing over the deep canal with a depth of $d = 0.15$ m are shown in Figure 5.10. These simulated streamlines did not reach the bottom of the canal during the passage of the turbulent bore. The simulated streamlines near the canal bottom gradually rose with time at $t_* = 1.0$ s.

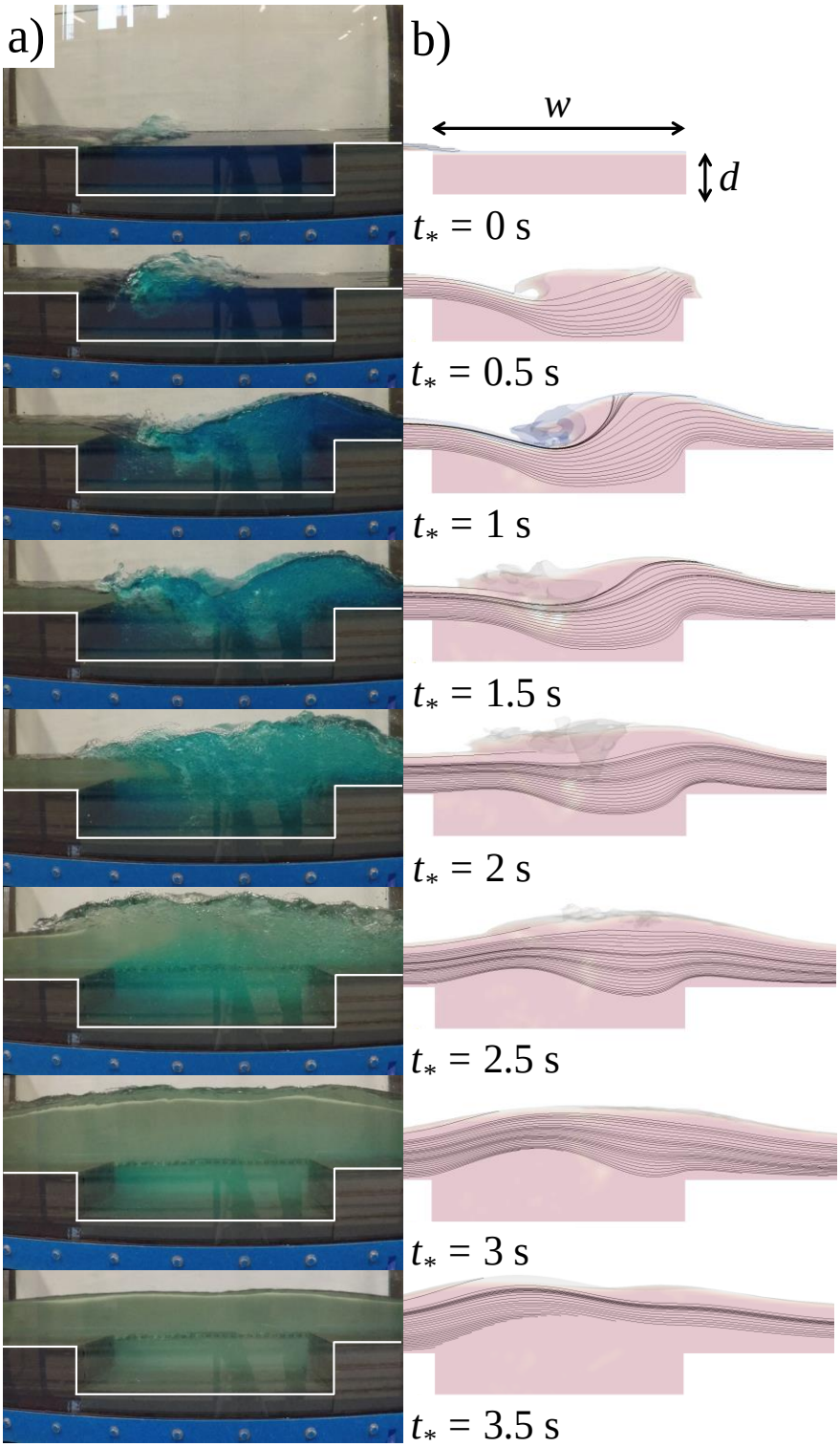

Figure 5.9. Time history of water surface profiles of a bore from an impoundment with a depth of d_o = 0.3 m, passing over a canal with a width of w = 0.6 m and a depth of d = 0.10 m: a) side-view images; b) simulated water surface profile and streamlines.

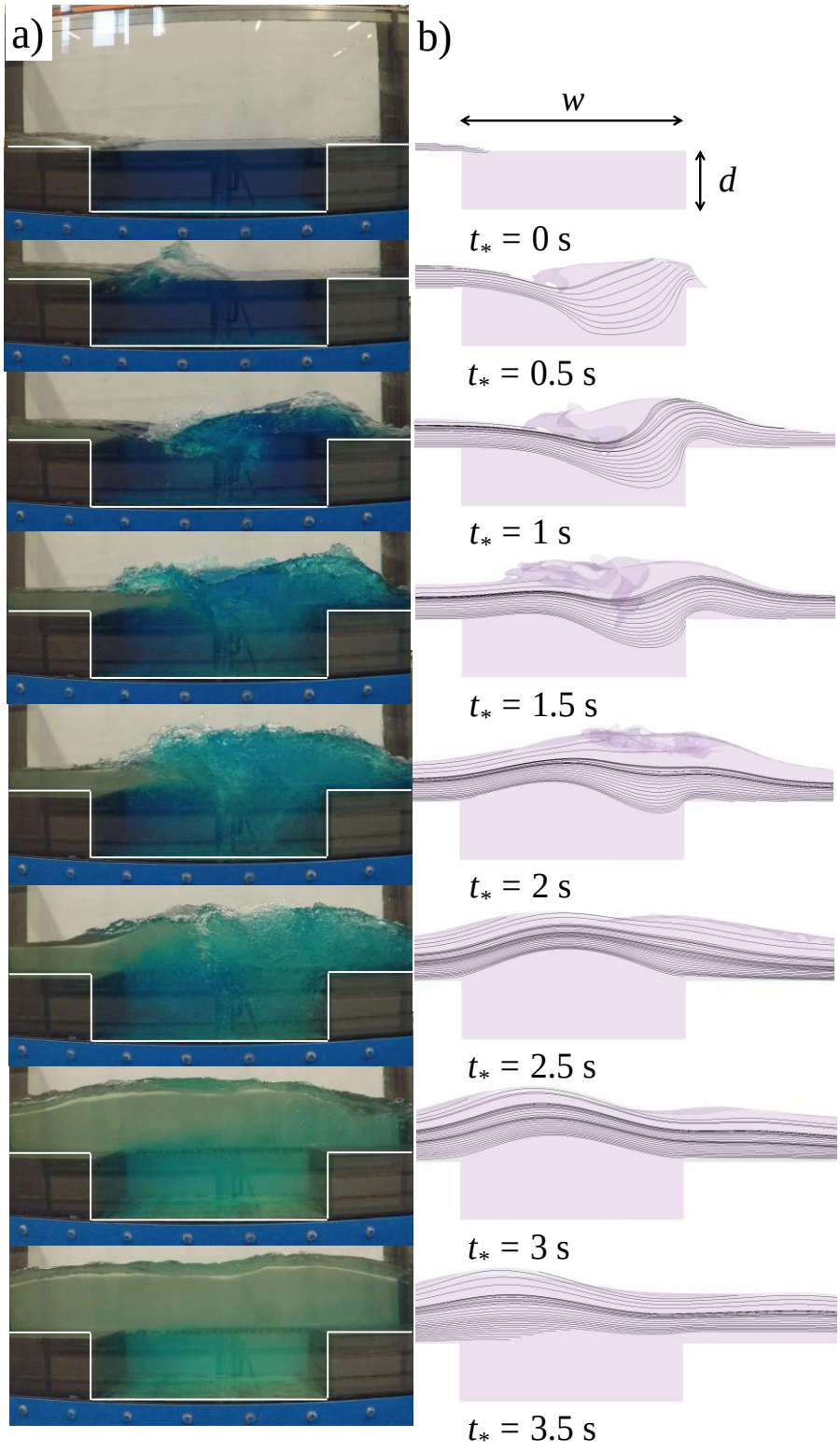

Figure 5.10. Time history of water surface profiles of a bore from an impoundment with a depth of d_o = 0.3 m, passing over a canal with a width of w = 0.6 m and a depth of d = 0.15 m: a) side-view images; b) simulated water surface profile and streamlines.

5.4.3 Velocity Fields

The time-history contour plots of the velocities of hydraulic bores passing over the mitigation canal were extracted from the validated numerical models in order to study the effect of canal depth on the hydrodynamics of a turbulent bore and its interaction with the canal. Figure 5.11. shows the time histories of the contour plots of the bore velocity and the velocity vector field of a turbulent bore, generated using an impoundment with a depth of d_o = 0.3 m, passing over a rectangular canal (w = 0.6 m, d = 0.05 m). It can be seen that the red area of the maximum bore velocity (i.e., $u \geq$ 1.5 m/s) decreases over time, indicating a significant momentum transfer due to the presence of the canal. The region of maximum bore velocity (i.e., $u \geq$ 1.5 m/s) did not reach the downstream end of the canal, indicating that the canal length is long enough to deflect the bore jet stream towards the bottom of the canal. At t_* = 0 s, the bore front reached the upstream of the canal, and the peak velocity jet stream reached the half-way point of the canal at t_* = 0.5 s. The maximum length of the jet stream occurred at a t_* between 1 s and 2.5 s. The eye of the vortex field formed in the vicinity of the upstream edge of the canal under the red area of the maximum bore velocity (i.e., $u \geq$ 1.5 m/s), as shown by the yellow spot in Figure 5.11. The vortex eye was formed 0.05 m from the upstream wall of the canal and moved slowly downstream as the bore passed over the canal. At t_* = 1.5 s, the maximum bore velocity reached the longest distance of 0.45 m from the upstream edge of the canal. Once the turbulent bore front passed the canal, the bore energy decreased, and the bore jet stream decayed. As a result, the peak velocity jet stream retreated back to the first half of the canal. The upward deflection of the peak velocity jet stream at t_* = 3.5 s increased the recirculation zone in the upstream edge of the canal and gradually moved the eye of the vortex upward, from 0.05 m to 0.12 m. Tidal currents usually generate river bores. Similar flows can be generated in controlled environments such as wave flumes. A number of experimental investigations have been conducted to determine some of the main features of hydraulic bores. The relatively slight discrepancy in the experiments could be partially attributed to the vorticity generated by the discharge method used to produce the undular bore. Vorticity, in particular, is a main factor which influenced the constant discharge bores. Some authors have suggested that bottom friction influences the emergence of an undular bore. If the conditions are suitable, a nearly constant profile of undulations can be observed in a river bore (Shugan et al., 2020; Vargas-Magaña et al., 2021; El et al., 2005; Amaechi et al., 2021; Hatland and Kalisch, 2019; El et al., 2005; El et al., 2005).

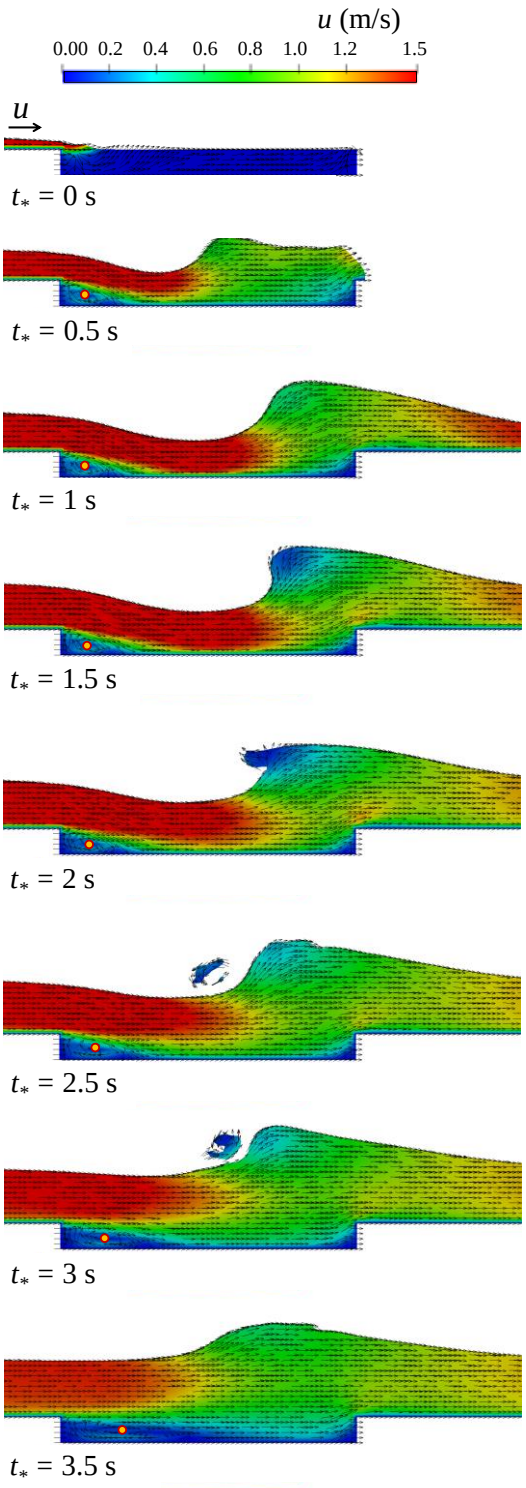

Figure 5.11. Variations of the contour plots of velocity and velocity vector fields with time, for a bore from an impoundment with a depth of d_o = 0.3 m, passing over a canal with a width of w = 0.6 m and a depth of d = 0.05 m. The dots in the contour plots show the eye of the vortex.

The contour plots of the bore velocities and velocity vector fields for turbulent bores with an impoundment depth of d_o = 0.3 m, passing over a medium-depth canal (d = 0.10 m) and a deep canal (d = 0.15 m), are shown in Figures 5.12. and 5.13, respectively.

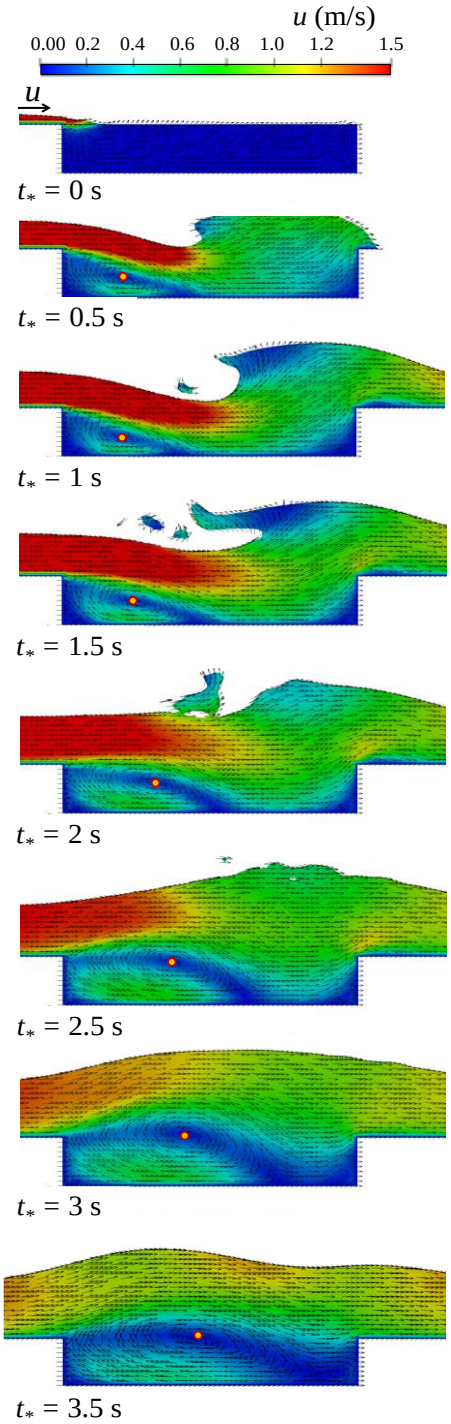

Figure 5.12. Variations of the contour plots of velocity and velocity vector fields with time, for a bore from an impoundment with a depth of d_o = 0.3 m, passing over a canal with a width of w = 0.6 m and a depth of d = 0.10 m. The dots in the contour plots show the eye of the vortex.

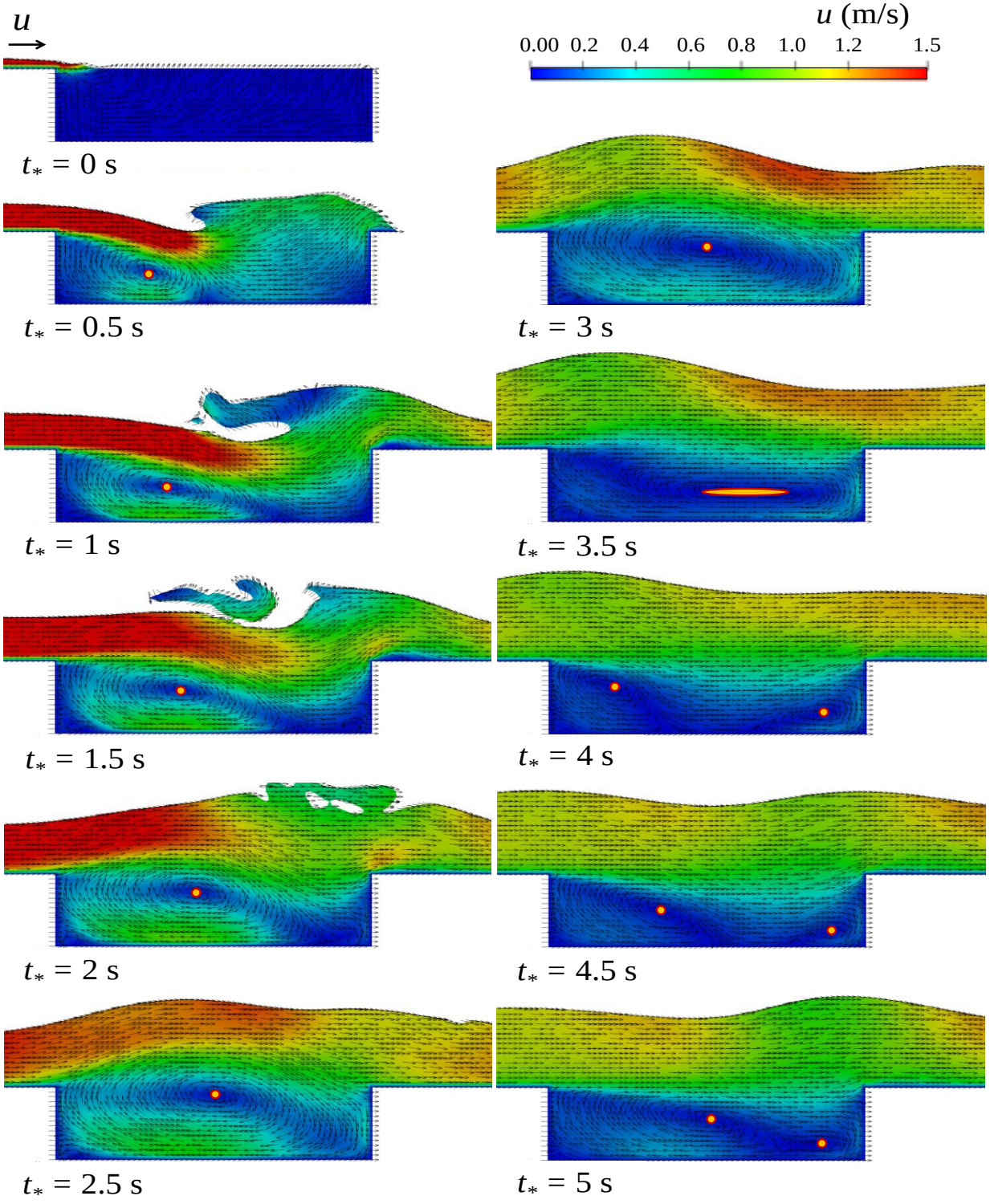

Figure 5.13. Variations of the contour plots of velocity and velocity vector fields with time, for a bore from an impoundment with a depth of d_o = 0.3 m, passing over a canal with a width of w = 0.6 m and a depth of d = 0.15 m. The dots in the contour plots show the eye of the vortex.

Similar to Figure 5.11, the maximum bore velocity was indexed at a velocity range of $u \geq 1.5$ m/s. As can be seen, the jet stream of the peak velocity plunged downward into the canal and reached the half-way point of the canal at $0.5 \text{ s} \leq t_* \leq 2.50$ s. The penetration length of the jet stream with the maximum bore velocity decreased as the canal depth increased. In addition, the vortex eyes in the medium-depth ($d = 0.10$ m) and deep ($d = 0.15$ m) canals gradually moved downstream until they reached the longest distance from the upstream wall of the canals, i.e., 0.27 m at $t_* = 3.5$ s and 0.31 m at $t_* = 3$ s, respectively. The authors conclude that the location of the vortex eye as measured from the upstream wall of the canal increased with an increase in canal depth.

At $t_* = 3.5$ s, the vortex eye elongated as a result of water circulation through the entire width of the canal. At $t_* \geq 4.0$ s, the vortex eye in the deep canal split into two vortices, and the velocity vectors show that the bore plunged downward into the middle of the canal. The new smaller vortices were generated in the vicinity of the upstream and downstream walls of the canal as the walls restricted the movement and propagation of the bore inside the canal. The vortex near the upstream wall started to move towards the downstream direction until it reached the middle of the canal at $t_* = 5.0$ s.

The energy dissipation (loss) of the hydraulic jump is equal to the variation between the specific energy at 0.20 m upstream and downstream of the hydraulic jump, and was calculated using $E_L = E_1 - E_2 = (h_1 + u_1^2/2g) - (h_2 + u_2^2/2g)$ (where h is the flow depth, u is the flow velocity, E_L is the energy dissipation, E_1 is the specific energy at 0.20 m upstream of the canal, and E_2 is the specific energy at 0.20 m downstream of the canal). Figure 5.14 displays the energy dissipation time histories of the of three canal depths of $d = 0.05$ m, 0.10 m, and 0.15 m, canal width of $w = 0.60$ m, and three impoundment depths of $d_o = 0.2$ m, 0.3 m, and 0.4 m.

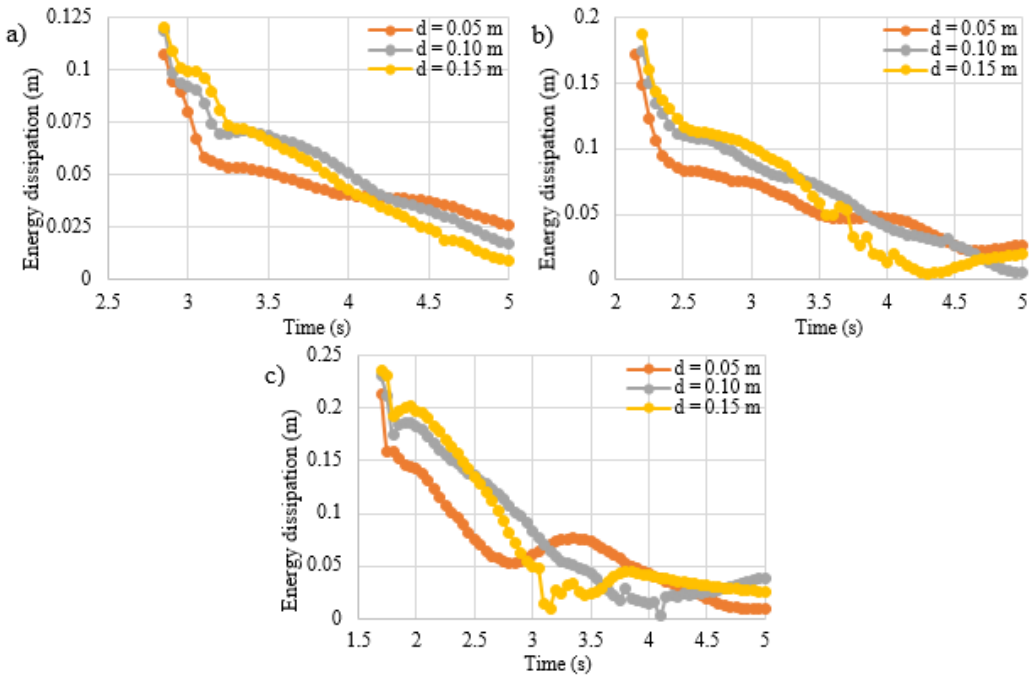

Figure 5.14. Energy dissipation time history variations between 0.20 m upstream and downstream of the canal with three canal depths and for the three impoundment depths (a) 0.20 m, (b) 0.30 m, and (c) 0.40 m.

The variation in energy dissipation for the three canal depths as produced by the three impoundment depths of 0.20 m, 0.30 m, and 0.40 m confirmed a similar trend for durations of approximately 0.5s, 1.15s, and 0.75s, respectively as the surges reached downstream of the canal. Thus, the energy dissipation is dependent on the canal depth for the three different impoundment depths. After that, the energy dissipation becomes independent of canal depth for the three different impoundment depths. The energy dissipation time histories for the three canal depths as produced by the three impoundment depths 0.20 m, 0.30 m, and 0.40 m become less than 0.05 m after 4.0 s from the opening of the gate.

The energy dissipation of the leading edge of the surge front is similar for the three canal depths and for the three impoundment depths. Figure 5.14a shows that the maximum energy dissipations for the surge from the 0.20 m impoundment depth passing over the three different canal depths d = 0.05 m, 0.10 m, and 0.15 m were 0.107 m, 0.118 m, and 0.121 m, respectively. The variations in energy dissipation for the 0.30 m impoundment depth are shown in Figure 5.14b. As can be seen, the maximum energy dissipations of the canals with depths d = 0.05 m, 0.10 m, and 0.15 m were 0.172 m, 0.174 m, and 0.187 m, respectively. Figure 5.14c shows the energy dissipation for the 0.40 m impoundment depth. It was observed that the maximum energy dissipations were 0.214 m, 0.231 m, and 0.236 m, for the canal depths d = 0.05 m, 0.10 m, and 0.15 m, respectively. As can be observed, the maximum energy dissipations increased as the impoundment depth increased, and achieved slightly higher values for the canal depth of 0.15 m in comparison with the canal widths of 0.10 m and 0.05 m for the three impoundment depths.

5.5 Discussion

The mitigation effects of a perpendicular canal on various dam-break waves were examined using laboratory experiments and numerical simulations. The effect of a mitigation canal on the wave hydrodynamics, namely the time histories of the water surface levels and velocities, was studied by employing a rectangular canal with a constant width of w = 0.6 m and three depths of d = 0.05 m, 0.10 m, and 0.15 m. The experimental results were also modelled with an OpenFoam multi-phase, three-dimensional numerical model. The differences between the maximum water depth predictions and measurements in the absence of a canal at WG (1.0 m upstream of the gate), US1 (0.20 m upstream of the canal), US2 (0.20 m downstream of the canal), and US3 (0.58 m downstream of the canal) were 4%, 10%, 6%, and 7%, respectively. Similarly, the performance of the validated numerical model in predicting the maximum water depth in the presence of a canal at WG, US1, US2, and US3 was 5%, 1%, 6%, and 9%, respectively. The performance of the validated numerical model in predicting the bore velocity at ADV1 (0.20 m upstream of the canal), ADV2 (0.20 m downstream of the canal), ADV3 (0.58 m downstream of the canal), and in the absence of a canal was 9.5%, 11%, and 11.5%, respectively. In the presence of a canal, the difference between the experimental and numerical results in velocity predictions at ADV1, ADV2, and ADV3 were 20%, 1%, and 17%, respectively.

The accuracy of the numerical models in predicting the time history of the bore water surface was found to be reasonable, within an error margin of approximately 5%. Three turbulence models were tested to predict the bore hydrodynamics when propagating over a canal. It was found that the classic k-ε turbulence model performed well, with an RMSE < 6.7% and a relative error of <

8.4%. Both the numerical and experimental results showed that the depth of the canal plays a significant role in influencing bore wave hydrodynamics. As such, when considering the design of a mitigation canal, the interaction of the tsunami inundation bore with the canal depth must be taken into account. A suitable choice of canal geometry may considerably modify water levels and the associated turbulent bore velocity. A reduction of the bore velocity in particular leads to a reduction in the tsunami-induced momentum and the hydrodynamic loading of structures located near the canal.

The time history of the water surface showed that the quasi-steady state influence of a water surface profile, owing to the interaction of the passing bore with the canal, can reduce the bore momentum and energy and hence reduce the hydrodynamic loading on the other side of the canal. For the canal depth of d = 0.05 m, simulated streamlines near the canal bottom did not reach the level of the flume bed throughout the whole time history (t_* = 3.5 s), while for the canal depths of d = 0.10 m and d = 0.15 m, the simulated streamlines did reach the flume bed level. Streamline motion was also faster for the case of mitigation canals with greater depth.

The highest bore velocity decreased over time, suggesting a major reduction in momentum due to the presence of the canal. The penetration lengths of the jet stream with the highest bore velocity were reduced as the depth of the canal increased. The position of the eye of the vortex was located near the upstream wall of the canal; its size decreased as the canal depth decreased. It can therefore be concluded that as the canal depth increased, energy dissipation proportionally increased. This was inferred from the fact that the jet stream of the maximum bore velocity decreased as the canal depth increased due to the higher capacity of the deep canal to dissipate the energy generated by the bore–canal interaction. As the canal depth increased, the volume of water contributing to the eddy generation in the initial flow direction decreased; as a result, the distance of the vortex eye from the canal edge increased. In addition, two vortices formed at 4.0 s ≤ t_* ≤ 5.0 s for the deep (d = 0.15 m) canal after the original vortex eye stretched due to the circulation of the water in the canal. As a result, the original vortex separated into two smaller, separate vortices due to the bore plunging downward into the middle of the canal.

The bore front plunges into the canal, generates a high splash, interacts with the stagnant water in the canal, and then dissipates energy. Energy dissipation due to the turbulence generated by the interaction of the high-speed bore with the stagnant water is significant. In the presence of the canal, the bore's impact on the canal results in the water propagating with a larger depth and a slower velocity as compared to the same conditions but in the absence of the canal. The time histories of the water surface level of the experimental and the numerical simulation results generally show good agreement as the developed numerical model simulates the turbulent kinetic energy dissipation occurring in the canal, which is triggered by the interaction between the bore and the stagnant water in the canal

Finally, while the scope of this preliminary study has limitations, the authors conclude that mitigation canals have the potential to act as measures that reduce hydrodynamic loading on critical infrastructure located in nearshore areas.

5.6 Conclusions

• Three turbulence models were tested to predict the time history of the water level; they performed very well for the propagation of the bore over the flat flume bed and in the presence of the mitigation canal, with an RMSE < 6.7% and a Relative Error < 8.4%. The accuracy of numerical models in predicting the time history of the water surface profiles was found to be within an error of approximately 5%.

• The experimental and numerical results indicated that the maximum water levels increased and the maximum flow velocity decreased as the turbulent bore propagated over the canal in comparison to the case when the canal was not present. The tsunami bore front plunged into the canal, generating a high splash and interacting with the stagnant canal water. The energy of the tsunami bore front decreased significantly due to the turbulence generated by the dynamic impact of the bore.

• As the canal depth increased, its capability to suppress the momentum of the bore increased.

• The jet stream of the maximum bore velocity in shallow, medium-depth, and deep canals reached their longest distance from the upstream edge of the canal, with values of 0.45 m, 0.40 m, and 0.37 m, respectively. The energy dissipation of the bore plunging into the canal increased as the canal depth increased, and the jet stream of the maximum bore velocity decreased as the canal depth increased. Therefore, the maximum bore velocity jet stream for canals with depths of 0.05 m, 0.1 m, and 0.15 m extended to the furthest location downstream of the canal, with values of 0.45 m, 0.40 m, and 0.37 m, respectively.

• The location of the vortex eye for different canal depths gradually moved down-stream until reaching distances of 0.12 m, 0.27 m, and 0.31 m from the upstream canal edge, for canal depths of 0.05 m, 0.1 m, and 0.15 m, respectively.

• The mitigation canals have the potential to act as measures that reduce hydrodynamic loading on critical infrastructure located in tsunami-prone areas. The incipient research proposed in study confirms some of the field observations during tsunami forensic engineering events (Chock et al., 2013).

6 Article 3

Tsunami-Induced Bores Propagating over a Canal, Part II: Numerical Experiments Using the Standard *k*-*ε* Turbulence Model

Nuri Elsheikh, Amir H. Azimi, Ioan Nistor, and Abdolmajid Mohammadian

Abstract

This companion paper presents the results of a series of numerical experiments examining the effects of a mitigation canal on the hydrodynamics of a tsunami-like turbulent bore proceeding over a horizontal bed. The hydraulic bores were generated by a dam-break setup which employed impoundment depths of d_o = 0.20 m, 0.30 m, and 0.40 m. The bore propagated downstream of the impoundments in the flume and interacted with a canal with varying geometry located downstream. The bore then left the flume through a drain located further downstream of the canal. In this study, the effect of the canal depth on the specific momentum and specific energy of hydraulic bores passing over a rectangular canal is numerically studied. The canal width was kept constant, at w = 0.6 m, while the canal depths were varied as follows: d = 0.05 m, 0.10 m, and 0.15 m. The time history of mean flow energy during the bore's passing over the mitigation canal indicates that the jet stream of the maximum mean flow energy is controlled by the canal depth. The time required to dissipate the jet stream of the maximum vorticity, the turbulent kinetic energy, and the energy dissipation rate all increased as the canal depth decreased. The effect of canal orientation on the bore hydrodynamics was also numerically investigated, and it was found that the impulsive momentum and specific energy reached the highest values for canal orientations of 45 and 60 degrees. For the same canal depth, the highest peak specific momentum occurred with the highest degree of canal orientation (θ = 60°).

Keywords: tsunami wave; coastal structures; canal orientation; dam-break wave; tsunami mitigation; hydraulic bore; wave hydrodynamics; OpenFOAM; momentum flux; specific energy.

6.1 Introduction

Tsunami waves can impact coastal areas and can cause devastating outcomes and have enormous impacts on people, coastal infrastructure, and natural habitats. The recent tsunami incidents in the Indian Ocean in 2004, Chile in 2010, Japan in 2011, and Indonesia in 2018 have shown the importance of effective safety and mitigation measures to protect people and coastal infrastructure in affected regions (Nistor et al., 2005; Al-Faesly et al., 2012; Wüthrich et al., 2019). Current tsunami design guidelines (FEMAP646, 2012; ASCE7-16 2017; Macabuag et al., 2018) indicate that the hydrodynamic loads are substantially more significant than the equivalent hydrostatic loads and that the ratio of these two loads is controlled by the wave characteristics and other coastal

features (topography) and structural geometry and properties. Several laboratory experiments and numerical simulations have been conducted to study the hydrodynamic loads induced by tsunami waves (Nistor et al., 2009; Nistor and Palermo 2015; Sarjamee et al., 2017a; Wüthrich et al. 2018a, 2018b, 2018c; Asadollahi et al., 2019a, and 2019b). Chanson (2006) found a relationship between dam-break waves propagating over a horizontal surface and tsunami-induced bores. Researchers have used dam-break wave generation techniques in the laboratory to model the flooding caused by tsunami waves, and this technique consists of the sudden release of impounded water either by means of a swing gate or by a vertical lifting gate (Nistor et al., 2009; Asadollahi et al., 2019a, 2019b; Lauber and Hager, 1998; Stolle et al., 2019; Sarjamee et al., 2017b; Ghodoosipour et al., 2019a, 2019b; Crespo et al., 2008; Duarte et al. 2011; Oertel and Bung, 2012; Aureli et al., 2015 Madsen et al., 2008; Leal et al., 2009; Khankandi et al., 2012; Baldock et al., 2012; Shafiei et al., 2016b; Liu et al., 2017).

Laboratory experiments have been conducted to investigate the effects of mitigation structures on minimizing the energy and momentum fluxes of approaching tsunami waves. Hydrodynamic forces from tsunami waves are exerted on nearshore natural and man-made structures such as pine forests (Tanaka et al., 2009), coastal dunes (Fadly and Murakami, 2012), natural and artificial structures such as coastal headlands and buildings (St-Germain et al., 2014), rivers, and canals (Dao et al., 2013; Elsheikh et al., 2020). Field studies have shown substantial changes in the bore propagation characteristics when such bores pass over natural streams (Wüthrich, et al., 2018a). In such cases, it has been inferred that hydrodynamic parameters such as the bore height and its velocity are influenced by canal geometry and can provide a measure of energy dissipation.

Watanabe et al. (2016) conducted a series of laboratory experiments and found that overflow bore velocity decreased due to the existence of a rectangular canal in its path. It was found that a mitigation canal absorbs significant energy and momentum of tsunami inundation, and that the downstream bore height increases due to bore deceleration caused by the impact with the mitigation canal. Additionally, a series of laboratory experiments was performed by Rahman et al. (2017) to study the effect of a mitigation canal partially filled by water on the hydrodynamics of tsunami inundation. In their experiments, a rectangular canal was placed perpendicular to the direction of bore in order to measure the water surface levels and velocities before and after the canal. Velocity measurements were collected at a considerable distance after the canal, at distances between 5 and 10 times the canal width, and therefore their data may not precisely reflect the effect of the mitigation canal on bore hydrodynamics. In contrast, the current study aims to investigate the effects of a mitigation canal fully filled by water on the turbulent bore propagation by collecting the water surface levels and velocities in the vicinity of the canal at distances between 1/3 and 2.9/3 of the canal width in order to study the immediate impacts of the canal on both the upstream reflection bore and on the dissipated bore in the downstream direction. The laboratory experiments showed that the bore velocity decreased after passing over the canal and that the maximum velocity reduction occurred for the deepest and widest canal. However, the laboratory experiments were restricted to a small range of canal aspect ratios ranging from w/d = 4 to 10, where w is the canal

width and d is the canal depth. Especially with the widest canals, the canal dimensions affected significant increases in the bore height. The experiments showed similar tsunami-inundation reduction for canals of the same width but different depths. A time lag in the tsunami arrival time was observed in all tests, indicating velocity-damping in all canal configurations. It was found that the tsunami inundation bore energy was partially absorbed by the reflected wave produced by the canal.

A series of laboratory experiments was recently conducted to study the impacts of canals with a rectangular profile on the hydrodynamics of turbulent bores before and after the canals (Elsheikh et al., 2020). The mitigation canals were installed perpendicular to the flow direction. Previous experimental studies focused on a very narrow range of canal aspect ratios (i.e., $4 \leq w/d \leq 10$) and relatively smaller impoundment depths (i.e., $d_o \leq 0.25$ m). Elsheikh et al. (2020) proposed a series of experimental tests for a wide range of canal aspect ratios (i.e., $4 \leq w/d \leq 60$) in order to study the effects of canal geometry on the hydrodynamic characteristics of the turbulent bore before and after the canal and found that the differences in water elevation and bore wave velocities before and after the rectangular canal were the key parameters in optimizing the canals' performance and aspect ratio.

Numerical simulations have been performed to better understand the hydrodynamics of turbulent bores. St-Germain et al. (2014) employed the Weakly Compressible Smoothed Particle Hydrodynamics (WCSPH) numerical model to simulate the experimental tests of Al-Fasely et al. (2012), employing two different flume widths of 1.3 m and 2.6 m. They confirmed that by increasing the width of the flume, the simulated net streamwise force and the bore run-up height decreased shortly after the initial impact. Wei et al. (2015) investigated the dynamic interaction between bores and bridge piers, and used the experimental results reported in Arnason's (2005) for model validation. The flume width was extended to study the forces resulting from the influence of the sidewalls. The simulation outcomes indicated that the hydrodynamic forces were reduced when the flume width was increased. Comparison of the profiles of the bore surfaces flowing through flumes with different widths showed an adverse correlation between flume width and obstruction-related water build-up.

Sarjamee et al. (2017a) performed Large Eddy Simulations of tsunami-like bores over a triangular obstacle, and found that the numerical results for time histories in the water surface were not in agreement with the experimental data. Such differences were attributed to the entrainment of air bubbles in the water pool that formed over the downstream slope of the triangular obstacle. Some discrepancies between the physical and numerical models were deemed to occur due to the effects of the flume sidewalls. Asadollahi et al. (2019a) performed a series of numerical simulations to study the effect of channel sidewalls and flow orientation on bore characteristics such as the wave height and induced net stream wise forces. A wide range of blockage ratios, defined as the ratio of the structure width to the flume width of BR = 0.24, 0.15, 0.10, 0.07, 0.05 and, 0.03, were tested to investigate the effect of sidewalls, and two model orientations of $\theta = 0°$ and 45° were also tested

to study the effect of flow orientation. It was found that the effects of the blockage ratio for the tests with BR = 0.24 and 0.07 were noticeable 2.7 s after the gate opening. The surface roller dissipated prior to approaching the sidewalls for the extended flume, and no water accumulation occurred behind the upstream side of the structural model. At t = 1.3 s, a bore run-up on the upstream face of the column was observed for the model orientation of θ = 0°, while no bore run-up was observed on the upstream face of the column for θ = 45°, as the bore was divided into two streams by the corner facing the incoming bore. The effect of model orientation was also noticeable during the transient period. At t = 2.3 s, a higher flow depth was observed behind the upstream wall, indicating a greater hydrodynamic load for the test with θ = 0° in comparison to the test with θ = 45°. Similar results were also reported in the experimental study by Shafiei et al. (2016).

To the best of the authors' knowledge, no recommendations are available in existing design codes such as FEMA-P646 (2012) and ASCE7-16 (2017) for determining the effect of mitigation canals on time histories of specific momentum and energy. The mitigation effects on tsunami waves by rectangular canals have been briefly examined in the literature (Dao et al., 2013; Watanabe et al., 2016); however, the effects of canal alignment have not been examined. The main objective of the second part of the present companion paper is to investigate the effect of canal depth and orientation on the hydrodynamics of tsunami bores passing over a mitigation canal. The dynamic parameters, such as specific momentum flux, mean flow, turbulent kinetic energy, and vorticity, were extracted from the numerical outcomes of the validated model. The time histories of the defined parameters were extracted to better understand the momentum and energy transfer in a tsunami-like bore before and after the interaction with a mitigation canal. In the first part of the companion paper, a three-dimensional numerical model was developed using the OpenFOAM software (OpenFOAM, 2019), and the time series of the water surface levels of the numerical outputs were compared with the results of laboratory experiments. Good agreement was found between the experimental and numerical water surface profiles, with a root mean square error (RMSE) of less than 6.7% and a relative error of less than 8.4%. The effects of channel orientation on the bore wave impact and time histories of specific momentum and energy are investigated herein, and the results of the present numerical simulation have a widespread range of applications, such as in river and coastal flooding mitigation plans. These results can be utilized to optimize new design guidelines and parameters for infrastructure that is affected by extreme flows.

6.2 Numerical Simulation

A numerical model was used in order to simulate the propagation of a tsunami-like turbulent bore over a smooth horizontal bed. The tsunami-like turbulent bore was generated by a dam-break release mechanism and the bore front plunged into a rectangular mitigation canal, and after the impact propagated towards the downstream end of the flume. After the model validation, twelve tests were simulated (see Table 6.1) to investigate the effects of canal characteristics and the impoundment depths used to generate the bores.

Table 6.1. Experimental parameters used to generate hydraulic bores passing over a flat surface (F-series) and a rectangular canal (C-series).

Test No.	Test name	d_o (m)	w (m)	d (m)	B (m)	w/d (-)	θ (^{o})
1	F-0.2	0.20	0	0	0.38	0	0
2	F-0.3	0.30	0	0	0.38	0	0
3	F-0.4	0.40	0	0	0.38	0	0
4	C-0.2-4	0.20	0.60	0.15	0.38	4	0
5	C-0.2-6	0.20	0.60	0.10	0.38	6	0
6	C-0.2-12	0.20	0.60	0.05	0.38	12	0
7	C-0.3-4	0.30	0.60	0.15	0.38	4	0
8	C-0.3-6	0.30	0.60	0.10	0.38	6	0
9	C-0.3-12	0.30	0.60	0.05	0.38	12	0
10	C-0.4-4	0.40	0.60	0.15	0.38	4	0
11	C-0.4-6	0.40	0.60	0.10	0.38	6	0
12	C-0.4-12	0.40	0.60	0.05	0.38	12	0

The flume boundary effect should be minimized in order to study the effect of canal orientation and the interaction of the bore front with the canal. The flume dimensions in the numerical domain were increased to 20.76 m × 1.8 m × 0.60 m in order to minimize the flume boundary effect (see Figure 6.1).

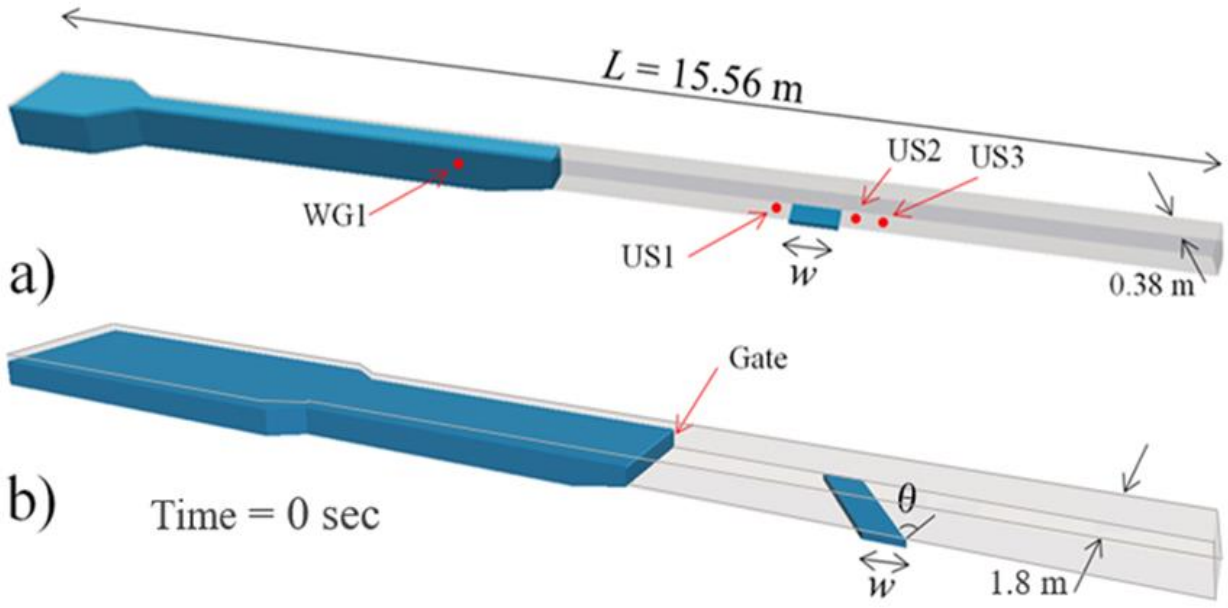

Figure 6.1. Computational domain for numerical experiments: a) perpendicular channel, θ = 0°; b) oblique channel, θ = 15°, 30º, 45°, and 60°.

The computational domain was extended laterally, by increasing its width, to eliminate the constriction effects of the sidewalls on the bore characteristics such as bore height, velocity,

specific momentum, and specific energy (Al-Faesly et al., 2012; St-Germain et al., 2014; Wei et al., 2015; Arnason, 2005). Five tests with an impoundment depth of d_o = 0.3 m and canal depth of d = 0.10 m were modeled in order to study the effect of canal orientation, and sixteen tests were performed to investigate the effect of canal depth for an impoundment depth of d_o = 0.40 m. In all cases, the canal width was constant, at w = 0.60 m, and the orientation angles varied from 0° to 60° (see Table 6.2).

Table 6.2. The configuration parameters in the numerical simulation of hydraulic bores passing over a rectangular canal with different angles from the bore.

Test No.	Test name	d_o (m)	w (m)	d (m)	B (m)	w/d (-)	θ (^{o})
1	C-0.3-6-0	0.30	0.60	0.10	1.80	6	0
2	C-0.3-6-15	0.30	0.60	0.10	1.80	6	15
3	C-0.3-6-30	0.30	0.60	0.10	1.80	6	30
4	C-0.3-6-45	0.30	0.60	0.10	1.80	6	45
5	C-0.3-6-60	0.30	0.60	0.10	1.80	6	60
6	C-0.4-4-0	0.40	0.60	0.15	1.80	4	0
7	C-0.4-4-15	0.40	0.60	0.15	1.80	4	15
8	C-0.4-4-30	0.40	0.60	0.15	1.80	4	30
9	C-0.4-4-45	0.40	0.60	0.15	1.80	4	45
10	C-0.4-4-60	0.40	0.60	0.15	1.80	4	60
11	C-0.4-6-0	0.40	0.60	0.10	1.80	6	0
12	C-0.4-6-15	0.40	0.60	0.10	1.80	6	15
13	C-0.4-6-30	0.40	0.60	0.10	1.80	6	30
14	C-0.4-6-45	0.40	0.60	0.10	1.80	6	45
15	C-0.4-6-60	0.40	0.60	0.10	1.80	6	60
16	C-0.4-12-0	0.40	0.60	0.05	1.80	12	0
17	C-0.4-12-15	0.40	0.60	0.05	1.80	12	15
18	C-0.4-12-30	0.40	0.60	0.05	1.80	12	30
19	C-0.4-12-45	0.40	0.60	0.05	1.80	12	45
20	C-0.4-12-60	0.40	0.60	0.05	1.80	12	60
21	F-0.40	0.40	0	0	1.80	0	0

Similar to the simulations performed for model validation, the initial values of the phase fraction, wave velocity, water height, pressure, and force were set to zero. For the initial boundary condition, the phase fraction of the reservoir was set to 1.0, indicating that the reservoir was filled with water. Figure 6.1 shows the computational domains of the original and extended flumes and the water level at the initial condition (i.e., t = 0). The simulated flumes and water levels at the initial condition (i.e., t = 0) are shown using ParaView software, which is independent from OpenFOAM. In addition to the length of the tank, the flume was elongated from 1.2 m to 6.4 m in the flow direction to ensure that sufficient volume of impounded water was available for the simulation time of t = 20 s.

All the boundaries of the numerical domain, except for the outlet, were set to the "wall-type boundary with no-slip condition" to ensure zero velocity at the wall and zero pressure at the water surface. The boundary condition for the flume outlet was set to the "zero gradient boundary condition", which allowed water to exit the computational freely domain. Several flume geometries were generated to simulate flumes transversally perpendicular and various canal orientations with respect to the flume's longitudinal axis. A mesh-independent analysis was performed to determine the optimum cell size in order to reduce computational cost while ensuring accuracy and mesh independency. The mesh-independent analysis was performed by systematically reducing the cell size from a coarse mesh to a refined mesh with a known aspect ratio (Azimi et al. 2011, 2012).

A more refined mesh resolution was selected for downstream of the canal due to a significant change in the water surface and the need for accurate results at the locations of the monitoring equipment. The Ultrasonic Sensors (US) and the Acoustic Doppler Velocimetry (ADV) probes were located upstream and downstream of the canal. The US1 and ADV1 probes were located 0.2 m upstream of the canal, US2 and ADV2 were located 0.2 m downstream of the canal, and US3 and ADV3 were placed 0.58 m downstream of the canal.

Initially, the effect of mesh variation was examined using various mesh resolutions. The grid cell size was first refined for the entire computational domain of the flume and then locally around locations of specific interest, such as the locations of the ultrasonic sensors and the acoustic Doppler velocimetry probes. In the numerical simulations, the grid cell size was gradually decreased from the upstream end towards the downstream end of the flume, focusing on the location of the equipment. For flumes with lower-degree canal orientations (i.e., θ = 0°, 15°, and 30°), the cell size dimensions in the *x*-direction were set at 20 mm downstream of the gate, 30 mm upstream of the gate, and 40 mm upstream of the reservoir contraction. In the *y*- and *z*-directions, the cell size dimensions were set at 20 mm. For the flumes with higher-degree canal orientations (i.e., θ = 45° and 60°), the cell size dimensions in the *x*-direction were adjusted to 10 mm and 20 mm downstream and upstream of the gate, respectively. In the *y*- and *z*-directions, the cell sizes were adjusted to 10 mm. In the first part of this companion paper, three different turbulence models were employed in numerical simulation in order to establish the best agreement concerning the physical experiments. The time histories of the water surface levels and velocities at four locations were extracted from the numerical models, and the outcomes were compared with the measurements. The model validation was performed both in the absence and presence of a rectangular canal.

Another parametric study was undertaken in order to assess the performance and select the best turbulence model for the current simulation. To improve the accuracy of the simulations, three *k*-ε-based turbulent models (i.e., classic *k*-ε, Realizable *k*-ε, and RNG *k*-ε) were implemented. There was no significant difference between these three models; however, the root mean square error (RSME) displayed a slightly better agreement for the standard *k*-ε model. As a result, although the

use of all three turbulence models provided good agreement with the experimental results, the standard k-ε model provided the best fit.

As such, the well-known standard k-ε turbulence closure model was further used for all the subsequent numerical simulations, as it provided the highest accuracy during the model validation (see Part One of the present companion paper). A dynamic time step was selected in the numerical simulations in order to ensure simulation stability and guarantee that the maximum Courant number was always less than unity. The computation times ranged from approximately four hours for the flumes with higher-degree canal orientations and coarse mesh, to 16 h for the flumes with lower-degree canal orientations and fine mesh.

6.3 Simulation Results

6.3.1 Momentum Flux Time Histories

The specific momentum flux per unit mass and per unit width of the flume was calculated as hu^2, where h is the flow depth and u is the flow velocity at a specific location. The three-dimensional numerical simulation results such as h, and u can be obtained and extracted using object-oriented post-processing software (ParaView). The specific momentum simply contains the flow depth and velocity term, since adjacent positions have about the same pressure. The time histories of the specific momentum for different canal geometries and locations upstream and downstream of the canal were extracted from the numerical results, and are shown in Figure 6.2. The latter shows the effects of mitigation canals on the time history of the specific momentum upstream and downstream of the canal. The impoundment depth for the tsunami-like wave is d_o = 0.3 m. In this case, the width of the canal was kept constant (w = 0.6 m) and different canal depths of d = 0 m, 0.05 m, 0.1 m, and 0.15 m are compared. A large discrepancy was observed in the time histories of specific momentum in the presence of the canal and its absence. The difference between the maximum specific momentum compared to the absence of the canal showed an approximately 9.3% reduction between US2 and US3. For a canal depth of d = 0.05 m (see Figure 6.2b), the maximum specific momentum decreased by 27% and 13.7% at US2 and US3, respectively. However, for canal depths of d = 0.10 m and 0.15 m, the maximum specific momentum decreased by approximately 28.3% and 27.9%, respectively, at US2, and by approximately 14.5% and 16.9% at US3, respectively. The instant at which the specific momentum reached its maximum magnitude were different upstream and downstream of the canal. This may be attributed to the canal-related turbulent flow that was generated.

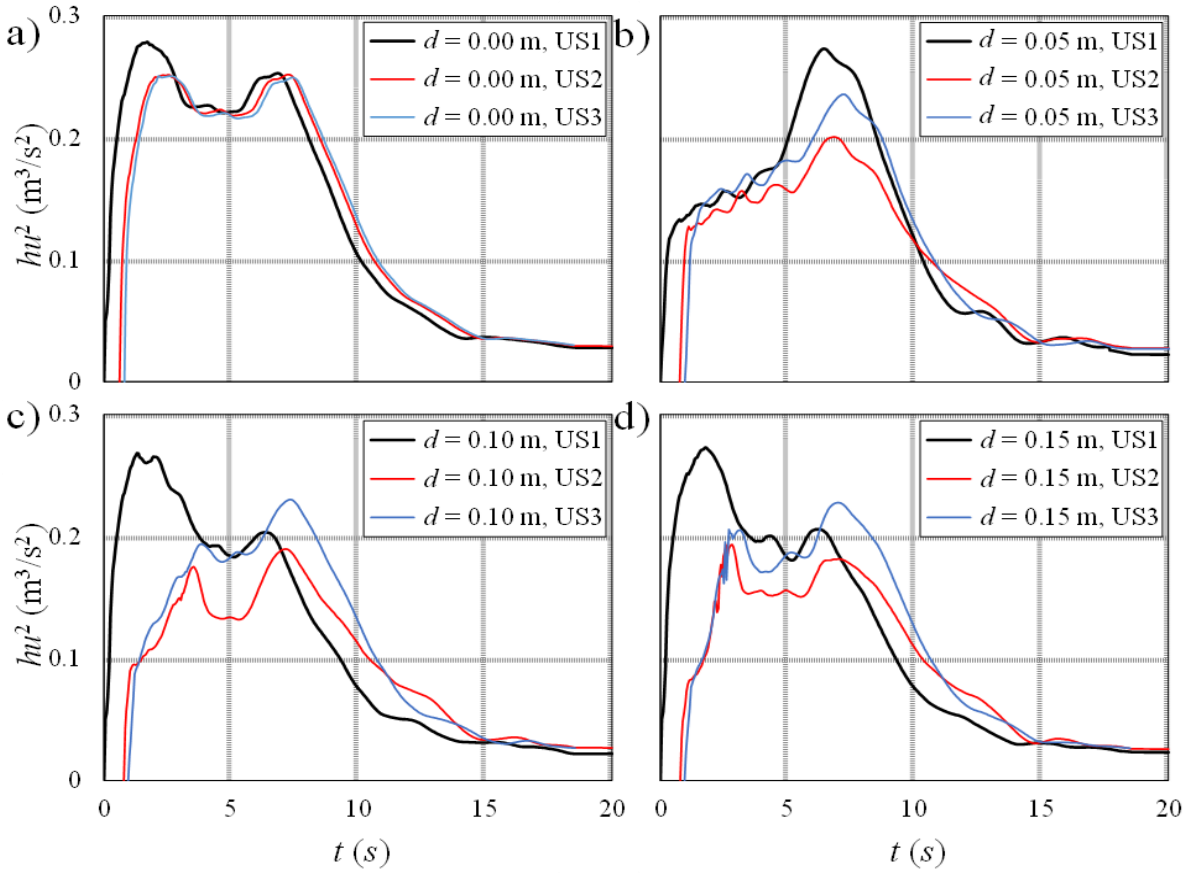

Figure 6.2. Effects of canal depth, d, on the time history of the rate of change of specific momentum at locations before and after the canal. The impoundment depth is d_o = 0.30 m and the canal width is w = 0.60 m: a) d = 0.00 m; b) d = 0.05 m; c) d = 0.10 m; d) d = 0.15 m.

Figure 6.3. shows the time history of the ratio between the downstream and upstream peak specific momentums $(hu^2)_d/(hu^2)_u$ with canal depth and for impoundment depths of d_o = 0.2 m, 0.3 m, and 0.4 m.

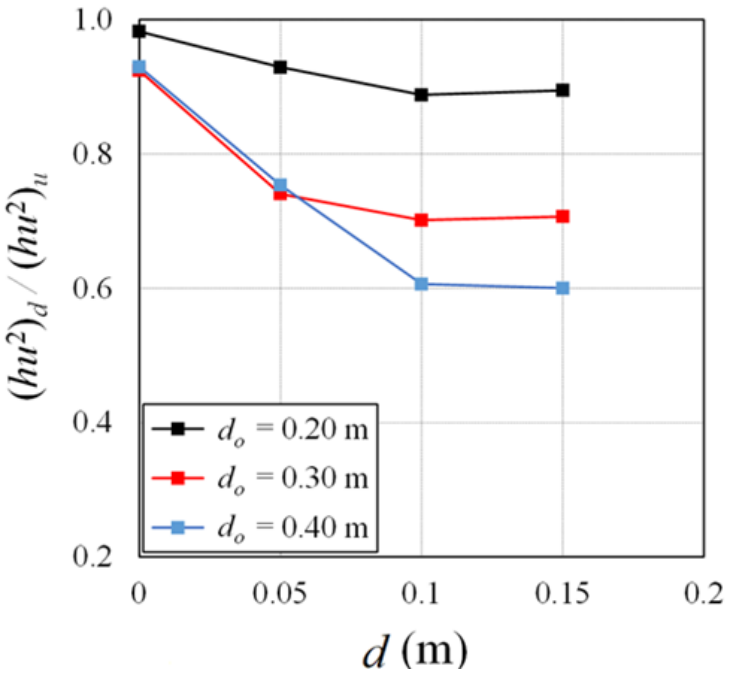

Figure 6.3. Effect of impoundment depth on variations of the ratio of the downstream and upstream rate of change of specific momentum with canal depth.

The pressure of the specific momentum per unit mass per unit width is assumed to be approximately the same at the location 0.20 m upstream and the location at 0.2 m downstream of the canal. The lowest specific momentum ratio between the downstream and upstream peak of the canal was 60% for the canal depth of $d \geq 0.10$ m and impoundment depth of $d_o = 0.4$ m, while the lowest specific momentum ratios between the downstream and upstream peak of the canal were 89% and 70% for the canal depth of $d \geq 0.10$ m and impoundment depths of $d_o = 0.2$ m and 0.3 m, respectively. In contrast, the respective maximum specific momentum ratios for the impoundment depths of $d_o = 0.2$ m, 0.3 m, and 0.4 m were as high as 99%, 94%, and 93% of the specific momentum ratio without a canal. It was noted that for the 0.40 m impoundment depth, the maximum specific momentum ratio decreased to approximately 60% as the canal depth was increased from $d = 0$ m to $d = 0.10$ m. Lower reductions were observed for the impoundment depths of $d_o = 0.2$ m and 0.3 m. Generally, the variation of the ratio of downstream to upstream peak specific momentum decreased as the impoundment depth increased.

6.3.2 Time history of Mean Flow Energy

Figure 6.4. shows the effects of canal depth on time histories of the contour plots of mean flow energy for a bore passing over a canal from an impoundment with a depth of $d_o = 0.3$. The canal width in all tests was kept constant ($w = 0.6$ m), and different canal depths of $d = 0.05$ m, 0.10 m, and 0.15 m were tested.

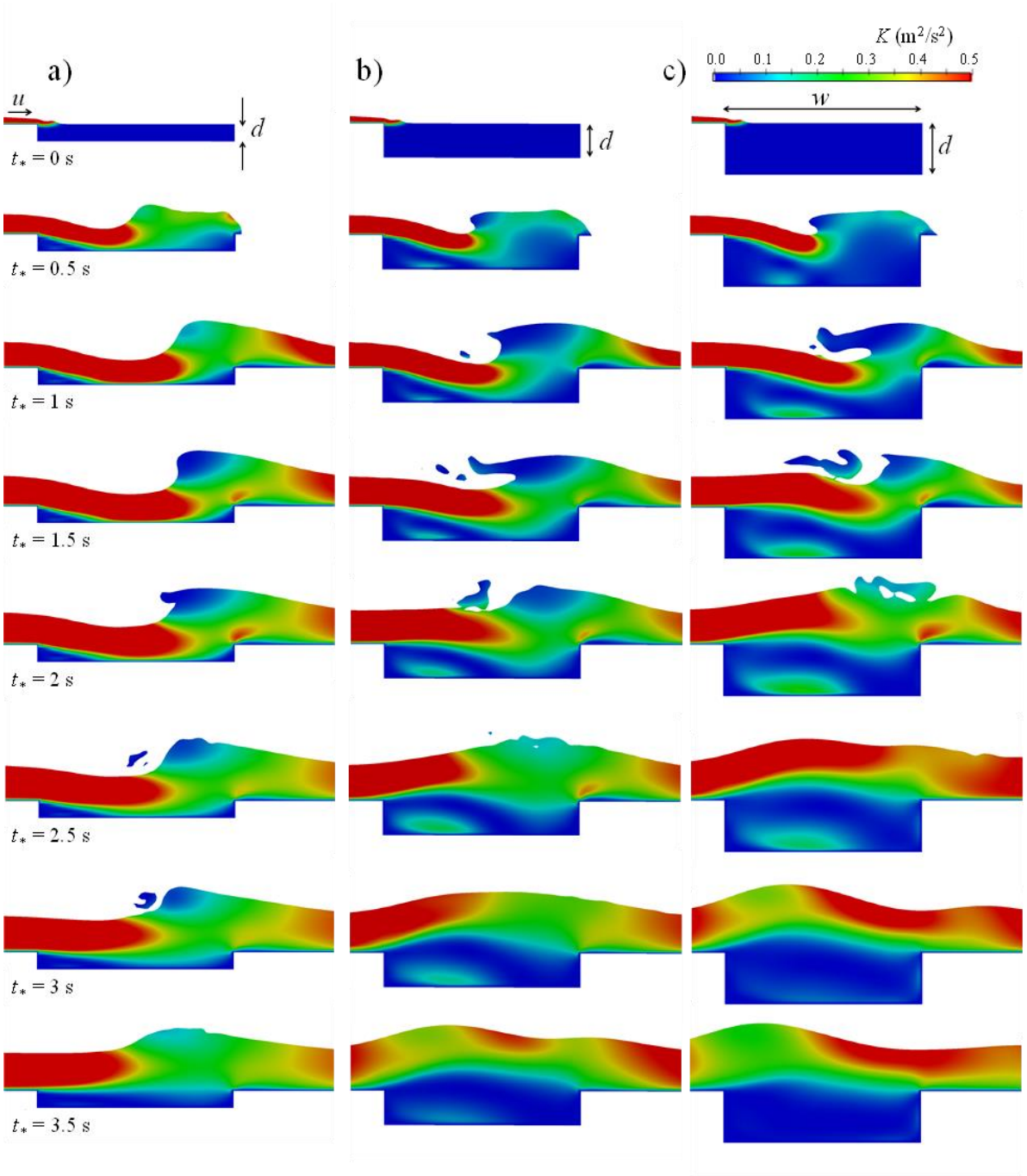

Figure 6.4. Effect of the canal depth, d, on the time histories of the mean flow energy, K, with time for a bore from an impoundment with a depth of d_o = 0.30 m passing over a canal with a width of w = 0.60 m: a) d = 0.05 m; b) d = 0.10 m; c) d = 0.15 m.

Figure 6.4a shows the contour plot of the shallowest canal (d = 0.05 m). The time at which the bore front reached the mitigation canal was set as the initial time of t_* = 0. At t_* = 0.50 s, the bore front plunged into the canal without reaching its bottom yet, and the jet stream of the maximum mean flow energy reached half of the canal width in longitudinal direction. The jet stream then

slowly moved in the downstream direction. At $t_* = 1.0$ s, the jet stream of the maximum mean flow energy touched the bottom of the canal and reached a maximum distance of 0.47 m from the upstream edge of the canal. At $t_* = 1.5$ s, the jet stream of the maximum mean flow energy reached its farthest distance from the upstream canal edge at nearly 0.50 m, which was more than 80% of the canal width. At $t_* = 2$ s, the jet stream of the maximum mean flow energy moved back in the upstream direction, and gradually rose with time from the bottom of the canal until it reached the horizontal bed of the flume at $t_* = 3$ s. The time histories in the contour plots of the mean flow energy with time in the medium ($d = 0.10$ m) and deep ($d = 0.15$ m) canals indicated that the jet streams of the maximum mean flow energy reached their maximum length at $t_* = 1.5$ s and at approximately 0.41 m and 0.47 m, respectively, (see Figures 6.4b and 6.4c).

The mean flow energy, K, for different canal geometries, different locations upstream and downstream of the canal, and the same impoundment depth were calculated using $K = (u^2 + v^2 + w^2)/3$, where u, v, w were the components of the flow velocity in the x-, y-, and z-directions, respectively. Figure 6.5. shows the variations in the ratio of mean flow energy before and after the canal, K_d/K_u, with canal depths and for different impoundment depths of $d_o = 0.2$ m, 0.3 m, and 0.4 m.

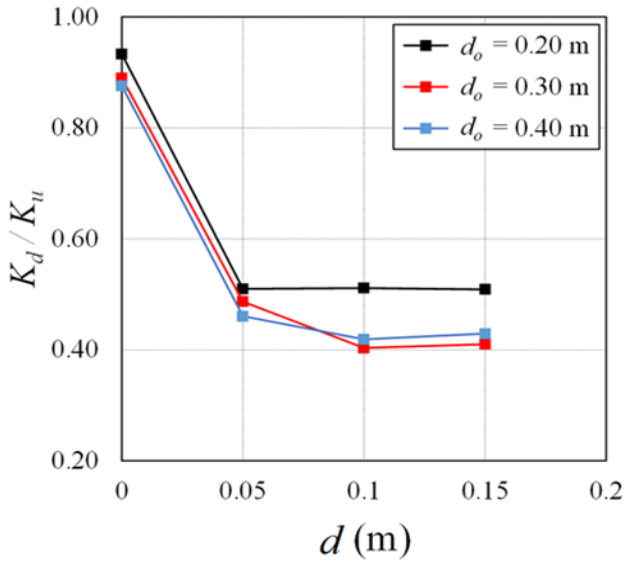

Figure 6.5. Variations of the ratio of the downstream and upstream mean flow energies with canal depth for hydraulic bores from impoundments with different depths.

The lowest mean energy ratio, with the value of $K_d/K_u = 41\%$, was observed in the test with the canal depth of $d = 0.10$ m and impoundment depth of $d_o = 0.3$ m. In contrast, the maximum mean energy ratios were observed in tests without a canal with the values of 93%, 89%, and 87% for $d_o = 0.2$ m, 0.3 m, and 0.4 m, respectively. The variations in the ratio of mean energy noticeably declined as the canal depth increased from $d = 0$ m to $d = 0.05$ m. The energy ratios were almost constant as the canal depth increased from $d = 0.10$ m to $d = 0.15$ m, and they were independent

of impoundment depth. For both canal depths of d = 0.10 m and 0.15 m, there were nearly the same minimum specific momentum and mean energy ratios and that they were independent of impoundment depth.

The total specific energy per unit width, E, was calculated based on the water depth and velocity at different measurement locations, as $E = h + u^2/(2g)$. It only contains the water depth and velocity term, since nearby locations have approximately the same pressure. Figure 6.6. shows the effects of a mitigation canal on the time histories of specific energy, E, of a bore before and after the canal. The impoundment depth of the bore was d_o = 0.3 m, the canal width was constant with a value of w = 0.6 m, and the canal depths were d = 0 m, 0.05 m, 0.1 m, and 0.15 m.

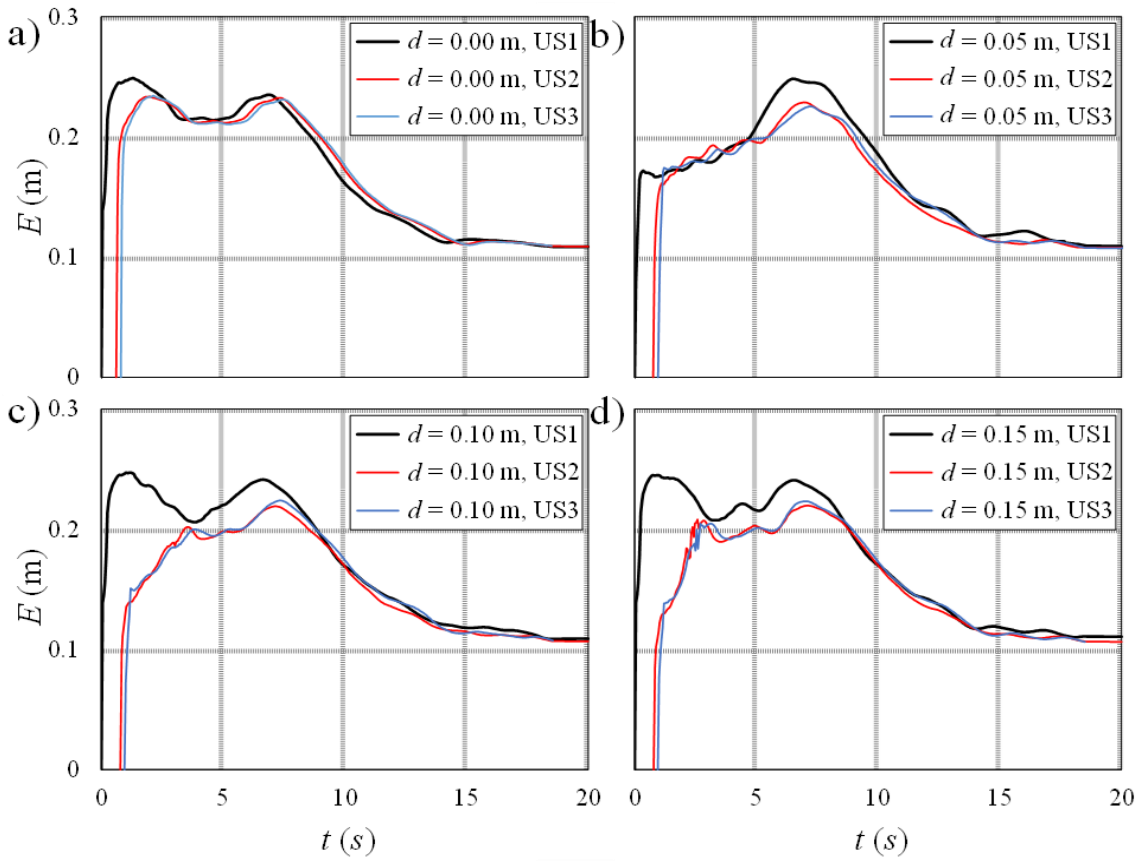

Figure 6.6. Effects of the mitigation canal on time histories of total specific energy, E, with time for a bore from an impoundment with a depth of d_o = 0.30 m passing over a canal with a width of w = 0.60 m: a) d = 0.00 m; b) d = 0.05 m; c) d = 0.10 m; d) d = 0.15 m.

Figure 6.6a shows the time histories of the specific energy over the horizontal bed. The peak specific energy decreased by approximately 5.7% between the measurement locations of US2 and US3 (see Figure 6.6a). For the tests with a canal depth of 0.05 m (see Figure 6.6b), the peak total specific energy decreased by approximately 7% and 7.6% of that measured at the points of US2 and US3, respectively. The difference between the peak total specific energies at the two

measurement locations increased in tests with canal depths of d = 0.1 m and 0.15 m. As can be seen in Figures 6.6c and 6.6d, the peak specific energies decreased by approximately 10.2% and 9.6% for canal depths of d = 0.10 m and 0.15 m, respectively.

6.3.3 Vertex Structure

Figure 6.7 shows the time histories in the contour plots of bore vorticity, ω, and the velocity vector fields for a constant canal depth of w = 0.6 m, impoundment depth of d_o = 0.3 m, and different canal depths of d = 0.05 m, 0.1 m, and 0.15 m.

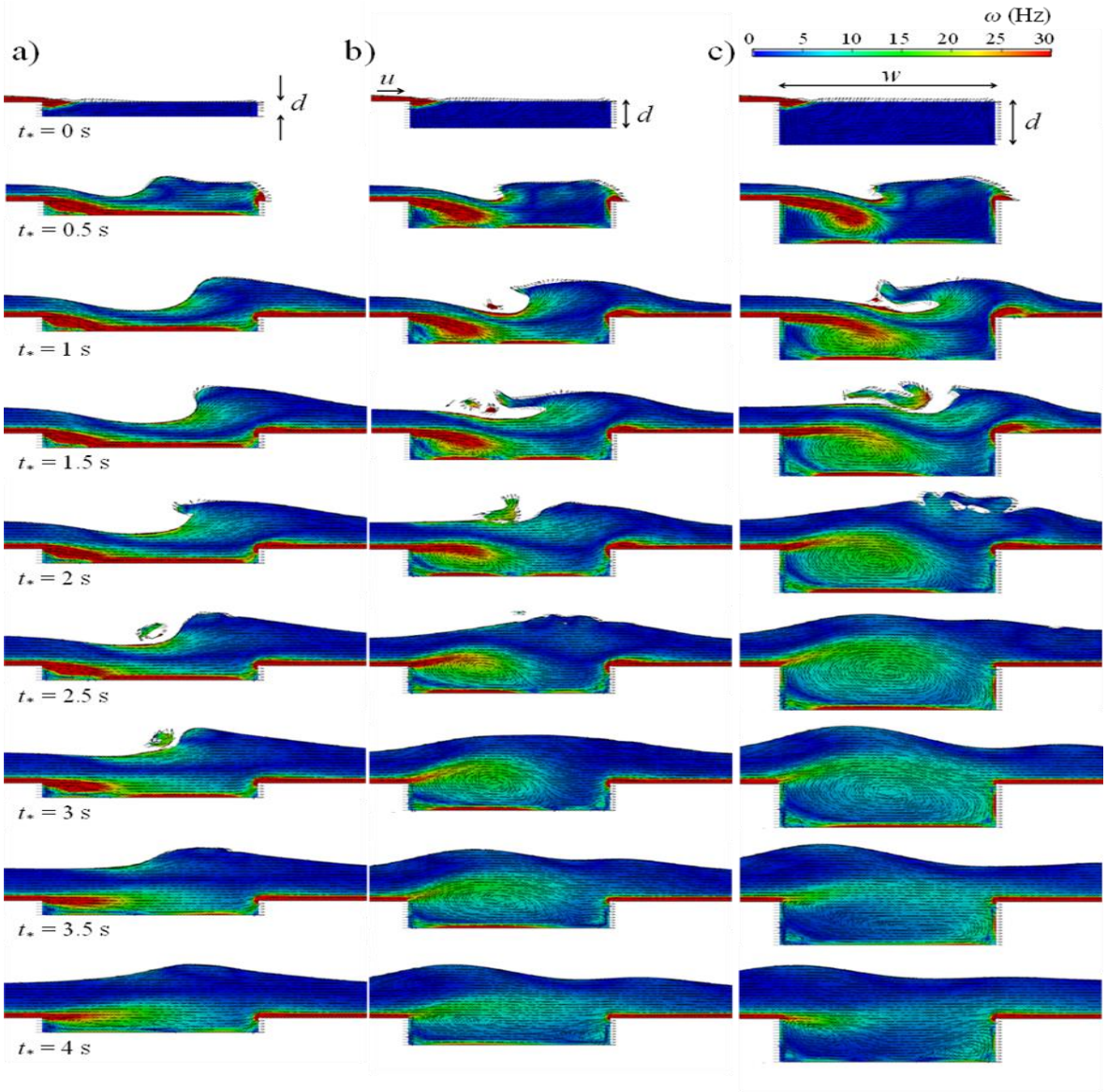

Figure 6.7. Effects of the canal depth on time histories of bore vorticity, ω, with time for a bore from an impoundment with a depth of d_o = 0.30 m passing over a canal with a width of w = 0.60 m: a) d = 0.05 m; b) d = 0.10 m; c) d = 0.15 m.

A river bore is an upstream proceeding transition between two various flow depths generally produced by tidal pressure. Analogous flows can be created in structured environments such as wave flumes, and many experimental investigations have been achieved to discover some of the key characteristics of bores. Thus, the relatively slight inconsistency with the experiments could be attributed partially to the vorticity induced by the discharge used to create the undular bore. Vorticity, in particular, appears to be a significant factor in the bores produced by a constant discharge. Some authors (Sturtevant, 1965; Byatt-Smith, 1971) have indicated the significance of bottom friction on the appearance of an undular bore. In a river bore, if the circumstances are appropriate, an approximately steady profile of undulations can be observed. A bore can be categorized by the bore strength or Froude number (Vargas-Magaña et al., 2021; El et al., 2006; El et al., 2005; Amaechi et al., 2021; Amaechi et al., 2022; El et al., 2005; El et al., 2005; Hatland and Kalisch, 2019).

Figure 6.7a shows the time histories in the vorticity contour plots for a canal depth of d = 0.05 m, and the area of maximum vorticity is marked as $\omega \geq 30$ Hz. As shown in Figure 6.7a, at $t_* = 0.5$ s, the peak vorticity formed in the vicinity of the upstream edge of the canal and extended 0.17 m downstream of the upstream wall of the canal. A vortex eye formed in the vicinity of the upstream edge of the canal. At $t_* = 0.5$ s, the vortex eye formed at approximately 0.05 m downstream of the upstream wall of the canal, and it advanced slowly as the bore advanced through the canal. At $t_* = 3.5$ s, the maximum vorticity reached its farthest distance from the upstream wall at approximately 0.20 m from the upstream wall, and then decreased at $t_* = 4.0$ s. At $t_* = 4.0$ s, the vortex eye reached its farthest distance from the upstream wall of the canal at nearly 0.12 m. In the numerical simulation, the bore front plunged into the canal, generating a surface hydraulic jump. The bore height then increased due to an increase in pressure force caused by the surface hydraulic jump at the downstream edge of the canal. The bore front then transferred more momentum to the volume of water in the canal, resulting in a strong surface jump reaching the downstream edge of the canal. The bore energy decreased as it passed through the canal. The upward deflection due to pressure force caused by the surface hydraulic jump of the greatest bore vorticity expanded the recirculation zone upstream of the canal and gradually pushed the vortex eye downstream.

As shown in Figures 6.7b and 6.7c, the locations of maximum vorticity in the medium depth and the deep canals reached the upstream wall at 0.24 m for 0.5 s $\leq t_* \leq$ 2.0 s and 0.30 m at $t_* = 1.0$ s, respectively. Then, the maximum bore vorticity decreased with time. The vortex eyes in the medium and deep canals gradually advanced towards the downstream wall of the canal until they reached their longest distance from the upstream wall of the canal at 0.26 m ($t_* = 3.5$ s) and 0.30 m ($t_* = 3$ s), respectively. The location of the maximum bore vorticity in the water vorticity contour plots increased as the canal depth increased, indicating more transition of momentum and energy as the canal depth increased. This happened due to the higher capability of the deep canal to absorb the bore and dissipate the energy generated by the bore-canal interaction.

Figure 6.8. shows the variations in the location of the eye of the vortex inside the canal as a function of the non-dimensional time *t/T* for bores generated from impoundments depths of d_o = 0.30 m and 0.40 m.

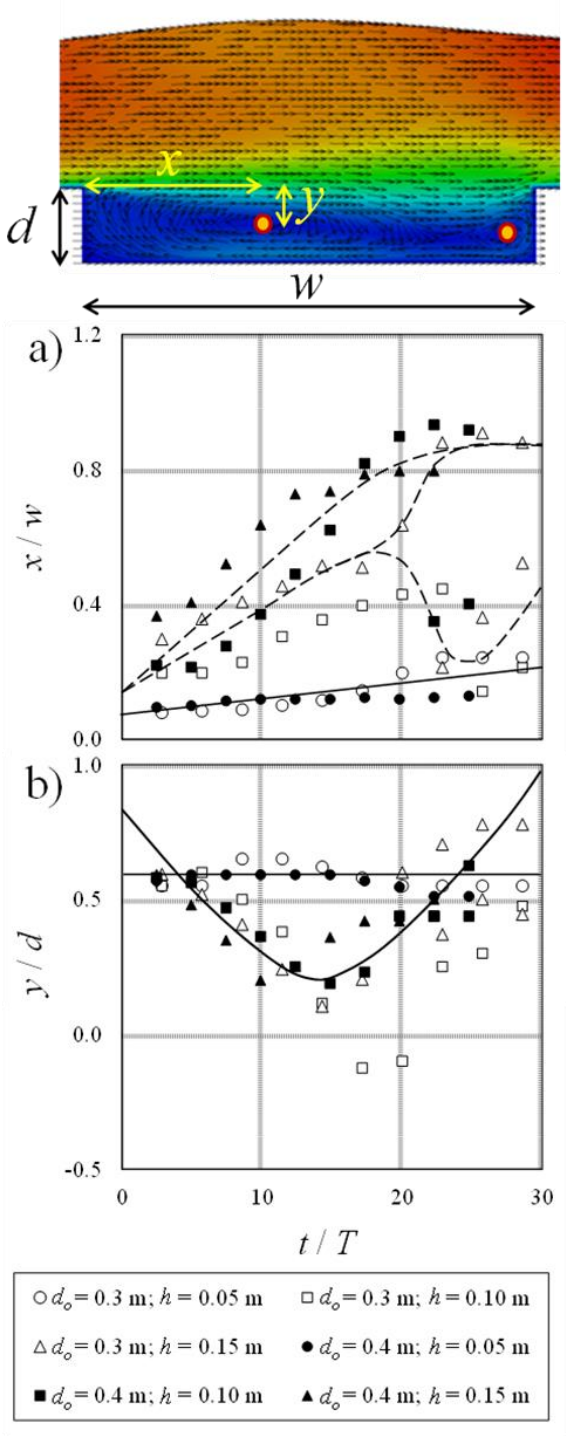

Figure 6.8. Variations in the locations of the eyes of vortices in the canal with non-dimensional time, *t/T*: a) variations of *x/w* with *t/T*; b) variations of *y/d* with *t/T*.

The horizontal, x, and the vertical, y, distances of the eye of the vortex from the walls of the canal were normalized with the canal width and depth as x/w and y/d, respectively. Figure 6.8a shows the correlations between the normalized time, t/T, and normalized horizontal distance of the vortex eye, x/w, for bores with different canal and impoundment depths. As shown in this figure, the normalized horizontal distance of the vortex eye increased linearly with time for the canal depth d = 0.05 m. The maximum variations of x/w for the canal depth d = 0.05 m were 0.26 and 0.14 for d_o = 0.30 m and 0.40 m at t/T = 29 and 25, respectively. However, for the canal depths, d = 0.10 m and 0.15 m, the variations of x/w gradually increased until reached peak values of 0.45 and 0.80 for d_o = 0.30 m and 0.40 m, respectively. For the canal depths d = 0.10 m and 0.15 m, the variations of x/w with time indicate a gradual increase until the separation of the vortex eye began at x/w = 0.58 and t/T = 18. Following the separation, the variations of x/w with time slightly increased to reach the x/w of the deep canal with the highest impoundment depth. Figure 6.8b shows the variations of y/d with t/T for different impoundment and canal depths. The vertical distance from the canal bed was found to be time independent in shallow canals (i.e., d = 0.05 m), and the value of y/d was found to be equal to 0.59. However, for the canal depth d = 0.10 m, the variations in y/d started from y/d = 0.59 and gradually decreased until reaching the lowest value of y/d = 0.20 at t/T = 15. As time passed, the value of y/d increased from the minimum to approximately the same range as y/d = 0.59. In the deep canal (d = 0.15 m), the variations of y/d with time were similar to those with the medium depth canal and reached their minimum value at y/d = 0.20.

6.3.4 Time Histories of Turbulent Kinetic Energy

The effects of canal depth on the time histories of the turbulent kinetic energy, k, are shown in Figure 6.9.

The impoundment depth and canal width were kept constant, with values of d_o = 0.3 m and w = 0.6 m, respectively. In this figure, the contour plots of the turbulent kinetic energy for different canal depths of d = 0.05 m, 0.10 m, and 0.15 m are presented. At t_* = 0.5 s, the turbulent kinetic energy of the bore jet stream developed in the vicinity of the upstream wall of the canal and propagated gradually downstream as the bore passed over the canal. At t_* = 1.5 s, the area with the maximum turbulent kinetic energy reached its highest value in the shallow, medium, and deep canals. The region of the bore's maximum turbulent kinetic energy (i.e., k = 0.20 m²/s²) started disappearing gradually once the bore reflecting in the upstream direction of the canal. Then, at t_* = 2.0 s, the area of peak turbulent kinetic energy started decreasing in time. However, at t_* = 3.5 s, the region with the maximum turbulent kinetic energy remained in the shallow- and medium-depth canals, but completely disappeared in the deep canal. It can be concluded that the region of maximum turbulent kinetic energy disappeared rapidly as the canal depth increased.

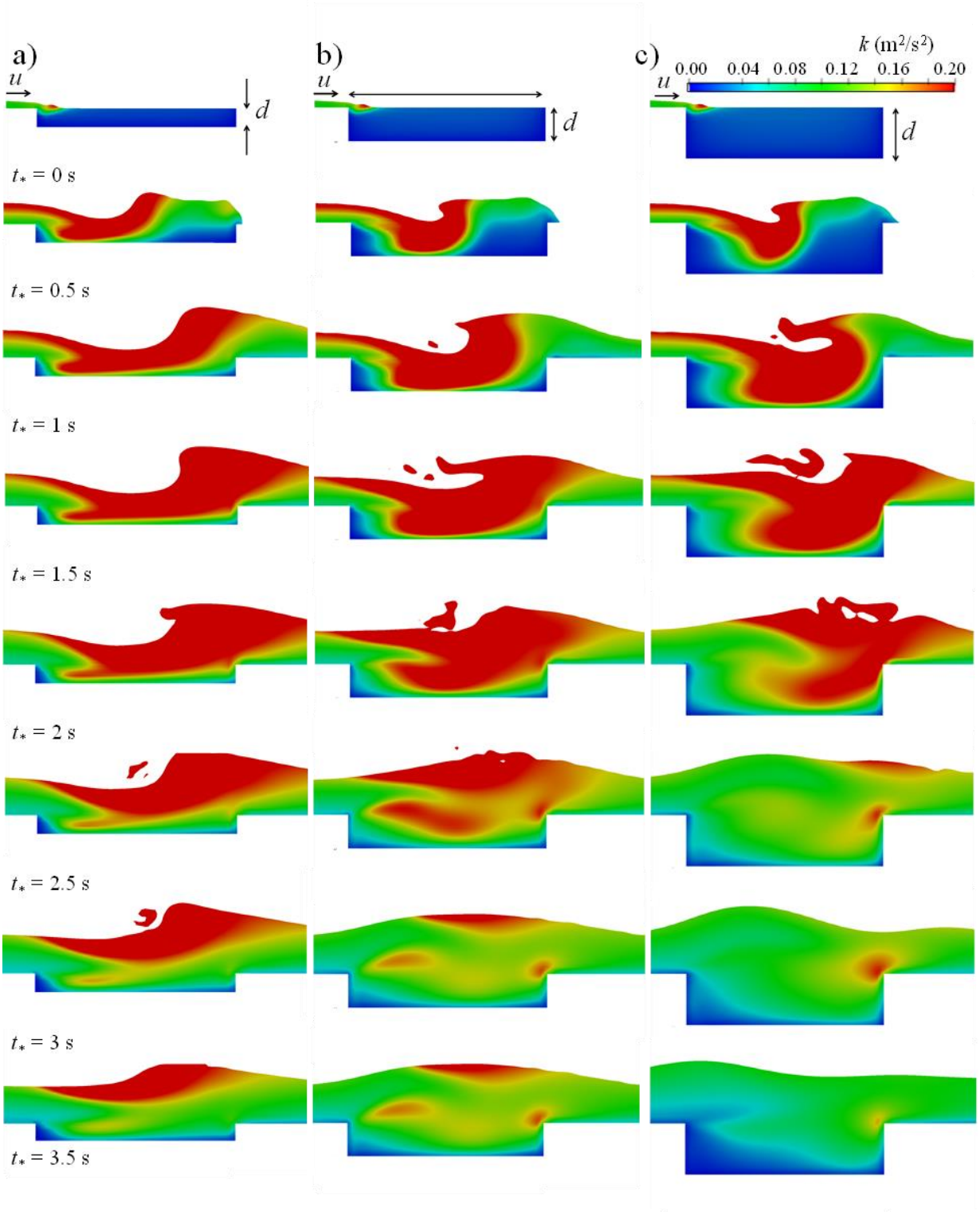

Figure 6.9. Effects of the canal depth on the time histories of turbulent kinetic energy, *k*, with time for a bore from an impoundment with a depth of d_o = 0.30 m passing over a canal with a width of w = 0.60 m: a) d = 0.05 m; b) d = 0.10 m; c) d = 0.15 m.

Figure 6.10 shows the effects of canal depth on the time histories of the energy dissipation rate, ε, for tests with an impoundment depth of d_o = 0.3 m and canal width of w = 0.6 m, respectively.

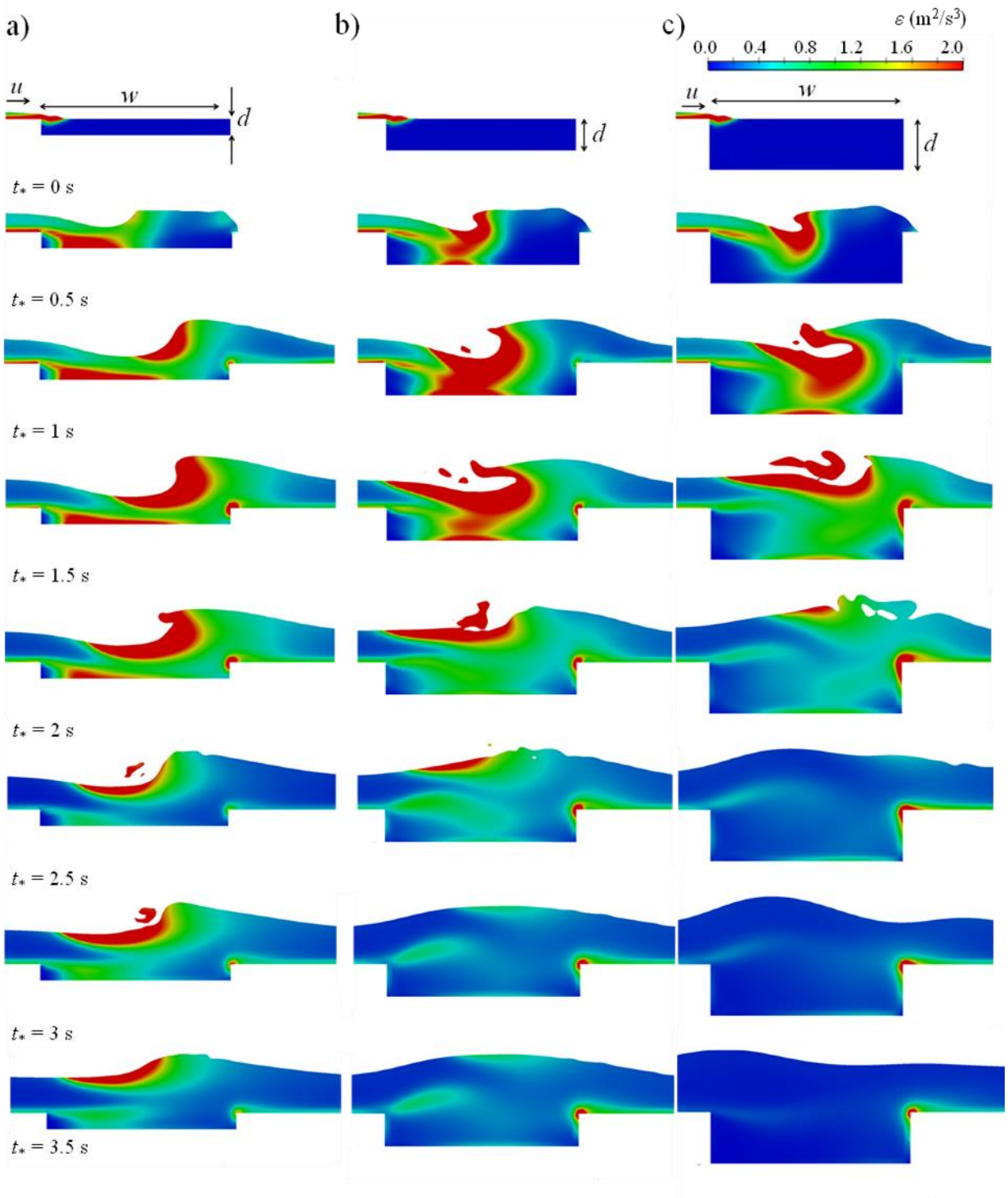

Figure 6.10. Effects of the canal depth on the time histories of energy dissipation rate, ε, with time for a bore from an impoundment with a depth of d_o = 0.30 m passing over a canal with a width of w = 0.60 m: a) d = 0.05 m; b) d = 0.10 m; c) d = 0.15 m.

A region with an energy dissipation rate of 2 m^2/s^3 is labeled as an area with a strong energy dissipation rate. A region with a strong energy dissipation rate formed in the middle of the canal and decreased with time. The region of strong dissipation gradually moved towards the downstream part of the canal. For shallow, medium, and deep canals, the strong energy dissipation region reached the longest distance from the upstream wall of the canal at $t_* = 1.5$ s with values of 0.55 m, 0.47 m, and 0.54 m, respectively. Those regions gradually moved back towards the upstream wall of the canal. The upward deflection of the region of maximum energy dissipation increased the water recirculation over the canal and gradually moved towards the upstream wall of the canal. In the medium and deep canals, the region of maximum energy dissipation disappeared at $t_* = 3$ s and 2.5 s, respectively, while this region still appeared in the shallow canal even at $t_* = 3.5$ s. The contour plots of the energy dissipation rate indicated that the overall energy dissipation rate decreased with increased canal depth.

6.4 Numerical Experiments

Recent tsunami calamities have caused overwhelming damage to well-engineered coastal infrastructure, showing that the existing design guidelines still require development in order to properly quantify tsunami load estimations for the design of tsunami-resistant infrastructure. The outcomes of the present numerical simulation have a widespread range of applications, such as in river and coastal flooding mitigation plans, and can contribute to improving new design guidelines for infrastructure affected by extreme flows, such as mitigation canals, coastal structures, submerged pipes, and communities located in coastal regions.

6.4.1 Specific Momentum

A series of numerical experiments was performed in order to investigate the effects of canal orientation with respect to the incoming direction of the flow on the specific momentum flux and energy in the upstream and downstream parts of mitigation canals. The schematic view of the computational domain for the original and extended flume is shown in Figure 6.1.

The hydrodynamic forces are a combination of the friction forces produced as water propagates around the structure and the lateral forces produced from the pressure loads of the flowing mass of water. The hydrodynamic forces during a tsunami depend on the combination $(hu^2)_{max}$, and by using existing simulation data or running a comprehensive numerical simulation model, the maximum value of hu^2 can be determined. FEMA P-646 suggests that running a detailed numerical simulation in the run-up region ought to be done with a fine mesh resolution to confirm sufficient precision in the estimation of the momentum flux $(hu^2)_{max}$. Accordingly, the maximum momentum has been assumed to rely on the combination $(hu^2)_{max}$ in this study. Thus, the pressure is considered to be approximately the same at the measurement locations. Figure 6.11. shows the effects of canal orientations of $\theta = 0°$, 15°, 30°, 45°, and 60° on time histories of specific momentum per unit mass per unit width. The specific momentum simply contains the flow depth and velocity term, since the two adjacent positions have about the same pressure.

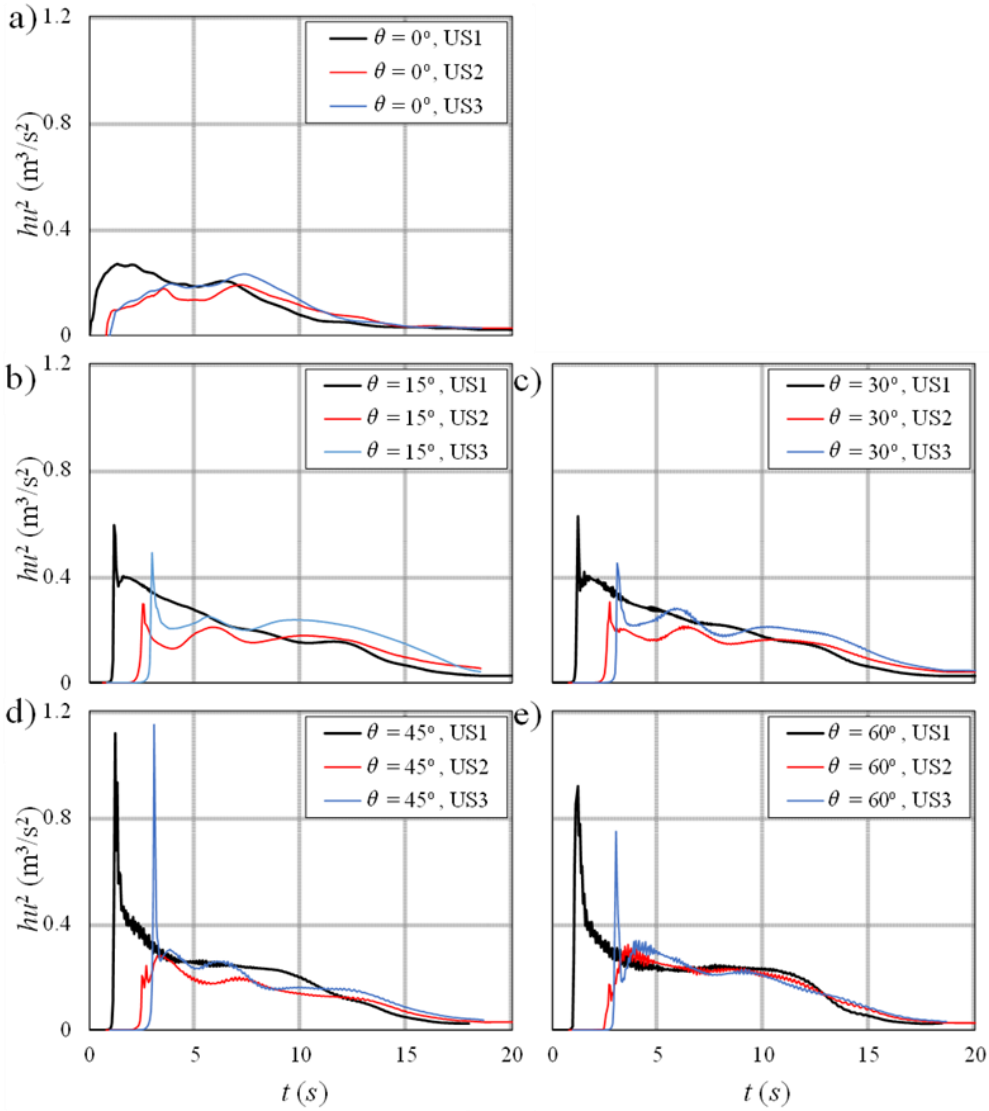

Figure 6.11. Effects of the mitigation canal alignment, θ, on the time histories of the rate of change of specific momentum with time for a bore from an impoundment with a depth of d_o = 0.30 m passing over a canal with a width of w = 0.60 m and depth of d = 0.10 m: a) θ = 0°; b) θ = 15°; c) θ = 30°; d) θ = 45°; e) θ = 60°.

The impoundment depth, canal width, and depth used in this simulation were d_o = 0.3 m, w = 0.6 m, and d = 0.1 m, respectively. The flume width was extended from 0.38 m to 1.8 m to reduce the wall effect in oblique canals. The maximum specific momentums in tests with perpendicular canals (i.e., θ = 0°) and at US1, US2, and US3 were 0.27 m^3/s^2, 0.19 m^3/s^2, and 0.23 m^3/s^2, respectively, and the peak specific momentums occurred at approximately t = 1.4 s, 7.1 s, and 7.3 s, respectively (see Figure 6.11a). The reduction in the specific momentum at 0.2 m and 0.58 m downstream of the canal may be due to the formation of a surface hydraulic jump and the impact of the flow stream with the canal. Figure 6.11a shows that the maximum specific momentums in the canal downstream and at US2 and US3 were approximately 30%, and were 15% less than the peak specific momentum at US1.

Figure 6.11b shows the time history of the specific momentum in the mitigation canal with an alignment of θ = 15°. The peak specific momentums at the US1, US2, and US3 sensors were 0.59 m^3/s^2, 0.31 m^3/s^2, and 0.49 m^3/s^2, respectively. The peak specific momentums in the location of US1, US2, and US3 sensors occurred at approximately t = 1.2 s, 2.5 s, and 3.0 s, respectively. The maximum specific momentums at the locations of US2 and US3 downstream of the canal were approximately 47% and 17% less than the peak specific momentum at the position of US1. As shown in Figure 6.11, the peak specific momentums increased with increasing angle of canal orientation, θ. Figure 6.11c shows the peak specific momentum for a canal with θ = 30°. It was found that the maximum specific momentums at the locations of the US1, US2, and US3 sensors were 0.63 m^3/s^2, 0.31 m^3/s^2, and 0.45 m^3/s^2, and that they occurred at t = 1.2 s, 2.5 s, and 3.0 s, respectively. Generally, the maximum specific momentum reached its highest value at the location of US3 for the canal orientation of θ = 45° (see Figure 6.11d). The maximum specific momentum at US3 for the canal orientation of θ = 45° was approximately 5 times the maximum specific momentum in the benchmark test (i.e., θ = 0°).

Figure 6.12 shows the variations in the maximum specific momentum flux, $(hu^2)_{max}$, for five different canal orientations, θ, for the same impoundment depths of d_o = 0.40 m and different canal depths of d = 0.05 m, 0.10 m, and 0.15 m. The values of peak specific momentum were taken at 0.20 m upstream (US1) and 0.20 m (US2) and 0.58 m (US3) downstream of the canal.

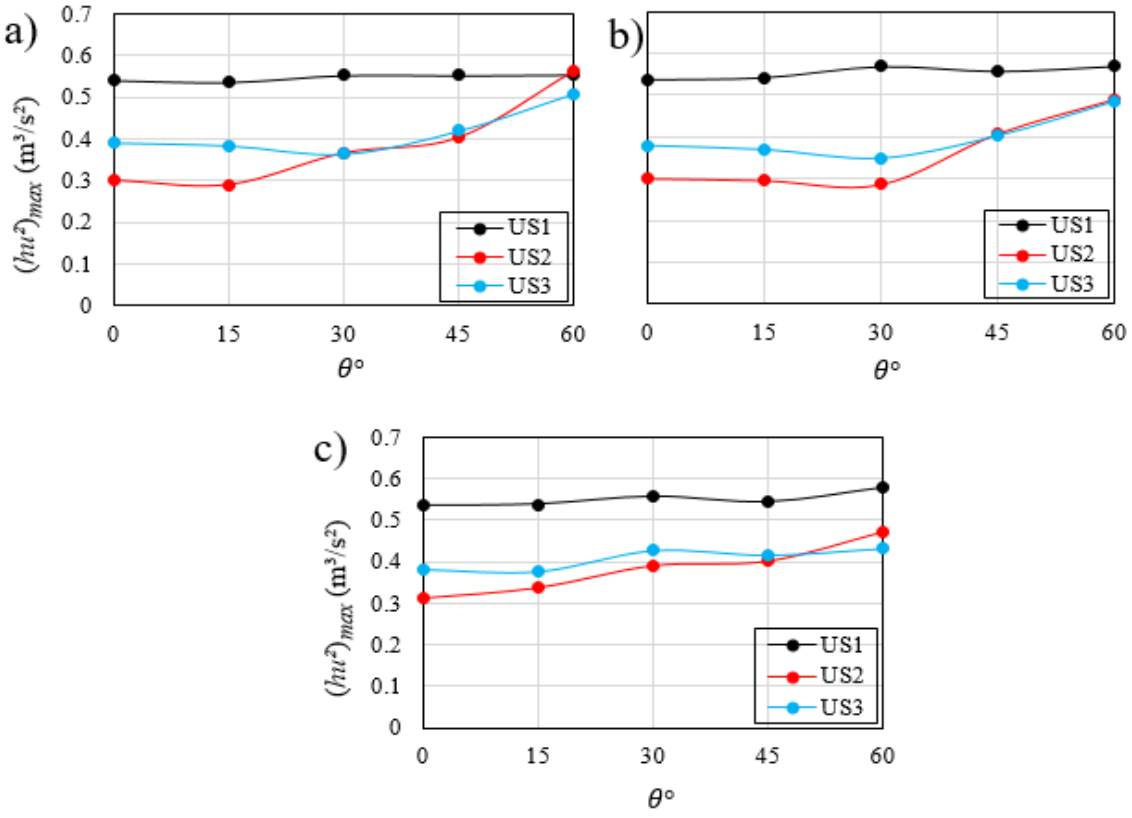

Figure 6.12. Effect of the channel alignment, θ, on the variations of the maximum rate of change of specific momentum before and after the canal for d_o = 0.40 m, and w = 0.60 m: a) d =0.05 m; b) d = 0.10 m; c) d = 0.15 m.

Figure 6.12a shows the correlation of the maximum specific momentum with the canal orientation for d = 0.05 m. The maximum specific momentums at the locations of US2 and US3 gradually increased as the canal orientation increased with respect to the longitudinal axis, while the peak specific momentums were constant at a location 0.2 m upstream of the canal. The lowest maximum specific momentum for θ = 15° and 30° and at the locations of US2 and US3 sensors were 0.29 m^3/s^2 and 0.37 m^3/s^2, respectively, while the highest peak specific momentum at the same locations were observed for the canal orientation of θ = 60° and values of 0.56 m^3/s^2 and 0.51 m^3/s^2, respectively.

Figure 6.12b shows the variations in the peak specific momentum with canal orientation for a simulation with a canal depth of d = 0.10 m. Similar to the shallow canal, the maximum specific momentums were invariant with respect to the canal orientation for the sensor locations of US1, US2, and US3 for a canal orientation $\theta \leq 30$. The lowest value of the maximum specific momentum for θ = 30° and at the locations of US2 and US3 were 0.29 m^3/s^2 and 0.35 m^3/s^2, respectively, whereas the highest value of the maximum specific momentum became independent of the sensor location for $45° \leq \theta \leq 60°$. The peak specific momentum downstream of the canal and for θ = 45° was 0.41 m^3/s^2 and reached the highest value of 0.49 m^3/s^2 for θ = 60°. Figure 6.12c shows the effect of canal orientation on the variations of peak specific momentum for a canal depth of d = 0.15 m. It was observed that the maximum specific momentum increased linearly with the canal orientation. Downstream of the canal, the lowest peak specific momentums for θ = 0° and 15° were 0.31 m^3/s^2 and 0.38 m^3/s^2, respectively, while the highest peak specific momentums for the test with θ = 60° were 0.47 m^3/s^2 and 0.43 m^3/s^2, respectively.

6.4.2 Specific Energy

Figure 6.13. displays the time histories of the influences of canal alignment angles of θ = 0°, 15°, 30°, 45°, and 60° on discrepancies in the specific energy. Water from an impoundment with a depth of d_o = 0.3 m proceeded over a canal with a width of w = 0.6 m and depth of d = 0.1 m.

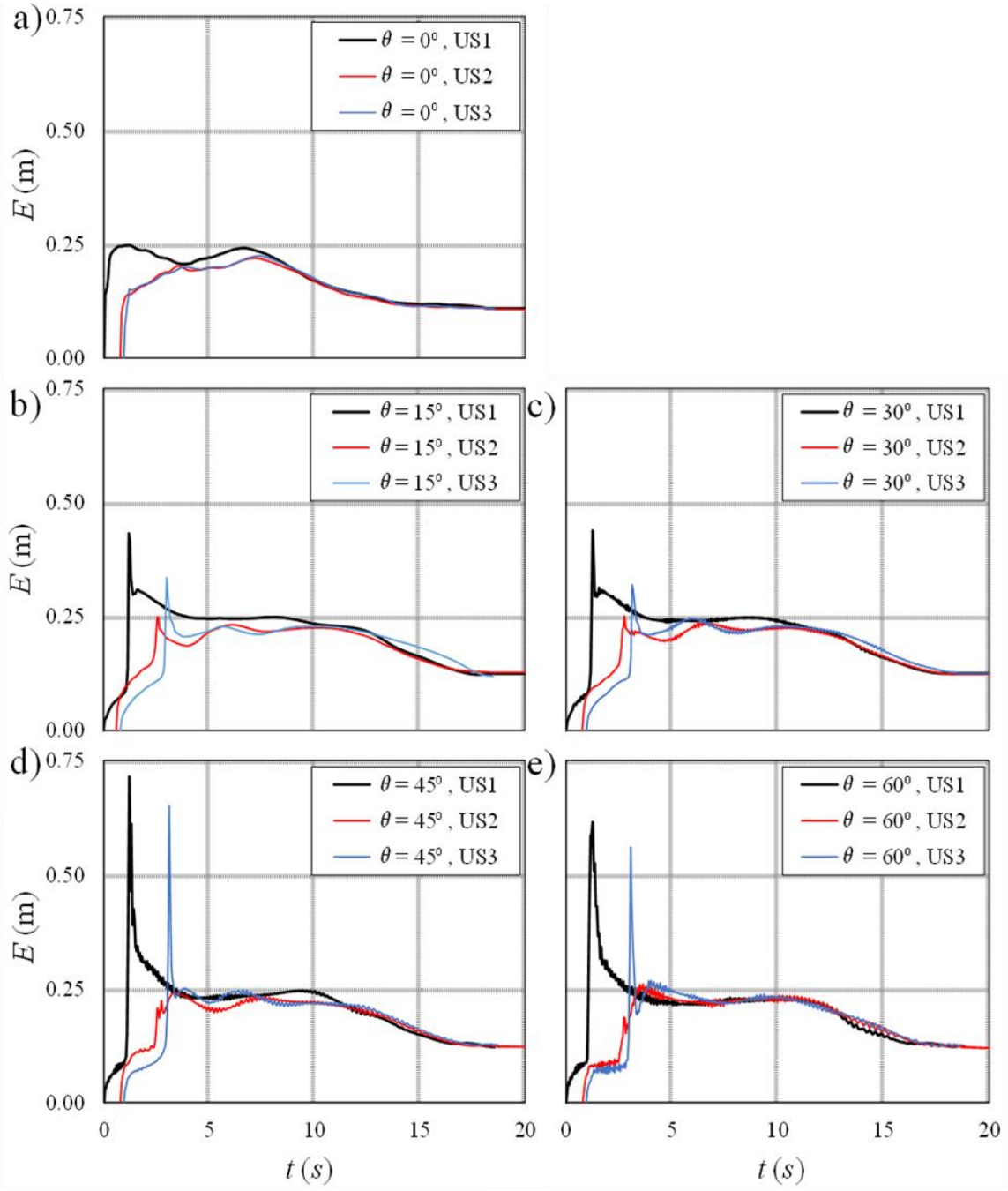

Figure 6.13. Effects of the mitigation canal alignment, θ, on the time histories of the specific energy, E, with time for a bore from an impoundment with a depth of d_o = 0.30 m passing over a canal with a width of w = 0.60 m and depth of d = 0.10 m: a) θ = 0°; b) θ = 15°; c) θ = 30°; d) θ = 45°; e) θ = 60°.

The width of the flume was increased to 1.8 m to diminish the boundary effect in the canals. For an initial canal orientation of θ = 0°, the maximum specific energy at US1, US2, and US3 was nearly 0.25 m, 0.22 m, and 0.23 m, respectively (see Figure 6.13a). The maximum specific energy at US2 and US3 was 12% and 8% lower than the maximum specific energy measured at US1.

In Figure 6.13b, the peak specific energy in the tests with a canal alignment of θ = 15° at US1, US2, and US3 was 0.43 m, 0.25 m, and 0.34 m, respectively, and the peak specific energy at the positions US2 and US3 was approximately 42% and 21%, respectively, lower than the peak specific energy at US1. The maximum specific energy in the experiments with an orientation angle of θ = 30° is shown in Figure 6.13c. The maximum specific energy at US1, US2, and US3 was found to be 0.44 m, 0.25 m, and 0.32 m, respectively. The peak specific energy at the positions of US2 and US3 was found to be approximately 43% and 27%, respectively, lower than the peak specific energy recorded at the position of US1.

Overall, the peak specific energy had a higher value at the position of US1 when computed for a canal alignment of θ = 45°. The peak specific energy at US1 for a canal alignment of θ = 45° was almost 3 times greater than for the alignment of θ = 0° at the corresponding location. The differences in the maximum specific energy may be due to the distant location from the flume sidewalls of the two upstream corners of the canal with θ > 0°. Thus, the projected width facing the flow path increased as θ increased.

Figure 6.14 displays the time histories in the specific momentum flux generated with a canal orientation of θ = 30°, impoundment depth of d_o = 0.40 m, canal width of w = 0.60 m, and canal depths of d = 0.0 m, 0.05 m, 0.10 m, and 0.15 m.

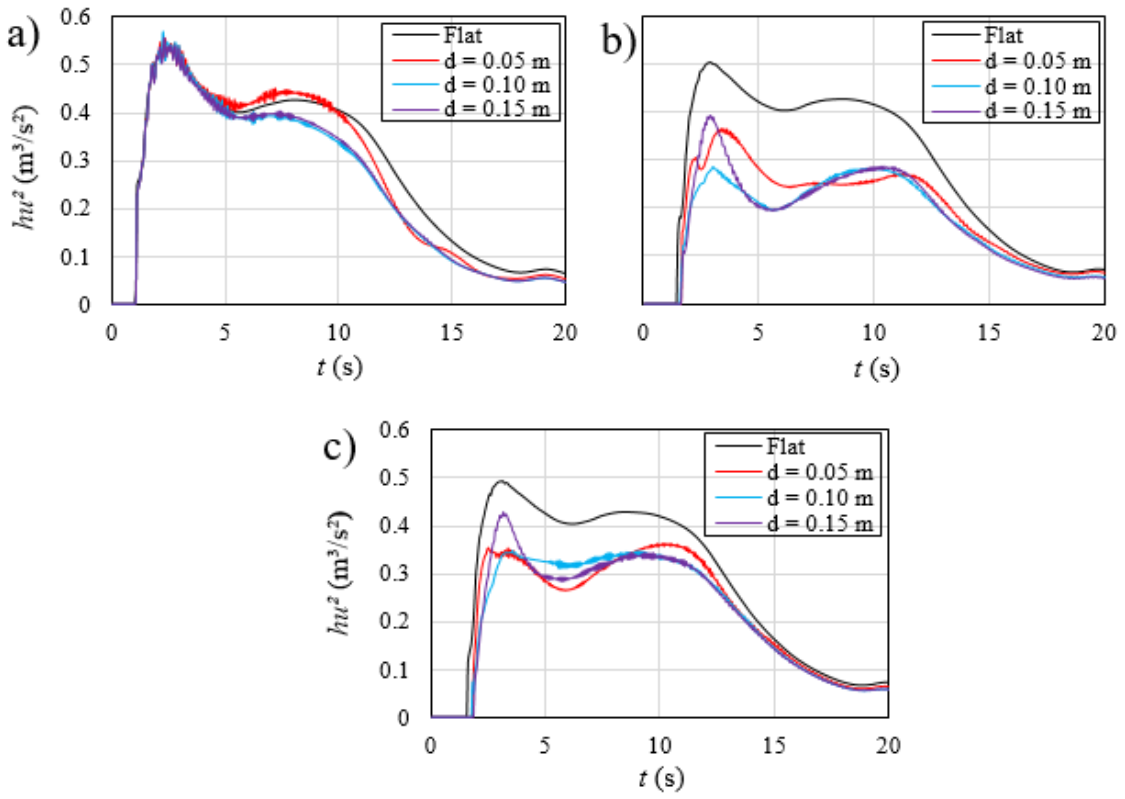

Figure 6.14. Effect of the canal depth, d, on the time history of specific momentum flux for a bore from an impoundment with a depth of d_o = 0.40 m passing over a rectangular canal with a width of w = 0.60 m and canal alignment of θ = 30°: a); US1; b) US2; c) US3.

The values of the specific momentum flux were measured at three different positions, at 0.2 m before the canal (US1) and 0.2 m (US2) and 0.58 (US3) after the canal. As Figures 6.14a, 6.14b, and 6.14c show, the highest peak specific momentum fluxes over the horizontal surface at US1, US2, and US3 were 0.53 m^3/s^2, 0.51 m^3/s^2, and 0.50 m^3/s^2, respectively. Figure 6.14a shows that the peak bore specific momentum fluxes at US1 propagating over various canal depths of d = 0.05 m, 0.10 m, and 0.15 m were 0.55 m^3/s^2, 0.57 m^3/s^2, and 0.56 m^3/s^2, respectively. The specific momentum fluxes confirmed a nearly similar bore trend at US1.

In Figure 6.14b, the maximum specific momentum fluxes at US2 passing over canals with depths of d = 0.05 m, 0.10 m, and 0.15 m were 0.37 m^3/s^2, 0.29 m^3/s^2, and 0.39 m^3/s^2, respectively. Smaller peak specific momentum fluxes were observed for the bore propagating over the shallow, medium-depth, and deep canals, with percentages of approximately 28.7%, 43.5%, and 22.8%, respectively, in comparison with the tests without the presence of a canal. Figure 6.14c shows that the maximum specific momentum fluxes at US3 propagating over canals with depths of d = 0.05 m, 0.10 m, and 0.15 m were 0.37 m^3/s^2, 0.35 m^3/s^2, and 0.43 m^3/s^2, respectively. The specific momentum fluxes for the bore propagating across the shallow, medium-depth, and deep canals had lower peaks, with percentages of 26.4%, 29.6%, and 13.7%, respectively.

The turbulent bore development within and around the canals led to increasing energy losses downstream. The highest values of the specific momentum fluxes at the location of US1 passing over canals with depths of d = 0.05 m, 0.10 m, and 0.15 m had higher percentages, of approximately 33.9%, 49.6%, and 29.8%, respectively, in comparison with the same tests at the location of US2. Additionally, when comparing the tests at US1 passing over canals with depths of d = 0.05 m, 0.10 m, and 0.15 m with the corresponding tests at US3, the highest values for the specific momentum fluxes at US1 had higher percentages, of nearly 34.1%, 38.6%, and 23.1%, respectively. In general, no such change was observed for the maximum specific momentum flux at US1 for different canal depths. The specific momentum flux per unit mass per unit width hu^2 is an important factor directly affecting the hydrodynamic loading on structures. FEMA P-646 points out that $(hu^2)_{max}$ does not precisely equal $(h_{max} * u^2_{max})$, as the maximum flow depth and flow velocity may not occur at certain locations at the same time. The highest value of hu^2 can be found by using current simulation data or by running the numerical simulation model. The maximum specific momentum flux at the location of US1 of a bore passing over a canal with depth of d = 0.10 m had the highest percentages, of approximately 49.6% and 38.6%, respectively, in comparison with the same tests at the locations of US2 and US3. However, the maximum specific momentum flux for the canal with a depth of d = 0.10 m had the highest percentages at US2 and US3 in comparison with canal depths of d = 0.05 m, and 0.15 because of the maximum flow depth and minimum flow velocity (vice-versa, minimum flow depth and maximum flow velocity) occurring at certain locations at the same time.

6.5 Discussion

The mitigation of dam-break waves propagating over a rectangular canal located perpendicular on the direction of the flow and which is fully filled with water was analyzed numerically. The effects of the canal depth and its orientation were investigated by modeling this canal with a constant

width of w = 0.6 m, depths of d = 0.0 m, 0.05 m, 0.10 m, and 0.15 m, and with orientations of θ = 0°, 15°, 30°, 45°, and 60°. The peak specific momentum without the presence of the canal exhibited a decrease of approximately 9.3% at the locations of US2 and US3 compared to US1. For the 0.05 m canal depth, the peak specific momentum decreased by 27% and 13.7% at US2 and US3, respectively. For canal depths of 0.10 m and 0.15 m, however, the peak specific momentum declined by almost 28.3% and 27.9% at US2, respectively, and declined by nearly 14.5% and 16.9%, respectively, at US3. Similarly, the differences in the maximum specific energy over a horizontal bed exhibited a nearly 5.7% decrease at the locations of US2 and US3. For the 0.05 m canal depth, the maximum specific energy decreased by approximately 7.0% and 7.6% at US2 and US3, respectively, although the 0.10 m and 0.15 m canal depths exhibited higher differences compared to the 0.05 m canal depth and horizontal bed, such as the maximum specific energies decreasing by around 10.2% and 9.6%, respectively, at both locations downstream of the canal. Overall, higher downstream variations were found in the time histories of specific momentum and energy in the presence of a canal.

The non-dimensional specific momentum and mean flow energy downstream and upstream of the canal exhibited similar patterns for the three impoundment depths and three canal depths. For the 0.4 m impoundment depth, the lowest non-dimensional specific momentum was as low as 60% of that of the 0.10 m and 0.15 m canal depths, while the lowest non-dimensional specific momentums were 70% and 89% for the 0.3 m and 0.2 m impoundment depths, respectively, and canal depths $\geq$ 0.10 m. Additionally, the lowest non-dimensional mean flow energy was as low as 41% of that of the 0.10 m canal depth and the 0.3 m impoundment depth. For the three impoundment depths, the 0.10 m and 0.15 m canal depths had the lowest, and nearly equal, non-dimensional specific momentum and mean flow energy.

It can be inferred that the jet stream of maximum vorticity in the shallow, medium-depth, and deep canals reached their longest distances at 0.20 m, 0.24 m, and 0.30 m, respectively, from the upstream edge of the canal. The longest movement of the vortex eyes in the shallow, medium-depth, and deep canals were 0.12 m, 0.26 m, and 0.30 m, respectively, from the upstream edge of the canal. Additionally, the normalized horizontal distance of the eye of the vortex x/w gradually increased with time, reaching maximum values of 0.26 and 0.14 for d_o = 0.30 m and 0.40 m, respectively, for d = 0.05 m. The variations in x/w with time increased steadily for the canal depths of d = 0.10 m and 0.15 m and reached their maximum values of 0.45 and 0.80 for d_o = 0.30 m and 0.40 m, respectively. For the medium-depth and deep canals, the variations in x/w showed a steady rise until separation of the eye of the vortex occurred at x/w = 0.58 and t/T = 18. The normalized vertical distance of the vortex eye y/d was found to be time-independent for d = 0.05 m, with a value of 0.59. However, the variations y/d gently declined for d = 0.10 m from y/d = 0.59 until reaching the lowest value of y/d = 0.20 at t/T = 15. Then, the value of y/d rose from its lowest point to about y/d = 0.59. Similarly, the variations in y/d with time reached their minimum value at y/d = 0.20 for d = 0.15 m.

The region of maximum turbulent kinetic energy reduced gradually as after the initial bore passed over the canal, indicating a dissipation of energy due to the existence of the mitigation canal, and it may be concluded that the region of maximum turbulent kinetic energy vanished with increased canal depth. Additionally, the maximum penetration length of the energy dissipation formed in the

middle of the canal and then traveled steadily downstream. The maximum energy dissipation regions reached their longest distances from the upstream edges of the shallow, medium, and deep canals with values of 0.55 m, 0.47 m, and 0.54 m, respectively. Then, the maximum bore jet stream moved slowly back in the upstream direction of the canal.

It can be observed that with the canal orientation of θ = 45°, the maximum specific momentum reached its highest value at the location of US3. The maximum specific momentum of θ = 45° at US3 was approximately 5 times greater than the maximum specific momentum for θ = 0° at the corresponding location. However, the maximum specific energy approached its highest value of θ = 45° at US1. In the case of θ = 45°, the maximum specific energy was nearly 3 times higher than that of θ = 0° at US1, although the values of the maximum specific momentum and maximum specific energy remained almost equal at US2 for the different canal orientations.

The correlation of maximum specific momentum with canal orientation for d = 0.05 m shows that the lowest (best) maximum specific momentums at the US2 and US3 sensors for θ = 15° and 30° were 0.29 m^3/s^2 and 0.36 m^3/s^2, respectively. For the canal depth of d = 0.10 m, the lowest (best) maximum specific momentums at the positions of US2 and US3 and for θ = 30° were 0.29 m^3/s^2 and 0.35 m^3/s^2, respectively, while the lowest (best) peak specific momentums for θ = 0° and 15° were 0.31 m^3/s^2 and 0.38 m^3/s^2, respectively, for the canal depth of d = 0.15 m. In the first part of this companion paper, three different numerical turbulence models, i.e., the classic *k-ε*, Realizable *k-ε*, and RNG k-ε models, were used in order to determine the best match with the physical experiments. The experimental and numerical water surface profiles matched well, with a root mean square error (RMSE) of less than 6.7% and a relative error of less than 8.4%. Although all of the numerical simulations agreed well with the experimental results, the standard k-*ε* model provided the best match. As a result, the standard k-*ε* turbulence model was employed to investigate the present work.

The strong turbulent formation of bores within and around canals increase specific momentum and energy losses downstream. Higher peak specific momentum fluxes were observed at US1, with nearly 33.9%, 49.6%, and 29.8% for bores proceeding over canals with depths of d = 0.05 m, 0.10 m, and 0.15 m, respectively, in comparison with corresponding measurements at US2. Additionally, when compared to measurements taken at US3, US1 had greater bore specific momentum flux peaks, of nearly 34.1%, 38.6%, and 23.1%, for bores propagating over canals with depths of d = 0.05 m, 0.10 m, and 0.15 m, respectively.

6.6 Conclusions

The present study attempted to investigate, using a numerical model and based on experimental work conducted by the authors, the effects of mitigation canals on the propagation of a turbulent bore propagating over it. The authors drew the following conclusions:

- Mitigation canals are capable of reducing the maximum specific momentum and energy of the turbulent bores as they propagated over them.

- For the same bore depth, an increase in the depth of the canal from shallow (d = 0.05 m) to medium and deep canals ($d \geq$ 0.10 m), led to a reduction in the turbulent bore maximum specific

momentum and energy. This reduction can be attributed to the greater amount of entrained air in the abovementioned canals ($d \geq 0.10$ m) which leads to lower specific momentum and energy.

- For the different bore depths employed, an increase in the depth of the canal from shallow (d = 0.05 m) to medium and deep canals ($d \geq 0.10$ m) led to a reduction in the bore ratio of the downstream to upstream specific momentum.

- For the different bore depths, the medium and deep canals ($d \geq 0.10$ m) achieved similar dimensionless specific momentum and mean flow energy. Generally, the variation of the ratio of downstream and upstream peak specific momentum and mean flow energy decreased as the impoundment depth increased. Thus, the three canal depths more practical with higher bore depths.

- The area of the jet stream of the maximum turbulent kinetic energy, and vorticity, as well as the energy dissipation, were shown to dissipate faster over the same period of time for higher canal depths compared to the jets generated by small canal depths. In general, bores plunging into the deeper canals generated higher energy and momentum dissipation and thus are more affected by the presence of the canal, whereas shallower canal depths generated bores have less energy and momentum dissipation and thus are less affected by the presence of the canal. Thus, this area of the jet stream was assumed to dissipate faster due to an increase in the energy and momentum dissipation over the deeper canal.

- Generally, the presence of the canal, for both the perpendicular and the angled ones, caused the maximum specific momentum and energy of the turbulent bore to decrease downstream of the canal. The maximum specific momentum and energy reached the highest value for a canal orientation of $\theta = 45°$. In the case of the angled canals ($\theta = 15°$, 30°, 45° and 60°), the maximum specific momentum and energy were higher when compared with the perpendicular one. This may be attributed to the distant positions from the flume sidewalls of the two upstream corners of the canal with $\theta > 0°$. Thus, the projected width facing the flow path increased as θ increased. As a result, the significant formation of turbulent bores around and within the canal increased specific momentum and energy losses after the canal.

- The lowest (highest reduction of the) maximum specific momentums of the turbulent bores for different canal depths and orientations was 0.286 m^3/s^2 for $\theta = 30°$. The effect of canal orientation on the turbulent bore of specific momentum and energy have a wide variety of applications in river and coastal flooding mitigation measures. The results can be used to optimize new design guidelines and specifications for infrastructure affected by severe floods.

- The hydrodynamic forces induced by tsunami flow are a direct function of the momentum flux $(hu^2)_{max}$. By employing the numerical model results the time history of the maximum value of hu^2 could be determined.

7 Conclusions and Recommendations for Future Work

7.1 Conclusions

In this thesis, a series of laboratory tests was conducted to examine the influence of a mitigation rectangular canal on the time-history of the water surface level, velocity, momentum and energy of turbulent bores at locations upstream and downstream of the canal. A dam-break wave approach was employed in the experimental to simulate a broken tsunami wave propagating on a horizontal bed with and without the presence of the mitigation canal. Furthermore, the laboratory results were compared with the results of a three-dimensional unsteady Computational Fluid Dynamics (CFD) model developed in OpenFOAM. The conclusions extracted from this thesis are listed as follows:

7.1.1 Experimental Investigations of Hydraulic Surges Passing over a Rectangular Canal

In this study, an experimental program was conducted to evaluate the effect of a rectangular mitigation canal on turbulent bores propagate over it. The time-series of the water surface and the flow velocity of the bore profiles were calculated at both upstream and downstream locations from the canal to assess the effects of the geometry of the canal on bores generated from three water depths. Time-histories of the water surface and flow velocity while the bore propagated over the canal were compared with the base experiment performed in the absence of the canal with the intention of estimating the effects produced by the presence of the canal. The bore propagating over dry bed were measured at seven different locations alongside its propagation, revealing four regimes describing the time-history of the water surface. In stage I, the water surface profile rapidly amplified from zero and extended nearly 50% of the maximum of the water surface elevation during three to five seconds from the gate lifting. In stage II, the water surface elevation was amplified with a smaller rise compared to stage I, and the water surface level of the extended to its peak, h_{max}. The peak velocity with the depth of impoundment was scalable, and the dimensionless periods at US1 and US3" were nearly equivalent to t/T = 47 and 11, respectively. Stage III in the time-series of the water surface level is defined from at the maximum height and to up to 50% of the maximum water surface level at a particular time, t_q. For stage IV, the quasi steady state condition was characterized by a slowly decreasing water level (hence the name quasi-steady). An equation has been proposed to relate the start of the relatively quasi-steady time t_q with the impoundment depth.

The peak water surface levels of the surge upstream and downstream of the canal, h_{max}, have been derived from the time-series, and they were standardized with the maximum water surface levels of the surge in the absence of a canal, h_o. It was found that the maximum water surface level upstream of the 0.6 m width canal was amplified to 1.4 h_o of the relatively small upstream reservoir head ratio of $d_o/d \leq 4$, and the canal influence on discrepancies of the standardized water surface of the surge become trivial for $4 < d_o/d \leq 8$. The influence of canal geometry on the maximum water surface levels before d = 0.05 m canal was trivial; nevertheless, in the case of the deeper canals, the maximum water surface level of the bore was amplified by 60 % and 40 % for d = 0.15

m and 0.10 m, respectively. The water surface level after the canal was amplified between 10 % and 50 % of the water surface level surge in the absence of a canal. Thus, the standardized water surface level of the surge was amplified by the increased in the upstream reservoir head with mean magnitudes of 40 %, 30 %, and 20 % for impoundment depths of d_o = 0.40 m, 0.30 m, and 0.20 m, respectively, irrespective of the dimensions of the canal.

The aspect ratio of the canal influences on the peak surge water surface level after the canal showed that the standardized maximum water surface level of the surge and the upstream reservoir heads became independent for $w/d \leq 20$. The standardized maximum water surface level of the surge reduced from 1.15 ± 0.05 for w/d = 4 and decreased to a minimum magnitude of h_{max}/h_o = 1.02 ± 0.035 for w/d = 20. For $w/d > 20$, the standardized maximum water surface level of the surge related with the upstream reservoir heads had magnitudes of 1.24, 1.18, and 1.10 for d_o = 0.4 m, 0.3 m, and 0.2 m as propagating on a wide-ranging extenuation canal (i.e., w/d = 60).

The time-series of the flow velocity of the bore was calculated before and after the canal. The maximum flow velocity declined prior to its arrival at the canal compared to the equivalent result in the absence of a canal. The deceleration of the surge was due to the surface formation of a hydraulic jump at the downstream edge of the canal. It was noticed that the maximum speed decreased as the surge passed over the canal. For the shallow canals (i.e., d/d_o = 1/8), the maximum flow velocity at 0.2 m downstream of the canal was reduced by nearly 60% of the maximum velocity recorded in the absence of the canal. This attributed to the substantial dissipation of momentum. For the deep and medium-depth canals (i.e., d/d_o = 3/8and1/4), the maximum flow velocities were reduced by 40% and 50% of the maximum speed calculated in the absence of a canal, respectively.

7.1.2 Tsunami Induced Bore Propagating over a Canal-Part 1: Laboratory Experiments and Numerical Validation

The influence of the mitigation canal on the bore propagation were investigated both experimentally and numerically. The influence of the canal depth on the wave hydrodynamics such as time-history of the water surface elevation and its flow velocity was measured and numerically simulated for a canal with a fixed width of w = 0.6 m, and four various depths of d = 0 m, 0.05 m, 0.10 m, and 0.15 m. The results of the experimental tests were reproduced by a newly developed three-dimensional multi-phase numerical model. Generally, good agreement was observed between the experimental and numerical results. The performance of the three different turbulence models (the standard k-ε, the Realizable k-ε, and the RNG k-ε) was judged to be good, based on the reasonable estimation of the time-history of the water surface. These three turbulence models achieved almost the same profiles of the water surface propagating over a flat surface and canal, with RMSE < 6.7 % and Relative Error < 8.4. The standard k-ε simulation method was more effective than the other two turbulence models (the Realizable k-ε, and the RNG k-ε), and in both cases the flat surface and the canal, it had the lowest percentage error. It was thus concluded that standard k-ε was a suitable approach to simulate bores.

The experimental and numerical results both indicated that, for all the investigated depths of the canal the maximum water levels increased and the maximum flow velocity decreased as the turbulent bore propagated over the canal in comparison to the case when the canal was not present. The tsunami bore front plunged into the canal, generating a high splash and interacting with the stagnant canal water. The energy of the tsunami bore front decreased significantly due to the turbulence generated by the dynamic impact of the bore with the stagnant canal water. The canal depth was shown to play a significant role in the alteration of bore's water depth and flow velocity both upstream and downstream of the canal. As such, when designing a canal with the precise purpose of alleviating the influence of incoming tsunami flooding, the canal depth should be taken into consideration. A careful selection of the canal depth may increase the elevation of the water surface but significantly decrease the flow velocity of the bore, thus decreasing the tsunami-induced loading on structures situated in its pathway.

As the canal depth increased, results have shown its capability to significantly reduce the momentum of the bore.

The maximum surge velocity decreased, resulting in a large decrease of the momentum as the bore passed over the canal. The vortex eye of the flow moved downstream of the upstream wall of the canal of varying depths at maximum distances of 0.12 m, 0.27 m, and 0.31 m in shallow, medium, and deep canals, respectively.

It was concluded that the mitigation canal has the potential to act as measures which could reduce hydrodynamic loading on critical infrastructure located in tsunami-prone areas. The incipient research proposed in study confirms some of the field observations during past tsunami forensic engineering events.

7.1.3 Tsunami-Induced Bores Propagating over a Canal; Part II: Numerical Experiments Using the Standard k-ε Turbulence Model

By using a numerical model and based on experimental work conducted by the candidate, the present study attempts to investigate the effects of mitigation canals on the propagation of a turbulent bore. The authors drew the following conclusions:

The results of the numerical simulations for the effects of a rectangular mitigation canal filled with water on a tsunami-like turbulent bore propagating over a smooth horizontal surface were presented. The prompt release of water from impoundment reservoirs with depths of d_o = 0.20 m, 0.30 m, and 0.40 m was employed to produce surges analogous to tsunami-induced inundations. Different canal orientations with respect to the transversal axis of the flume of θ = 0°, 15°, 30°, 45°, and 60° as well as canal depths of d = 0.0 m, 0.05 m, 0.10 m, and 0.15 m, with a constant canal width of w = 0.60 m were tested numerically. A significant difference between up- and downstream side of the canal was found in the time series of the maximum specific momentum and energy. The mitigation canal is capable of reducing the maximum specific momentum and energy of a turbulent bore as the latter propagates over the canal. For the same bore depth, an increase in the depth of the canal from shallow (d = 0.05 m) to medium or deep ($d \geq$ 0.10 m), led to a reduction in the maximum specific momentum and energy of the bore. This reduction can be

attributed to the extra amount of entrained air in the deeper canals ($d \geq 0.10$ m), which led to lower specific momentum and energy through dissipation.

However, for the different bore depths employed, an increase in canal depth from shallow (d = 0.05 m) to medium or deep ($d \geq 0.10$ m) canals led to a reduction in the bore specific momentum between the upstream and downstream sections. Generally, variations in the ratio of downstream to upstream peak specific momentum and mean flow energy decreased as the impoundment depth increased. Thus, the canal, regardless of depth, is more effective for higher bore heights. The jet stream of the maximum turbulent kinetic energy and vorticity, as well as of the energy dissipation, were shown to dissipate quicker over the same period of time for deeper canals compared to the jets observed within the smaller canal depths. In general, bores plunging downward into deeper canal depths generated higher energy and momentum dissipation and thus were more affected by the presence of the canal, whereas bores encountering shallower canal depths exhibited less energy and momentum dissipation and are thus less affected by the presence of the canal.

Generally, the presence of a canal, whether perpendicular or at an angle to the direction of the bore propagation, caused the maximum specific momentum and energy of the turbulent bore to decrease downstream of the canal. The maximum specific momentum and energy reached the highest value for the canal orientation of θ = 45°. In the case of the canal placed at an angle (θ = 15°, 30°, 45° and 60°), the maximum specific momentum and energy were higher compared with a perpendicular one. This may be attributed to the fact that the projected width facing the flow path increased as θ increased, and as a result, the turbulence around and within the canal increased the specific momentum and energy losses downstream of the canal. The lowest maximum specific momentum of the turbulent bores for different canal depths and orientations was 0.286 m^3/s^2 for θ =30°. The effect of canal orientation on the specific momentum and energy of turbulent bore could find application in river and coastal flooding mitigation measures.

7.2 Recommendations for Future Work

The current study opens new possibilities for using mitigation canals to add to the provisions of exiting design guidelines for tsunami resistant infrastructure. The suggested future developments are detailed as follows:

1. In this study, the effect of downstream dry bed conditions in the presence of a rectangular canal filled with water was analyzed. However, investigations of the downstream effects in the presence of a mitigation canal with a structure located downstream of the canal equipped with instrumentation could further prove the concept of using the mitigation o reduce the hydrodynamic forces on structures.

2. Tests considering a wide variety of factors such as blockage and aspect ratios of the canal and downstream structures should be investigated.

3. A series of investigations is highly recommended to study the influence of different characteristics of canals located downstream of a reservoir, such as trapezoidal canals, different canal water surface orientations could be considered.

4. A series of examinations to study the influence of multiple structures with different characteristics in the presence of a mitigation canal could be considered. Including macro-roughness elements located in the canal or around it could be considered.

5. To perfectly model entrapped air in order to decrease its effect on water surface profiles when a surge plunges into a canal, a more complex numerical model should be developed. Furthermore, inspecting and comparing the effect of different turbulence models with RANS, LES, and DES should be performed.

Appendix

Data processing

Three different filters were used to post-process the experimental data. These filters have the ability to clean up signals, remove noise, create a smoothing effect, average data, and design decimation and interpolation filters. The first filter was a function used in MATLAB which is based on a criterion for the derivative of the signals. The input parameter is a signal with an acceptable error value. For each signal value, when the derivative is too high, then the signal is smoothed. As such, the lower the acceptable error, the smoother the signal. The second filter was the moving average. This function was used in MATLAB, and the input parameters are the signal and the coefficient of the moving average "a". For each value of the signal x_i, the filter calculates the average of the a-previous and the a-following values of x_i. The result of the filter is a smoother signal. The higher the value of "a", the smoother the signal. The third filter was the "Butterworth", which is a function subroutine in MATLAB. The input parameters are the signals and the bandwidth frequencies. The filter cuts all the values which are not inside the bandwidth, and the result of the filter is a smoother signal. The larger the bandwidth, the smoother the signal.

The challenge was to find the right values for the coefficients for each filter. If the signal is overly smoothed, some peaks and variations are probably lost. Conversely, if the signal is not smoothed enough, there is still too much noise. To find a balance, the candidate had to modify each of the filters' coefficients, depending also on the signal. No filter was better than another, and the results were dependent on the signal. The candidate had to compare each signal to determine which filter was the most efficient. After reducing the noise, the goal was to be able to compare different signals. For this, two problems arose. The first one was that all the signals did not begin at the same instant; secondly, the signals did not all have the same sampling frequency. Therefore, we wrote two MATLAB functions to overcome these issues. To put all the curves at the time starting point (t_o), the candidate wrote the function "zeros.m", which finds the initial moment of the experiment, and set it as $t_o = 0$. The function finds when there is the first sudden increase of the signal and assigns this instant time $t_o = 0$. Also, to put two different signals at the same frequency, the candidate wrote the function "frequency.m". This function selects the signal which has the higher sampling frequency, calculates the ratio between the frequency of the two signals, and deletes from the "higher frequency" signal all the values which do not correspond to the sampling frequency of the "lower frequency" signal. Then, the two signals are comparable and mathematical operations can be done on them if needed.

Froude Number

Froude numbers were calculated for the impoundment depth d_o = 0.40 m for the tests with the presence of the three canals with widths of w = 0.60 m, 1.60 m, and 3.0 m, and depths of d = 0.05 m, 0.10 m, and 0.15 m, respectively (see Figure A.1).

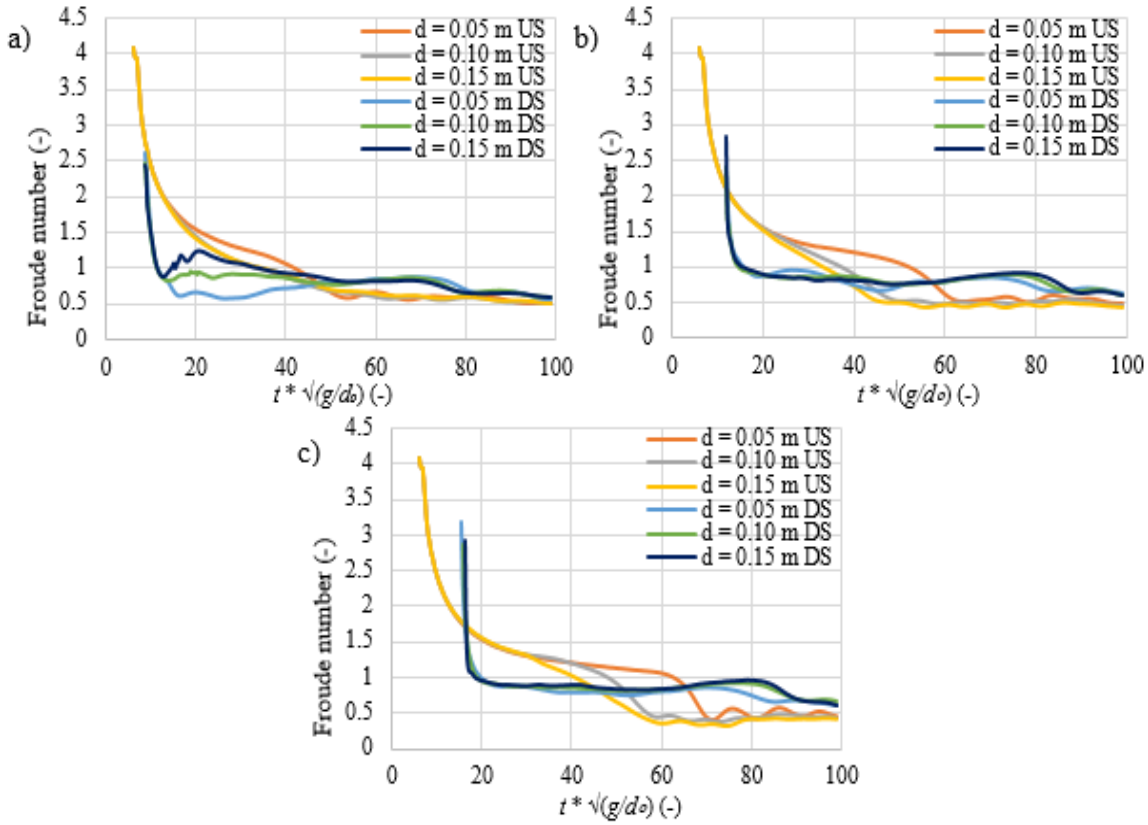

Figure A.1. Froude number time history variations for 0.20 m upstream and downstream of the canal for impoundment depth d_o = 0.40 m, three canal depths d = 0.05 m, 0.10 m, and 0.15 m, and three canal widths (a) 0.60 m, (b) 1.60 m, and (c) 3.0 m.

The Froude number for the bore caused by the canal width 0.60 m for a location placed 0.20 m upstream of the canal's upstream edge sharply decreases, from approximately 4.1 to 1.0 during 36 dimensionless times after the surge initial arrival time, as shown in Figure A.1a. Then, the Froude number continuously drops when the bore reaches the quasi-steady-state flow condition. The Froude number for a location downstream of the canal dropped from about 2.6 to 1.0 after 4 non-dimensional times from the bore's arrival. Then, it further decreased below 1.0 for nearly 3 dimensionless times before raising above 1.0 for approximately 20 non-dimensional times. Figure A.1b. shows the Froude number calculated for the surge caused by the canal with a width of 1.60 m and three different depths at 0.20 m before and after the canal. The Froude number for a location placed 0.20 m upstream of the canal's upstream edge decreased from approximately 4.1 to 1 after 46 dimensionless times from the arrival of the bore, and from approximately 2.4 to 1 after 4 dimensionless times for the location at 0.20 m downstream of the canal. For upstream of the canal with a width of 3.0 m and with three depths (see Figure A.1c), the Froude number declined from nearly 4.1 to 1 after 57 dimensionless times. Following the arrival of the surge, the Froude number for downstream of the canal for the three different canal depths decreased from approximately 2.5 to 1 after 4 dimensionless times. It should be mentioned that the surge upstream of the canal was supercritical, $F_r > 1$, for the three canal widths w = 0.60 m, 1.60 m, and 3.0 m for almost 36, 46, and 57 non-dimensional times, respectively. Also, the surge was supercritical downstream of the canal for nearly 4 non-dimensional times for the three canal widths.

References

Akan, A. O. (2006). Open Channel Hydraulics, Elsevier Ltd., Burlington, MA.

Al- Faesly, T., Palermo, D., Nistor, I., & Cornett, A. (2012). "Experimental modeling of extreme hydrodynamic forces on structural models." *International Journal of Protective Structures*, 3(4), 477-505.

Al-Faesly, T. Q. (2016). "Extreme Hydrodynamic Loading on Near-Shore Structures." *PhD Thesis*, University of Ottawa, 356 p.

Altomare, C., Crespo, A. J., Domínguez, J. M., Gómez-Gesteira, M., Suzuki, T., & Verwaest, T. (2015). "Applicability of smoothed particle hydrodynamics for estimation of sea wave impact on coastal structures." *Coastal Engineering*, 96, 1-12.

Amaechi, C.V.; Wang, F.; Ye, J. (2021). "Mathematical Modelling of Bonded Marine Hoses for Single Point Mooring (SPM) Systems, with Catenary Anchor Leg Mooring (CALM) Buoy Application—A Review." J. Mar. Sci. Eng. 9, 1179.

Amaechi, C.V.; Wang, F.; Ye, J. (2022). "Experimental study on motion characterization of CALM buoy hose system under water waves." J. Mar. Sci. Eng. 10, 204.

Árnason, H. (2005). "Interactions between an incident bore and a free-standing coastal structure." UMI Dissertation Services.

Arnason, H., Petroff, C., & Yeh, H. (2009). "Tsunami bore impingement onto a vertical column." *Journal of Disaster Research*, 4(6), pp. 391-403.

Asadollahi Shahbaboli, N. (2016). "Numerical Modeling of Extreme Flow Impacts on Structures." (Master dissertation, Université d'Ottawa/University of Ottawa), 100 p.

Asadollahi, N. Nistor, I. and Mohammadian, A. (2019a). "Numerical investigation of tsunami bore effects on structures." part I: drag coefficients. *Natural Hazards*, 96(1), pp. 285-309.

Asadollahi, N. Nistor, I. and Mohammadian, A. (2019b). "Numerical investigation of tsunami bore effects on structures." part II: effects of bed condition on loading onto circular structures. *Natural Hazards*, 96(1), pp. 331-351.

ASCE 7-16. (2017). "Minimum Design Loads and Associated Criteria for Buildings and Other Structures.". American Society of Civil Engineers.1, 834p.

ASCE 7-22. (2022). "Minimum Design Loads and Associated Criteria for Buildings and Other Structures.". American Society of Civil Engineers. 1,072 pp. / 2 vols.

Aureli, F., Dazzi, S., Maranzoni, A., Mignosa, P., & Vacondio, R. (2015). "Experimental and numerical evaluation of the force due to the impact of a dam-break wave on a structure." *Advances in Water Resources*, 76, pp. 29-42.

Azimi, A. H., Zhu, D. Z., and Rajaratnam, N. (2011) "Effect of particle size on the characteristics of sand jet in water." *Journal of Engineering Mechanics*, ASCE, Vol. 137, No. 12, pp. 822-834.

Azimi, A., Zhu, D. Z., and Rajaratnam, N. (2012). "Computational Investigation on Vertical Slurry Jets." *Int. J. Multiphase Flow* 47: pp. 94–114.

Baldock, T. E., Peiris, D., & Hogg, A. J. (2012). "Overtopping of solitary waves and solitary bores on a plane beach." *Proceedings of the Royal Society A: Mathematical, Physical and Engineering Sciences*, 468(2147), pp. 3494-3516.

Bardina, J.E., Huang, P.G., Coakley, T.J. (1997), "Turbulence Modeling Validation, Testing, and Development." NASA Technical Memorandum 110446.

Berberovic, E. (2010). "Investigation of free-surface flow associated with drop impact: numerical simulations and theoretical modeling" (Doctoral dissertation, Technische Universität).

Bhattacharya, S., Hyodo, M., Goda, K., Tazoh, T., & Taylor, C. A. (2011). Liquefaction of soil in the Tokyo Bay area from the 2011 Tohoku (Japan) earthquake. *Soil Dynamics and Earthquake Engineering*, *31*(11), 1618-1628.

Biscarini, C., Francesco, S. D., & Manciola, P. (2010). "CFD modelling approach for dam break flow studies." *Hydrology and Earth System Sciences* 14(4), 705-718.

Bricker, J.D. (2015). "On the need for larger Manning's roughness coefficients in depth-integrated tsunami inundation models." Coast. Eng. J., 57, 1550005.

Byatt-Smith, J.G.B. (1971). "The effect of laminar viscosity on the solution of the undular bore." J. Fluid Mech. 48, 33–40.

Cable, M. (2009). "An evaluation of turbulence models for the numerical study of forced and natural convective flow in Atria" (Doctoral dissertation, Queen's University), 136pp.

Carollo, F. G., Ferro, V., & Pampalone, V. (2009). New solution of classical hydraulic jump. *Journal of Hydraulic Engineering*, *135*(6), 527-531.

Chamani, M., & Beirami, M. K. (2002). Flow characteristics at drops. *Journal of hydraulic engineering*, *128*(8), 788-791.

Chamani, M.R., Dehghani, A.A., Beirami, M.K., and Gholipour, R. (2013). "Fluid mechanics."2ed Ed., IUT Publishing, p 613.

Chanson, H. (2004). The Hydraulic of Open Channel Flow: An Introduction (2nd ed.). Butterworth-Heinemann. ISBN 978-0-7506-5978-9.

Chanson, H. (2005). "Analytical solution of dam-break wave with flow resistance: Application to tsunami surges." In Proceedings 31st Biennial IAHR Congress, September 2005, Seoul, Korea Vol. 137, pp. 3341-3353.

Chanson, H. (2006). "Tsunami surges on dry coastal plains: Application of dam break wave equations." Coastal Engineering Journal, 48(04), 355-370.

Chanson, H. (2009). "Application of the method of characteristics to the dam break wave problem." Journal of Hydraulic Research, 47(1), 41-49.

Chanson, H. (2009a). Current Knowledge in Hydraulic Jumps and Related Phenomena. A Survey of Experimental Results. *European Journal of Mechanics B/Fluids*, Vol. 28, No. 2, pp. 191–210 (DOI: 10.1016/j.euromechflu.2008.06.004).

Chanson, H. (2009). Development of the Bélanger equation and backwater equation by Jean-Baptiste Bélanger (1828). *Journal of Hydraulic Engineering*, *135*(3), 159-163.

Chanson, H., & Carvalho, R. (2015). Hydraulic jumps and stilling basins. *Energy Dissipation in Hydraulic Structures; Chanson, H., Ed.; CRC Press: Leiden, The Netherlands*, 65-104.

Chanson, H., & Gualtieri, C. (2008). Similitude and scale effects of air entrainment in hydraulic jumps. *Journal of Hydraulic Research*, *46*(1), 35-44.

Chaudhry, M. H. (2008). Open-Channel Flow, Springer Science and Business Media, LLC, New York, NY.

Chock, G. (2015). "The ASCE 7 tsunami loads and effects design standard for the United States." In Handbook of coastal disaster mitigation for engineers and planners (pp. 437-460).

Chock, G. Y. (2016). "Design for tsunami loads and effects in the ASCE 7-16 standard." *Journal of Structural Engineering*, 142(11), 04016093.

Chock, G.; Roberson, I.; Kriebel, D.; Francis, M; Nistor, I. (2013). "Tohoku Japan Tsunami of March 11, 2011—Performance of Structures under Tsunami Loads." ASCE/SEI Report; ASCE, 1801 Alexander Bell Drive, Reston, Virginia, 20191-4400, USA: 2013; p. 359.

Chow, V. (1959). "Open Channel Hydraulics." McGraw-Hill Book Company, Inc.: New York, NY, USA.

Clifford, N. J., & Richards, K. S. (1992). The reversal hypothesis and the maintenance of riffle-pool sequences: A review and field appraisal. In *Lowland floodplain rivers. Geomorphological perspectives* (pp. 43-70).

Crespo, A. J., Gómez-Gesteira, M., & Dalrymple, R. A. (2008). "Modeling dam break behavior over a wet bed by a SPH technique." *Journal of waterway, port, coastal, and ocean engineering*, 134(6), pp. 313-320.

Dao, N. X., Adityawan, M. B., & Tanaka, H. (2013). "Sensitivity analysis of shore-parallel canal for tsunami wave energy reduction." *Journal of Japan Society of Civil Engineers, Ser. B3 (Ocean Engineering)*, 69(2), pp. 401-406.

Dao, N. X., Adityawan, M. B., & Tanaka, H. (2013). Numerical model study on the effect of the canal in reducing tsunami energy. *Tohoku journal of natural disaster science*, *49*, 193-198.

Deshmukh, A. A., Sudharsan, N., Vasudeo, A. D., & Dattatraya Ghare, A. (2019). Effect of roughness on sequent depth in hydraulic jumps over rough bed. *Građevinar*, *71*(02.), 105-111.

Douglas, S., & Nistor, I. (2015). "On the effect of bed condition on the development of tsunami-induced loading on structures using OpenFOAM." *Natural Hazards*, 76(2), 1335-1356.

Douglas, S. (2016). "Numerical Modeling of Extreme Hydrodynamic Loading and Pneumatic Long Wave Generation: Application of a Multiphase Fluid Model." (Master dissertation, Université d'Ottawa/University of Ottawa), 116 p.

Dressler, R. F. (1952). "Hydraulic resistance effect upon the dam-break functions." *National Bureau of Standards*. Vol. 49, No. 3,217-225.

Dressler, R. F. (1954). "Comparison of theories and experiments for the hydraulic dam-break wave." *Int. Assoc. Sci. Hydrology*, 3(38), 319-328.

Duarte, R., Ribeiro, J., Boillat, J. L., & Schleiss, A. (2011). "Experimental study on dam-break waves for silted-up reservoirs." *Journal of Hydraulic Engineering*, 137(11), pp. 1385-1393.

Ead, S. A., & Rajaratnam, N. (2002). Hydraulic jumps on corrugated beds. *Journal of Hydraulic Engineering*, *128*(7), 656-663.

El, G.A.; Grimshaw, R.H.J.; Kamchatnov, A.M. (2005). "Wave Breaking and the Generation of Undular Bores in an Integrable Shallow Water System." Stud. Appl. Math. 114, 395–411.

El, G.A.; Grimshaw, R.H.J.; Kamchatnov, A.M. (2005). "Analytic model for a weakly dissipative shallow-water undular bore." Chaos Interdiscip. J. Nonlinear Sci. 15, 037102.

El, G.A.; Grimshaw, R.H.J.; Smyth, N.F. (2006). "Unsteady undular bores in fully nonlinear shallow-water theory." Phys. Fluids, 18, 027104.

El, G.A.; Khodorovskii, V.V.; Tyurina, A.V. (2005). "Undular bore transition in bi-directional conservative wave dynamics. Phys. D Nonlinear Phenom." 206, 232–251.

Elsheikh, N., Azimi, A. H., Nistor, I., & Mohammadian, A. (2020). Experimental Investigations of Hydraulic Surges Passing Over a Rectangular Canal. *Journal of Earthquake and Tsunami*, Vol. 14 No. 5, 31p.

Fadly, U., & Murakami, K. (2012). "Study on reducing tsunami inundation energy by the modification of topography based on local wisdom." *Journal of Japan Society of Civil Engineers, Ser. B3 (Ocean Engineering)*, 68(2), pp. 66-71.

FEMAP646, (2012). "Guidelines for Design of Structure for Vertical Evacuation from Tsunamis*", Federal Emergency Management Agency*. 2nd ed., Redwood, California, USA.

Ferziger, J.H.; Perić, M. (2002). "Computational Methods for Fluid Dynamics." Springer: Berlin/Heidelberg, Germany.

Fourie, J. G., & Du Plessis, J. P. (2003). A two-equation model for heat conduction in porous media (I: Theory). Transport in porous media, 53(2), 145-161.

Fraser, S., Leonard, G., Matsuo, I., & Murakami, H. (2012). "Tsunami evacuation: Lessons from the Great East Japan earthquake and tsunami of March 11th 2011" (p. 89). GNS Science.

Fritz, H. M., Borrero, J. C., Synolakis, C. E., & Yoo, J. (2006). 2004 Indian Ocean tsunami flow velocity measurements from survivor videos. *Geophysical Research Letters*, *33*(24).

Fritz, H.M., Phillips, D.A., Okayasu, A., Shimozono, T., Liu, H., Mohammed, F., Skanavis, V., Synolakis, C.E., Takahashi, T. (2012). "The 2011 Japan tsunami current velocity measurements from survivor videos at Kesennuma Bay using LiDAR." Geophys. Res. Lett, 39.

George, W. K. (2013). "Lectures in Turbulence for the 21st Century." Chalmers University of Technology.

Ghobarah, A., Saatcioglu, M., & Nistor, I. (2006). "The impact of the 26 December 2004 earthquake and tsunami on structures and infrastructure." *Engineering structures*, 28(2), 312-326.

Ghodoosipour, B. (2021). *Extreme Hydrodynamic Loading on Horizontal Pipelines* (Doctoral dissertation, Université d'Ottawa/University of Ottawa), 112 p.

Ghodoosipour, B. Stolle, J. Nistor, I. Mohammadian, A. and Goseberg, N. (2019a). "Experimental study on extreme hydrodynamic loading on pipelines." Part 1: Flow hydrodynamics." *Journal of Marine Science and Engineering*, 7(251), 20 p.

Ghodoosipour, B. Stolle, J. Nistor, I. Mohammadian, A., and Goseberg, N. (2019b). "Experimental study on extreme hydrodynamic loading on pipelines." part 2: Induced force analysis." *Journal of Marine Science and Engineering*, 7(262), 18 p.

Gill, M. A. (1980). Effect of boundary roughness on hydraulic jump. *Int. Water Power Dam Constr.;(United Kingdom)*, *32*(1).

Goseberg, N., Stolle, J., Nester, I., & Shibayama, T. (2016). "Experimental analysis of debris motion due the obstruction from fixed obstacles in tsunami-like flow conditions." *Coastal Engineering*, 118, 35-49.

Gualtieri, C., & Chanson, H. (2007). Experimental analysis of Froude number effect on air entrainment in the hydraulic jump. *Environmental Fluid Mechanics*, *7*(3), 217-238.

Gualtieri, C., & Chanson, H. (2010). Effect of Froude number on bubble clustering in a hydraulic jump. *Journal of Hydraulic Research*, *48*(4), 504-508.

Hager, W. H. (1985). B-jumps at abrupt channel drops. *Journal of hydraulic Engineering*, *111*(5), 861-866.

Hager, W. H. (1992). *Energy Dissipators and Hydraulic Jump* (Vol. 8). Springer Science & Business Media.

Hager, W. H., & Bretz, N. V. (1986). Hydraulic jumps at positive and negative steps. *Journal of hydraulic research*, *24*(4), 237-253.

Hager, W.H.; Sinniger, R. (1985) "Flow characteristics of the hydraulic jump in a stilling basin with an abrupt rise." J. Hydraul. Res., 23, 101–113.

Hammack, J. L. (1973). "A note on tsunamis: their generation and propagation in an ocean of uniform depth." *Journal of Fluid Mechanics*, 60(4), 769-799.

Hassanpour, N., Hosseinzadeh Dalir, A., Farsadizadeh, D., & Gualtieri, C. (2017). An experimental study of hydraulic jump in a gradually expanding rectangular stilling basin with roughened bed. *Water*, *9*(12), 945.

Hatland, S.D.; Kalisch, H. (2019). "Wave breaking in undular bores generated by a moving weir." Phys. Fluids. 31, 033601.

Heyns, J.A.; Malan, A.G.; Harms, T.M.; Oxtoby, O.F. (2013). "Development of a compressive surface capturing formulation for modelling free-surface flow by using the volume-of-fluid approach." Int. J. Numer. Methods Fluids, 71, 788–804.

Huang, M. F., Lau, I. W. H., Chan, C. M., Kwok, K. C., & Li, G. (2011). A hybrid RANS and kinematic simulation of wind load effects on full-scale tall buildings. Journal of wind engineering and industrial aerodynamics, 99(11), 1126-1138.

Hughes, W. C., & Flack, J. E. (1984). Hydraulic jump properties over a rough bed. *Journal of Hydraulic engineering*, *110*(12), 1755-1771.

Husain, D., Alhamid, A. A., & Negm, A. A. M. (1994). Length and depth of hydraulic jump in sloping channels. *Journal of Hydraulic Research*, *32*(6), 899-910.

Issa, R. I. (1986). "Solution of the implicitly discretised fluid flow equations by operator-splitting." *Journal of computational physics*, 62(1), 40-65.

Jánosi, I. M., Jan, D., Szabó, K. G., & Tél, T. (2004). "Turbulent drag reduction in dam-break flows." *Experiments in Fluids*, 37(2), pp. 219-229.

Jasak, H., Jemcov, A., & Tukovic, Z. (2007, September). "OpenFOAM: A C++ library for complex physics simulations." In International workshop on coupled methods in numerical dynamics (Vol. 1000, pp. 1-20). IUC Dubrovnik, Croatia.

Keller, E. A. (1971). Areal sorting of bed-load material: the hypothesis of velocity reversal. *Geological Society of America Bulletin*, *82*(3), 753-756.

Khankandi, A.; Tahershamsi, A.; Soares-Frazão, S. (2012) "Experimental investigation of reservoir geometry effect on dam-break flow." J. Hydraul. Res., 50, 376–387.

Kim, Y., Choi, G., Park, H., & Byeon, S. (2015). Hydraulic jump and energy dissipation with sluice gate. Water, 7(9), 5115-5133.

Kolmogorov, A. N. (1942). Equations of motion of an incompressible turbulent fluid. Izv Akad Nauk SSSR Ser Phys, 6, 56-58.

Lauber, G., & Hager, W. H. (1998). "Experiments to dambreak wave: Horizontal channel." *Journal of Hydraulic research*, 36(3), 291-307.

Leal, J.G.; Ferreira, R.M.; Cardoso, A.H. (2009). "Maximum Level and Time to Peak of Dam-Break Waves on Mobile Horizontal Bed." J. Hydraul. Eng., 135, 995–999.

Lee, J., Lee, J. H., Lee, J. H., & Sung, H. J. (2010). Coherent structures in turbulent boundary layers with adverse pressure gradients. *Journal of Turbulence*, *11*(28), 1-20.

Lien, F. S., Yee, E., & Cheng, Y. (2004). Simulation of mean flow and turbulence over a 2D building array using high-resolution CFD and a distributed drag force approach. Journal of Wind Engineering and Industrial Aerodynamics, 92(2), 117-158.

Liu, H.; Liu, H.; Guo, L.; Lu, S. (2017). "Experimental Study on the Dam-Break Hydrographs at the Gate Location." J. Ocean. Univ. China, 16, 697–702.

Macabuag, J. Raby A., Pomonis, A., Nistor, I., Wilkinson, S., Rossetto, T. (2018). "Tsunami design procedures for engineered buildings: a critical review." *Proc. Inst. Civ. Eng., Civ. Eng.,* Vol. 171 (4), pp. 166-178.

MacVicar, B. J., & Rennie, C. D. (2012). Flow and turbulence redistribution in a straight artificial pool. *Water Resources Research*, *48*(2), W02503, doi:10.1029/2010WR009374.

Madsen, P. A., Fuhrman, D. R., & Schäffer, H. A. (2008). "On the solitary wave paradigm for tsunamis." Journal of Geophysical Research: Oceans, 113(C12), 1-22.

Menter, F. R. (1993). Zonal two equation *k*-turbulence models for aerodynamic flows. AIAA paper, 2906, 1993.

Miyagi Prefecture, 2013. Teizan Canal Recovery and Reconstruction Vision, [Online]. Available: http://www.pref.miyagi.jp/uploaded/ attachment/284379.pdf [Access date: 30 August 2015]. (in Japanese)

Mohammadi, M., Nazari-Sharabian, M., & Karakouzian, M. (2021). A Novel Analytical Method for Evaluating the Characteristics of Hydraulic Jump at a Positive Step. *Water*, *13*(15), 2005.

Moore, W. L., & Morgan, C. W. (1959). Hydraulic jump at an abrupt drop. Transactions of the American Society of Civil Engineers, 124(1), 507-516.

Mossa, M., Petrillo, A., & Chanson, H. (2003). Tailwater level effects on flow conditions at an abrupt drop. *Journal of Hydraulic Research*, *41*(1), 39-51.

Nakamura S. (1973). "On Hydraulic bore and its Application to Tsunami Generation." Transaction of Sakhalin Complex Natural Science Research Institute (Memorial Issue for IUGG71 Moscow) 32: pp. 129–151. (In Russian).

Nandasena, N. A. K., Paris, R., & Tanaka, N. (2011). Reassessment of hydrodynamic equations: minimum flow velocity to initiate boulder transport by high energy events (storms, tsunamis). Marine Geology, 281(1-4), 70-84.

Nandasena, N. A. K., Sasaki, Y., & Tanaka, N. (2012). Modeling field observations of the 2011 Great East Japan tsunami: Efficacy of artificial and natural structures on tsunami mitigation. *Coastal Engineering*, *67*, 1-13.

Negm, A. A. M. (1996). Hydraulic jumps at positive and negative steps on sloping floors. *Journal of Hydraulic Research*, *34*(3), 409-420.

Nistor I, Saatcioglu M, Ghobarah A (2005) "The 26 December 2004 earthquake and tsunami-hydrodynamic forces on physical infrastructure in Thailand and Indonesia." *2005 Canadian coastal engineering conference,* Halifax, Canada, CD-ROM, 15 p.

Nistor, I., Palermo, D., Nouri, Y., Murty, T., and Saatcioglu, M. (2009). "Tsunami-induced forces on structures." *Handbook of Coastal and Ocean Engineering*. Singapore, World Scientific, pp. 261-286.

Nistor, I., Palermo, D., Cornett, A., & Al-Faesly, T. (2010). "Experimental and numerical modeling of tsunami loading on structures." Paper presented at the Proceedings of the Coastal Engineering Conference, Retrieved from www.scopus.com.

Nistor, I., & Palermo, D. (2015). "Post-Tsunami Engineering Forensics: Tsunami Impact on Infrastructure—Lessons from 2004 Indian Ocean, 2010 Chile, and 2011 Tohoku Japan Tsunami Field

Surveys." In *Handbook of coastal disaster mitigation for engineers and planners, Butterworth-Heinemann*, pp. 417-435.

Nouri, Y. (2008). "The impact of hydraulic bores and debris on free standing structures." (Doctoral dissertation, University of Ottawa (Canada).

Nouri, Y., Nistor, I., Palermo, D., & Cornett, A. (2010). "Experimental investigation of tsunami impact on free standing structures." *Coastal Engineering Journal*, 52(01), 43-70.

Oertel, M., & Bung, D. B. (2012). "Initial stage of two-dimensional dam-break waves: laboratory versus VOF." *Journal of Hydraulic Research*, 50(1), pp. 89-97.

OpenCFD Ltd. (2015a). OpenFOAM User Guide, v. 2.4.0. OpenFOAM Foundation Ltd., Available at: http://foam.sourceforge.net/docs/Guides-a4/UserGuide.pdf.

OpenFOAM (2014). OpenFOAM: the open source CFD toolbox. http://www.openfoam.com

OpenFOAM 2019. OpenFOAM: The Open Source CFD toolbox. http://www.openfoam.com.

Pagliara, S., Lotti, I., & Palermo, M. (2008). Hydraulic jump on rough bed of stream rehabilitation structures. *Journal of Hydro-Environment Research*, *2*(1), 29-38.

Peakall, J. Warburton, J. (1998). "Surface tension in small hydraulic river models- The significance of the Weber number." J. Hydrol. (New Zealand), 35, 199–212.

Rahman, M. M., Schaab, C., & Nakaza, E. (2017). "Experimental and numerical modeling of tsunami mitigation by canals." Journal of Waterway, Port, Coastal, and Ocean Engineering, 143(1), 04016012.

Rajaie, M., Azimi, A. H., Nistor, I., & Rennie, C. D. Experimental investigations on hydrodynamic characteristics of tsunami-like hydraulic bores impacting a square structure. *Journal of Hydraulic Engineering*, 2022, 148(3), 04021061

Rajaratnam, N., 1967, Hydraulic Jumps, Advances in Hydrological Sciences, ed. V. T. Chow, pp. 197-280, Academic Press, New York.

Rajaratnam, N., & Ortiz, N. V. (1977). Hydraulic jumps and waves at abrupt drops. Journal of the Hydraulics Division, 103(4), 381-394.

Ramalingeswara, R. B., Vijayaraghavan, D., Sarma, S. D., and Satyanaraya-nan, M. (2005). "Buckingham Canal saved people in Andhra Pradesh (India) from the tsunami of 26 December 2004." Paper to be presented at the Asia Oceania Geosciences Society, 2nd Ann. Meeting and Conf., Suntec, Singapore (June 20–24, 2005).

Ramsden, J. D. (1993). Tsunamis: Forces on a vertical wall caused by long waves, bores, and surges on a dry bed, Ph.D. thesis, California Institute of Technology, Pasadena, CA.

Ritter, A. (1892). The propagation of water waves. Ver Deutsch ingenieur zeitschr, 36(33 part 3), 947-954.

Salim, S. M., Buccolieri, R., Chan, A., & Di Sabatino, S. (2011). Numerical simulation of atmospheric pollutant dispersion in an urban street canyon: Comparison between RANS and LES. Journal of Wind Engineering and Industrial Aerodynamics, 99(2-3), 103-113.

Sarjamee, S. (2016). Numerical Modelling of Extreme Hydrodynamic Loading on Coastal Structures (Mater dissertation, Université d'Ottawa/University of Ottawa), 85 p.

Sarjamee, S. Nistor, I. and Mohammadian A. (2017a). "Numerical Investigation of the Influence of Extreme Hydrodynamic Forces on the Geometry of Structures Using OpenFOAM." *Natural Hazards* 87(1), pp. 213–35.

Sarjamee, S. Nistor, I. and Mohammadian, A. (2017b). "Large eddy simulation of extreme hydrodynamic forces on structures with mitigation walls using OpenFOAM." *Natural Hazards*, 85(3), pp.1689-1707.

Sawyer, A. M., Pasternack, G. B., Moir, H. J., & Fulton, A. A. (2010). Riffle-pool maintenance and flow convergence routing observed on a large gravel-bed river. *Geomorphology*, *114*(3), 143-160.

Shafiei, S.; Melville, B.W.; Shamseldin, A.Y. Experimental investigation of tsunami bore impact force and pressure on a square prism. Coastal Engineering, 2016, 110, 1-16.

Sharp, J. J. (1974). Observations on hydraulic jumps at rounded step. *Journal of the Hydraulics Division*, *100*(6), 787-795.

Shafiei, S.; Melville, B.W.; Shamseldin, A.Y. (2016). "Experimental investigation of tsunami bore impact force and pressure on a square prism." Coast. Eng., 110, 1–16.

Shafiei, S.; Melville, B.W.; Shamseldin, A.Y.; Beskhyroun, S.; Adams, K.N. (2016). "Measurements of tsunami-borne debris impact on structures using an embedded accelerometer." J. Hydraul. Res. 54, 435–449.

Shugan, I.V.; Chen, Y.-Y.; Hsu, C.-J. (2020). "Experimental and Theoretical Study on Flood Bore Propagation and Forerunner Generation in Dam-Break Flow." Phys. Wave Phenom. 28, 274–284.

Soares Frazão, S. (2002). Dam-break induced flows in complex topographies. Theoretical, numerical and experimental approaches. Louvain-la-Neuve, Belgium: Université catholique de Louvain. PhD Thesis.

Streeter, V.L.; Wylie, E.B. (1979). Fluid Mechanics. New York: McGraw-Hill Book Company. ISBN 978-0-07-062232-6.

St-Germain, P. (2012). "Numerical modeling of tsunami-induced hydrodynamic forces on free-standing structures using the SPH method." University of Ottawa (Canada), 316 p.

St-Germain, P., Nistor, I., & Townsend, R. (2012). Numerical modeling of the impact with structures of tsunami bores propagating on dry and wet beds using the SPH method. International Journal of Protective Structures, 3(2), 221-255.

St-Germain, P., Nistor, I., Townsend, R., & Shibayama, T. (2014). "Smoothed-particle hydrodynamics numerical modeling of structures impacted by tsunami bores." *Journal of Waterway, Port, Coastal, and Ocean Engineering*, 140(1), pp. 66-81.

Stolle, J., Ghodoosipour, B., Derschum, C., Nistor, I., Petriu, E., & Goseberg, N. (2019). "Swing gate generated dam-break waves." *Journal of Hydraulic Research*, Vol. 57(5), pp. 675-678.

Sturtevant, B. (1965). "Implications of experiments on the weak undular bore." Phys. Fluids, 8, 1052–1055.

Sumer, B.M., Fredsøe, J. (2006) "Hydrodynamics Around Cylindrical Structures." World Scientific Publishing Company: Singapore.

Tanaka, N. (2009). "Vegetation bioshields for tsunami mitigation: review of effectiveness, limitations, construction, and sustainable management." *Landscape and Ecological Engineering*, 5(1), pp. 71-79.

Tcheukam-Toko, D., Mokem-Chetchueng, M., Mouangue, R., Beda, T., & Murzyn, F. (2013). Characterization of hydraulic jump over an obstacle in an open channel flow. *International Journal of Hydraulic Engineering (IJHE)*, *2*(5), 2013.

Thompson, D. M. (2006). The role of vortex shedding in the scour of pools. *Advances in Water Resources*, *29*(2), 121-129.

Thompson, P. L., & Kilgore, R. T. (2006). Hydraulic Design of Energy Dissipators for Culverts and Channels: Hydraulic Engineering Circular Number 14 (No. FHWA-NHI-06-086). National Highway Institute (US).

Tokida, K., and Tanimoto, R. (2012). "Lessons and views on hardware countermeasures with earth banks against tsunami estimated in 2011 great east Japan earthquake." Proc., Int. Symp. on Eng. Lessons Learned from the 2011 Great East Japan Earth, Tokyo, Japan, 463–474.

Van Balen, W., Uijttewaal, W. S., & Blanckaert, K. (2009). Large-eddy simulation of a mildly curved open-channel flow. *Journal of Fluid Mechanics*, *630*, 413-442.

Vargas-Magaña, R.M.; Marchant, T.R.; Smyth, N.F. (2021). "Numerical and analytical study of undular bores governed by the full water wave equations and bidirectional Whitham–Boussinesq equations." Phys. Fluids, 33, 067105.

Versteeg, H.K.; Malalasekera, W. (2007) "An Introduction to Computational Fluid Dynamics." The Finite Volume Method, 2nd ed.; Pearson Education Ltd.: Harlow, UK; New York, NY, USA.

von Häfen, H., Goseberg, N., Stolle, J., & Nistor, I. (2019). "Gate-Opening Criteria for Generating Dam-Break Waves." *Journal of Hydraulic Engineering*, 145(3), 04019002.

Watanabe, S., Mikami, T. & Shibayama, T. (2016). "Laboratory Study on Tsunami Reduction Effect of Teizan Canal.". *Proceedings of the 6th International Conference on the Application of Physical Modelling in Coastal and Port Engineering and Science (Coastlab16) Ottawa*, Canada, May 10-13, 2016

Wang, H., & Chanson, H. (2015). Air entrainment and turbulent fluctuations in hydraulic jumps. *Urban Water Journal*, *12*(6), 502-518.

Wei, Z.; Dalrymple, R.A.; Hérault, A.; Bilotta, G.; Rustico, E.; Yeh, H. SPH modeling of dynamic impact of tsunami bore on bridge piers. J. Coastal Eng., 2015, 104, 26–42.

Weller, H. G. (2008). A new approach to VOF-based interface capturing methods for incompressible and compressible flow. OpenCFD Ltd., Report TR/HGW, 4.

Whitham, G. B. (1955, January). The effects of hydraulic resistance in the dam-break problem. In Proceedings of the Royal Society of London A: Mathematical, Physical and Engineering Sciences (Vol. 227, No. 1170, pp. 399-407). The Royal Society.

Wilcox, David C (1998). "Turbulence Modeling for CFD." Second edition. Anaheim: DCW Industries, 1998. pp. 174.

Wilkinson, S. N., Keller, R. J., & Rutherfurd, I. D. (2004). Phase-shifts in shear stress as an explanation for the maintenance of pool–riffle sequences. *Earth Surface Processes and Landforms*, *29*(6), 737-753.

Wu, S., & Rajaratnam, N. (1995). Free jumps, submerged jumps and wall jets. *Journal of Hydraulic Research*, *33*(2), 197-212.

Wüthrich, D., Pfister, M., Nistor, I., & Schleiss, A. J. (2017). "Experimental Study of Tsunami-Like Waves on Dry and Wet Bed Generated with a Vertical Release Technique." *Journal of Waterway, Port, Coastal, and Ocean Engineering.*

Wüthrich, D., Pfister, M., Nistor, I., & Schleiss, A. (2017). "Estimation of Wave Propogation Velocity on a Channel with Smooth and Rough Bed." In Proceedings of the 37th IAHR World Congress (No. CONF, pp. 3522-3528).

Wüthrich, D., Pfister, M., Nistor, I., & Schleiss, A. J. (2018a). "Experimental study of tsunami-like waves generated with a vertical release technique on dry and wet beds." *Journal of Waterway, Port, Coastal, and Ocean Engineering*, *144*(4), 04018006.

Wüthrich, D., Pfister, M., Nistor, I., & Schleiss, A. J. (2018b). "Experimental study on the hydrodynamic impact of tsunami-like waves against impervious free-standing buildings." *Coastal Engineering Journal*, *60*(2), 180-199.

Wüthrich, D., Pfister, M., Nistor, I., & Schleiss, A. J. (2018c). "Experimental study on forces exerted on buildings with openings due to extreme hydrodynamic events." *Coastal Engineering*, *140*, 72-86.

Wüthrich, D., Pfister, M., Nistor, I., & Schleiss, A. J. (2019). "Effect of building overtopping on induced loads during extreme hydrodynamic events." Journal of Hydraulic Research, 58(2), 1-16.

Xie, X., Liu, C.H., Leung, D.Y.C., Leung, M.K.H. (2006). "Characteristics of air exchange in a street canyon with ground heating." Atmospheric Environment 40 (33), 6396–6409.

Xing, T., Shao, J., & Stern, F. (2007, August). BKW-RS-DES of unsteady vortical flow for KVLCC2 at large drift angles. In Proceedings of the 9th International Conference on Numerical Ship Hydrodynamics (pp. 5-8).

Yakhot, V. and Orszag, S.A. (1986). "Renormalization group analysis of turbulence. I. Basic theory." *Journal of scientific computing*, 1(1), pp.3-51.

Yeh, H., Sato, S., & Tajima, Y. (2013). "The 11 March 2011 East Japan earthquake and tsunami: Tsunami effects on coastal infrastructure and buildings." *Pure and Applied Geophysics*, *170*(6-8), 1019-1031.